

The source mechanisms of low frequency seismic events on volcanoes

Sandra Karl

Submitted in accordance with the requirements for the degree of
Doctor of Philosophy

The University of Leeds
School of Earth and Environment
June 2014

Declaration

The candidate confirms that the work submitted is his own and that appropriate credit has been given where reference has been made to the work of others.

This copy has been supplied on the understanding that it is copyright material and that no quotation from the thesis may be published without proper acknowledgement.

The right of Sandra Karl to be identified as Author of this work has been asserted by her in accordance with the Copyright, Designs and Patents Act 1988.

Acknowledgements

Firstly, I would like to express my gratitude to my supervisor Jürgen (Locko) Neuberg for introducing me to, and passing on his knowledge about volcano-seismology. You have opened many doors for me, and inspired a deep love of Sancerre wine. I am grateful for all the (financial) support and opportunities to do field work, go to conferences, and network with other scientists. Additionally, I feel indebted to Sebastian Rost and Marge Wilson for taking on supervisor and advisory roles halfway through my PhD. I would like to sincerely thank you both, not only for the excellent scientific support, but especially for the personal and moral support that you have provided during what was a difficult time for me. I also acknowledge Sebastian Heimann and Simone Cesca from GFZ Potsdam for providing the codes I worked with, and also for warmly welcoming me during a very useful visit to Potsdam. Special thanks also to Richard Rigby for making the impossible possible when it came to any IT problems.

Thanks to all members, past and present, of the Volcanology Research Group at the University of Leeds which offered a friendly environment to practice talks and pass by new ideas. I particularly would like to thank Mark Thomas, who always had a minute to spare, no matter how dumb my question - you have greatly contributed to my volcanological understanding.

Doing a PhD is a rollercoaster of emotions, and who could know that better than my office mates and friends?! Thank you all for helping me get to where I am now, the human pyramids, and for finding supportive and cheerful words when I was down. The Geo-Babes, and in particular Hollie, Jo, Katie, Laura, and Sarah have brought about much banter and caused many tears of joy. You have enriched every single uni day, and made my weekends and evenings truly enjoyable. Special thanks also to: Curls, Emma, James, Julia and Luke.

During my time in Leeds, I have found dearest friends that I never want to miss again. Dave, my (gossip) partner in crime and very close friend, thank you for introducing me to this lovely city, non-Lager beers, and so much more. Hannah, thank you for encouraging me to stay true to myself. I feel truly fortunate to share many hilarious and joyful moments and memories with you two. I feel very lucky for having been accompanied by Becky and Kathi, two of my very best friends. Thank you for always

being game for anything during many field trips, conferences and holidays. And an even bigger thank you for all the hugs, love, and encouragement you offered me to any day- and nighttime. We are in this together - all the way!

For accepting me the (crazy) way I am I would like to give my warmest thank you to my best friend and house mate Lyndsey. It is hard to put into words how grateful I am for every single day in the dreamflat, the uncountable bottles of gin (“I can drink it neat!”), and invaluable chats I had with you. You have even made the many many hours spent in hospitals a pleasure.

Yoni, thank you so much for bringing music, fun and love into my life. Your gentleness and patience with me go beyond words. Thank you also for proof reading my thesis even though it is no ‘Volcano Hell’. I am greatly looking forward to all the adventures yet to come!

Am Allermeisten möchte ich jedoch meiner Familie danken. Mama, Papa, Manu und Andi: ohne euren Glauben an mich und eure Unterstützung wäre nichts von Alledem möglich gewesen! Ihr habt mir das wertvollste Geschenk von allen gemacht, indem ihr mich lieb habt, und mir helft, meinen Traum zu leben. Danke auch für die finanziellen Notspritzen in den 10 (!!) Jahren meiner Uni-Laufbahn. Und natürlich auch Danke dir, liebe Anna, dass du mir immer wieder zeigst, wie viel Liebe und Glück in den einfachsten Dingen stecken kann!

This PhD has been funded by The University of Leeds Research Scholarship and VUELCO.

Abstract

Volcanoes generate a variety of seismic signals. One specific type, the so-called low frequency (LF) event, has proven to be crucial for understanding the internal dynamics of the volcanic system. While many endeavours have concentrated on the nature and cause of the seismic coda, the actual trigger mechanism of these events is still poorly understood. Several conceptual source models have been developed, ranging from magma-water interaction, stick-slip motion of magma plugs, magma flow instabilities, repeated release of gas-ash mixtures into open cracks, magma wagging, to brittle fracturing of magma.

All but one trigger model, namely brittle failure of magma in the glass transition as response to the upwards movement of magma, fail to explain all observed characteristics of LF volcanic seismicity. Here, a spatially extended source, the ring fault structure, is developed to mimic the proposed source mechanism. The extended LF source is modelled as an arrangement of 8, 16 and 32 double couples (DCs) approximating a 30 m, 50 m and 70 m wide circular ring fault bounding the circumference of the volcanic conduit. Due to (partial) destructive interference, P-wave amplitudes of a ring fault structure are greatly reduced compared to single double couples and compensated linear vector dipoles (CLVDs), by 350% and 470%, respectively. It is shown here that these seismic amplitude differences may result in the underestimation of average slip and thus magma ascent rate by a factor of up to 3.5 when using an over simplified point source.

To resolve the driving forces of LFs, synthetic seismograms representing both point and spatially extended sources were inverted for the apparent physical source mechanism using moment tensor inversion techniques (MTI). If original input parameters were unknown, MTI results of the ring fault would indicate a combination of 63% isotropic and 37% CLVD components. The proposed moment tensor strongly resembles that of a real CLVD case. The results of this study give evidence that slip along the conduit walls yields the same MTI results as a subhorizontal tensile crack, and the importance of knowledge about the source nature becomes eminently significant.

Spatially extended source geometries describe an alternative to point dislocation sources. Additionally to the ring fault structure, this study provides a catalogue of further com-

plex source scenarios involving new spatially extended sources, such as slip along a dike, conduit segments, two simultaneously acting ring fault structures, and helix-like flow patterns. P-wave amplitudes and waveforms vary largely with source geometry, stressing that source geometry is key for source interpretations and thus it is not sufficient to assume a point source nature of the processes involved to generated the observed seismicity.

Contents

List of Figures	ix
List of Tables	xiii
1 Introduction	1
1.1 Modern understanding of volcanoes	1
1.2 Monitoring and forecasting tools at active volcanoes	2
1.3 Seismic signals in volcanic settings	3
1.3.1 Volcano-tectonic earthquakes	4
1.4 Low frequency volcanic earthquakes	5
1.4.1 Characteristics	6
1.4.2 Link between LF cyclic activity and deformation	7
1.5 Source mechanisms of low frequency seismicity	8
1.5.1 The trigger mechanism	9
1.5.2 The resonator	10
1.6 Moment tensor inversions	14
1.6.1 The earthquake moment tensor	14
1.6.2 Isotropic earthquake sources	15
1.6.3 Single force	16
1.6.4 Double couple (DC)	17
1.6.5 Compensated linear vector dipole	17
1.7 Soufrière Hills Volcano, Montserrat	19
1.7.1 Geological background and recent eruption history	19
1.7.2 Seismicity	21
1.8 Aims of this study	23
1.9 Thesis Outline	24
2 A quantitative approach to volcano seismic sources	26
2.1 Waveform modelling	26
2.1.1 Source time function	27
2.1.2 Global model parameters	27
2.1.3 Algorithm verification	28
2.2 Development of dike and cylindrical conduit source models	29

2.2.1	Ring fault	30
2.2.2	Dike	31
2.2.3	Input parameters: spatially extended sources	32
2.3	Comparison of simple and complex source mechanisms	34
2.3.1	Amplitudes	34
2.3.2	Waveforms	42
2.4	Dependency of waveforms on the source geometry	43
2.4.1	Number of point sources	44
2.4.2	Source diameter	46
2.5	Implications of the source nature on the occurring slip	48
2.6	Discussion and Summary	50
3	Radiation patterns of spatially extended seismic sources	53
3.1	First motions	54
3.2	Body wave radiation patterns	57
3.2.1	Double couple	57
3.2.2	Compensated linear vector dipole	59
3.3	2D body wave radiation patterns of the ring fault structure	60
3.3.1	P-wave radiation pattern	60
3.4	3D body wave radiation patterns of the ring fault structure	62
3.4.1	P-wave radiation pattern	62
3.5	3D body wave radiation patterns of a dike	64
3.5.1	P-wave radiation pattern	64
3.6	Comparison with conventional radiation patterns	65
3.7	Summary	67
4	Catalogue of synthetic complex sources	69
4.1	Simultaneous extended sources	70
4.1.1	Half conduit	71
4.1.2	Quarter conduit	74
4.2	Multiple sources	76
4.2.1	Two simultaneous ring faults	77
4.2.2	Staggered sources	79
4.2.3	Helix	81
4.3	Discussion and Summary	84
5	Classic moment tensor inversions of complex volcano seismic sources	87
5.1	Methodology	88
5.1.1	Application to volcanoes	90
5.1.2	Green's functions	91
5.1.3	Data	92
5.1.4	Moment tensor inversion tool	93
5.2	Results	94

5.2.1	Single double couple	94
5.2.2	CLVD	97
5.2.3	Ring fault	99
5.2.4	Dike	101
5.2.5	Ring fault segments	101
5.2.6	Two simultaneous ring faults	110
5.2.7	Staggered sources	113
5.2.8	Helix	113
5.3	Discussion and Summary	118
6	A Case Study: Soufrière Hills Volcano, Montserrat	122
6.1	The Montserrat Seismic Network	123
6.2	Dataset	124
6.3	First motions	127
6.4	Moment tensor inversion results	131
6.4.1	Inversion bandwidth 0.5-4 Hz	132
6.4.2	Inversion bandwidth 0.5-2 Hz	139
6.5	Comparison with inversions of synthetic data	156
6.6	Summary	158
7	Discussion and Conclusions	160
7.1	Implications of spatially extended sources for waveforms and amplitudes	160
7.2	Source depth and implications on first motions	163
7.3	Subhorizontal tensile crack vs. conduit model	164
7.4	Overview of conclusions	168
7.5	Future Work	170
A	Seismometer locations and responses	172
A.1	Seismometer and digitiser specifications	172
A.2	Signal restitution	172
B	Earthquake location tables	177
B.1	Absolute locations of long period earthquakes	177
B.1.1	Methodology	177
B.1.2	Results	177
C	Supplementary seismograms and moment tensor inversion results	183
	References	238

List of Figures

1.1	The volcanic edifice	2
1.2	Types of volcano seismic signals	3
1.3	Typical low frequency event	6
1.4	Crack and conduit model geometries	11
1.5	Equivalent body force system for an isotropic source	15
1.6	Equivalent body force system: single force	16
1.7	Equivalent body force system: double couple	17
1.8	Equivalent body force system: CLVD	18
1.9	Geological setting of Montserrat	20
1.10	Relationship between LF seismicity and tilt at SHV, Montserrat	22
1.11	Increase in LF seismicity prior to dome collapse event at SHV	23
2.1	Source time function wavelet and the delta impulse	28
2.2	Conceptual trigger model for LF seismicity	30
2.3	Octagonal arrangement of double couples as ring fault approximation	31
2.4	Trigonometric relationships for the ring fault segments	32
2.5	Receiver network for synthetic study	35
2.6	P-waveform of ring fault and normal fault	36
2.7	P-waveforms of the ring fault structure at receivers at $\alpha = 10^\circ$ to $\alpha = 40^\circ$	37
2.8	P-waveforms of the ring fault structure at receivers at $\alpha = 50^\circ$ to $\alpha = 80^\circ$	38
2.9	P-waveforms of a dike	40
2.10	P-waveforms of a CLVD source	41
2.11	The first order derivative relationship between double couple and ring fault	42
2.12	Ringfault amplitude and waveform dependency on epicentral distance	43
2.13	Azimuthal dependence of ring fault waveforms	44
2.14	Ring fault approximation using 16 point sources	45
2.15	Ring fault approximation using 32 point sources	45
2.16	Effect of number of acting point sources on waveforms	46
2.17	Effect of conduit diameter changes on waveforms	47
2.18	P-waveforms of the ring fault structure	51
3.1	Fault geometry used in earthquake studies	55

3.2	First motions of P-waves	56
3.3	Focal mechanism for a vertical dip-slip earthquake	56
3.4	The body force equivalent to a vertical dip-slip fault	57
3.5	P-wave radiation pattern: DC source	58
3.6	Focal mechanism: CLVD source	59
3.7	P-wave radiation pattern for a CLVD source	59
3.8	Geometrical relationship of ring fault segments	60
3.9	2D P-wave radiation pattern of the ring fault	62
3.10	3D P-wave radiation pattern of the ring fault	64
3.11	Zoom in of the octagon 3D P-wave radiation pattern	64
3.12	3D P-wave radiation pattern of the ring fault	64
3.13	Zoom in of the ring fault 3D P-wave radiation pattern	64
3.14	3D P-wave radiation pattern of the dike	65
3.15	Radiation pattern through a volcanic edifice	66
4.1	Source orientation of a half conduit (1)	71
4.2	Source orientation of a half conduit (2)	71
4.3	P-waveforms of a half conduit (1)	72
4.4	P-waveforms of a half conduit (2)	73
4.5	Source orientation of a quarter conduit (1)	74
4.6	Source orientation of a quarter conduit (2)	74
4.7	P-waveforms of a quarter conduit (1)	75
4.8	P-waveforms of a quarter conduit (2)	76
4.9	P-waveforms of two simultaneously acting ring faults	78
4.10	P-waveforms of single and two ring faults	79
4.11	P-waveforms of 4 staggered RF sources	81
4.12	Configuration of two helix like slip histories	82
4.13	P-waveforms of a helix (1)	83
4.14	P-waveforms of a helix (2)	84
5.1	A seismogram as a convolution of three effects	88
5.2	Displacement seismogram for N striking DC source	92
5.3	Schematic of the moment tensor inversion strategy	93
5.4	MTI solution: Step 1, point source solution for a single double couple .	95
5.5	MTI solution: Step 1, moment tensor solution for a single double couple	96
5.6	MTI solution: Step 2, point source solution for a single double couple (1)	97
5.7	MTI solution: Step 2, point source solution for a single double couple (2)	98
5.8	MTI solution: Step 2, moment tensor solution for a CLVD	100
5.9	MTI solution: Step 1, point source solution for a 50 m wide ring fault .	102
5.10	MTI solution: Step 1, moment tensor solution for a 50 m wide ring fault	103
5.11	MTI solution: Step 2, moment tensor solution for a 50 m wide ring fault	104
5.12	MTI solution: Step 2, moment tensor solution for a EW striking dike . .	105
5.13	MTI solution: Step 2, moment tensor solution for a half conduit (1) . .	106

5.14	MTI solution: Step 2, moment tensor solution for a half conduit (2)	108
5.15	MTI solution: Step 2, moment tensor solution a quarter conduit (1)	109
5.16	MTI solution: Step 2, moment tensor solution for a quarter conduit (2)	111
5.17	MTI solution: Step 2, 2 simultaneously acting ring faults	112
5.18	MTI solution: Step 2, staggered RF sources	114
5.19	MTI solution: Step 2, helix (1)	116
5.20	MTI solution: Step 2, helix (2)	117
6.1	The 1997 Montserrat seismic network	123
6.2	Vertical component seismograms of example event 07/06/97 04:04:33	125
6.3	Vertical component seismograms of example event 22/06/97 19:10:04	126
6.4	First motion polarity rose diagram	128
6.5	First motion polarity rose diagrams (1)	129
6.6	First motions of example event	130
6.7	Qualitative CLVD interpretation of example event	131
6.8	MTI solution: event 07/06/97, 04:03:33 (1 km source depth), inversion bandwidth 0.5-4 Hz	133
6.9	MTI solution: event 07/06/97, 04:03:33 (1.5 km source depth), inversion bandwidth 0.5-4 Hz	134
6.10	MTI solution: event 07/06/97, 04:03:33 (2 km source depth), inversion bandwidth 0.5-4 Hz	135
6.11	MTI solution: event 07/06/97, 04:03:33 (1 km source depth), inversion bandwidth 0.5-4 Hz	136
6.12	MTI solution: event 07/06/97, 04:03:33 (1.5 km source depth), inversion bandwidth 0.5-4 Hz	137
6.13	MTI solution: event 07/06/97, 04:03:33 (2 km source depth), inversion bandwidth 0.5-4 Hz	138
6.14	MTI solution: event 22/06/97, 19:10:04 (1 km source depth), inversion bandwidth 0.5-4 Hz	140
6.15	MTI solution: event 22/06/97, 19:10:04 (1.5 km source depth), inversion bandwidth 0.5-4 Hz	141
6.16	MTI solution: event 22/06/97, 19:10:04 (2 km source depth), inversion bandwidth 0.5-4 Hz	142
6.17	MTI solution: event 22/06/97, 19:10:04 (1 km source depth), inversion bandwidth 0.5-4 Hz	143
6.18	MTI solution: event 22/06/97, 19:10:04 (1.5 km source depth), inversion bandwidth 0.5-4 Hz	144
6.19	MTI solution: event 22/06/97, 19:10:04 (2 km source depth), inversion bandwidth 0.5-4 Hz	145
6.20	MTI solution: event 07/06/97, 04:03:33 (1 km source depth), inversion bandwidth 0.5-2 Hz	146
6.21	MTI solution: event 07/06/97, 04:03:33 (1.5 km source depth), inversion bandwidth 0.5-2 Hz	147

6.22	MTI solution: event 07/06/97, 04:03:33 (2 km source depth), inversion bandwidth 0.5-2 Hz	148
6.23	MTI solution: event 07/06/97, 04:03:33 (1 km source depth), inversion bandwidth 0.5-2 Hz	150
6.24	MTI solution: event 07/06/97, 04:03:33 (1.5 km source depth), inversion bandwidth 0.5-2 Hz	151
6.25	MTI solution: event 07/06/97, 04:03:33 (2 km source depth), inversion bandwidth 0.5-2 Hz	152
6.26	MTI solution: event 22/06/97, 19:10:04 (1 km source depth), inversion bandwidth 0.5-2 Hz	153
6.27	MTI solution: event 22/06/97, 19:10:04 (1.5 km source depth), inversion bandwidth 0.5-2 Hz	154
6.28	MTI solution: event 22/06/97, 19:10:04 (2 km source depth), inversion bandwidth 0.5-2 Hz	155
7.1	Time derivative relationship btw. DC and RF	163
7.2	Dependence of source depth on RF and CLVD first motions	164
B.1	Location results	178

List of Tables

2.1	Theoretical and picked P wave arrival times for an explosion source . . .	29
2.2	Ring fault segment model parameters	33
2.3	Azimuthal dependence of ring fault vertical ground velocity	36
2.4	Amplitude ratios between normal fault and ring fault	39
5.1	Summary of MTI results	118
6.1	The 1D velocity model for Soufrière Hills Volcano	124
A.1	Seismometer locations and specifications	173
A.2	The instrument responses for the Güralp CMG-40T (30 s) and Integra L100 instruments expressed in poles and zeros as velocity in Hz.	173
A.3	The instrument responses for the Güralp CMG-40T (30s) and Integra L100 instruments expressed in poles and zeros as velocity in radian/s.	175
A.4	The instrument responses for the Güralp CMG-40T (30s) and Integra L100 instruments expressed in poles and zeros as displacement in radian.	175
A.5	Step by step determination of the calibration factors to obtain true amplitude velocity and displacement seismograms from uncorrected traces. The values in the top three rows correspond to the Güralp CMG-40T (30 s) broadband instruments, while the bottom row represents the calibration factors for the single component Integra L100.	176
B.1	Absolute location results	180

Chapter 1

Introduction

There are a variety of volcanically-induced seismic signals observed on active volcanoes, whose source mechanisms are different from tectonic earthquakes. Seismic records of volcano related earthquakes often indicate a variety of complicated source mechanisms. In the history of volcano seismology, several conceptual models have been proposed to explain the complex source mechanisms of volcanic seismic sources, and to link sub-surface processes to the corresponding observed seismic signals. Seismicity on volcanoes is routinely recorded by many volcano observatories all over the world, but the potential to use these signals to forecast the eruptive behaviour of volcanoes is somewhat limited unless we understand the exact role of the source mechanism in a wider volcanological context. This research aims to contribute towards this understanding by taking a first step towards a quantitative rather than merely conceptual model of the excitation mechanisms of low frequency volcano-seismic activity. This introduction serves as a review of the relevant background and outlines the motivation and aims of this research.

1.1 Modern understanding of volcanoes

Throughout history, human beings have been thrilled by the spectacular displays volcanoes can bring about. Ancient societies often related these marvels to deities or evil spirits and therefore treated volcanoes with respect, but also with superstitious fear (Vitaliano, 1973; Blong, 1982). Only much later, in 1795, Hutton (1795) succeeded in throwing light on the phenomena that form the roots of volcanoes: in his work he introduced a steady-state model of the Earth which pioneered the now globally accepted concept that basaltic magmas originate due to heat in the interior of the Earth. Hutton's ideas were picked up and driven forward by Scrope (1825) who wrote the first

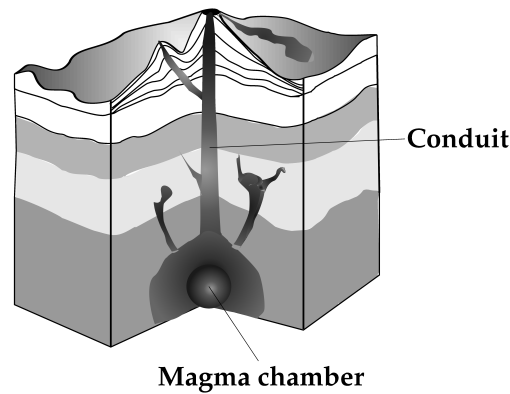


Figure 1.1: Sketch of a volcanic edifice showing a simplified view of the conduit which links the magma chamber to the surface. After Schmincke (1982).

textbook on volcanology, and first theorised the role of fractures to serve as channels for the rising magma. Evolved from these pioneer studies, our modern understanding of volcanic systems involves the rise of magma from the asthenosphere through areas where the lithosphere is fractured or otherwise weakened, until a fraction of it eventually reaches the surface through the conduit (Fig. 1.1) (Schmincke, 1982). However, the pathways magma takes to reach the surface are highly branched and intertwined, and the commonly used conduit model where magma ascends within a single channel is likely an over-simplified representation of the real sub-surface structure.

1.2 Monitoring and forecasting tools at active volcanoes

Volcanic activity and eruptions are often preceded and accompanied by various deviations from the quiescence state of a volcano. To ensure reliable hazard assessment, eruption forecasting, as well as risk mitigation, many volcanoes are continuously monitored using geophysical techniques. A number of physical parameters of a volcanic system can be monitored this way. Volcano seismology is the most commonly used geophysical surveillance tool to forecast the short to medium-term behaviour of a volcano. One of the key advantages of volcano seismology over other geophysical monitoring techniques is that it can link ground displacements measured at the surface to physical processes at depth, which makes it the only short-term forecasting tool deployed in real time.

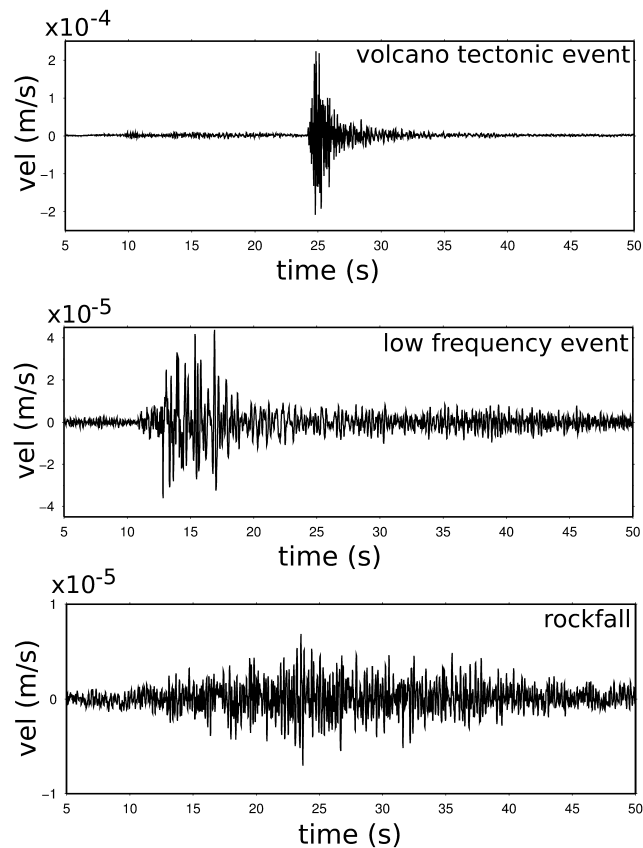


Figure 1.2: Different event types of seismicity on volcanoes as recorded on Soufrière Hills Volcano, Montserrat; *top*: volcano tectonic event (VT), *middle*: low frequency event (LF), *bottom*: rockfall event (RF).

1.3 Seismic signals in volcanic settings

Seismic signals observed in volcanic settings carry important information about the level and kind of activity at a specific volcano. This has made volcano seismology and seismic volcano monitoring an important tool in gaining insights into the sub-surface physical processes that lead to, and accompany volcanic eruptions (Sparks, 2003; Burlini et al., 2007). Prior to eruptions, rising magma interacts with its surrounding rocks and fluids, e.g., compressing and fracturing wall-rocks. These interactions perturb the stress distribution and pore fluid pressure, often resulting in fracturing and numerous small-magnitude earthquakes. The shape and characteristics of the observed seismograms can be related to particular volcanic phenomena, such as rock fracture, fluid oscillation and melt migration. Thus, a variety of seismic signals triggered by different physical mechanisms can be recorded prior to and during eruptions.

Volcano seismology has adapted many terms and methods from tectonic earthquake seismology, although proposed source mechanisms and related analysis techniques may differ. The complexity of volcanic earthquakes has led to confusions in nomenclature, and problems still arise from conflicting terminology in modern volcano seismology (Neuberg, 2011). Generally, five types of earthquakes can be identified in volcanic settings, and examples for the three mostly studied types are shown in Fig. 1.2: volcano-tectonic earthquakes (VTs), low frequency earthquakes (LFs), very-long period events (VLPs), explosion earthquakes and surficial events. For the scope of this study, volcanic tremor is interpreted as a superposition of discrete LF earthquakes and is therefore included as a sub-category of low frequency earthquakes. A detailed discussion of the links between LFs and volcanic tremor is given in Chapter 1.4.1.

With improving broadband seismometers, VLP events with typical periods in the range 3-100 s or longer (McNutt, 2002) have been observed at a number of volcanoes, including Stromboli and Aso volcano, and are commonly linked to the bursting of gas slugs (Neuberg et al., 1994) or hydrothermal processes (Yamamoto et al., 1999). Explosion events often coincide with visual observations or infrasonic (acoustic) signals (Green, 2005), and surface-generated signals such as rockfalls and pyroclastic flows (e.g. pyroclastic density currents and lahars) which are prevalently associated with active dome growth at silicic volcanoes.

Since the majority of studies concentrate on VTs and/or LFs these two sub-categories of volcano seismicity are discussed in detail below. A whole section is devoted to low frequency volcano seismic signals, their characteristics and origin, as they represent the core of this study.

1.3.1 Volcano-tectonic earthquakes

Events with clear P- and S-wave onsets occurring at depths of 1-10 km and with dominant frequencies ranging from 5-15 Hz are called volcano-tectonic (VT) or sometimes also high-frequency (HF) earthquakes (Miller et al., 1998a). The underlying source mechanism is usually interpreted as shear failure or slip along a fault, and makes VTs indistinguishable from ordinary double couple tectonic earthquakes in seismic records. At volcanoes, these events predominantly appear in swarms rather than in mainshock-aftershock sequences (Chouet et al., 2003), and are commonly considered as one of the

earliest precursory signs for an acceleration in volcanic activity (Roman and Cashman, 2006). The study of VT events mostly concentrates on the determination of the stress conditions and orientations, and VT earthquake locations are used to give a general idea of the size and shape of the magmatic plumbing system and its development with time. However, once magmatic pathways are established without further changes to the stress field, the dynamics of the volcanic system can be determined through the analysis of low frequency events and their link to sub-surface processes becomes crucial.

1.4 Low frequency volcanic earthquakes

Characteristically, low-frequency (LF) or long period (LP) seismicity shows harmonic frequency content ranging between 0.5 and 5 Hz (Chouet, 1996a; Neuberg et al., 1998). Since a tragic incident in 1993 at Galeras volcano, Columbia (Baxter and Gresham, 1997), where scientists failed to identify LF seismicity as precursory signals prior to a deadly eruption, the huge potential of this particular type of volcano seismic signal for eruption forecasting has been recognised (Fischer et al., 1994; Chouet, 1996a). After the Galeras fatalities in 1993, the occurrence of low frequency events alone has been used as an indicator of an acceleration of the volcanic system, and LFs have been interpreted successfully as seismic activity prior to an eruption at a number of volcanoes such as: Soufrière Hills Volcano (SHV), Montserrat (Miller et al., 1998a; Neuberg et al., 1998); Redoubt volcano, Alaska (Chouet et al., 1994; Stephens et al., 1994) and Asama volcano, Japan (Sawada, 1994).

However, to use the full potential of LFs as a forecasting tool, a full understanding of the physical source processes is crucial (Chouet, 1996a). Generally, their origin is thought to be associated with resonating fluid-filled conduits or fluid movements, and several models exist to explain their characteristics and origin: magma-water interaction (Zimanowski, 1998), stick-slip motion of magma plugs (Goto, 1999; Iverson et al., 2006), magma flow instabilities (Julian, 1994), repeated release of gas-ash mixtures into open cracks (Molina et al., 2004), magma wagging (Jellinek and Bercovici, 2011), and brittle fracturing of magma (Neuberg et al., 2006).

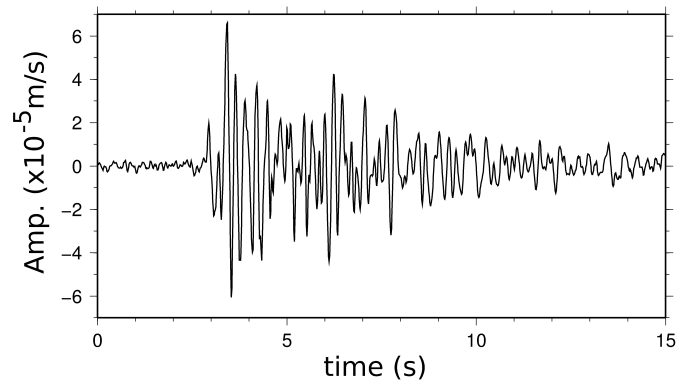


Figure 1.3: Vertical component seismogram of a typical low frequency event recorded at station MBGA on Montserrat. The initial trace was corrected for instrument response and digitiser gain to give this true amplitude seismogram.

1.4.1 Characteristics

With improving monitoring techniques and seismic networks being deployed on more and more volcanoes, low frequency seismicity has been observed at an increasing number of volcanoes worldwide. Its occurrence does not seem to be restricted to a particular tectonic setting or type of volcano, yet subtle property changes can be observed.

Low frequency earthquakes is a collective term for seismic events spanning over a spectral continuum, with long period earthquakes and so-called hybrid events forming end member seismic categories within it. An example of a typical LF event observed on Montserrat can be seen in Fig. 1.3. While hybrid events show an additional high frequency onset compared to long period earthquakes, single events can be recorded as either, dependent on the location of the receiver, as has been demonstrated on Montserrat (Neuberg et al., 2000). Hence, both long period and hybrid events seem to originate from the same seismic source, and have therefore been grouped together under the more generic term ‘low frequency volcanic earthquakes’ (Neuberg et al., 2000).

Independent of the volcanic system, LF volcanic seismicity exhibits one or several of the following characteristics when observed: (1) they occur in swarms, with (2) highly similar waveforms and (3) highly regular (re-)occurrences that, with increasing frequency of events, may (4) merge into continuous tremor, and most importantly, (5) often precede episodes of increased volcanic activity such as major dome collapses or sizeable explosions (Miller et al., 1998a; Aspinall et al., 1998; Hellweg, 2003). Low frequency

seismic activity usually occurs as discrete events with slowly decaying harmonic codas. Nonetheless, a large number of LFs with highly similar waveforms can often be observed within hours. Such swarms suggest a stationary and repetitive source process, as high waveform similarities are indicative of common source locations and travel paths from source to receiver (Green and Neuberg, 2006). However, as inter-event times shorten and the system accelerates such swarms can merge into tremor, lasting from minutes to days (Hammer and Neuberg, 2009). LF tremor often shows narrow-banded frequency content, and unsteady magma flow or fluid transport in the shallow plumbing system have been proposed as underlying physical source processes (Chouet, 1996b). Harmonic tremor, a special case of tremor signal, involves a peaked spectrum of integer harmonics, and can originate in two ways: by repetitive re-occurrence of identical wavelets where the fundamental frequency is determined by the repeat interval, or by a resonating system whose eigenfrequencies are manifested in the spectral peaks (Neuberg et al., 2000). These narrowly banded frequencies are sometimes observed to change systematically within minutes or days, producing so-called ‘gliding lines’ in the frequency spectrogram of the recorded signals (Benoit and McNutt, 1997; Neuberg et al., 1998). Depending on the assumed source model, the sudden temporal changes and associated gliding lines can either be explained by changes in the triggering frequency of discrete events (Powell and Neuberg, 2003) or variations of the physical parameters that underlie and control the eigenoscillations (Benoit and McNutt, 1997).

This, together with similar spectral ranges of tremor and LF events, gave ground for the idea of a common source process (Chouet, 1996a), and has found application in several studies since (e.g. Neuberg et al., 2000; Chouet, 1996a). Here I will use a common physical trigger to investigate the source mechanism of LF volcanic seismicity, using the conceptual trigger model of Neuberg et al. (2006) (see also Chapter 2.2).

1.4.2 Link between LF cyclic activity and deformation

Cyclic behaviour of active volcanic complexes takes place on a huge range of timescales, from a few minutes or hours up to decadal cycles or even beyond. Whilst eruptive behaviour of silicic volcanoes is the most obvious and frequently recognised parameter undergoing periodic changes, there are a number of other geophysical observables that follow similar patterns. With eruption prediction and hazard management in mind, a

multi-disciplinary approach, considering episodic changes in e.g. seismicity, ground deformation, gas flux, and other measurable parameters, is thus the key to understanding the controlling processes yielding such cyclic behaviours.

In a study based on SHV,Montserrat, Neuberg et al. (2000) first identified an 8 – 12 hour cyclicality of low frequency seismicity, which subsequently was successfully correlated with ground deformation measurements of the volcanic edifice (Voight et al., 1998). The maximum number of low frequency earthquakes within a swarm is generated when a maximum in tilt is reached (Voight et al., 1998). Furthermore, the initiation of LF swarm activity coincides with the inflection point corresponding to the maximum of the first time derivative of the tilt signal (Fig. 1.10) (Green, 2005). The cyclicality of tilt was proposed to be caused by the traction of magma on the conduit wall which exerts a shear force (Green et al., 2006), while stress relaxation in the volcano is thought to be responsible for the seismic cycles (Neuberg et al., 2006). These discoveries provide insights into the source mechanisms that generate low frequency seismicity, and provide a way to link quantitatively geophysical observables to physical processes in the sub-surface such as shallow magma movement and magma ascent rates.

1.5 Source mechanisms of low frequency seismicity

Despite their undoubted potential as eruption precursors and the many endeavours to gain a detailed understanding of them (e.g. Chouet, 1996a; Neuberg et al., 2000), the precise origin of low frequency earthquakes in volcanoes poses an unresolved challenge to the scientific community. To date, no single model has been able to explain the characteristics detected at all volcanoes. In fact, even for silicic systems alone, volcanologists still disagree over the excitation mechanisms and general nature of low frequency events. Low frequency events have been described as a consequence of path effects rather than source processes, an example being Harrington and Brodsky (2007) who ascribe low frequency events observed at Mount St. Helens volcano to brittle failure events with slow rupture velocities and complicated paths. An argument against this perception is the frequently observed common spectral characteristics of a single low frequency event across several stations within a seismic network (e.g. Fehler and Chouet, 1982; Gómez and Torres, 1997). Therefore many authors advance the view that the low frequency content of most observed signals must be due to a source ef-

fect, and that understanding the physical processes acting at the source of such LFs is crucial to exploiting the full potential of low frequency seismicity as a monitoring tool. Chouet (1996b) introduced the concept of a combination of a ‘trigger’, which generates the initial seismic energy, and a ‘resonator’, which traps the seismic energy and sustains the characteristic low frequency coda of the signal.

My work is fundamentally based on this concept, and the next sections present a detailed discussion of the suggested models for both of these two key components, with brittle failure of melt at the conduit walls being the favourite candidate for the source mechanism, and resonance of a fluid-filled body acting as resonator.

1.5.1 The trigger mechanism

Based on cross-correlation analysis of the recorded waveforms, the existence of event families of low frequency events at Soufrière Hills Volcano, Montserrat, has been proven (Rowe et al., 2004; Green and Neuberg, 2006; Ottenmöller, 2008). A specific event family only contains events that exhibit a high degree of waveform similarity, and can be active over hours, days, and even months, indicating the same trigger mechanism. Similar event families with almost identical waveforms have also been identified on many other volcanoes, such as Unzen Volcano, Japan (Umakoshi et al., 2008) and Volcàn de Colima, Mexico (Varley et al., 2010).

From the high similarity of low frequency events it can be concluded that all events belonging to one event family originated in a small source region and share a common travel path to a given receiver. The emitted frequencies of those events require a stable, non-destructive and repeatable source mechanism. Neuberg et al. (2006) introduced a conceptual model to describe a possible trigger mechanism for LP seismic signals that fulfils all required criteria. Based on field observations, experimental investigations, and numerical magma flow modelling, they suggested that low-frequency events at Montserrat may be triggered by the brittle failure of magma.

Neuberg et al. (2006) considered a highly viscous melt that succumbs to high strain rates at the conduit walls, and as a result ruptures. High strain rates at the conduit walls can occur due to the high lateral viscosity gradient controlled by gas and heat loss through the magma - host rock boundary (Collier and Neuberg, 2006). Once a

critical strain rate is reached, the so-called glass transition is crossed (Dingwell, 1996), and in a narrow depth range the highly viscous melt can rupture in a brittle manner (Tuffen et al., 2008). This generates seismic energy which then excites the resonance responsible for the long period coda of the observed LF signals (Neuberg et al., 2006). It has also been suggested that resonance in the conduit can occur in an area where magma has a high impedance contrast to the surrounding country rock (Neuberg et al., 2006).

A number of alternative source processes that could be responsible for triggering the seismic energy release needed for low frequency volcanic earthquakes have been proposed. These include: episodic interaction of super-heated water with magma (Zimanowski, 1998), fluid dynamic instabilities during ash venting (Julian, 1994), and stick-slip motion of magma ascending in the conduit (Iverson et al., 2006). In the following, I assume magma rupture (Neuberg et al., 2006) and stick-slip (Iverson et al., 2006) as the source model. I will advance these models by: (1) expanding the conceptual model to a quantitative investigation of waveform amplitudes and (2) exploring the actual fracture mechanism through a moment tensor analysis, using a set of complex sources instead of the common fault plane assumption.

1.5.2 The resonator

The idea of a resonating fluid-filled body as the underlying source for low frequency signals was first proposed several decades ago. The earliest models, however, could not overcome fundamental problems; for example the fluid-driven crack model of Aki et al. (1977) faced complications when trying to simulate the observed long duration of LF events. In their model, the fluid could not support acoustic waves and resulted in weak resonance and strong radiation loss. Additionally, in order to obtain periods of the length scale of those seen on volcanoes such as Mount Aso in Japan, very large magma reservoirs acting as resonators were required, at least when using only the acoustic velocity of the fluid to determine the resonance frequency of the crack. This issue was solved when a huge modelling effort by a group of scientists discovered the significance of interface waves. These are also called slow waves or crack waves (Chouet and Julian, 1985; Chouet, 1986, 1988). This type of ‘tube wave’ was first detected in borehole seismology, close to and within fluid-filled boreholes (Biot, 1952). They are fundamentally

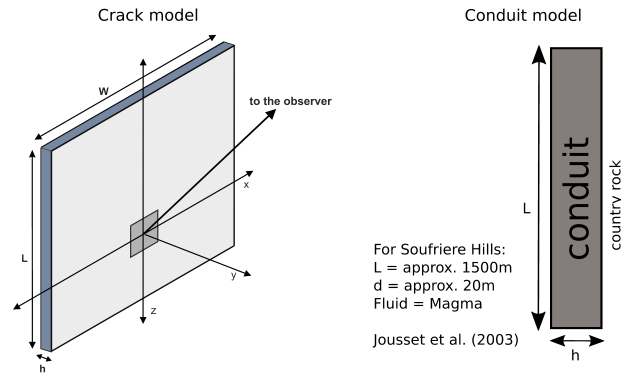


Figure 1.4: Schematic diagram showing the competing crack and conduit model geometries. *left:* The crack model, with large aspect ratios (length to height, L/h), containing compressible, low density and low viscosity fluids, such as gas or ash-gas mixtures. *right:* The conduit model, with low aspect ratios (L/h), containing comparatively high viscosity fluids such as magma. Figures modified from Collier (2005) and Jousset et al. (2003).

different from harmonic standing waves, whose resonant eigenfrequencies exclusively depend on the acoustic velocity of the fluid and the resonator length (Neuberg et al., 2000). Similarly, Ferrazzini and Aki (1987) studied an inviscid fluid layer sandwiched between two elastic half-spaces. They derived an analytical expression for the phase velocity of interface waves confined to the fluid-solid boundaries, and recognised that one mode of these highly dispersive waves has phase velocities lower than the acoustic velocity of the fluid. Owing to the ground-breaking findings of Chouet (1986, 1988) and Ferrazzini and Aki (1987), it was first understood that comparatively small bodies are capable of generating the desired low frequency resonance.

Yet ideas about the nature of the resonating source body as well as its geometry deviate from each other, depending on the aspect ratio of the body and the nature of the fluid proposed. Although diverse, all existing model geometries can broadly be grouped into two categories: crack models and conduit models (Fig. 1.4), and these will be discussed more closely in the subsequent sections.

Crack models

Aki et al. (1977) first proposed a fluid-filled ‘container’ embedded in an elastic solid which produces sustained harmonic waveforms. Magma migration within a narrow fluid-filled crack is driven by excess fluid pressure. They suggest that this is the source of the low frequency content of volcanic tremor on Kilauea volcano, Hawai’i. Aki et al.

(1977) also defined the ability of the fluid-filled body to resonate by the ‘crack stiffness factor’ C :

$$C = \begin{cases} \frac{B\lambda}{\mu h} & \text{for an infinitely long crack.} \\ \frac{BL}{\mu h} & \text{for a crack with finite length.} \end{cases} \quad (1.1)$$

In Equation 1.1, B is the volume modulus of the fluid in the crack, μ is the rigidity of the surrounding wall rock, h is the crack width, and for the case of an infinitely long crack λ is the wavelength of the propagating wave, which for a crack of finite length is replaced by the crack length L . The phase velocity of the interface wave decreases with increasing stiffness factor, and thus bodies with large aspect ratios (L/h) or big elastic moduli contrasts (B/μ) can trigger LF signals (Ferrazzini and Aki, 1987). Alternatively, Chouet (1986, 1988) investigated the fluid-driven crack model by studying the seismic wavefield associated with resonance in such narrow bodies.

Crack models have been suggested by multiple authors subsequently, all having aspect ratios between 100 and 10^4 . The crack must contain a highly compressible and low viscosity fluid, such as ash-charged gas (Morrissey and Chouet, 2001) or steam (Chouet et al., 1994). An example of a steam-filled crack is shown in Chouet et al. (1994), matching forward models to observed spectral characteristics on Redoubt Volcano, Alaska, which proposed the existence of a crack containing water and steam with dimensions $280 - 380\text{m} \times 140 - 190\text{m} \times 0.05 - 0.2\text{m}$ as the source of low frequency events.

Many investigators apply moment tensor inversions to resolve the signal coda, trying to find the geometry and directivity of the resonating body. This technique allows unravelling of the structure of point sources, and many authors have interpreted their results as resonance in shallow vertical or sub-horizontal crack-like structures within, or near to the volcanic feeding system. However, the point source approach brings huge ambiguities with it, and various geometries can be responsible for a given moment tensor inversion result (Chouet, 1996b) as is shown in Chapter 5. Studies applying this technique to low frequency events on volcanoes almost exclusively concentrate on the directivity of the resonating part of the signal, and include: Kusatso-Shirane Volcano,

Japan (Kumagai et al., 2002; Nakano et al., 2003; Nakano and Kumagai, 2005), Kilauea Volcano, Hawai'i (Kumagai et al., 2005), and Cotopaxi Volcano, Ecuador (Molina et al., 2008). The latest of a series of waveform inversions of low frequency earthquakes on Mount St. Helens involves the repeated pressurisation of a subhorizontal crack in the volcanic edifice (Waite et al., 2008). Gradually expanding steam pressurises the crack until a pressure threshold is reached and partial collapse and resonance of the crack is induced, generating the low frequency coda. Contrasting to the endeavours towards understanding the origin of the resonance, I concentrate on the actual source process, or trigger, which lies at the origin of the seismic energy that eventually sustains into LF volcanic seismicity. Hence, moment tensor inversions as carried out in Chapters 4 and 5 focus on inverting the first, high frequency, onset of seismicity, which is indicative of the physical process generating the volcanic seismicity.

This study concentrates on the trigger mechanism and the wavefield generated at the origin of LF events only, and therefore disregards attenuation of the signal as it advances through the medium. More information on the effects of attenuation on LF waveforms can be found in Smith (2010) whose PhD research concentrated on the attenuation effects on LF volcanic seismic signals.

Conduit resonance

Conduit models, in which resonance takes place in a conduit or dike, represent the opposing approach to the crack model, with the major difference being the lower aspect ratios (less than 100) of the resonating body. Amongst others, Neuberg et al. (2000) and Jousset et al. (2003, 2004) have described example geometries that fall into this category, and in one study proposed an approximately 600-1500 m long and 20 m wide conduit section as the source for the low frequency content of the signals. In contrast to the highly compressible gas mixtures employed in the crack models, conduit resonance is thought to take place in a conduit or dike filled with a silicic three phase magma consisting of melt, gas and crystals (Neuberg and O'Gorman, 2002).

Since the stiffness factor C (Equ. 1.1) includes both geometry properties and fluid parameters, models proposing large crack-like resonating bodies effectively require the fluid involved in the process to be a low viscosity ash and gas mixture. In theory, both types of model can explain the low frequency nature of the observed signals. After

the sustained resonance within highly viscous and bubble-rich magmas was challenged (Chouet, 1996b), Collier (2005) showed that under realistic pressure conditions resonance in conduits and cracks can be sustained. However, the geological plausibility of steam-filled cracks a few hundred meters wide may be questioned, since such structures have not been observed in nature. In contrast, dikes and conduits with low aspect ratios, a few meters wide and a few hundred meters long, like those proposed in most conduit models, can be found in the geological record, and in particular at silicic volcanoes (Eichelberger, 1995). Such low frequency events have been observed at volcanoes including Galeras volcano (Fischer et al., 1994) and Soufrière Hills Volcano, Montserrat (Neuberg et al., 1998).

1.6 Moment tensor inversions

Most quantitative investigations into the focal mechanisms of seismic signals have been based on the assumption that earthquakes are caused by shear faulting. However, the representation of non-double couple sources is of pivotal importance for investigating volcanic areas, where the driving forces are thought to be more complex. Information about the sub-surface processes yielding an earthquake signal can be obtained by comparing observed and synthetic waveforms and adjusting the source parameters until a suitable fit is obtained. This can be done using either a forward or inverse approach. I will use both forward and inverse techniques to take the study of non-double couple sources in volcanic settings a step further, and will add a set of new sources to the existing source catalogue for potential volcanic sources. The sources introduced represent the first numerical attempt to describe the excitation process of LF volcanic seismicity using spatially extended sources instead of a point source approach.

The seismic moment tensor offers insight into earthquake source parameters as it is capable of describing volumetric sources such as explosions and implosions as well as shear dislocation sources, and mixed volumetric and dislocation sources.

1.6.1 The earthquake moment tensor

The seismic moment tensor, \mathbf{M} , and its nine force couples M_{ij} ,

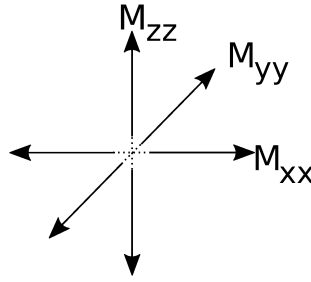


Figure 1.5: Explosion sources radiate energy equally in all directions, and are described using a triple dipole (shown here) as their equivalent body force system.

$$\mathbf{M} = \begin{pmatrix} M_{xx} & M_{xy} & M_{xz} \\ M_{yx} & M_{yy} & M_{yz} \\ M_{zx} & M_{zy} & M_{zz} \end{pmatrix}, \quad (1.2)$$

serve as a mathematical description of the forces acting during complex ruptures on potentially irregular faults. It is expressed by equivalent body forces, which, if acting on a point source at the earthquake's hypocentre, would produce the same displacement at a seismic station as the earthquake itself (Gilbert, 1970). The moment tensor describes both the source geometry of an event, by a combination of different moment tensor components, and its size, via the scalar moment, M_0 , of the earthquake.

As M is a tensor, standard tensor operations can be performed on it. Thus, M can be rotated in order to obtain a diagonal matrix, m , with elements corresponding to the eigenvalues of M . By decomposing m into its isotropic and deviatoric parts, it is then possible to gain information about the source mechanisms. The isotropic term describes any volume change during the earthquake, whereas the deviatoric component describes the deformation of the body at a stable volume V . An example of the latter is the so-called CLVD (Compensated Linear Vector Dipole) mechanism, which often serves to describe volcanic sources and will be further discussed in Chapter 1.6.5.

1.6.2 Isotropic earthquake sources

While many explosions are man made, fluid and gas migration linked to magmatic processes, or with sudden phase transitions or metastable minerals, can cause an isotropic signal naturally. In homogeneous media, the physical processes at the source of an

explosion differ from those of a conventional earthquake, leading to the exclusive generation of a P-wave. The initial shock wave expands and diminishes in amplitude until a point is reached at which deformations are small enough to occur elastically, generating a spherical P-wave. Other phases such as SV and Rayleigh waves are generated through P-wave interactions with interfaces in the propagation medium. It should be noted that pre-existing asymmetric or non-isotropic stress distributions in the subsurface may lead to the generation of an additional direct S-phase in nature.

$$\mathbf{M} = \begin{pmatrix} M_0 & 0 & 0 \\ 0 & M_0 & 0 \\ 0 & 0 & M_0 \end{pmatrix}. \quad (1.3)$$

For explosion and implosion events the radiation based on the moment tensor is the same in all directions, all compressional or all dilatational, respectively, and is modeled using a triple dipole as an equivalent body force system (Fig. 1.5). The moment tensor comprises three non-zero and equal diagonal terms with a resulting non-zero trace $3M_0$ (Equ. 1.3), which represents a volume change.

1.6.3 Single force

Originally, single forces (SF) (Fig. 1.6) were used to model shear faulting in tectonic settings. In the 1960s, however, Maruyama (1963) and Burridge and Knopoff (1964) established that faulting in isotropic elastic media should be represented by pairs of force couples whose torques cancel each other to conserve momentum.

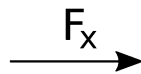


Figure 1.6: Equivalent body force system for a horizontal single force.

To the present day, single forces remain apparent in addition to the moment tensor solutions of volcanic seismicity. In volcanoes, SFs are generally linked to mass transfer or viscous fluid movements (Takei and Kumazawa, 1994), and have been interpreted as upwelling magma in the volcanic edifice (Ohminato et al., 2006). However, it has been shown that apparent strong SF components can also be an artifact resulting from uncertainties in both source location and velocity structure (Ohminato et al., 1998;

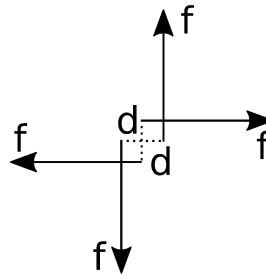


Figure 1.7: Schematic of a pair of force couples, a so-called double couple. Double couples are the equivalent body force description of shear faulting and are used to model the source mechanism of high frequency seismic events in volcanic systems.

Chouet et al., 2003; Bean et al., 2008; De Barros et al., 2013).

1.6.4 Double couple (DC)

In tectonic settings, shear faulting is the most common cause of earthquakes (Gilbert, 1984; Lawson, 1908). This type of rupture also finds application in volcanology where shear faulting is thought to be the cause of high frequency seismic events. The corresponding equivalent body forces for such a scenario are a double couple force system (Fig. 1.7). One force couple points in the direction of slip on the fault, while the second force couple is needed to avoid angular momentum on the fault. Due to the presence of two perpendicular force couples the double couple representation of shear faulting is ambiguous, and slip on either the fault or its perpendicular auxiliary plane both result in the same equivalent body forces, and therefore the same seismic radiation.

Earthquake source mechanisms related to volcanic settings, in particular the physical processes underlying low frequency volcano seismic signals, often deviate from a simple shear faulting scenario, and non-double couple focal mechanisms have to be considered.

1.6.5 Compensated linear vector dipole

Compensated linear vector dipoles (CLVDs) are one class of non-DC seismic sources. All but the three diagonal force couples of the moment tensor are zero, with one of the diagonal terms being -2 times the magnitude of the others. The zero trace of the moment tensor, where λ and μ are the Lamé elastic constants, indicates no volume change:

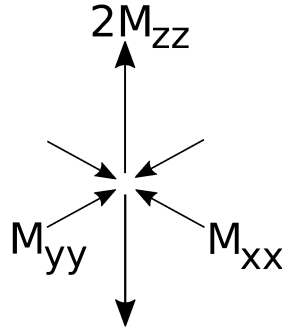


Figure 1.8: The compensated linear vector dipole as an equivalent body force system finds application in volcanic areas.

$$\mathbf{M} = \begin{pmatrix} -\lambda & 0 & 0 \\ 0 & \lambda/2 & 0 \\ 0 & 0 & \lambda/2 \end{pmatrix}. \quad (1.4)$$

This type of earthquake representation finds application in volcanic areas, because it can explain the seismic records observed in volcanic environments. Two primary explanations for the nature of CLVD source processes exist. The concept of an inflating magma dike was introduced by Aki and Richards (1980), and later adapted by Chouet (1996b) for the idea of an opening fluid-filled crack generating low frequency volcano seismic events. Most recently, Waite et al. (2008) have interpreted the compensated linear vector dipole solution as a horizontally dipping, steam-filled crack. The moment tensor representation for this system is:

$$\mathbf{M} = \begin{pmatrix} \lambda & 0 & 0 \\ 0 & \lambda & 0 \\ 0 & 0 & \lambda + 2\mu \end{pmatrix}, \quad (1.5)$$

which can be decomposed into an isotropic and a CLVD component:

$$\begin{pmatrix} \lambda & 0 & 0 \\ 0 & \lambda & 0 \\ 0 & 0 & \lambda + 2\mu \end{pmatrix} = \begin{pmatrix} \lambda + 2/3\mu & 0 & 0 \\ 0 & \lambda + 2/3\mu & 0 \\ 0 & 0 & \lambda + 2/3\mu \end{pmatrix} + \begin{pmatrix} -2/3\mu & 0 & 0 \\ 0 & -2/3\mu & 0 \\ 0 & 0 & 4/3\mu \end{pmatrix} \quad (1.6)$$

On the other hand, in agreement with equations 1.3 and 1.4, it has been suggested that CLVDs are due to near-simultaneous earthquakes on nearby faults of different geometries or orientations (Nettles and Ekström, 1998). They considered reverse faulting on cone-shaped ring faults surrounding the magma chamber to explain data from a volcano in Iceland. The superposition of two double couple sources of different orientations and with moments M_0 and $2M_0$ can be expressed as:

$$\begin{pmatrix} M_0 & 0 & 0 \\ 0 & 0 & 0 \\ 0 & 0 & -M_0 \end{pmatrix} + \begin{pmatrix} 0 & 0 & 0 \\ 0 & -2M_0 & 0 \\ 0 & 0 & 2M_0 \end{pmatrix} = \begin{pmatrix} M_0 & 0 & 0 \\ 0 & -2M_0 & 0 \\ 0 & 0 & M_0 \end{pmatrix} \quad (1.7)$$

1.7 Soufrière Hills Volcano, Montserrat

The case study described in Chapter 6 focuses on Soufrière Hills Volcano (SHV), Montserrat, and all modelling parameters for input into the numerical investigations in Chapters 2 to 4 were chosen to fit values appropriate for this particular volcano. SHV provides excellent conditions for the study of the source mechanisms of low frequency events: the volcano has been well monitored since its re-awakening in 1995, and the extensive seismic network deployed on the island has recorded LF signals consistently during this period (e.g. Neuberg et al., 2000). This presents a great opportunity to add to the knowledge on low frequency events in general, and to take advantage of, but also to complement pre-existing studies based on Montserrat.

1.7.1 Geological background and recent eruption history

Montserrat, West Indies, is a volcanic island located in the northern part of the Lesser Antilles (Fig. 1.9). Magmatic activity is the result of the subduction of oceanic lithosphere of the Atlantic Plate beneath the Caribbean Plate (LeFriant et al., 2004). The island of Montserrat is small, with maximum dimensions of 10 km (E-W) by 16 km (N-S). Montserrat has experienced active volcanism for approximately 4.3 Ma, and is made up of at least three volcanic complexes, with decreasing age from north to south (Rea, 1974; Harford et al., 2002). SHV in the south of the island is the youngest complex of these volcanic centres and is assumed to have been active from at least 170 ka to the present (Harford et al., 2002). There is evidence from $^{40}\text{Ar}/^{39}\text{Ar}$ dating and morphological studies indicating the existence of at least four former domes and a history of dome collapse events within SHV (Rea, 1974; Harford et al., 2002).

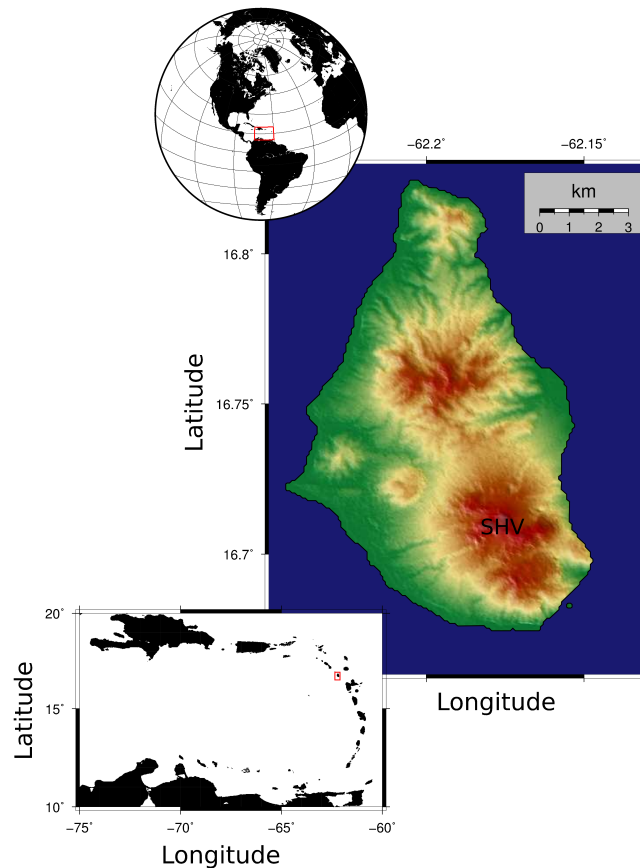


Figure 1.9: Geological setting of Montserrat island. The top left inset gives the position of the Lesser Antilles on the globe, while the lower left inset displays the volcanic arc itself. The red box indicates Montserrat's position within the Lesser Antilles. Soufrière Hills Volcano (SHV) is located in the south of Montserrat island, within the area of increased elevation.

The currently ongoing eruption of SHV began in July 1995 after approximately 340 years of dormancy, and following a period of elevated earthquake activity since 1992 (Young et al., 1998). The magmatic feeder system is believed to transport magma from about 6 km depth into a 30 m wide conduit in the last few hundred meters below the surface (Barclay et al., 1998; Watts et al., 2002).

Initially slow extrusion rates steadily increased through 1996 and 1997, culminating in a lateral sector collapse on 26 December 1997. A period of repetitive Vulcanian explosions followed and resulted in a second dome collapse event on June 25th 1997 (Druitt et al., 2002). Extrusive phases of lava dome growth have alternated with distinct 1.5-2 year periods of relative quiescence (Wadge et al., 2010), with several major dome collapses in December 1997 (Voight et al., 1998), March 2000 (Carn et al., 2004), July

2003 (Herd et al., 2003), May 2006 (Loughlin et al., 2007), and February 2010 (Cole et al., 2010) punctuating these cycles.

1.7.2 Seismicity

Volcano-tectonic earthquakes

As discussed in Chapter 1.3.1, volcano-tectonic earthquakes are one type of volcano seismic signal that have been observed and studied on numerous volcanoes worldwide. Montserrat, where VT events with frequencies above 5 Hz and characteristic impulsive P- and S-wave onsets have been observed and interpreted as brittle failure of the conduit wall-rocks throughout the entire eruptive history, is no exception. At SHV, VTs have been used to obtain the local stress conditions of the volcanic system: Roman and Cashman (2006) and Roman et al. (2008) attempted to link changes in the dominant azimuth of the P-axis of VT fault plane solutions to magma intruding into a dike below the edifice.

Rockfall and pyroclastic density flow signals

With episodic dome growth periods and at times high enough extrusion rates to cause dome instabilities, rockfall and surface flow signals have been one of the most common seismic signals detected on SHV during the ongoing eruption, with more than 27,000 individual events being recorded in the years 1996 to 1998 alone (Calder et al., 2002). It is therefore perhaps unsurprising that changes in the rockfall event frequency, dominant direction and event durations can be well correlated with temporal changes in extrusion rates (Calder et al., 2005), eruption style (Calder et al., 2002), as well as variations in speed and direction of the extrusion of dome lobes (Watts et al., 2002). The study of rockfall signals at Soufrière Hills Volcano has also been shown to provide useful information to improve and constrain extrusion rate and dome and talus slope evolution models (e.g. Hale et al., 2009). The waveform characteristics of surface flow signals, in particular the lack of clear P- or S-wave onsets (Miller et al., 1998a), make event location using conventional travel time techniques impossible. However, Jolly et al. (2002) successfully applied an alternative location technique to rockfall signals and could, by inspecting relative signal amplitudes at several stations, provide invaluable information on the direction of pyroclastic flows on the flanks of SHV.

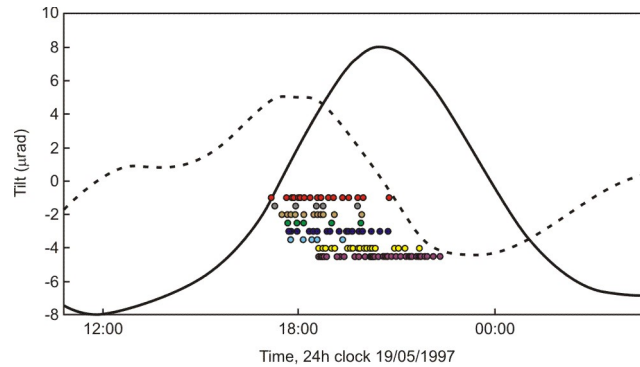


Figure 1.10: Relationship between LF seismicity and tilt at SHV, Montserrat, on 19 May 1997. Dots represent individual events, while colours group event families. Onset and duration of event families are compared to tilt (solid line) and tilt derivative (dashed lines) recorded of the same period (adapted from Neuberg et al. (2006)).

Low frequency seismicity

Low frequency seismicity at SHV can be distinguished from other seismic signals such as VTs or rockfalls, due to its characteristic high-frequency onset and slowly decaying harmonic codas. The high frequency onset is, however, not always observed, and thus the identification of events of this type is sometimes misleading and has led to confusion in nomenclature. Despite these minor differences in waveforms, both types of seismic signal should, however, be regarded as resulting from the same source processes, with low frequency (lacking high frequency onsets) and hybrid events simply representing end-members of a continuum of low frequency seismicity at SHV (Neuberg et al., 2000).

Low frequency events at SHV have been observed to occur periodically, with large numbers being recorded in the earlier stages of the eruption in 1995-1996 (White et al., 1998) and 1997-1998 (Neuberg et al., 1998), as well as preceding major explosions such as on July 29, 2008 (Stewart et al., 2008). During a single eruptive period many hundreds of thousands of low frequency events may occur, with thousands of them taking place within a few hours (White et al., 1998). In an approach to identify systematic changes and patterns in the activity of SHV, Green (2005) introduced a classification scheme that grouped similar events into families or multiplets based on their particular waveforms. Low frequency event families were found to correlate with deformation and tilt signals of the volcanic edifice, with the maximum positive derivative of tilt and the onset of low frequency seismic activity coinciding (Fig. 1.10) (Green et al., 2006; Neu-

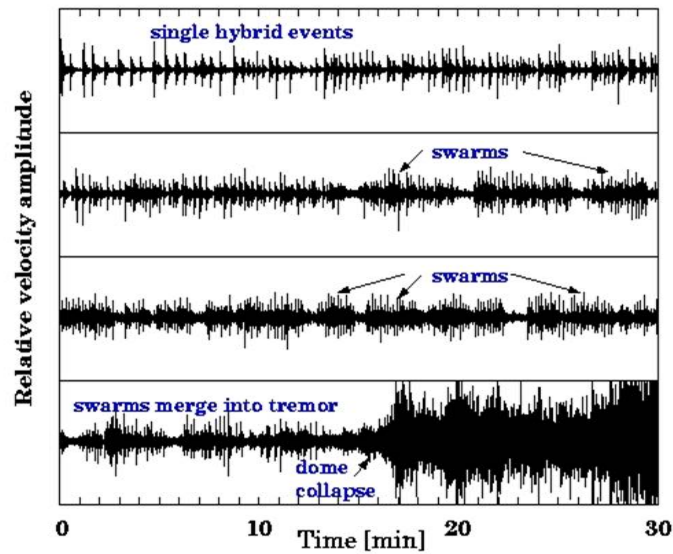


Figure 1.11: Single LF events merge into distinct swarms and, a short time before a dome collapse, into tremor. Observations from Montserrat, station MBGA, vertical component, 25/6/97. Illustration taken from (Neuberg, 2000).

berg et al., 2006). With increasing tilt, event families were shown to evolve throughout the seismic swarm, and ceased once the derivative of the tilt reached a minimum. With this in mind and taking the tilt derivative as a proxy for the rate of magma movement in the volcano, Green et al. (2006) concluded that low frequency events must be directly related to changes in the magma ascent rate within the edifice or conduit system.

The key feature of low frequency events at SHV for this study, however, is the fact that they occur in swarms which are often observed to precede major dome collapse events or explosions (Neuberg, 2000) (Fig. 1.11), and that their dynamics can be related to the magma ascent rate (Hammer and Neuberg, 2009).

1.8 Aims of this study

The primary aim of this study is to improve our understanding of the physical processes responsible for LF seismicity at volcanoes. This project aims to explore a wide domain of potential source processes to contribute to the quantitative study of this type of seismic signal from volcanoes. While most investigations of LF seismicity at volcanoes have concentrated on the origin of the long period coda of these events, this study aims to provide a better understanding of the actual excitation process at the source of LF

seismicity. In particular, the objectives of this study are therefore:

1. To introduce spatially extended sources as possible triggers of LFs. Advancing from point source descriptions to spatially extended sources will contribute to a more realistic approach to model the trigger mechanism of LF seismicity.
2. To explore a wide domain of spatially extended sources as possible excitation mechanisms of LFs. The geometry of a number of spatially extended sources is developed within this study; seismograms for ring faults, dikes, ring fault segments, multiple ring faults, as well as sources with time history, were calculated and analysed to provide a catalogue of potential source mechanisms of LF earthquakes for comparison with real data examples.
3. To establish the P-wave radiation patterns of spatially extended sources such as the ring fault structure which is proposed as the excitation process of low frequency volcanic signals.
4. To investigate the scale of error introduced when inverting spatially extended sources using classical moment tensor inversion techniques. Assuming point sources, as in most moment tensor inversion codes, the actual source mechanism will not be resolved, but will instead be *mapped* into a point source description, introducing an inevitable error into the solution. Here, the consequences this can have concerning interpretations of observed LF seismicity and its origin are outlined.
5. To compare and contrast the quantitative data analysis of synthetic data obtained within this study with a chosen dataset of LF signals from Montserrat.

1.9 Thesis Outline

Chapter 2 forms the main body of this study. It describes the development of spatially extended sources from classic point source descriptions of the source mechanisms underlying LF seismicity at volcanoes. Synthetic seismograms are calculated for these novel sources, and analysed concerning P-waveforms and amplitudes, and compared to those of a single double couple. The P-wave radiation patterns for ring fault and dike in both 2D and 3D are derived and described in Chapter 3. Chapter 4 provides a catalogue of a number of spatially extended sources. These form an excellent collection

of sources that real data examples can be compared against when investigating their source mechanisms. In Chapter 5, classical moment tensor inversions of all introduced spatially extended sources were carried out to evaluate the error that is introduced into the source solution and interpretation when assuming a point source instead of a spatially extended source nature. The final data chapter, Chapter 6, presents a case study of LF seismicity recorded prior to a dome collapse at SHV, Montserrat. Earthquake locations as well as moment tensor inversions were carried out for a chosen set of events. This work is rounded off with an overall discussion of this research in Chapter 7, and some concluding remarks including suggestions for future work in Chapter 8.

Chapter 2

A quantitative approach to volcano seismic sources

The study of seismic sources and the resulting radiated seismic energy provides insight into the rupture processes that generate earthquakes. To investigate the source geometry and the earthquake size, amplitudes and waveforms of the radiated seismic energy are analysed. Synthetically generated seismic waveforms at different distances and azimuths allow a quantitative study of the influence of the spatial extent of the source on the observed waveforms. This provides a deeper understanding of the processes which generate volcanic earthquakes.

This chapter introduces the basic idea of a spatially extended source mechanism generating low frequency type earthquakes in volcanic settings. Combinations of two or more double couple sources are used to derive more complex, but perhaps more appropriate and realistic, source models for low frequency (LF) earthquakes at volcanoes. The resulting waveforms and amplitudes of such spatially extended sources are analysed and compared to existing and widely used source classifications.

2.1 Waveform modelling

Different algorithms exist to model the wave field generated by a seismic event. Generally, the following approaches can be identified: Finite difference and finite element methods, which have the advantage of enabling the implementation of arbitrary heterogeneous media. If wavelengths and flexion of the seismic waves are much smaller than the geological structure under investigation, ray methods yield more accurate re-

sults. Ultimately, the most accurate results for horizontally layered media are gained using waveform integration methods which calculate the complete response of a medium to a seismic impulse. In this study, synthetic seismograms were generated using the FORTRAN code ‘qseis’ by Wang (1999), which is based on a frequency wavenumber integration method. The software is part of the open source ‘KIWI Tools’ package (Heimann, 2011) which can be downloaded from: <http://kinherd.org/kiwitools/>.

2.1.1 Source time function

By definition the source time function $\dot{M}(t)$ is the time derivative of the seismic moment function:

$$\dot{M} = \frac{\partial}{\partial t} M(t) = \mu \frac{\partial}{\partial t} (Au(t)) \quad (2.1)$$

where $M(t)$ is the seismic moment function which depends on fault area A and slip history $u(t)$ (Stein and Wysession, 2003).

Magma ascent within a volcanic edifice can be mathematically described as a step function, and using the definition above, the source time function for all models presented in this study is a delta impulse, the derivative of a step function. In fact, the input wavelet is a half sinusoid approximation to a delta impulse and is described by:

$$x(t) = \frac{2}{\tau} \sin^2 \left(\frac{\pi t}{\tau} \right) \quad \text{for } 0 \leq t \leq \tau, \quad (2.2)$$

where τ is the duration of the pulse. Figure 2.1 shows the simulated physical motion, vertical slip along a fault plane, represented by a step function, and its source time function, the delta impulse. The wavelet duration was 1.0 s for all analyses.

2.1.2 Global model parameters

Most LF seismicity in Montserrat occurs between 1 km and 2 km below the surface, with a strong cluster of events located at about 1.5 km depth (Green, 2005)(see also Chapter 6). I do not account for the complexities in the structure of volcanic edifices in order to avoid effects of path heterogeneities on the waveforms, and hence allow a

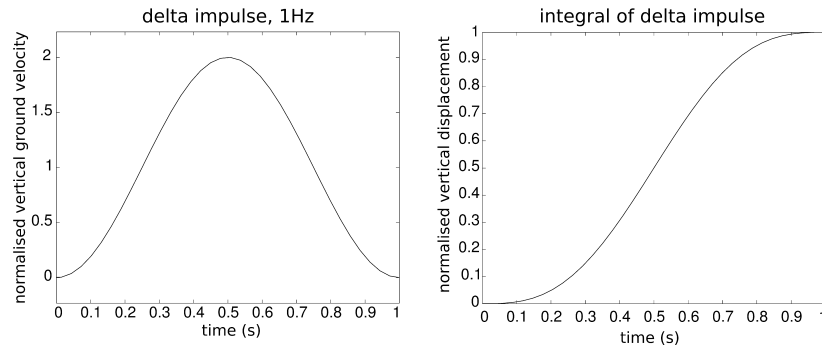


Figure 2.1: 1 Hz half sinusoid approximation to a delta impulse, used as input wavelet in the modelling, and its integral, representing the simulated physical motion.

concentrated study of the impact of source geometry on the observed seismicity. Based on this, the source in this synthetic approach was embedded at $z = 1.5$ km depth, within a homogeneous halfspace with a velocity structure in the range of estimated velocities for P- and S-waves (v_p and v_s) and densities (ρ) for volcanic settings (Equ. 2.3) (Dziewonski and Anderson, 1981). Quality factor values Q_p and Q_s were chosen high to disregard attenuation (i.e. $Q > 100$ (Smith, 2010)). Topography has been neglected, resulting in a static receiver altitude of 0 m in all cases.

$$v_p = 3.5\text{km/s} \quad v_s = 2.0\text{km/s} \quad \rho = 2200\text{kg/m}^3 \quad Q_p = 1378 \quad Q_s = 600 \quad (2.3)$$

2.1.3 Algorithm verification

To ensure reliability of the waveform integration approach, a thorough test study was carried out. For this purpose, a 1 Hz explosion was simulated at 3km depth, and its radiated seismic energy was modelled at receivers to the north, at 0 degrees azimuth, in 1 km increments to up to a 10 km epicentral distance. An explosion event as source mechanism was chosen because only a P-wave but no S-wave is generated, and to study the P-wave amplitudes and arrivals a separation of the two phases is therefore redundant. The source was embedded in a homogeneous halfspace with input parameters given in Equ. 2.3. As input moment $M_0 = 1.0$ Nm was chosen. The resulting synthetic traces were sampled at 100 Hz to ensure sufficient sampling to catch all frequencies of interest.

Table 2.1 shows a perfect match between theoretical and picked P-wave arrivals for all

Source depth	Epicentral distance	Hypocentral distance	P arrival (theor.)	P arrival (picked)
3.00 km	1.00 km	3.16 km	0.33 s	0.33 s
3.00 km	2.00 km	3.61 km	0.38 s	0.38 s
3.00 km	3.00 km	4.24 km	0.45 s	0.45 s
3.00 km	4.00 km	5.00 km	0.53 s	0.53 s
3.00 km	5.00 km	5.83 km	0.61 s	0.61 s
3.00 km	6.00 km	6.71 km	0.71 s	0.71 s
3.00 km	7.00 km	7.62 km	0.80 s	0.80 s
3.00 km	8.00 km	8.54 km	0.90 s	0.90 s
3.00 km	9.00 km	9.49 km	1.00 s	1.00 s
3.00 km	10.00 km	10.44 km	1.10 s	1.10 s

Table 2.1: Calculated hypocentral distances from epicentral distances between 1km and 10km and 3 km source depth, corresponding theoretical P-wave arrival times for a P-wave velocity $v_p = 9.500$ km/s, and picked P-wave arrivals.

distances which, together with the waveform consistency, indicates that this algorithm produces correct synthetic seismic traces. Advancing from this simple explosion source, the study of volcano seismic signals requires more complicated models to describe the physical processes likely involved in exciting the observed seismic signals. In the following, a model to simulate seismogenic slip along the conduit walls of a volcanic complex is derived in an attempt to explain the excitation processes of LF volcanic seismicity, and its body wave characteristics are examined.

2.2 Development of dike and cylindrical conduit source models

Neuberg et al. (2006) introduced a conceptual model for the driving forces of LF events at Montserrat based on experimental and numerical studies (Fig. 2.2). Highly viscous silicic melts can, under certain circumstances, behave in a solid-like brittle manner (Alidibirov and Dingwell, 1996; Dingwell, 1996; Webb and Dingwell, 1990), and these circumstances can be realised in volcanic edifices (Collier and Neuberg, 2006; Gonnermann and Manga, 2007; Thomas and Neuberg, 2012). As silicic magma ascends in the volcanic conduit the ambient pressure drops, allowing gases to exsolve from the magma and escape, leading to an increase in melt viscosity and a transition from Newtonian to Non-Newtonian behaviour in the melt (Webb and Dingwell, 1990; Alidibirov and Dingwell, 1996). Seismogenic brittle failure of the melt then occurs in response to a

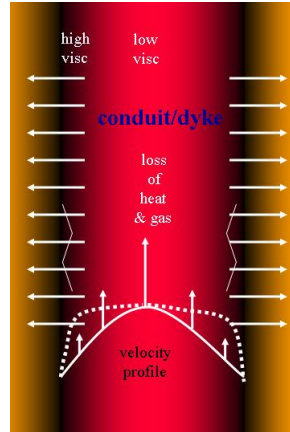


Figure 2.2: Neuberg et al. (2006) proposed that LF events on Montserrat may be triggered by the failure of magma at a depth where viscosity and strain rates are high enough to result in brittle behaviour of the melt. In their model, a resonator - the conduit itself - gives the seismic energy its low frequency content.

build up of high shear stresses and strain rates during the upwards movement of the magma in the volcanic edifice. The required conditions for brittle failure of magma in the glass transition are reached at the conduit walls, and within a certain depth window (Collier and Neuberg, 2006; Neuberg et al., 2006; Thomas and Neuberg, 2012). The seismic energy is then trapped in the magma column itself as tube waves generating the long-period coda on the recorded seismograms (Neuberg et al., 2006). The repeatability of LF events has been attributed to periodic fracturing and healing of the magma (Gonnermann and Manga, 2003; Tuffen et al., 2003; Kendrick et al., 2014), which creates a mechanism to explain a rechargeable, non-destructive source process for LF seismicity (Green and Neuberg, 2006).

Based on this conceptual model, the system under investigation can be described as either brittle failure on a single but curved fault plane, or simultaneous slip and superposition along several fault planes representing a dike or conduit. In the following, a novel approach is introduced by superimposing the wave fields of several point sources to mimic spatially extended sources, which are understood to be at the source of LF seismicity at volcanoes.

2.2.1 Ring fault

To model a spatially extended LF source and therefore approach the conceptual model described in Chapter 2.2, we can consider the approximation of a cylindrical fault

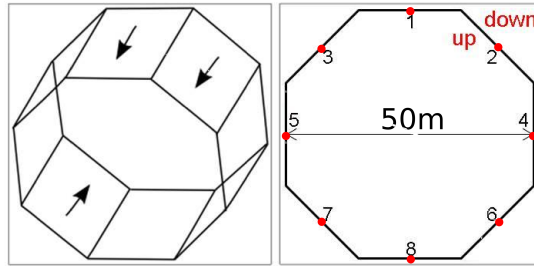


Figure 2.3: Instantaneous slip and accompanying shear failure of a dike, or all around the edge of a cylindrical fault, is approximated by an octagonal arrangement of 2 or 8 slip surfaces (segments 1-8), respectively, with upwards movement inside, and relative downwards movement outside the octagon. Double couple sources are indicated as red dots.

system by an octagonal arrangement of double couples bounding the circumference of the volcanic conduit, with upwards movement inside the octagon and downwards movement outside the octagon (Fig. 2.3). The octagon is the shape with the minimum number of point sources required to mimic slip along a cylindrical fault. It fulfils the required symmetry features of the cylindrical conduit. The effect of the ring fault diameter and number of input sources on the resulting waveforms is investigated further in Chapter 2.4. The resulting waveforms are then a superposition of the seismic traces generated by individual ring fault segments.

2.2.2 Dike

Two oppositely directed double couple sources are sufficient to simulate the upwards movement of magma in a dike, realised by slip and brittle failure along the dike walls. The two double couples are one dike width apart and act simultaneously. Using the same setup as shown in Fig. 2.3, segments 1 and 8 serve as slip surfaces. The overall recorded waveform at a given station is then a superposition of the two radiated seismic waves.

Throughout this work I will use the term 'dike' to describe two shear dislocation sources with opposite polarities as defined in this section. This should not be confused with dike sources from the literature which are often assumed to be crack sources radiating opening dislocation waves.

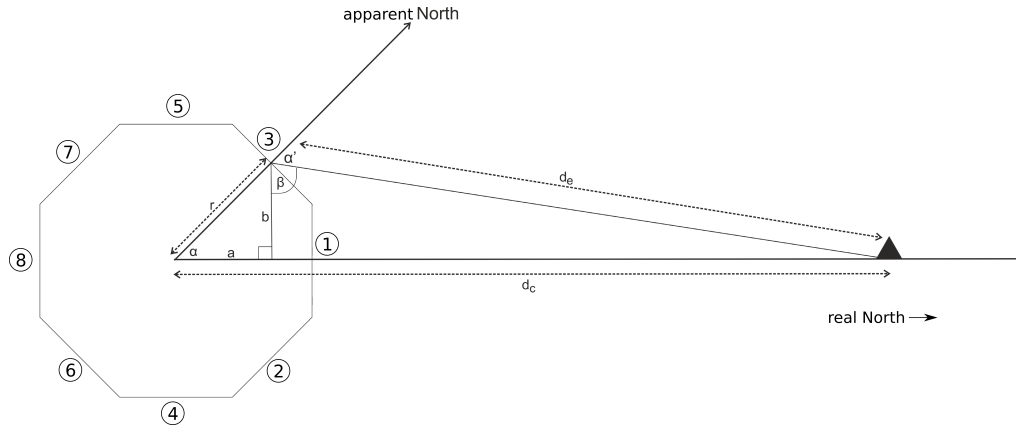


Figure 2.4: Trigonometric relations used to determine the epicentral distance d_e and azimuth α' between segment 2 and receiver. The input parameters for segments 1 and 3 to 8 were derived accordingly. Note that with a static fault orientation the coordinate system and thus the relative azimuth to the receiver location will change for each ring fault segment.

2.2.3 Input parameters: spatially extended sources

The seismic modelling approach using ‘qseis’ requires a static fault geometry which was chosen to be a normal fault with a strike of 90 degrees. To enable the calculation of all eight individual sources in one model run, the reciprocal relationship between source and receivers was used, swapping receiver and source, respectively (Aki and Richards, 1980). Input parameters, such as epicentral distance d_e and azimuth α' for each ring fault segment, are dependent on the ring fault diameter d , which was chosen as $d = 50$ m, and changing azimuths α between static source and 8 receivers, by using basic trigonometry. Fig. 2.4 shows the distance and angular relationships for segment 2. This gives:

$$\sin \alpha = \frac{b}{r} \quad \text{and} \quad \cos \alpha = \frac{a}{r},$$

where r is the radius of the ringfault, a lies on the connection between ring fault centre and receiver; b and a build an isosceles triangle with r , and b is perpendicular to a (Fig. 2.4). The segment epicentral distance, d_e , from source segment to receiver can then be determined using Pythagoras’ theorem:

$$b^2 + (d_c - a)^2 = d_e^2 \quad (2.4)$$

Table 2.2: The input parameters for 8 individual segments to simulate an extended ring fault structure using ‘qseis’. Shown are both segment-receiver distances, d_e , as well as apparent azimuths, α' , for receivers at 1 km and 5 km epicentral distance from the centre of the extended source.

$d_c = 1\text{km}$			$d_c = 5\text{km}$		
Segment	$d_e(\text{km})$	α'	Segment	$d_e(\text{km})$	α'
1	0.985	0°	1	4.985	0°
2	0.989	314.386°	2	4.989	314.878°
3	0.989	45.614°	3	4.989	45.122°
4	1.000	269.141°	4	5.000	269.828°
5	1.000	90.859°	5	5.000	90.172°
6	1.011	224.392°	6	5.011	224.879°
7	1.011	135.608°	7	5.011	135.121°
8	1.015	180°	8	5.015	180°

to find d_e :

$$d_e = \sqrt{b^2 + (d_c - a)^2} \quad (2.5)$$

where d_c is the epicentral distance of the ring fault centre to receiver. Inserting the following trigonometric functions for segments 1 to 4 and 5 to 8, respectively,

$$\beta_{1-4} = \arcsin\left(\frac{d_c - a}{d_e}\right) \quad \beta_{5-8} = \arcsin\left(\frac{d_c + a}{d_e}\right),$$

yields the apparent segment-station azimuth α' for input into ‘qseis’. For segment 2 this gives:

$$\alpha'_2 = 180^\circ - \beta - (180^\circ - 90^\circ - \alpha). \quad (2.6)$$

By keeping the fault orientation unchanged, but adapting the trigonometric functions to each individual case, the epicentral distances and azimuths for the remaining segments can be determined accordingly. Table 2.2 shows the input parameters calculated for a receiver at real azimuth $\alpha = 0^\circ$ and epicentral distances $d_c = 1$ km and $d_c = 5$ km.

To simulate a spatially extended source, the waveform contributions of each segment of the structure under investigation were generated individually and subsequently linearly stacked, simulating the superposition at the receivers.

2.3 Comparison of simple and complex source mechanisms

2.3.1 Amplitudes

The study of seismic wave amplitudes has proven advantageous in providing valuable information on earthquake source mechanisms. Different sources radiate seismic energy of varying intensity in different directions, and therefore generate different radiation patterns. Standard approaches in seismology are mostly based on the study of point sources. The interpretation of volcano seismic sources has almost exclusively focused on double couples. However, the physical source mechanisms underlying volcano seismic sources, and LFs in particular, are thought to be more complex than simple shear failure, and therefore require the study of sources beyond single double couples. The quantitative study of spatially extended sources such as the ring fault described in Chapter 2.2.1 is a novel approach to solving this, and lies at the core of this project.

To establish the importance and consequences of fundamentally changing the nature of the source, by advancing from point to spatially extended sources, the waveform attributes of both mechanisms are examined and compared. The P-wave radiation patterns for such spatially extended sources compared against well known point source radiation patterns will be discussed in detail in Chapter 3. Here, a synthetic approach, where the source characteristics are known, is used to determine amplitude ratios between point and spatially extended source mechanisms, and how these change with changing epicentral distances and azimuths between source and receivers. In particular, the resulting maximum P-wave amplitudes of simple shear faulting represented by a single double couple, and those resulting from a CLVD source, are compared to those of both dike and ring fault for a number of receiver locations.

To ensure a quantitative comparison, the input parameters were kept constant for all source scenarios. The source at depth $z = 1.5$ km was embedded in a homogeneous half-space as described in Chapter 2.1.2. The input moment for **each** ring fault segment was fixed to $M_0 = 1\text{Nm}$, so that the overall ring fault input moment M_0^{RF} matched

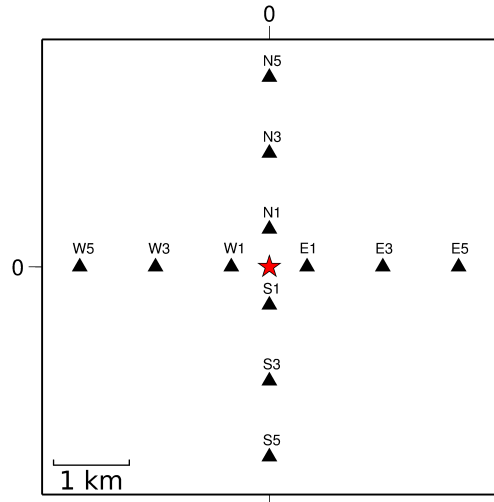


Figure 2.5: Receiver network for synthetic study. The red star indicates the extended source. Receiver locations were chosen to ensure good epicentral and azimuthal coverage. 12 stations were therefore located at 1 km, 3 km, and 5 km epicentral distances in the four cardinal directions.

that of the double couple and CLVD scenarios: $M_0^{RF} = M_0^{DC} = M_0^{CLVD} = 8 \text{ Nm}$. Equivalently, $M_0^{DIKE} = M_0^{DC} = M_0^{CLVD} = 8 \text{ Nm}$, yielding $M_0 = 4 \text{ Nm}$ for each dike segment. Based on the empirical relationship between seismic moment and magnitude Hanks and Kanamori (1979), an input moment of $M_0 = 8 \text{ Nm}$ corresponds to an earthquake magnitude of $M_w = -5.3$. While the chosen seismic input moment is too small for realistic scenarios, the results gained in this study can be translated into greater magnitudes by scaling the obtained P-wave amplitudes. Synthetic seismograms were calculated for a receiver network consisting of 12 stations: 3 each at the cardinal points at 1 km, 3 km, and 5 km epicentral distances (Fig. 2.5).

Ring fault

Synthetic velocity seismograms were generated for the ring fault and a northwards striking fault for comparison (Fig. 2.6). All sources were at 1.5 km source depth, with receiver locations at 1 km, 3 km, and 5 km epicentral distances, and varying azimuths to investigate the dependence of maximum P-wave amplitudes on both epicentral distance and azimuth.

P-wave amplitudes for receivers at 1 km, 3 km, and 5 km epicentral distances are summarised in Table 2.3. Maximum P-wave amplitudes and resulting amplitude ratios

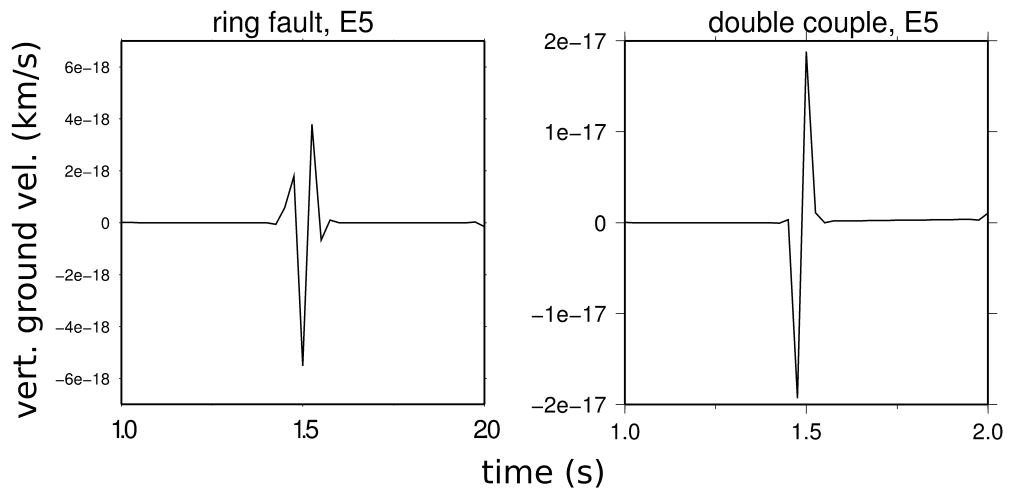


Figure 2.6: Comparison of ring fault (*left*) and normal fault (*right*) P-waveforms, for a source at 1.5 km depth and a receiver at 5 km epicentral distance and $\alpha = 90^\circ$. The normal fault P-wave represents a 2-sided non-zero phase K pper wavelet (K pper, 1985), while the ring fault waveform resembles a Ricker wavelet (Ricker, 1953).

Table 2.3: Azimuthal dependence of ring fault vertical ground velocity with receivers at 1 km and 5 km epicentral distances. It can be clearly seen that for a given epicentral distance the maximum observed ground velocity is unaffected by the receiver azimuth.

Source depth	Azimuth	Ring fault (km/s) ($d_c = 1\text{km}$)	Ring fault (km/s) ($d_c = 3\text{km}$)	Ring fault (km/s) ($d_c = 5\text{km}$)
1.5 km	0°	3.316×10^{-17}	1.635×10^{-17}	5.522×10^{-18}
1.5 km	10°	3.316×10^{-17}	1.635×10^{-17}	5.522×10^{-18}
1.5 km	20°	3.316×10^{-17}	1.635×10^{-17}	5.522×10^{-18}
1.5 km	30°	3.316×10^{-17}	1.635×10^{-17}	5.522×10^{-18}
1.5 km	40°	3.316×10^{-17}	1.635×10^{-17}	5.522×10^{-18}
1.5 km	50°	3.316×10^{-17}	1.635×10^{-17}	5.522×10^{-18}
1.5 km	60°	3.316×10^{-17}	1.635×10^{-17}	5.522×10^{-18}
1.5 km	70°	3.316×10^{-17}	1.635×10^{-17}	5.522×10^{-18}
1.5 km	80°	3.316×10^{-17}	1.635×10^{-17}	5.522×10^{-18}
1.5 km	90°	3.316×10^{-17}	1.635×10^{-17}	5.522×10^{-18}

between normal fault and ring fault at $z = 1.5$ km source depth and 5 km epicentral distance are summarised in Table 2.4, where receiver azimuths were varied from $\alpha = 0^\circ$ to $\alpha = 90^\circ$. The normal fault vertical ground velocity is zero at its nodal plane at $\alpha = 0^\circ$ azimuth, and exceeds that of the ringfault for receivers at azimuths $\alpha \geq 20^\circ$, steadily increasing to a maximum of -1.376×10^{-17} km/s at $\alpha = 90^\circ$ azimuth.

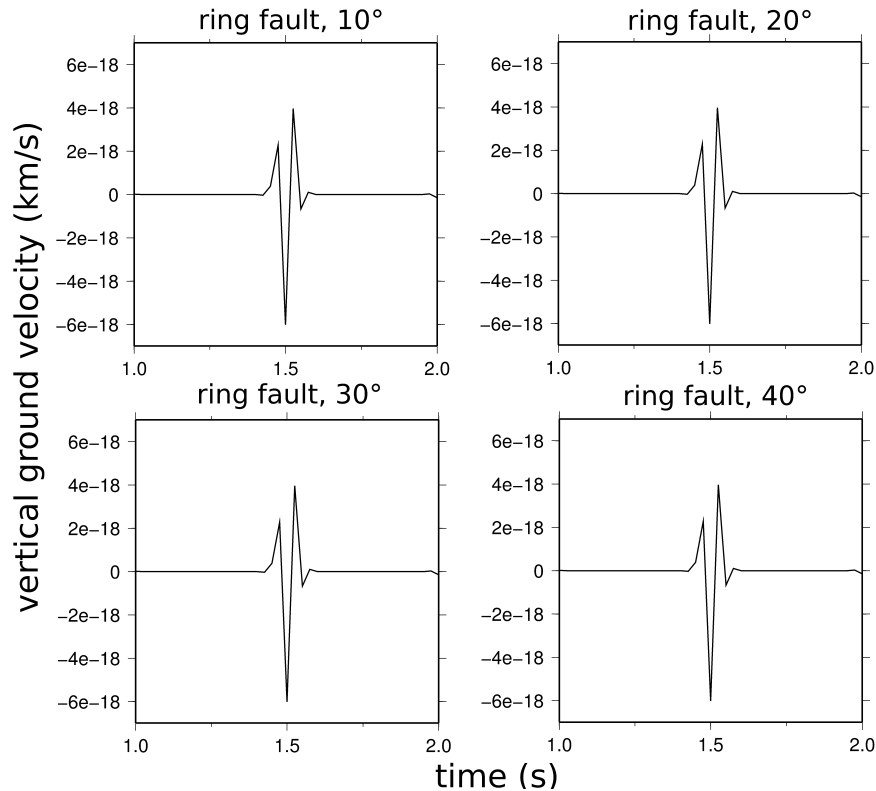


Figure 2.7: P-waveforms of a 1.5 km deep, 50 m wide ring fault. Receivers were located at 5 km epicentral distance and at azimuths $\alpha = 10^\circ$ to $\alpha = 40^\circ$. The waveforms do not show any dependence on receiver azimuths.

The radiated seismic energy from the ring fault source does not show this azimuthal dependence, resulting in a constant P-wave amplitude of -5.522×10^{-18} km/s for all azimuths (see also Figs. 2.7 and 2.8).

Consequently, the amplitude ratio between point source and spatially extended source changes with changing azimuth. At $\alpha = 90^\circ$, where the observed normal fault vertical ground velocity is greatest, the amplitude ratio reaches a maximum of 3.5:1, indicating that for constant input parameters across sources the observed maximum P-wave amplitude of a normal fault is more than 3 times that of the ring fault.

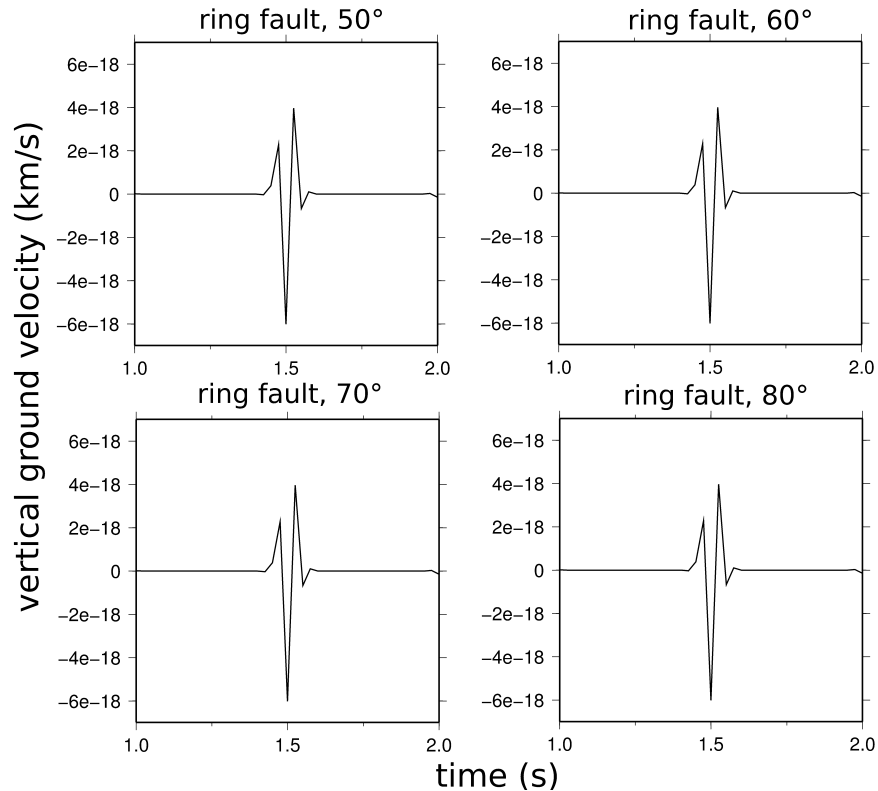


Figure 2.8: P-waveforms of a 1.5 km deep, 50 m wide ring fault. Receivers were located at 5 km epicentral distance and at azimuths $\alpha = 50^\circ$ to $\alpha = 80^\circ$. The waveforms do not show any dependence on receiver azimuths.

Dike

The superposition of two oppositely directed double couple sources describes the modelling approach of seismogenic magma ascent within a dike. To simulate slip along a EW striking dike, ring fault segments 1 and 8 were modelled to act simultaneously, producing wave trains whose superposition results in the seismicity of the dike structure. Body wave seismograms were produced for stations in 1 km, 3 km, and 5 km epicentral distances to the north, east, south and west of the event location. Fig. 2.9 shows the resulting dike P-waves at four stations at 5 km epicentral distance.

Both wave amplitudes and waveforms change with relative dike-receiver locations. For this EW striking dike, pairs of observed amplitudes to the east and west, as well as to the north and south of the source, are identical, with maximum vertical ground velocities of -3.112×10^{-19} km/s and 9.425×10^{-20} km/s, respectively. Since the overall waveforms are obtained by the superposition of two point sources, maximum

Table 2.4: Maximum vertical ground velocity and resulting amplitude ratios between normal fault and ring fault for varying receiver azimuths and fixed source depth and epicentral receiver location. The maximum observed ground velocity generated by the northwards striking normal fault is zero at its nodal plane at $\alpha = 0^\circ$ and increases to its maximum at $\alpha = 90^\circ$. The ring fault does not show this azimuthal dependence and the resulting P-wave amplitudes are identical at all azimuths.

Source depth	Epicentral distance	Azimuth ($^\circ$)	Normal fault (km/s)	Ring fault (km/s)	Amp. ratio
1.50 km	5.00 km	0	0	5.522×10^{-18}	N/A
1.50 km	5.00 km	10	3.357×10^{-18}	5.522×10^{-18}	0.56:1
1.50 km	5.00 km	20	6.613×10^{-18}	5.522×10^{-18}	1.10:1
1.50 km	5.00 km	30	9.667×10^{-18}	5.522×10^{-18}	1.61:1
1.50 km	5.00 km	40	1.243×10^{-17}	5.522×10^{-18}	2.06:1
1.50 km	5.00 km	45	1.376×10^{-17}	5.522×10^{-18}	2.28:1
1.50 km	5.00 km	50	1.481×10^{-17}	5.522×10^{-18}	2.59:1
1.50 km	5.00 km	60	1.674×10^{-17}	5.522×10^{-18}	2.78:1
1.50 km	5.00 km	70	1.817×10^{-17}	5.522×10^{-18}	3.02:1
1.50 km	5.00 km	80	1.904×10^{-17}	5.522×10^{-18}	3.16:1
1.50 km	5.00 km	90	1.933×10^{-17}	5.522×10^{-18}	3.5:1

amplitudes strongly depend on whether individual wave trains arrive at the receiver in, or out of phase, which in turn depends on the dike width d . The P-wave generated by segment 1 reaches station N5 Δt earlier than the oppositely polarised P-wave generated by segment 8, causing a slight phase shift corresponding to different travel times, which results in the waveform displayed on the left hand side of Fig. 2.9. The same happens at station S5, but with the P-wave generated by segment 8 being recorded Δt before that from segment 1.

Stations E5 and W5 lie in the same relative location to the dike, and therefore produce identical waveforms. Both wave trains reach the receiver at the same time, with the same polarities, and as a result constructive interference takes place, yielding double the maximum vertical ground velocities as a single segment.

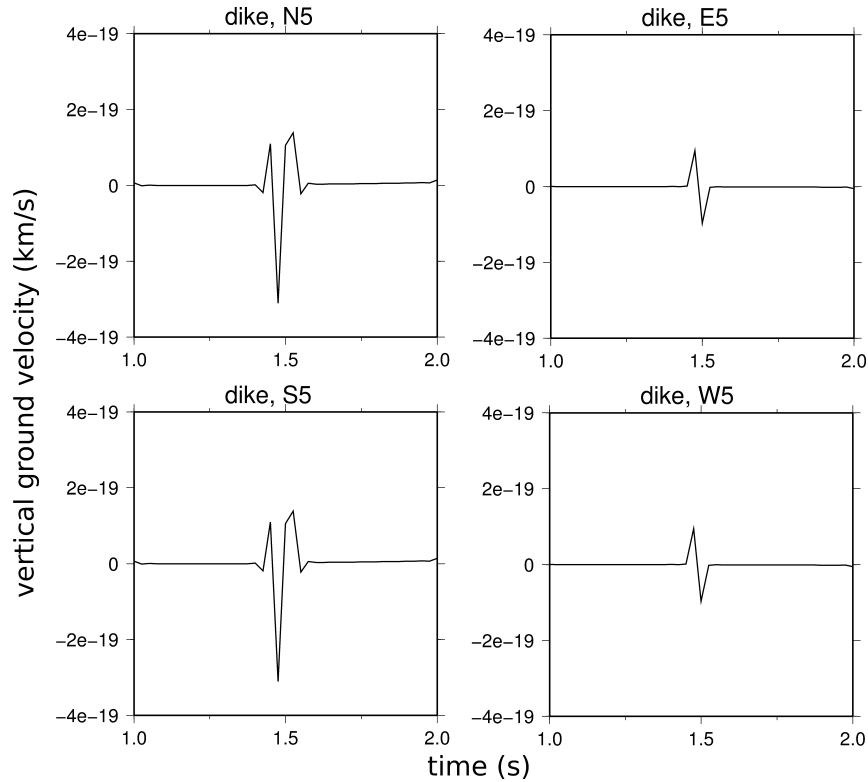


Figure 2.9: P-waveforms of a 1.5 km deep dike. Receivers were located at 5 km epicentral distance to the north, east, south and west (N5, E5, S5, W5). Due to the same relative source-receiver locations to the E and W, and N and S, respectively, the observed P-waveforms and amplitudes at these station pairs are identical.

The overall observed P-wave amplitudes of the dike are smaller than those of the vertically dipping, northwards striking fault. This is partly due to the spatial extent of the dike, introducing a difference in travel times of the generated seismic waves, and therefore resulting in partial destructive interference. However, constructive superposition takes place at E5 and W5, yet relative source receiver locations of EW striking dike segments yield overall smaller vertical ground velocities of the extended source compared to the northwards striking single fault.

Compensated linear vector dipole

The compensated linear vector dipole (CLVD) (see also Chapter 1.6.5) is an equivalent body force system which is often discussed in connection with the excitation processes of low frequency signals in volcanoes (Chouet, 1996b; Waite et al., 2008). To model such a source, input parameters were chosen as outlined in Chapter 2.1.2, and the selected input moment $M_0 = 8 \text{ Nm}$ enables comparison with the seismicity generated

by other sources under investigation in this chapter. The P-waveforms produced by such a non-DC source at receivers at 5km epicentral distance can be seen in Fig. 2.10.

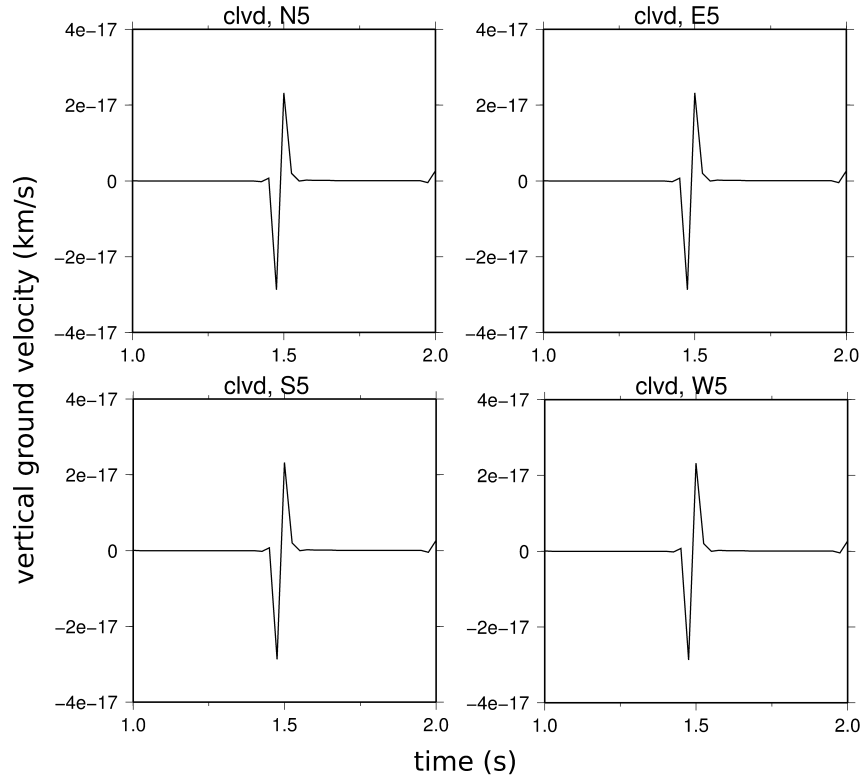


Figure 2.10: P-waveforms of a 1.5 km deep CLVD source. Receivers were located at 5 km epicentral distance to the north, east, south and west (N5, E5, S5, W5). The traces for such a non-DC source show no dependence on receiver azimuths, and have maximum vertical ground velocities of -2.874×10^{-17} km/s.

Similar to the ring fault P-waveforms, the resulting CLVD body wave seismicity does not show a dependence on receiver azimuth, which leads to identical observed traces in all four cardinal directions (Fig. 2.10). However, there is no resemblance between CLVD and ring fault P-waveforms themselves. While the ring fault P-waves resemble Ricker wavelets (Fig. 2.6), CLVD P-waves hold Küpper-like wavelet characteristics. With -2.874×10^{-17} km/s maximum P-wave amplitudes, CLVD amplitudes greatly exceed those of the ring fault structure (-5.522×10^{-18} km/s; Chapter 2.3.1). Furthermore, the independence on receiver azimuths of both ring fault and CLVD source yields a constant P-wave amplitude ratio of RF:CLVD= 1 : 4.77 (477%) at 5 km epicentral distance.

2.3.2 Waveforms

Due to the spatial extent of the source under investigation the released seismic energies reach the receiver at times Δt apart and are therefore partially phase shifted when superimposed. Despite the waveforms of individual segments representing those of a shear dislocation source, by advancing from a single point to an extended ring fault the waveform of the superimposed solutions deviates from that of a single double couple, producing a time derivative of the original (see Fig. 2.6).

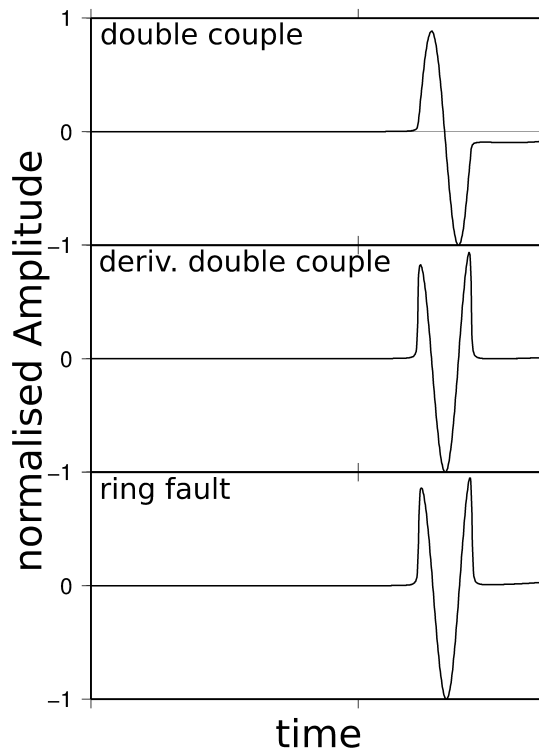


Figure 2.11: Normalised vertical ground displacement waveforms for a double couple, its derivative, and the ring fault structure, which is identical to the double couple derivative (bottom and middle traces).

The P-waveforms of a single double couple, its derivative, and the P-waveform of the ring fault structure are shown in Fig. 2.11. The latter is identical to the double couple derivative. This derivative is introduced by the nature of the source: the total observed seismic energy at a given seismic station is a result of a superposition of individual seismic waves generated a distance Δd apart from each other. This spatial difference yields an arrival time delay Δt between single segment contributions and the overall

seismic wavefield, causing an effect equal to a time derivative of the signal f :

$$\frac{df}{dt} = \frac{f(t) - f(t + \Delta t)}{\Delta t} \quad (2.7)$$

The vertical ground velocity synthetic seismograms for the ring fault source and receivers at common azimuth and 1 km, 3 km and 5 km epicentral distances deviate from each other in amplitudes only (Fig. 2.12), demonstrating that changes in epicentral distance between source and receiver leave the shape of the ring fault waveforms in an elastic medium unaffected.

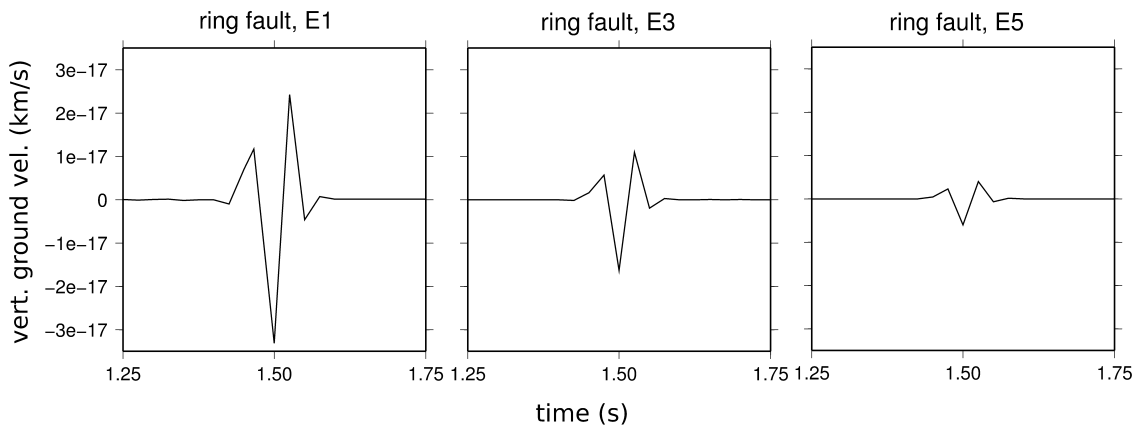


Figure 2.12: Vertical ground displacement waveforms for the ring fault structure at stations to the East in 1 km, 3 km, and 5 km epicentral distance. The waveform shape stays unchanged while an expected amplitude decrease with distance can be observed.

Furthermore, due to its azimuthal independence, the observed body waveform also stays unaffected by a change in receiver azimuth. Synthetic seismograms were generated for 0° to 90° . The first arrival waveforms at all azimuths are identical and representative waveforms at 10° , 60° , and 80° can be seen in Fig. 2.13.

2.4 Dependency of waveforms on the source geometry

It is the main challenge of volcanology to improve our understanding of volcanic complexes as such, and the physical processes that lead to eruptions. Despite many years of multi-disciplinary endeavours, the scientific community has not succeeded in drawing a detailed picture of the sub-surface structure of volcanoes. Properties such as the shape

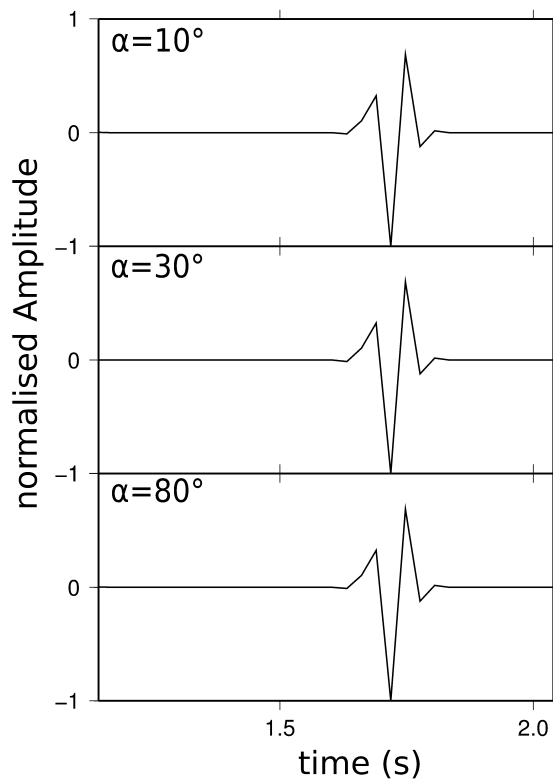


Figure 2.13: Azimuthal dependence of the ring fault waveforms for three receiver locations: 5km epicentral distance and *top*: azimuth $\alpha = 10^\circ$; *middle*: azimuth $\alpha = 60^\circ$; and *bottom*: azimuth $\alpha = 80^\circ$. It can be clearly seen that for a given epicentral distance the observed wave shape is unaffected by the receiver azimuth.

and extent of the conduit system are known in only a few cases, and these uncertainties need to be taken into account when attempting to model the complexity of volcanoes.

Here, the effect of conduit diameter changes on the resulting waveforms is investigated, assuming slip along a cylindrical ring fault as the trigger of LF seismic signals. Furthermore, the validity of approximating a cylindrical fault with an octagonal arrangement of 8 double couples is tested by increasing the number of point sources used to build the ring fault to 16 and to 32, and comparing the resulting waveforms to the ones obtained earlier in this work (Chapter 2.3).

2.4.1 Number of point sources

To show that an octagonal arrangement of double couples is sufficient to approximate the trigger of LF seismicity at volcanoes as suggested by Neuberg et al. (2006), slip along the ring fault structure was modelled using increased numbers of point sources. To

retain the symmetry properties of the source with increased numbers of point sources, the ring fault structure was approximated using 16 and 32 simultaneously acting double couples, whose geometric arrangement can be seen in Figs. 2.14 and 2.15. To enable

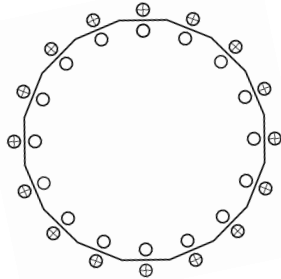


Figure 2.14: Ring fault approximation using 16 point sources. Upwards movement takes place inside, and relative downwards movement outside the conduit. 16 simultaneously acting double couple sources form the spatially extended source under investigation.

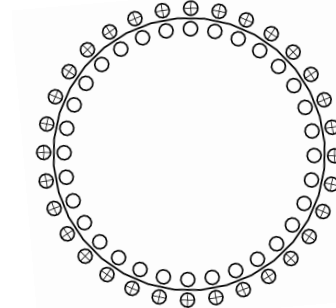


Figure 2.15: Ring fault approximation using 32 point sources. Upwards movement takes place inside, and relative downwards movement outside the conduit. 32 simultaneously acting double couple sources form the spatially extended source under investigation.

good comparison with the octagon, all input parameters but the number of simultaneously acting point sources were kept constant: double couple sources were embedded in 1.5 km depth in a homogeneous medium with a velocity structure as presented in Chapter 2.1.2 of this chapter. Twelve receivers were placed at 1 km, 3 km and 5 km epicentral distances, to the north, east, south, and west of the source epicentre. The source time function was, as in all earlier cases, a half-sinusoidal approximation of a delta impulse (see also Chapter 2.1.1) with a duration of $\tau = 1.0$ s. To ensure sufficient sampling to catch the spatial extent of the source, the signal was over-sampled at 1000 Hz, and subsequently downsampled to 40 Hz.

The resulting P-waveforms can be seen in Fig. 2.16. Shown here are the vertical ground velocities recorded at 5km epicentral distance, which enables a comparison with the octagonal arrangement of 8 double couples in Chapter 2.3.1. It can be seen that both P-wave amplitude as well as waveform stay unchanged in all cases, indicating that 8 double couple sources are sufficient to approximate the spatially extended source. This is due to the symmetry features of the proposed source, which are fully mimicked by the symmetry properties of the octagon.

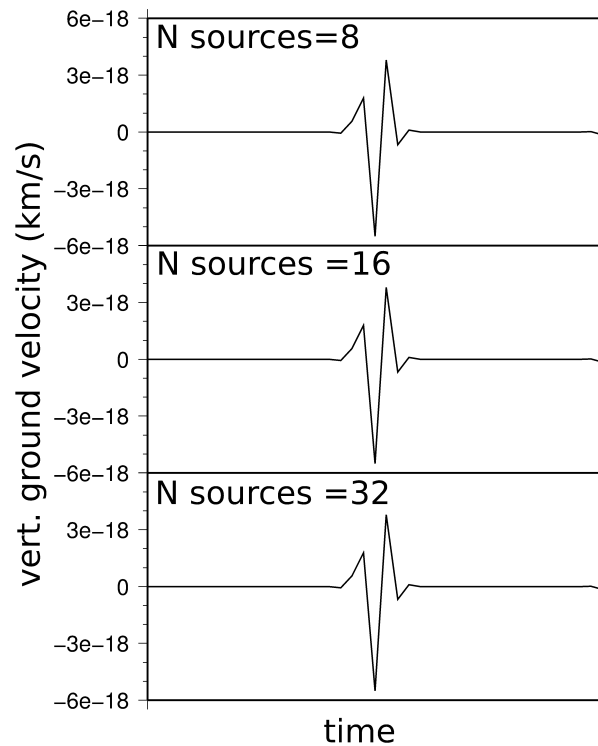


Figure 2.16: The effect of the number of point sources used to model the spatially extended ring fault structure. Vertical ground velocities generated by a 50 m wide conduit and recorded at 5 km epicentral distance are shown for a source built up by 8 (*top*), 16 (*middle*), and 32 (*bottom*) simultaneously acting double couple sources. P-wave amplitudes or shapes stay unchanged when increasing the number of point sources, proving that an octagonal arrangement of 8 DC sources is sufficient to model the proposed physical processes.

All spatially extended sources considered in this study exhibit a rotational symmetry. The P-waveforms obtained are strongly dependent on this feature, and would change greatly with a change from symmetric to asymmetric source configurations. The effect on waveforms and amplitudes should be considered in future investigations, and will be discussed in more detail in Chapter 7. The modelling endeavours here, however, aim to represent symmetric sources, such as the ring fault structure, and it has been shown in this previous section that an octagonal arrangement of 8 double couple sources is sufficient to achieve this.

2.4.2 Source diameter

Although little is known about the geometry of the shallow magmatic feeder system in volcanoes there are a number of studies investigating their width and complexity. For Montserrat, Hautmann et al. (2009) suggested a width of 30 m for the shallow parts of

the cylindrical conduit system. However, other volcanoes also exhibit LF seismicity, yet estimates for their shallow magmatic conduit diameters differ, with suggested values for other volcanoes of 18 m at Santiaguito volcano, Guatemala (Sakuma et al., 2008), to 50 m for Unzen volcano, Japan (Holland et al., 2011).

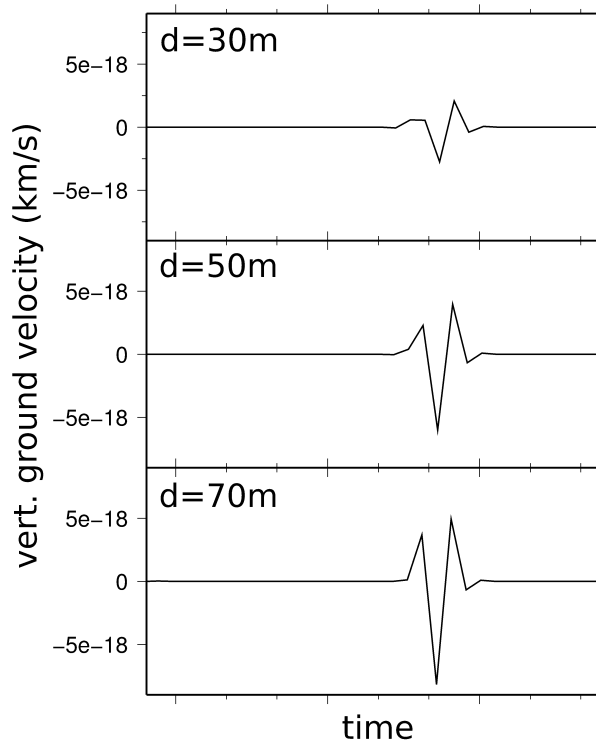


Figure 2.17: P-wave vertical ground velocities resulting from a ring fault structure with 30 m, 50 m, and 70 m diameter. Dependent on the diameter the seismic energy from individual point sources building up the spatially extended source interfere partially negatively to different degrees. The resulting P-wave amplitudes increase with an increase in diameter.

Whether seismic energy of a number of point sources superposes constructively, partially destructively, or cancels out, depends on the phase difference of individual traces when arriving at the receiver, which in turn is dictated by the differences in travel times, and hence the source diameter. It is therefore not surprising that observed P-wave amplitudes change with a change in diameter, with example cases of 30 m, 50 m and 70 m shown in Fig. 2.17. The P-wave amplitude increases with increasing source diameter, with the waveform obtained by a 70 m wide cylindrical source showing maximum P-wave amplitude of -8.187×10^{-18} km/s at 5 km epicentral distance. In the $d = 30$ m case the seismic energy radiated from the receiver farthest from the source is almost congruent, but oppositely directed, with the trace generated by the source closest to the

receiver leading to cancellation of much of the energy, and comparatively small vertical ground velocities (P-wave maximum at receiver at 5 km distance: 2.752×10^{-18} km/s, which corresponds to 33.6% of the biggest observed P-wave amplitude). A steady increase in source diameter will ultimately lead to travel time differences greater than the individual wavelet duration, yielding no superposition of waveforms but instead the recording of separate wave trains generated by individual segments.

It is therefore important to take into account information on the conduit geometry when interpreting volcanic seismicity. If disregarded, effects of conduit width may be misinterpreted, and could lead to highly inaccurate evaluations of the state of a volcano.

2.5 Implications of the source nature on the occurring slip

By definition, a seismogram is a convolution of the source, \mathbf{S} , Green's functions containing information on the path between source and receiver, \mathbf{G} , and instrument response of the recording seismometer, \mathbf{R} :

$$\text{Seismogram} = \mathbf{S} * \mathbf{G} * \mathbf{R}, \quad (2.8)$$

In synthetic studies the link between observed seismogram, source, path effects and instrument response is immensely simplified compared to real event data as both path and instrument response are known and can be kept constant. Amplitude changes can thus be directly linked to changes in the source. Therefore, the implications of changing the source nature from point to spatially extended source on the source parameters can be inferred from the synthetic seismogram amplitude ratios. The observed seismic amplitudes for double couple source and ring fault were generated using 1/8 of the double couple slip surface for each ring fault segment, so that the total slip surfaces $A_{DC} = A_{RF}$ and input moments $M_{DC} = M_{RF} = 8\text{Nm}$ of point and spatially extended source were equal. The resulting amplitudes can be described as:

$$\text{Seis}_{DC} = M_{DC} * G * R \quad (2.9)$$

and

$$\text{Seis}_{RF} = \sum_{i=1}^8 M_{DC,i} * G * R \quad (2.10)$$

Using the classic definition of the seismic moment for a double couple source:

$$M = \mu Ad, \quad (2.11)$$

where μ is the rigidity, A the fault slip area, and d the amount of slip, and considering equal overall input moments for ring fault and normal fault and constant slip surfaces A across source models we get an amplitude ratio of:

$$\frac{\text{Seis}_{DC}}{\text{Seis}_{RF}} = \frac{(\mu Ad_{DC}) * G * R}{(\mu Ad_{RF}) * \sum G_i * R} \quad (2.12)$$

The instrument response, rigidity and slip area are the same for both and cancels out, which leaves:

$$\frac{\text{Seis}_{DC}}{\text{Seis}_{RF}} = \frac{d_{DC}}{d_{RF}} * \frac{G}{\sum G_i} \quad (2.13)$$

For the two sources under investigation to result in the same seismic amplitude (amplitude ratio 1:1), the amount of slip along a ring fault would therefore have to be a factor of up to 3.5 bigger than that of a point source, assuming constant rigidity and area on which slip occurs. This becomes especially important when interpreting seismic data of an active volcano, where the main motivation is to extract information such as magma ascent rates from the observed seismograms. Once the recorded seismograms are free of instrument response and path effects, the remaining waveforms are purely due to source processes. The comparison of the residual seismograms to synthetically generated waveforms then allows the extraction of vital information on source characteristics. This is possible because in the synthetic case all source parameters such as input moment and source depth, as well as the seismic amplitudes and waveforms they result in at a given station, are known. By matching observed and synthetic maximum amplitudes, the input parameters of the best fit model can then be linked to the real

case.

The differences in resulting maximum amplitudes caused by different synthetic model geometries emphasise the need to understand the source mechanisms of LF volcano seismic events. Special care must be taken when linking waveform amplitudes to slip at depth, as amplitude-slip conversion for a point source results in much smaller slip distances than for the ring fault structure. The exact slip difference depends on the receiver location, as amplitude ratios change (see Chapter 2.3.1) with receiver azimuths.

It should be mentioned that this study was carried out assuming a common relationship $M = \mu Ad$ (see Equ. 2.11) between slip and associated input moment along both, DC and RF sources. Due to the spatially extended nature of the ring fault structure a higher order slip - seismic moment link is, however, should be taken into consideration in future investigations.

2.6 Discussion and Summary

The possibility of an extended source as the mechanism generating low frequency volcano seismic events has been investigated in a novel quantitative numerical approach. Both amplitudes and waveforms were considered in comparing the existing and commonly used source mechanisms to the novel and more realistic extended source that was developed within this study.

In Chapter 2.2, a crucial step towards the understanding of low frequency seismicity at volcanoes was taken by advancing from commonly used point sources to spatially extended source structures. Such a spatially extended source, i.e. the ring fault, resembles the proposed conceptual model introduced by Neuberg et al. (2006) much better than any previous attempts.

The results in Chapter 2.3 show that there are fundamental differences between point and extended source maximum P-wave amplitudes and waveforms. While source parameters, velocity model and receiver locations were kept constant, dike and ring fault consistently resulted in smaller amplitude seismic motions than DC and CLVD sources, except at receiver location azimuths close to the normal fault nodal planes. Addition-

ally, the radiated seismic energy created by a ring fault structure does not show a dependence on receiver location azimuth (2.18).

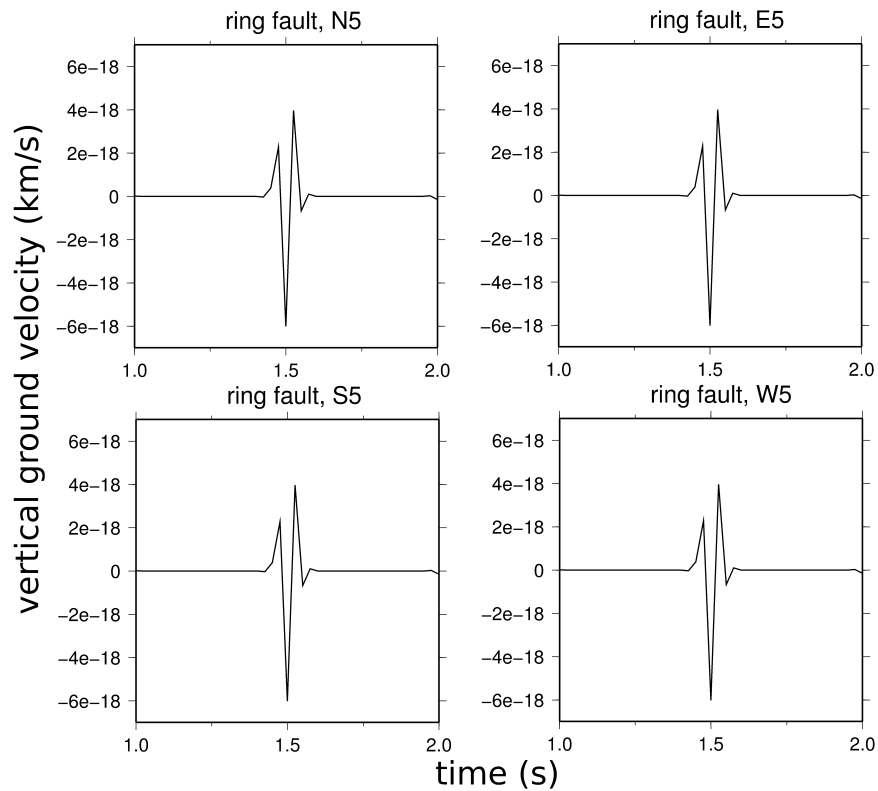


Figure 2.18: P-waveforms of a 1.5 km deep, 50 m wide ring fault. Receivers were located at 5 km epicentral distance to the north, east, south and west (N5, E5, S5, W5). The waveforms do not show any dependence on receiver azimuths.

Fig. 2.11 outlines the differences in waveforms between point and spatially extended sources, specifically the introduction of an extra time derivative of the observed waveforms. A severe consequence of (incorrectly) assuming a double couple source instead of the ring fault would result in the wrong time history of slip, meaning that the upwards movement of a magma batch, for example, would be misinterpreted as initial upwards followed by downwards movement of the magma.

Since changes in the source diameter of extended sources change both P-waveform amplitudes and shapes (Chapter 2.4.2) it becomes clear how important further investigations into the conduit geometry of individual volcanic edifices are in order to take further steps towards accurate forecasting of eruption dynamics.

The findings of Chapter 2.5 become especially important when interpreting seismic data recorded on the flanks of an active volcano. Based on the conceptual model by Neuberg et al. (2006), LF seismicity gives insight into the speed that magma rises in the conduit. Linking event amplitudes to magma ascent rates is therefore crucial for successful eruption forecasting. Point and extended source models with common total input moments yield great differences in observed P-wave amplitudes, leading to remarkable differences when interpreted as amount of slip and slip rates. It is therefore especially important to understand the source nature when attempting to estimate magma ascent rates from LF seismic events at volcanoes. In particular, observed amplitudes using the point source approximation, when in reality a spatially extended source acts at depth, yield an underestimation of actual slip by more than a factor of 3. Ultimately, this leads to an underestimation of the magma ascent rate, which could have important consequences for eruption forecasting.

To investigate this advancement from point sources to spatially extended sources further, the P-wave radiation patterns for both ring fault and dike structures are derived and discussed in Chapter 3. Waveforms resultant from the spatially extended sources in this chapter are used to carry out a moment tensor inversion study in Chapter 5, to investigate the implications of incorrectly assuming point sources during attempts to resolve the excitation processes from full waveform inversions.

Chapter 3

Radiation patterns of spatially extended seismic sources

The pattern of radiated seismic waves depends on the source geometry, and thus seismograms recorded at various locations away from the source can be used to derive the geometry of faulting during an earthquake. The study of first motions or polarity (direction) of body waves represents a simple but powerful technique to enable first order assumptions on the source structure (Aki and Richards, 1980). Using seismic source theory the amplitude radiation patterns for P- and S-waves radiated from the source can be derived and allow further conclusions about the source geometry (Aki and Richards, 2002). Radiation patterns for numerous source geometries exist (e.g. Julian et al., 1998). However, conventional radiation patterns are defined for point dislocation sources only, e.g. simple shear faulting along a fault described by a double couple source. In volcanic settings, where source geometries of earthquakes are thought to be more complex, observed first motions and radiation patterns often do not conform with those of simple point dislocation sources.

In this chapter, existing fault geometries, their first motions and body wave radiation patterns are used to develop the P-wave radiation pattern for a more advanced and realistic spatially extended volcanic source mechanism (see Chapter 2.2). Based on seismic source theory the ring fault radiation pattern in 2D and 3D is constructed as a combination of an infinite number of point sources arranged in a circle. The resulting P-wave radiation pattern for this spatially extended source is discussed and in a second step compared to conventional radiation patterns. The ring fault structure is considered as a likely candidate for the source of low frequency events at volcanoes, and the

deduction of its radiation pattern will contribute to developing the full potential of LFs as a forecasting tool.

3.1 First motions

At present, considerations of first motions and radiation patterns have almost exclusively been limited to seismic energy released from point sources. As the P-wave is the first wave to arrive at a seismic station its polarity is often easier to identify than that of later phases. As a consequence, most approaches choose the direct P phase and use the fact that the polarity of the first P-wave arrival varies with direction from an earthquake to explore the fault geometry of an earthquake source. For a given fault geometry, the direction of first motion at a given station can either be compressional (material near the fault moves towards the station) or dilatational (material near the fault moves away from the station), and whether the first motion on a seismogram is a push (upwards movement on a vertical-component seismogram) or a pull (downwards movement, respectively) will therefore change with receiver azimuth.

Since the overall radiation pattern depends on receiver location, source orientation, and the direction of slip along the fault, it is important to clarify the coordinate system used. This study follows the suggestions of Stein and Wysession (2003) who introduced two frameworks. They state that in some cases it is most useful to define the source with respect to the fault, where the x_1 axis aligns with the strike direction of the fault on which slip occurs, the x_3 axis points upwards, and x_2 is perpendicular to x_1 and x_3 . The angle of dip, δ , defines the fault orientation with respect to the surface. x_1 is arranged in such a way that the dip measured from the $-x_2$ axis is less than 90° . The slip angle, λ , represents the direction of motion. It is measured counterclockwise in the fault plane from the x_1 direction, describing the motion of the hanging wall block with respect to the foot wall block (Stein and Wysession, 2003). To place and orient this coordinate system relative to the geographic coordinate system, the fault strike ϕ_f is defined as the angle in the plane of the Earth's surface measured clockwise from north to the fault plane (x_1 axis). Fig. 3.1 shows all relations between these angles and the coordinate system.

An alternative, and in some cases more useful, coordinate system uses geographic co-

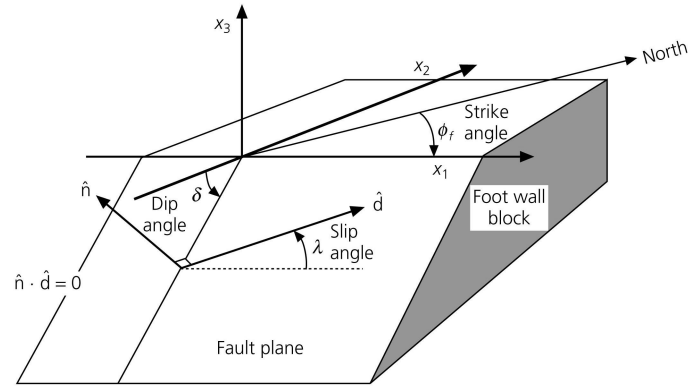


Figure 3.1: Fault geometry used in earthquake studies. Only the foot wall block is shown. The slip vector $\hat{\mathbf{d}}$ lies 90° from the normal vector $\hat{\mathbf{n}}$ and defines the motion of the hanging wall block with respect to the foot wall block. The coordinate axes x_1 , x_2 and x_3 for a coordinate system oriented in respect to the fault geometry are displayed, as well as slip angle λ and strike ϕ_f to define the direction in which slip occurs and the fault orientation, respectively (Stein and Wysession, 2003).

ordinates: $\hat{\mathbf{x}}$ points north, $\hat{\mathbf{y}}$ points east, and $\hat{\mathbf{z}}$ points up (Stein and Wysession, 2003).

The unit normal vector to the fault plane is then:

$$\hat{\mathbf{n}} = \begin{pmatrix} -\sin \delta \sin \phi_f \\ -\sin \delta \cos \phi_f \\ \cos \delta \end{pmatrix}, \quad (3.1)$$

and the slip vector, a unit vector in slip direction, is given by:

$$\hat{\mathbf{d}} = \begin{pmatrix} \cos \lambda \cos \phi_f + \sin \lambda \cos \delta \sin \phi_f \\ -\cos \lambda \cos \phi_f + \sin \lambda \cos \delta \sin \phi_f \\ \sin \lambda \sin \delta \end{pmatrix}, \quad (3.2)$$

Once determined, fault plane solutions for first motions can be represented by focal spheres. The focal sphere is established by projecting compressions and dilatations according to where source-receiver paths intersect the lower hemisphere onto an imaginary, spherical shell enveloping the earthquake source region (Stein and Wysession, 2003). By plotting the lower hemisphere of the focal sphere onto a plane via stereographic projection one obtains the traditional representation of focal mechanisms ('beach ball'). The P-wave first motions for slip along a vertically dipping fault are illustrated in Fig. 3.2. One compressional and one dilatational area can be identified. The change from compressional to dilatational first motion results in areas with small

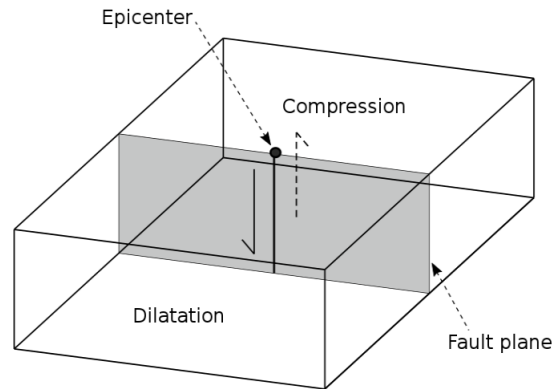


Figure 3.2: First motions of P-waves radiated from a vertical dip slip source. At seismometers located in various directions about the earthquake either a positive (compression) or negative (dilatation) first motion would be observed. Areas with zero radiated seismic energy, the so-called nodal planes, identify the fault plane and its corresponding auxiliary plane. Modified after Stein and Wysession (2003).

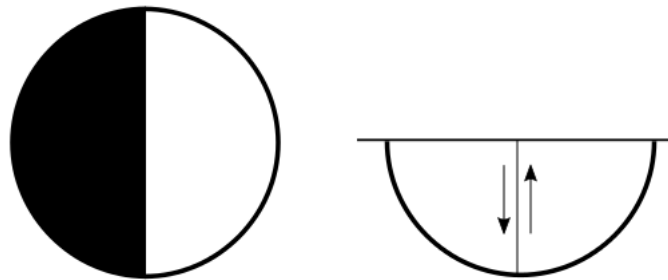


Figure 3.3: Focal mechanism for a vertical dip-slip earthquake on an N-S striking fault. *right:* front view sketch indicating the motion along the vertically dipping slip surface; *left:* Lower hemisphere projection of motion. Black areas indicate compressional first motion.

or zero first motions called nodal planes. Here, this division occurs along the fault plane and the plane perpendicular to it, the auxiliary plane. Yet there is an ambiguity in identifying the fault plane on which slip occurred, from its orthogonal, mathematically equivalent, auxiliary plane, and the study of first motions alone is therefore not sufficient to distinguish between the two. Additional information such as the orientation of pre-existing faults is often taken into account and proves to be useful in determining the actual fault geometry under investigation in a tectonic setting.

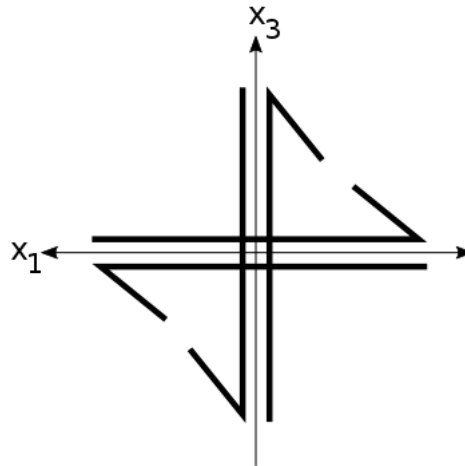


Figure 3.4: $x_1 - x_3$ plain view of the fault geometry and motion along a vertically dipping dip-slip fault, represented by the equivalent body forces of a vertical dip slip fault: a pair of force couples acting about the null axis.

3.2 Body wave radiation patterns

Body wave radiation patterns are determined using equivalent body forces to the actual physical motion (see Chapter 1.6.1). It is important to keep in mind that they only provide a partial picture and serve as a first step in constraining specific parameters, while additional geological and geophysical data are often taken into account in order to draw meaningful conclusions about the detailed rupture processes. In the next few sections the body wave radiation patterns for the most common equivalent body forces are outlined. They provide the knowledge required to derive the P-wave radiation pattern for the ring fault structure.

3.2.1 Double couple

Because the radiation patterns of double couple (DC) sources hold a natural symmetry about the fault plane they are normally considered in a coordinate system oriented along the fault. For vertical slip along a vertically dipping fault, the slip vector is parallel to the x_3 axis. The fault plane lies in the $x_2 - x_3$ plane, so it is normal to the x_1 axis (Fig. 3.4). As mentioned before, radiation patterns vary with varying receiver locations. To illustrate this variation, consider the radiation field in spherical coordinates, where θ is measured from the x_3 axis and ϕ is measured in the horizontal $x_1 - x_2$ plane. Seismic source theory shows that the far field displacement at a distance

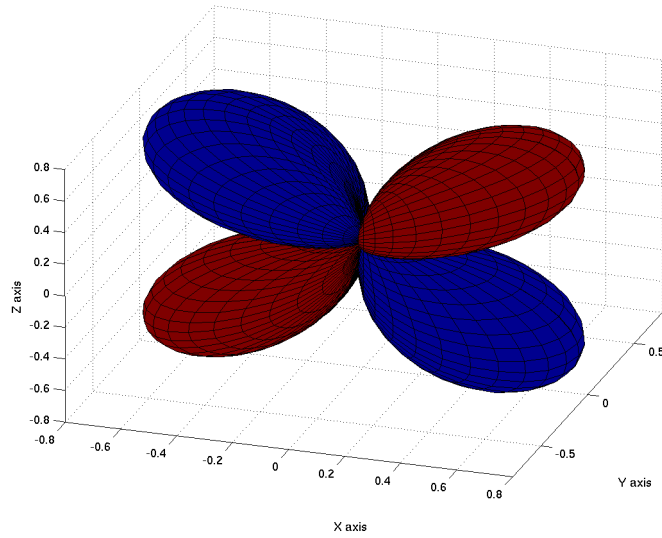


Figure 3.5: P-wave radiation pattern for a double couple source. It has four lobes, two compressional (red) and two dilatational (blue). The radiated seismic energy is zero at the nodal planes (fault plane $x_2 - x_3$ and auxiliary plane $x_1 - x_2$), and maximum amplitudes midway between the two.

r due to compressional waves in a medium with P-wave velocity v_p is given by (Aki and Richards, 2002):

$$u_r = \frac{1}{4\pi\rho v_p^3 r} \dot{M}(t - r/v_p) \sin 2\theta \cos \phi \quad (3.3)$$

noting that in a homogeneous medium the displacement resulting from such a wave will only be radiated in the radial direction (Aki and Richards, 2002). Equ. 3.3 consists of three terms: the first, $\frac{1}{4\pi\rho v_p^3 r}$, reflects the far field amplitude decay of $1/r$. The second term, in which \dot{M} is the source time function as defined earlier in Chapter 2.1.1, describes the energy pulse radiated from the fault which propagates away from the source at P-wavespeed v_p , and arrives at distance r and at a time $t - r/v_p$. The final term in Equ. 3.3 determines the actual shape of the double couple P-wave radiation pattern. This term, $\sin 2\theta \cos \phi$, defines four lobes, with two being compressional and two dilatational, with nodal planes along fault ($\theta = 90^\circ$) and auxiliary ($\phi = 90^\circ$) planes where displacement is zero. This results in the P-wave radiation pattern that can be seen in Fig. 3.5, with maximum amplitudes midway between the nodal planes.

3.2.2 Compensated linear vector dipole

The P-wave radiation pattern for non-DC sources cannot be derived from first motions alone. Instead, waveform analysis is often used to provide additional information. Compensated linear vector dipoles (CLVDs) are a class of non-DC seismic sources. As discussed in Chapter 1.6.5, these are sets of three force dipoles that are compensated, with one dipole twice the magnitude of the other two. In contrast to the ‘beach ball’ focal mechanisms of DCs, the first motions for CLVDs look like baseballs or eye balls (Fig. 3.6). Furthermore, the P-wave radiation pattern for a CLVD source consists of two positive lobes vertically above and below the source, and a ring of dilatational motion around it (Fig. 3.7). CLVD sources are often used to explain the source mecha-

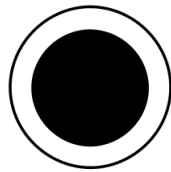


Figure 3.6: Focal mechanism for an example CLVD source. The P-wave first motions create a radiation pattern that looks like an eyeball.

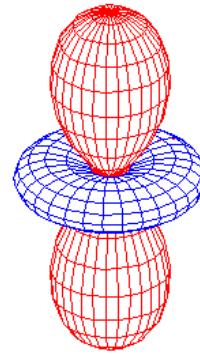


Figure 3.7: P-wave radiation pattern for a CLVD source. It consists of two positive (compressional, red) lobes directly above and below the source, and a ring of negative (dilatational, blue) motion around it.

nisms of low frequency events at volcanoes by a magma dike (e.g. Chouet, 1996b; Waite et al., 2008). Such a system can be modelled as the opening of a pressurised crack (see also Chapter 1.6.5). However, this only holds true when a point source mechanism is assumed to be the driving force of LFs.

In this study, the idea of an extended source mechanism triggering low frequency volcanic events is developed. Since spatially extended sources have so far been poorly investigated, the aim is to convey a better understanding by providing information which has long been accepted knowledge for point sources for a novel type of source. In Chapter 2 such a spatially extended source, the ring fault structure, has been introduced, and its P-phase amplitudes and waveforms were discussed and compared to

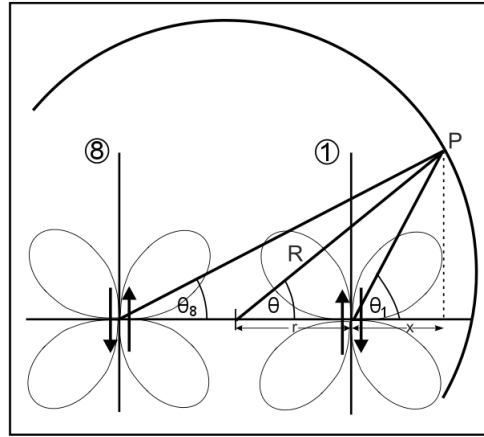


Figure 3.8: Geometrical relationship to determine the radiation pattern of a spatially extended source.

common point sources. Here, the 2D and 3D P-wave radiation patterns for such a ring fault structure are derived and compared to those of double couple and CLVD sources.

3.3 2D body wave radiation patterns of the ring fault structure

3.3.1 P-wave radiation pattern

The superposition of several point sources yields a P-wave radiation pattern that differs from that of a single double couple source. However, each of the 8 sources that build up the ring fault is represented by a double couple (see Chapter 2.2) and hence the P-wave radiation pattern of individual segments shows the ordinary P-wave radiation pattern (Fig. 3.5).

In 2D, where the azimuthal dependence of the radiation pattern is neglected and ϕ is thus kept 0, the ring fault reduces to 2 adjacent DCs. It is therefore sufficient to consider the superposition of two oppositely located segments (e.g. 1 and 8, Fig. 2.3) and sum the resulting amplitude A over a circle with the radius R to derive the desired radiation pattern (Hammer, 2007). Due to opposite orientations of the two double couples, subtraction of one from the other obtains the overall amplitude A :

$$A = \sin(2\theta_1) - \sin(2\theta_8). \quad (3.4)$$

Simple trigonometry (see Fig. 3.8) gives:

$$x = R \cos \theta - r \quad (3.5)$$

$$R \sin \theta = x \tan \theta_1, \quad (3.6)$$

The ratio between ring fault radius r and hypocentral distance R is defined as q :

$$q = \frac{r}{R} = \frac{\text{distance between DCs}}{\text{hypocentral distance}} \quad (3.7)$$

. Using this definition, and inserting Equ. 3.5 into 3.6 and solving for θ_1 then results in:

$$\theta_1 = \arctan \left(\frac{\sin \theta}{\cos \theta + q} \right); \theta_8 = \arctan \left(\frac{\sin \theta}{\cos \theta - q} \right). \quad (3.8)$$

Repeating this for the second double couple and inserting yields the superposition of two double couple sources, projected onto the circle with radius R around the centre between the 2 DC sources, a distance r apart:

$$A = \sin \left[2 \arctan \left(\frac{\sin \theta}{\cos \theta + q} \right) \right] - \sin \left[2 \arctan \left(\frac{\sin \theta}{\cos \theta - q} \right) \right]. \quad (3.9)$$

Figure 3.9 shows the resulting 2D radiation pattern. The 2D radiation pattern consists of a lobe with compressional first motions directly above the source and a smaller amplitude negative ring to its sides. Beneath the source, the lobes are of the same amplitude but oppositely directed. The nodal planes of the ring fault do not, as in the case of a single double couple, coincide with the fault plane.

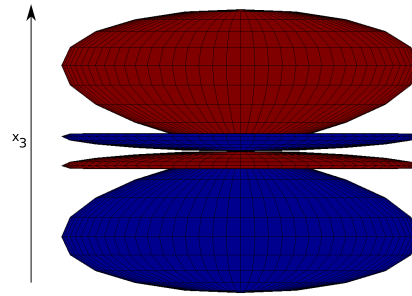


Figure 3.9: 2D P-wave radiation pattern of the ring fault. It consists of a positive (red, first motions compressional) directly above the source and two smaller amplitude negative rings to its sides. The lobes beneath the source are of the same amplitude but with oppositely directed first motions: dilatation (blue) directly below the source, and a ring of compressional first motions (red) to its sides.

3.4 3D body wave radiation patterns of the ring fault structure

3.4.1 P-wave radiation pattern

With the basic concept of the ring fault radiation pattern being a superposition of radiation patterns of several point sources, the 3D P-wave radiation pattern for the ring fault structure can be determined in the same way as in 2D, but with both θ and ϕ ranging from 0 to 2π . For the 3D case, the radiation pattern was calculated by superimposing and summing the amplitudes of the 8 octagon segments, and in an advanced step the P-wave radiation pattern for a true cylindrical ring fault was calculated by integrating over the cylindrical fault geometry.

For the octagon, the amplitudes for oppositely oriented segment pairs (see Fig. 2.3) can be derived using the relations shown in Fig. 2.4:

$$\begin{aligned}
A_1 &= \sin \left[2 \arctan \left(\frac{\sin \theta}{\cos \theta + q} \right) \right] \cos \left[\arctan \left(\frac{\sin \phi}{\cos \phi + q} \right) \right] \\
A_8 &= \sin \left[2 \arctan \left(\frac{\sin \theta}{\cos \theta - q} \right) \right] \cos \left[\arctan \left(\frac{\sin \phi}{\cos \phi - q} \right) \right] \\
A_2 &= \sin \left[2 \arctan \left(\frac{\sin \theta}{\cos \theta + q} \right) \right] \cos \left[\arctan \left(\frac{\sin(\phi + \pi/4)}{\cos(\phi + \pi/4) + q} \right) \right] \\
A_3 &= \sin \left[2 \arctan \left(\frac{\sin \theta}{\cos \theta - q} \right) \right] \cos \left[\arctan \left(\frac{\sin(\phi + \pi/4)}{\cos(\phi + \pi/4) - q} \right) \right] \\
A_4 &= \sin \left[2 \arctan \left(\frac{\sin \theta}{\cos \theta + q} \right) \right] \cos \left[\arctan \left(\frac{\sin(\phi + \pi/2)}{\cos(\phi + \pi/2) + q} \right) \right] \\
A_5 &= \sin \left[2 \arctan \left(\frac{\sin \theta}{\cos \theta - q} \right) \right] \cos \left[\arctan \left(\frac{\sin(\phi + \pi/2)}{\cos(\phi + \pi/2) - q} \right) \right] \\
A_6 &= \sin \left[2 \arctan \left(\frac{\sin \theta}{\cos \theta + q} \right) \right] \cos \left[\arctan \left(\frac{\sin(\phi - \pi/4)}{\cos(\phi - \pi/4) + q} \right) \right] \\
A_7 &= \sin \left[2 \arctan \left(\frac{\sin \theta}{\cos \theta - q} \right) \right] \cos \left[\arctan \left(\frac{\sin(\phi - \pi/4)}{\cos(\phi - \pi/4) - q} \right) \right]
\end{aligned} \tag{3.10}$$

The overall octagon radiation pattern is then gained by summing the eight segment contributions:

$$A = A_1 - A_8 + A_2 - A_3 + A_4 - A_5 + A_6 - A_7 \tag{3.11}$$

The result can be seen in Fig. 3.10. Above the source, a large compressional lobe can be identified, while directly below the source is a second lobe with the same amplitude but opposite polarisation (dilatation). To its sides, the octagon radiation pattern exhibits 8 pairs of compressional - dilatational tongues with very small amplitudes that can only be visualised when zooming into the source region (Fig. 3.11).

Instead of basic summation of 8 octagon segments it is possible to determine the body wave radiation pattern of a cylindrical ring fault by numerically integrating over a larger number of point sources along the fault edges. The ring fault radiation pattern can then be calculated for each possible combination of θ and ϕ . The result can be seen in Fig. 3.12. Again, two big amplitude lobes, compressional above and dilatational below the source, can clearly be identified. A zoom into the source region discloses one small

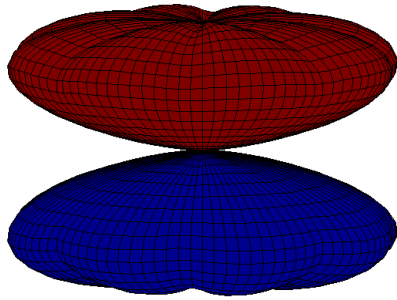


Figure 3.10: 3D P-wave radiation pattern of the octagon source distribution

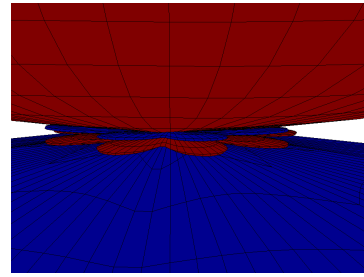


Figure 3.11: Zoom into the source region of the octagon 3D P-wave radiation pattern

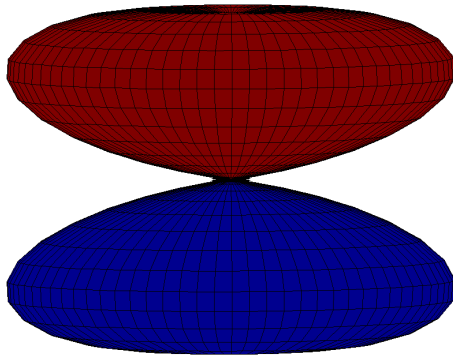


Figure 3.12: 3D P-wave radiation pattern of the ring fault

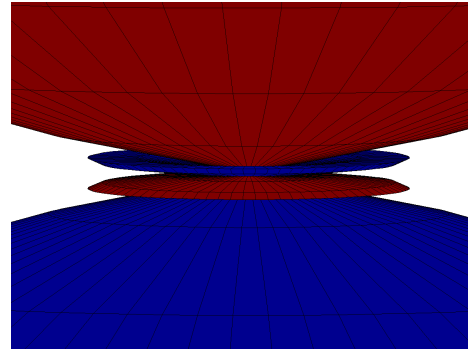


Figure 3.13: Zoom into the source region of the ring fault 3D P-wave radiation pattern

amplitude ring of dilatational first motions and a second one with matching amplitudes but opposite polarisation to the sides of the source, correspondingly (Fig. 3.13).

3.5 3D body wave radiation patterns of a dike

If magma ascent occurs in a dike-like structure, the corresponding P-wave radiation pattern can be calculated by using two oppositely oriented point sources that are the dike width d apart. In Chapter 2, a detailed waveform analysis for a source of this nature was carried out. Here, the P-wave radiation pattern is derived and presented in 3D. Note the difference between the 3D treatment of a pair of adjacent DCs and the previous description in 2D (Chapter 3.3.1).

3.5.1 P-wave radiation pattern

Fig. 3.14 shows the 3D radiation pattern of first P-wave motions as generated by a dike. The positive (compressional) lobe directly above the source shows that the

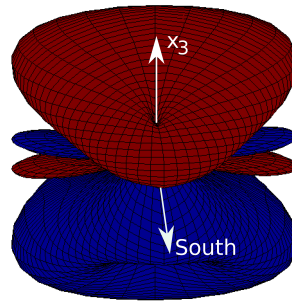


Figure 3.14: 3D P-wave radiation pattern of the dike

dike radiation pattern is not rotationally symmetric about the depth-axis (x_3). The positive lobe exhibits an area of decreased radiated P-wave energy. Located to the side of the source are two tongues of dilatational first motions, perpendicular to the dike orientation. Below the source, the radiation pattern features a mirror image of the described first motions, but with opposite polarisations: a big lobe of dilatational first P-wave arrivals, and a pair of compressional tongues to the side.

3.6 Comparison with conventional radiation patterns

The step from point to spatially extended source mechanism as the underlying physical process of low frequency seismic events in volcanoes is a major advancement in the understanding of this particular type of event and its potential as forecasting tool. To fully investigate the consequences of this progress it is important to not only derive the characteristics of such novel sources, but also to compare them against existing point source models. The P-waveforms and amplitudes of the ring fault and dike structures were discussed in Chapter 2. Here, the P-wave radiation pattern of the proposed systems are checked against conventional point source radiation patterns often used to interpret volcano seismological data sets.

Figures 3.10 and 3.12 illustrate highly similar P-wave radiation patterns for octagon and ring fault. This is not a surprising result as the numerical integration used to obtain the ring fault radiation pattern is simply an increase of fault planes from eight for the octagon to a larger number. The octagon can therefore be seen as a simplification, possessing the minimum amount of slip surfaces needed to reach the desired symmetry

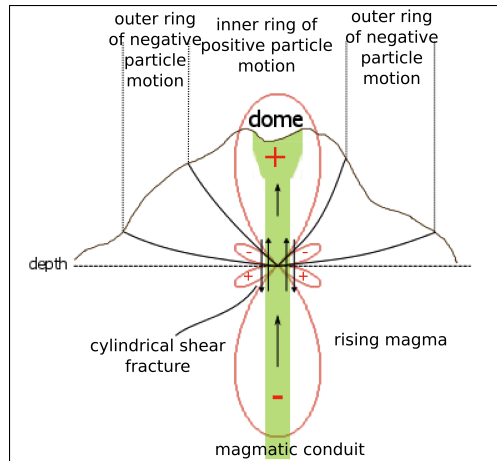


Figure 3.15: Schematic radiation pattern through a volcanic edifice for a shallow source

about z that a cylindrical fault exhibits. The ring fault radiation pattern is then the improved and most precise representation of the seismic energy that would be radiated by upwards movement of magma in a volcanic conduit.

Although the ring fault is a superposition of simultaneously slipping double couples, a comparison of the sources' P-wave radiation patterns does not show any similarities. While the nodal planes of a double couple are the fault plane and its auxiliary plane, and therefore depend on the fault orientation, this is not the case for the ring fault structure. The areas of no direct P-wave radiation depend on q (distance between DCs/hypocentral distance; Fig. 3.7), but independent of azimuth ϕ . When disregarding attenuation the maximum observed first arrival seismic energy at a given point and the rate of amplitude decrease with hypocentral distance is dependent on source depth and ring fault radius/dike width.

In the upper hemisphere, the P-wave radiation patterns of dike and ring fault show a certain degree of similarity with the CLVD point source radiation pattern: all three sources generate a lobe of compressional first motions above the source, and show areas of dilatation to the side (Figures 3.7, 3.12 and 3.14). Figure 3.15 illustrates the difficulty of capturing the differences between these source geometries from seismic records in volcanic settings. While in this case a schematic of the ring fault P-wave radiation pattern is shown in relation to a volcanic edifice, the radiation patterns can be replaced by those of both the dike and CLVD. Dependent on source depth and

station distribution first arrival polarities and amplitudes change for all three sources, complicating the ability to distinguish them from each other. This means that given a specific geography and station distribution these two fundamentally different physical processes, ascending magma in the conduit represented by the ring fault model on the one hand, and an oscillating, subhorizontal fluid filled crack represented by the CLVD model on the other hand, may result in the same observed first P-wave polarities (see Chapter 6.3) and indistinguishable amplitudes (see Chapter 7.2). This being the case, studies of first motion polarities of LF volcano seismic signals that inferred in CLVD source mechanisms, i.e. Waite et al. (2008), Iguchi (1994), or several examples summarised in a publication by Miller et al. (1998b), should therefore be revisited. The radiation patterns found in these cases should be critically assessed by considering the possibility of spatially extended sources, such as the ring fault structure, additionally to the commonly assumed point source trigger mechanism.

Only the seismic energy radiated below the source or precisely planned deployment of seismic recorders could shed light on this ambiguity. Regional seismic stations at greater distances from the source could thus be helpful in identifying the source processes. Very small event magnitudes, as well as the island setting in the case of Montserrat, however, complicate the use of regional stations. On volcanoes, it is therefore rare to capture rays travelling from below the source due to the small aperture of seismic networks.

Additional geological and geophysical parameters can be taken into account to resolve this issue. Field observations and magma flow modelling have supported a spatially extended source mechanism (Neuberg et al., 2006), and most recently an experimental study on frictional melting gave evidence for seismogenic slip along the conduit walls as a favourable source scenario (Kendrick et al., 2014). This study will therefore strongly contribute to driving our understanding of volcanic eruptions forwards.

3.7 Summary

The P-wave radiation pattern for two spatially extended sources, a ring fault and a dike structure, have been derived and compared to radiation patterns for existing conventional point source models. The 3D P-wave radiation patterns for spatially extended sources show areas of compressional and dilatational first motions, separated by nodal

planes. Although a superposition of single double couples, the overall radiation patterns for ring faults and dikes are fundamentally different to those of a single double couple. The ring fault radiation pattern shows a symmetry about the depth axis and exhibits an area with compressional first motions above the source and a dilatational ring to its sides. Below the source the picture of radiated energy is of the same amplitude but oppositely polarised.

Given the volcanic setting, and non-ideal distribution of seismic receivers on the flanks of active volcanoes, current recorded data are unlikely to be able to distinguish the different source mechanisms from each other, namely CLVD, ring fault, and dike sources, due to high similarities in radiation patterns in the upper hemisphere. The findings in this chapter show that a CLVD source is only one possible interpretation of the observed first motion polarities of LF volcanic seismicity. Therefore, the consideration of spatially extended sources, such as the ring fault structure, are indispensable when interpreting recorded P-wave radiation patterns. Further investigations into different wave phases as well as interdisciplinary volcanological studies could help to distinguish the two. The ring fault as a model for LF generation has been strengthened by field evidence, numerical and experimental studies, and thus seems more justifiable than alternative models while explaining the seismic datasets as well.

Chapter 4

Catalogue of synthetic complex sources

Synthetic modelling of seismic wavefields is a powerful tool in gaining information on the source mechanisms underlying volcano seismicity. Once instrument response and path effects have been removed, real data can be compared to synthetic models, and on the basis of a best-fit approach the obtained model parameters allow insights into the nature and geometry of the source. At present, investigations have almost exclusively provided conceptual ideas or involved numerical modelling of point sources. In volcanic settings, however, point source approximation is likely not sufficient in approximating the highly complex source processes acting at depth, as shown in Chapter 2. An alternative to point dislocation sources such as single double couples are spatially extended source geometries.

In Chapter 2 I developed two spatially extended sources, ring fault and dike, from a conventional double couple source. This chapter aims to provide a catalogue of further complex source scenarios involving new spatially extended sources. The fault geometries examined here are modifications of the ring fault structure and can generally be divided into two categories: (1) spatially extended sources with instantaneous slip, and (2) spatially extended sources with individual time history. The former involves instantaneous slip of at least two slip surfaces, and the considered cases that fall in this category are: quarter and half conduits, as well as two simultaneously acting ring faults at different source depths. Slip along conduit segments is considered to account for cases where critical strain rates and subsequent seismogenic slip occur at parts of the conduit only, i.e. due to geometry changes (Thomas and Neuberg, 2012). Two

simultaneously acting ring fault structures represent a case where two LF swarms are activated at the same time (Green and Neuberg, 2006). For spatially extended sources that exhibit slip with a time history, a helix like structure, where ring fault segments at different depths are triggered consecutively, will be analysed. Helix-like flow patterns have been observed in polymer flow as this type of flow represents the smallest surface area of defect that allows motion of one part of the lattice with respect to another (Elgasri et al., 2011; Piau et al., 2000; Kay et al., 2003). The case of a helix-like flow pattern is therefore considered here for the study of crystal rich magmas.

The waveforms and amplitudes of first arrival P-waves generated by such spatially extended sources are discussed and will provide an excellent collection of novel synthetic models. Real data examples can then be compared against the synthetic models, allowing insights into the source processes of low frequency events on volcanoes.

4.1 Simultaneous extended sources

The endeavours of this study have so far been restricted to cases where slip occurs along the complete circumference of the conduit, meaning that the entire magma column slips upwards. It is, however, somewhat more intuitive to imagine seismogenic slip occurring along only parts of the conduit. In the following, synthetic waveforms for ring fault segments are used to simulate seismogenic slip along sections of the conduit walls. In particular, quarter and half conduits are presented and examined.

All models discussed here have been calculated using 32 point sources to build the complete ring fault structure, while slip occurs along only a fraction of these individual sources. All cases were embedded in a homogeneous medium with a velocity structure as outlined in Chapter 2.1.2. To enable comparison with waveform amplitudes in Chapter 2 the total seismic moment was chosen to be $M_0 = 8.0 \text{ Nm}$ in each case. The source time function was a delta impulse approximation with a duration of $\tau = 1 \text{ s}$. The conduit diameter was set to $d = 50 \text{ m}$, and the waveforms were modelled for a total of 12 receivers, one each at 1 km, 3 km, and 5 km epicentral distance, in all four cardinal directions (N, E, S, W; see Fig. 2.5).

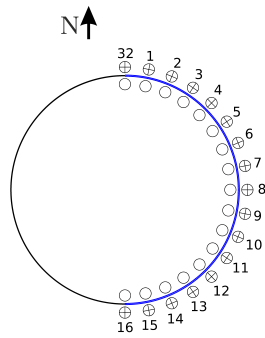


Figure 4.1: Orientation of a slipping half ring whose slip surface spans over azimuths $\alpha = 0^\circ - 180^\circ$. 17 (1-16, 32) of the 32 point sources building the ring fault act simultaneously along a 50 m wide bent slip surface.

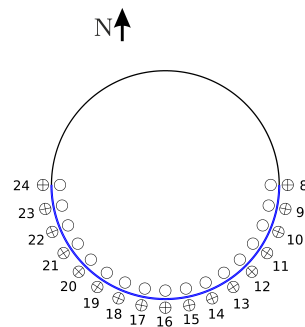


Figure 4.2: Orientation of a slipping half ring whose slip surface spans over azimuths $\alpha = 90^\circ - 270^\circ$. 17 (8-24) of the 32 point sources building the ring fault act simultaneously along a 50 m wide bent slip surface.

4.1.1 Half conduit

If slip occurs along half the ring fault walls the overall observed seismicity evolves from seismogenic slip along a bent slip surface. The superposition of seismic energy generated from a fraction of the 32 ring fault sources then results in the observed and recorded seismic signal at a given receiver location. Only the point sources located on the slipping half ring generate a seismic signal, and the recorded overall event at a given seismic station depends on the orientation of the half ring of simultaneously acting double couples in respect to each station. Here, two cases are considered: (1) slip along a half conduit whose bent slip surface starts at azimuth $\alpha = 0^\circ$ and ends at $\alpha = 180^\circ$ (Fig. 4.1); (2) slip along a half conduit whose slip surface spans between $\alpha = 90^\circ$ and $\alpha = 270^\circ$ (Fig. 4.2).

The P-waveforms resulting from a slipping half ring with orientation (1) at stations 5km to the north, east, south, and west can be seen in Fig. 4.3. Due to the orientation and symmetry of the bent slip surface the two receivers to the north and south (N5 and S5) have the same relative location in respect to the slip surface, and the recorded seismic P-waves therefore have the same shape and amplitudes (*top left* and *bottom left* of Fig. 4.3).

The receivers to the east and west (E5 and W5) lie on the symmetry axis of the half ring, meaning that pairs of traces with the same orientation arrive at the receiver at the same time and superimpose constructively. This is why the maximum P-wave

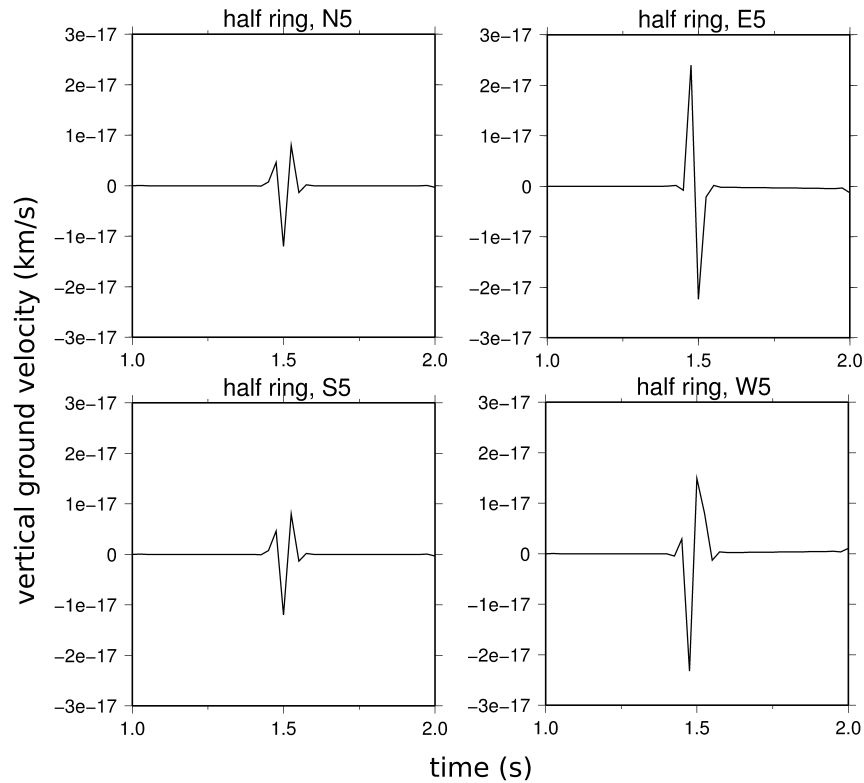


Figure 4.3: P-waveforms of a 1.5 km deep half conduit spanning from azimuths $\alpha = 0^\circ - 180^\circ$. Receivers were located at 5km epicentral distance to the north, east, south and west (N5, E5, S5, W5). Due to the same relative location of the slip surface in respect to stations N5 and S5, the resulting vertical P-wave ground velocities at these stations are identical. At these stations, partial destructive superposition takes place and yields Ricker-like wavelets with maximum P-wave amplitudes of -1.206×10^{-17} km/s. The waveforms at receivers E5 and W5 are 2-lobed and oppositely polarised, and have larger maximum P-wave amplitudes (-2.324×10^{-17} km/s, and 2.400×10^{-17} km/s respectively) than N5 and S5.

ground velocities at these stations are with -2.324×10^{-17} km/s, and 2.400×10^{-17} km/s respectively, greater than those recorded in the north and south (-1.206×10^{-17} km/s).

Additionally, the seismic energy radiated from double couple 8 (see Fig. 4.1) arrives at stations to the east before all other traces while it has the longest travel path to stations to the west of the source. This causes an alteration of wave shape, with the second lobe of the Küpper-like wavelet recorded to the west being wider (total P-wave duration: 0.2 s) than that recorded in the east (total P-wave duration: 0.15 s), which is shown in the *top right* and *bottom right* of Fig. 4.3).

Configuration (2) has the same properties as configuration (1), and therefore radiates

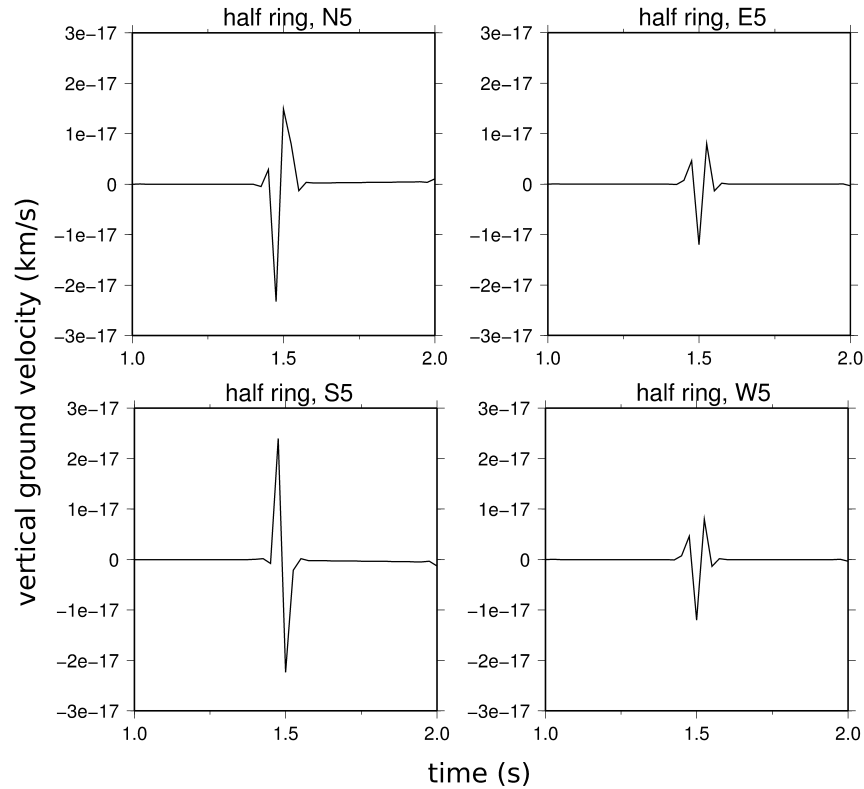


Figure 4.4: P-waveforms of a 1.5 km deep half conduit spanning from azimuths $\alpha = 90^\circ - 270^\circ$. Receivers were located at 5 km epicentral distance to the north, east, south and west (N5, E5, S5, W5). Resulting waveforms are comparable to half ring configuration (1), but 90° rotated: due to the same relative location of the slip surface in respect to stations E5 and W5, the resulting vertical P-wave ground velocities at these stations are identical. At these stations, partial destructive superposition takes place and yields Ricker-like wavelets with maximum P-wave amplitudes of -1.206×10^{-17} km/s. The waveforms at receivers N5 and S5 are 2-lobed and oppositely polarised, and have with -2.324×10^{-17} km/s, and 2.400×10^{-17} km/s respectively, larger maximum P-wave amplitudes than E5 and W5.

the same P-waveforms as such, but is 90° rotated. This can be seen in Fig. 4.4: P-waves recorded to the east and west of the half ring are identical (and also identical to the waveforms recorded to the north and south of half ring configuration (1)). To the north and south of half ring (2), the recorded P-waves are 2-lobed non-zero phase Küpper wavelets, with the one recorded to the north equivalent to the west in configuration (1), having a wider second lobe due to the longer travel time of double couple 16.

It should be noted that the waveforms recorded outside the symmetry axes of the half rings (N and S for configuration (1), E and W for configuration (2)) resemble those originating from the full ring fault structure and recorded at all azimuths (see Chapter 2).

4.1.2 Quarter conduit

Similar to the slipping half conduits in Chapter 4.1.1, two scenarios (Figs. 4.5 and 4.6) for slip along a quarter of the 50 m wide conduit were synthetically modelled and synthetic seismograms for stations at 5 km epicentral distance to the north, east, south and west can be seen in Figures 4.7 and 4.8. The two figures represent the P-waveforms for two different orientations of the bent slip surface: (1) slip along a quarter ring with azimuths $\alpha = 0^\circ - 90^\circ$, and (2) slip along a quarter ring spanning from $\alpha = 45^\circ - 135^\circ$ (see Figs. 4.5 and 4.6).

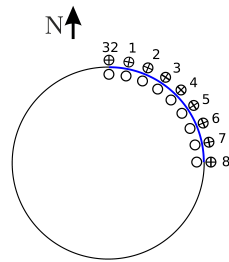


Figure 4.5: Orientation of a slipping quarter ring whose slip surface spans over azimuths $\alpha = 0^\circ - 90^\circ$. 9 (1-8, 32) of the 32 point sources building the ring fault act simultaneously along a 50 m wide bent slip surface.

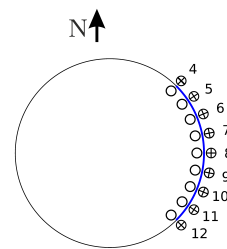


Figure 4.6: Orientation of a slipping quarter ring whose slip surface spans over azimuths $\alpha = 45^\circ - 135^\circ$. 9 (4 to 12) of the 32 point sources building the ring fault act simultaneously along a 50 m wide bent slip surface.

Due to the relative orientation of the 8 double couple sources arranged along the quarter ring (configuration (1)) in respect to the station distribution, the superimposed overall P-waveforms in the north and east (N5 and E5), and equivalently to the south and west (S5 and W5), are identical (Fig. 4.7). At N5 and E5, superposition of seismic energy originating from individual double couples is constructive, resulting in greater overall maximum vertical P-wave velocities ($4.984 \times 10^{-17} \text{km/s}$) than in the case of a slipping half ring where superposition is partially negative (Fig. 4.3).

All waveforms have the shape of non-zero phase Küpper wavelets, with the second lobe of the traces with longer travel times (S5 and W5) being wider than those of the nearby stations to the north and east. It is the contribution of DC 8 that is responsible for the widening of the second lobe of the waveform, because it has the longest travel time of all acting point sources (see Fig. 4.5).

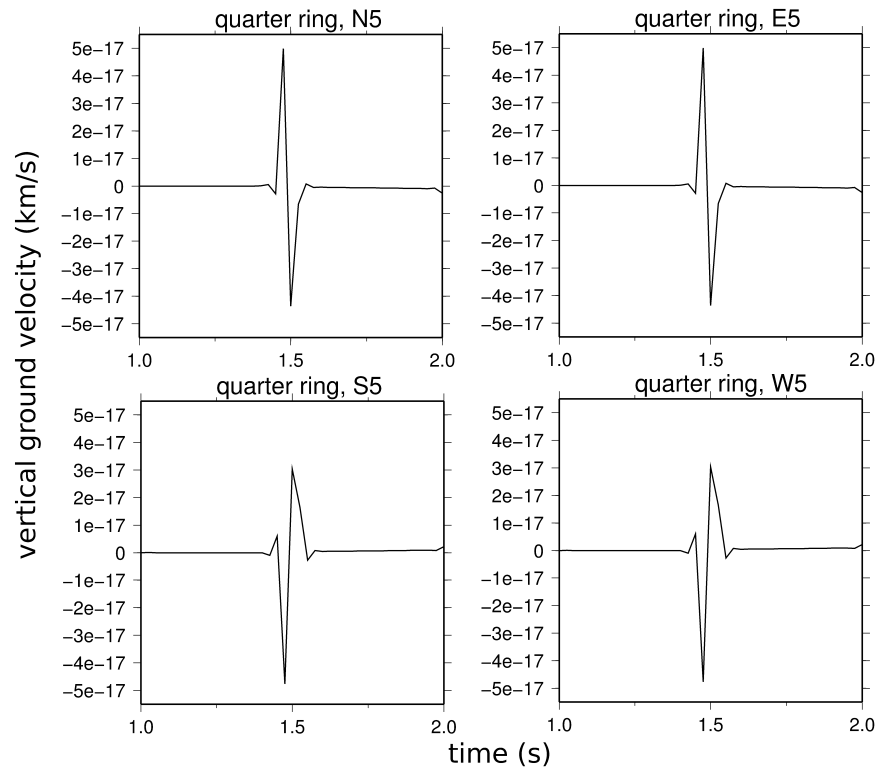


Figure 4.7: P-waveforms of a 1.5 km deep quarter conduit spanning from azimuths $\alpha = 0^\circ - 90^\circ$. Receivers were located at 5km epicentral distance to the north, east, south and west (N5, E5, S5, W5, Fig. 2.5). All wavelets are 2-lobed Küpper-like wavelets, with the second lobe of waveforms at S5 and W5 wider than those at N5 and E5. Due to the same relative location of the slip surface in respect to stations N5 and E5, as well as S5 and W5, the resulting vertical P-wave ground velocities are identical.

Changing the orientation of the slip surface in respect to the stations changes the way the individual seismic wave trains interfere with each other. With slip occurring along a quarter ring with azimuths $\alpha = 45^\circ - 135^\circ$ (configuration (2)) the resulting waveforms at receivers to the north and south, and to the east and west respectively, are identical, because of identical relative receiver locations to the slip surface (Fig. 4.6).

Stations E5 and W5 lie in the symmetry axis of the slipping quarter conduit (configuration (2)). This means that pairs of same polarity waves arrive at the station in phase, resulting in complete constructive superposition, and thus largest maximum vertical P-wave velocities of $\pm 6.972 \times 10^{-17}$ km/s (*top right* and *bottom right* in Fig. 4.8). In contrast to the complete constructive superposition of waveforms to the east and west, superposition at receivers N5 and S5 is mostly destructive, with much smaller maximum ground velocities of -7.948×10^{-18} km/s. Since travel paths of double couples

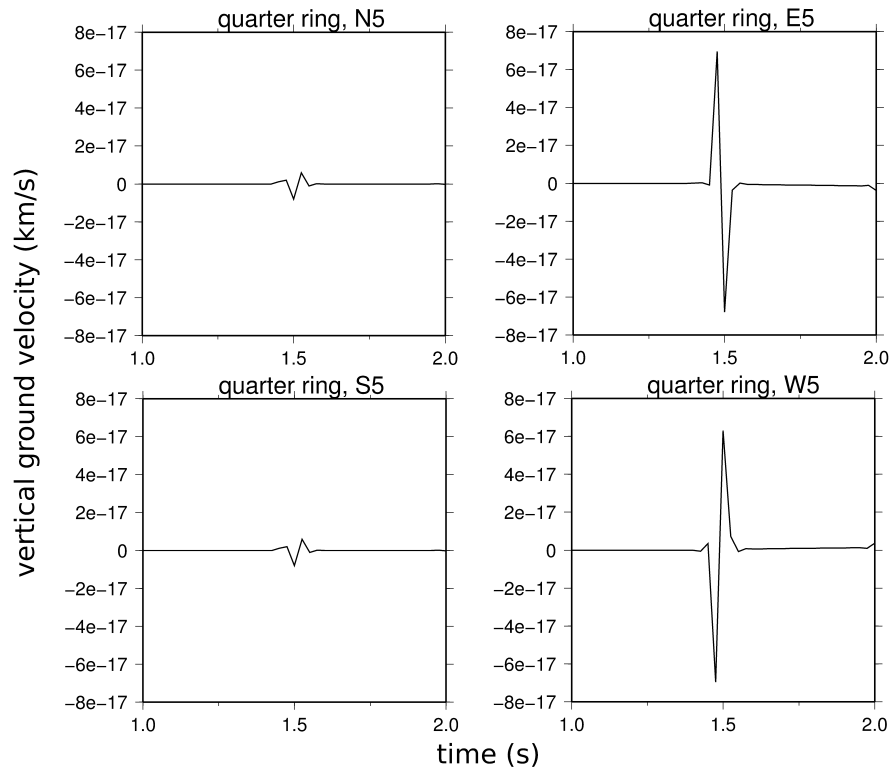


Figure 4.8: P-waveforms of a 1.5 km deep quarter conduit spanning from azimuths $\alpha = 45^\circ - 135^\circ$. Receivers were located at 5km epicentral distance to the north, east, south and west (N5, E5, S5, W5, Fig. 2.5). Due to the same relative location of the slip surface in respect to stations N5 and E5, as well as S5 and W5, the resulting vertical P-wave ground velocities are identical, but oppositely polarised. All seismic traces arrive at E5 and W5 in phase, fully constructive superposition takes place and results in large max. P-wave amplitudes. Contrarily, mostly destructive superposition of slightly out of phase and negatively polarised wave trains takes place at N5 and S5.

9 to 12 are longer than those of double couples 4 to 7 (Fig. 4.6), oppositely polarised pairs of P-waves arrive at the receiver out of phase, preventing complete cancellation of seismic energy (*top left* and *bottom left* in Fig. 4.8).

4.2 Multiple sources

Low frequency earthquakes can be grouped into event families, with oftentimes more than one family being active at the same time (Rowe et al., 2004; Green and Neuberg, 2006; Ottenmüller, 2008). Simultaneously acting event families indicate that seismicity is generated at multiple depths at the same time, with waveforms radiated from individual source locations likely overlapping to construct the observed wavefield at given receiver locations. Due to slightly differing source locations and path effects due to

inhomogeneities in the volcanic edifice the resulting waveforms can be exceptionally complicated. Here, I consider cases where the sources are too close to each other to be resolved in the seismic trace.

However complex the real scenario, synthetic modelling allows the study of the fundamental principles underlying these complex processes by reducing the complexity of the system with the help of assumptions. Here, a simplified model allows the concentrated study of the P-waveforms generated by two simultaneously slipping ring fault structures. The results will give insights into the effects on P-waveforms and amplitudes when more than one spatially extended sources are active at the same time.

4.2.1 Two simultaneous ring faults

When several sources act simultaneously, the observed seismic wavefield at a given source location will be the result of the superposition of individual wave trains. Travel time differences between individual source locations will affect the nature of the superposition that takes place: if wave trains with the same polarity arrive at the receiver in phase, constructive superposition will take place, and vice versa.

Here, two simultaneously acting ring faults are considered. The two spatially extended sources are vertically separated by 100m, at depths of 1400 m and 1500 m, respectively. Both ring faults have diameters of $d = 50$ m, assuming a stable conduit diameter in the conduit region under investigation, and are formed by 32 simultaneously acting point sources each, to simulate slip along a cylindrical conduit (see also Chapter 2.2). The input moment for each ring fault was $M_0 = 8.0$ Nm. The homogeneous model space as defined in Chapter 2.1.2 was adopted, and stations were positioned in all cardinal directions and a number of epicentral distances, which are illustrated in Fig. 2.5.

The P-waves of the combination of two simultaneously acting ring fault structures observed at stations 5 km to the north, east, south and west of the sources' epicentres are shown in Fig. 4.9. Comparable to the waveforms produced by a single ring fault, the superposition of seismic energies of two simultaneously acting ring faults yields identical waveforms for all azimuths. This indicates that, analogously to a single ring fault, the observed P-wavefield of two synchronously acting ring faults are independent of receiver azimuths.

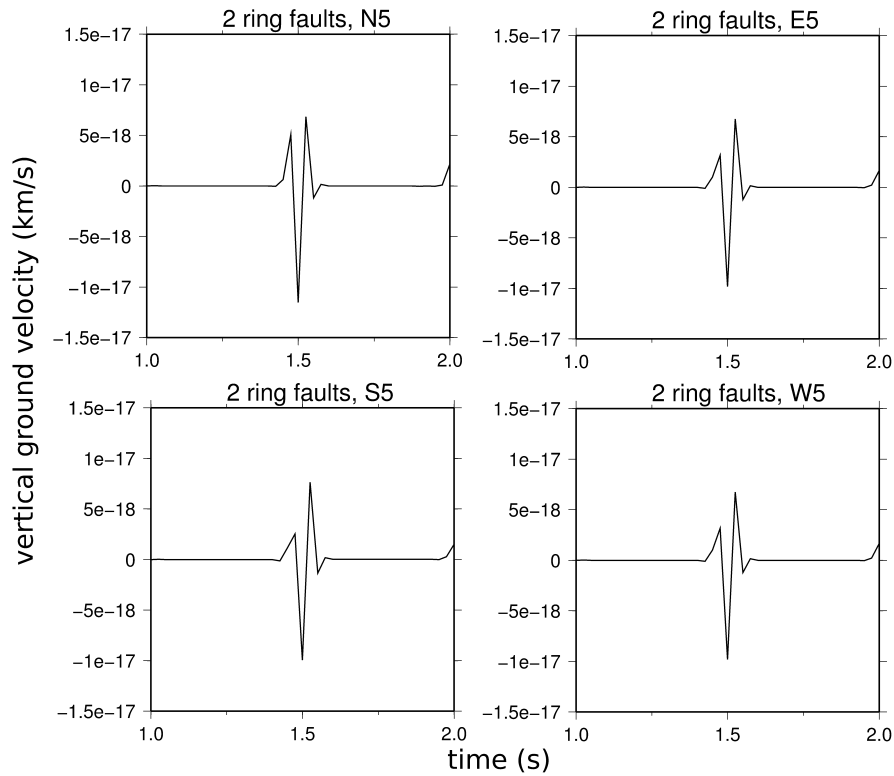


Figure 4.9: P-waveforms of a combination of two simultaneously acting ring faults at 1400 m and 1500 m source depths, respectively. Receivers were located at 5 km epicentral distance to the north, east, south and west (N5, E5, S5, W5). The resulting vertical P-wave ground velocities have the shape of Ricker wavelets, and are identical in all directions. For the given ring fault diameters (50 m), vertical source separation (100 m), and source receiver distances, constructive superposition takes place, resulting in greater maximum P-wave amplitudes than generated by a single ring fault structure.

The observed Ricker-like wavelets exhibit maximum velocities of -1.128×10^{-17} km/s, which exceed those of a single ring fault of 1500 m depth by 187% (5.248×10^{-18} km/s) (Fig. 4.10). In fact, maximum P-wave amplitudes resulting from the superposition of two ring faults are almost doubled compared to a single acting ring fault. This is because the collective scalar input moment is with $M_{\text{total}} = M_{\text{RF1}} + M_{\text{RF2}} = 16.0$ Nm twice that of a single ring fault structure, and constructive superposition of the two will contribute to the maximum observed P-wave ground velocities. Deviations from the exact doubling as observed here are likely due to slightly different travel paths and back azimuths of the incoming waves at a given station, due to different source depths.

The observed body waveforms of two simultaneously acting sources were generated and

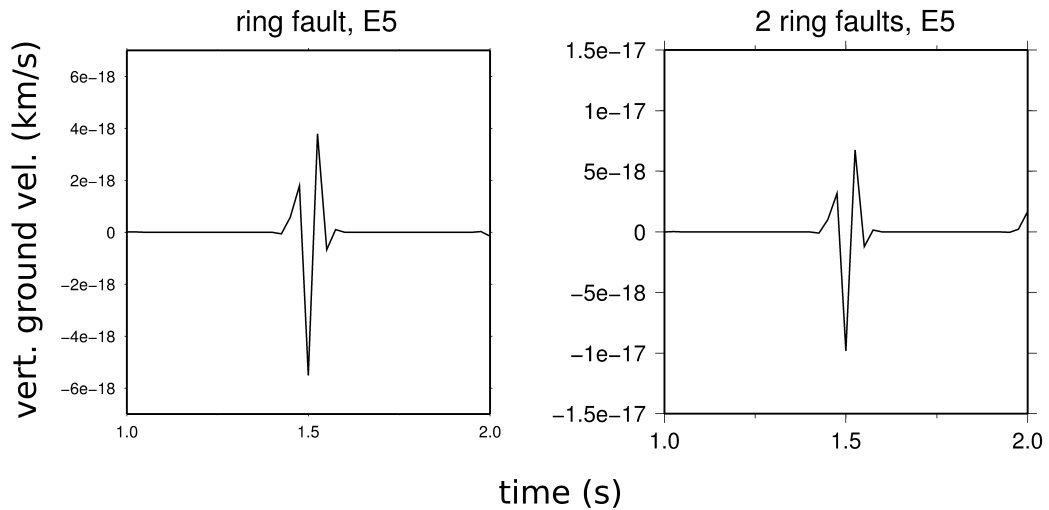


Figure 4.10: Comparison of single (*left*) and two ring faults (*right*) P-waveforms, for a source at 1.5 km depth and a receiver at 5km epicentral distance and $\alpha = 90^\circ$. The observed maximum ground velocities differ, with the P-wave contribution of two ring faults exceeding that of the single ring fault by 187%.

examined in the previous section. Triggered at the same time, both wave trains are radiated and superposed to give the final combined P-waveforms. The difference in source locations of 100m introduces slightly different travel paths - and hence times, resulting in slightly decreased maximum P-wave velocities compared to twice a single ring fault. It is important to note that observed travel time differences and accompanying phase shifts are strongly dependent on the properties of the medium, and results will change when, e.g., velocity layers are introduced to the model. Furthermore, this effect may be enhanced as the number of sources increase, and a time history for consecutive events is introduced. In the following, sources with time history are considered in more detail, and their P-waves are analysed and compared to already treated cases of spatially extended sources.

4.2.2 Staggered sources

The motivation for these model setups lies in the stress and strain distributions and changes in the volcanic conduit at locations and times where LF seismicity is generated. Considering brittle failure of magma in a shear sense as the only source mechanism of LF seismicity, LF events are first generated in conduit areas where a critical shear strain rate is overcome (Neuberg et al., 2006). Once primary fractures have occurred, the magma can then ascend aseismically, akin to friction-controlled slip along the newly

generated faults (Collier and Neuberg, 2006). As numerical modelling by Thomas and Neuberg (2012) suggests, the pressure profile across the conduit is affected by the generation of fractures in a way that moves the depth at which cracks along the conduit walls build down to lower depths.

To model the wave field produced by such a propagation of source depths of consecutive events, time staggered slip along the conduit walls, or different parts of it, is considered. Initially, slip occurs at a certain depth, generating seismicity, which then triggers a number of consecutive events further up or down the conduit. The P-waveforms of such time-delayed sources are then obtained by linearly stacking the individual contributions.

The case that will be discussed here involves time staggered slip along the circumference of a 50 m wide conduit at four different source depths. Embedded in a homogeneous halfspace as defined in Chapter 2.1.2 initial seismogenic slip of the first ring fault occurs at 1500 m source depth. Slip of ring faults at 1450 m, 1400 m, and 1350 m follows with $\Delta t = 0.001$ s time delay, and the observed P-waveforms at a given station network (Fig. 2.5) represent the superposition of all acting sources. The resulting P-waves at stations at 5 km epicentral distance can be seen in Fig. 4.11.

For a given epicentral distance, observed P-waves are identical in all cardinal directions. The time delay of $\Delta t = 0.001$ s in between sources causes a longer P-wave duration of 0.275 s compared to all modelled events without time history. Due to different trigger times and source - receiver distances, P-wave arrivals of individual RFs are different and phase shifted, which leads to complex P-waveforms compared to the superposition of two simultaneously acting ring faults as discussed in Chapter 4.2.1.

The seismic input moment of each RF was constant, with $M_0 = 8$ Nm, which gives a total scalar moment of $M_0 = 32$ Nm for four ring faults. Maximum vertical ground velocities are with -3.126×10^{-18} km/s, however, one order of magnitude smaller than those of the single ring fault case. This indicates partial destructive superposition of individual ring fault contributions due to different P-wave arrival times and accompanied phase shifts.

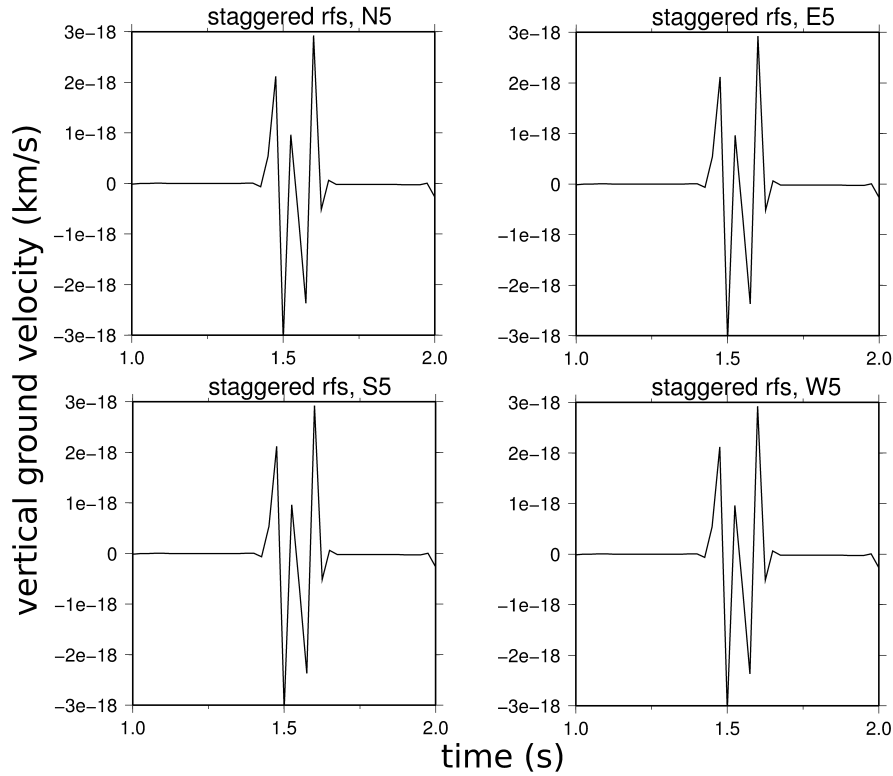


Figure 4.11: P-waveforms of 4 staggered RF sources with slip moving to shallower depths with time. Receivers were located at 5 km epicentral distance to the north, east, south and west (N5, E5, S5, W5).

4.2.3 Helix

To investigate the wave field of the scenario described by Thomas and Neuberg (2012), slip along a helix-shaped slip surface is implemented in the model. The eight slip surfaces involved are arranged in an octagon in plane view. Individual segments, however, are vertically separated by $\Delta z = 50$ m. A schematic of this time-delayed source structure can be seen in Fig. 4.12. Seismogenic slip of double couple 1 (Fig. 4.12) occurs at time $t = 0$ s, triggering double couple 2 $\Delta t = 0.001$ s later, until slip of DC 8 occurs $\Delta t = 0.008$ s after the first rupture. The input moment of each double couple was $M_0 = 1.0$ Nm, to obtain a total scalar moment of $M_0 = 8.0$ Nm for the combination of all eight slip surfaces. Two propagation direction configurations are considered here: (1) slip moves towards shallower depths with time, and (2) slip moves deeper with time. For both scenarios, the sources were embedded in a homogeneous halfspace as outlined in Chapter 2.1.2, and the receiver network as illustrated in Fig. 2.5 was implemented in the models.

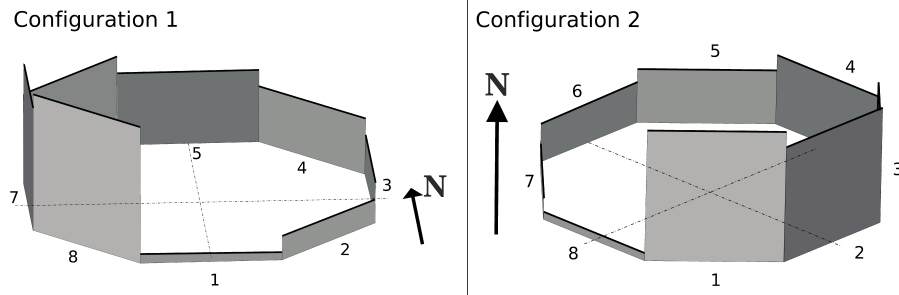


Figure 4.12: Configuration of two helix like slip histories. *left:* Configuration (1), where initial slip occurs at 1500m source depth, and triggers consecutive seismogenic slip at 50 m depth increments towards shallower depths. The last slip surface (slip surface 8) lies at 1150 m source depth. *right:* Configuration (2), where initial slip occurs at 1150 m source depth, and consecutive event source depths increase to a maximum source depth of segment 8 at 1500 m.

Configuration (1) involves the primary rupture occurring at 1500 m source depth, initiating a first P-wave radiating from this source location. In time increments of $\Delta t = 0.001$ s the remaining 7 double couples then gradually follow to slip. While segment 1 is at 1500 m depth, segments 2 and 3 lie at 1450 m and 1400 m respectively, up to segment 8 which is located at 1150 m depth, describing a total vertical extent of 350 m of the overall source (Fig. 4.12).

The waveforms shown in Fig. 4.13 display the observed P-waves from the superposition of 8 double couple sources staggered in time and space, and arranged in helix configuration (1). While N5 and S5 show complicated P-waves, the seismicity observed at E5 and W5 resembles Ricker wavelets, similar to the seismicity observed from a ring fault (Chapter 2.3.1). With individual segments triggered at time increments after the first event, the observed P-waves are, with a duration of 0.250 s, slightly longer than in previous cases where all sources were stimulated at the same time (ring fault event duration: 0.175 s). Time delays of $\Delta t = 0.001$ s between individual segments cause a superposition of waveforms to reach maximum vertical ground velocities of 1.642×10^{-18} km/s at E5 and -1.524×10^{-18} km/s at W5, respectively, which indicates partially destructive stacking of seismic energies, in contrast to corresponding ring fault values of 6.022×10^{-18} km/s.

Configuration (2) also spans over a vertical distance of 350m, with the first triggered double couple at 1150m depth, and source depths of consecutive events increasing in $\Delta z = 50$ m increments. Time steps between two back-to-back events are with

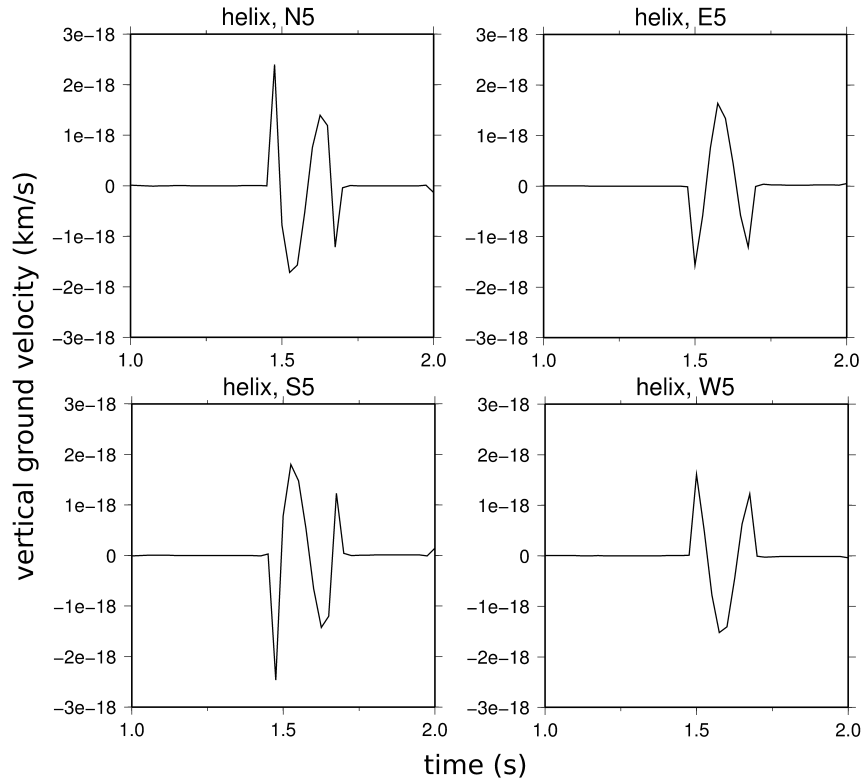


Figure 4.13: P-waveforms of a helix with slip moving to shallower depths with time. Receivers were located at 5 km epicentral distance to the north, east, south and west (N5, E5, S5, W5).

$\Delta t = 0.001$ s identical to helix configuration (1). The results from slip along the described helix-like configuration (2) can be seen in Fig. 4.14. Overall, waveforms hold similarities with the previous case, with observed P-waves at N5 and S5 highly complex, and 0.250 s long Ricker-like wavelets at stations E5 and W5. At E5 and W5, maximum P-wave amplitudes of 1.625×10^{-18} km/s and -1.549×10^{-18} km/s, respectively, in the vertical component seismograms only slightly deviate from those obtained from helix configuration (1). Furthermore, the modelled wave traces are consistently smaller than those from the ring fault structure.

The superposition of sources staggered in time and space yields complex, receiver location dependent P-waves. Generally, the two helix configurations investigated here produce smaller amplitude but longer in duration waveforms than slip along a corresponding ring fault at 1500m depth (as discussed in Chap. 2). For a $d = 50$ m wide conduit, time staggered wave trains produced by slip along two helix configurations arrive at receivers at 5 km epicentral distance out of phase, leading to partially destruc-

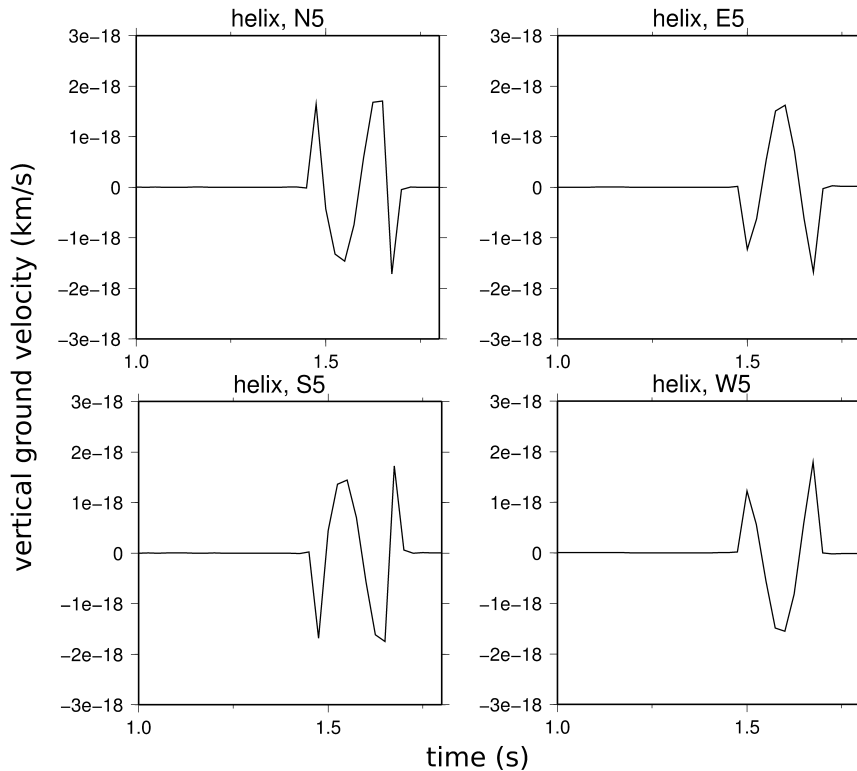


Figure 4.14: P-waveforms of a helix with slip moving to greater depths with time. Receivers were located at 5 km epicentral distance to the north, east, south and west (N5, E5, S5, W5).

tive superposition of individual seismic energies. This results in the smallest maximum P-wave amplitudes of all spatially extended sources under investigation in this study.

4.3 Discussion and Summary

Assuming a non-point source as the underlying excitation mechanism for LF volcano seismic earthquakes, this chapter has investigated a catalogue of extended source geometries. All cases considered here involve slip along a bent surface as the underlying physical motion responsible for generating seismic energy. To ensure comparability, the total seismic moment of each extended source was with $M_0 = 8 \text{ Nm}$ chosen to be equal to that of ring fault and dike in Chapter 2, unless otherwise stated.

In contrast to single and double ring faults, which do not show azimuthal dependence of P-waveforms and amplitudes, waveshapes and amplitudes of all other scenarios considered in this chapter change with receiver azimuths. For slip along half and quarter conduits, waveform amplitudes are greatest at receivers that lie on a symmetry axis of

the extended source (Fig. 4.3, Fig. 4.4, Fig. 4.7, and Fig. 4.8). Along symmetry axes of the source, waveforms of individual point sources are in phase with each other and superpose constructively, resulting in overall greater amplitudes than where waveforms are out of phase and partially cancel each other out. For quarter conduit configuration (2) this results in amplitude differences of 6.1772×10^{-18} km/s between traces, which corresponds to 8% of the maximum amplitude (Fig. 4.8). Equivalently, maximum amplitudes produced by a half ring are a factor of 2 (199%) greater than those where partial cancellation of seismic energy takes place (Fig. 4.3 and Fig. 4.4).

For the same seismic scalar moment, P-wave amplitudes vary largely with source geometry. For the same source depth and receiver network, recorded waveforms for a ring fault structure have maximum P-wave amplitudes of 6.022×10^{-18} km/s (Chapter 2.3.1), while maximum amplitudes for half and quarter conduits lie at 2.400×10^{-17} km/s and $\pm 6.972 \times 10^{-17}$ km/s, respectively. Due to constructive and destructive interference, the smallest overall P-wave amplitudes are generated when the most number of point sources act simultaneously. That is, the ring fault, with the smallest overall P-wave amplitudes, is built up by 32 individual point sources, while the two half conduit configurations, with 17 point sources each, and quarter conduits, with 9 simultaneously acting sources only, generate greater amplitude waveforms. This shows that source geometry, and not number of point sources, is the key feature influencing waveform amplitudes. The same input moment M_0 yields a whole range of P-wave amplitudes and waveforms, depending on the source geometry, and thus spatially extended sources cannot be approximated as point sources. Interpretation of observed amplitudes would yield seismic moments and magma ascent rates based on slip along a single slip surface which deviate from those that should be obtained from motion along bent slip surfaces such as half and quarter conduits.

Similarly to the P-wave amplitudes, the observed waveforms themselves also show a strong dependence on relative source receiver locations. The shape of recorded P-waves changes with source geometry as well as receiver azimuth. Slip along 50 m wide ring fault segments produces two end member waveforms: two-lobed Küpper-like wavelets and Ricker-like wavelets (Fig. 4.3, Fig. 4.4, Fig. 4.7, and Fig. 4.8). The shape of the recorded waveform depends, again, on whether individual waveforms arrive at a given seismic station in phase and at what time. Ultimately, this is affected by one

source parameter, the diameter of the ring fault. Since this influencing factor can only be defined for spatially extended sources, the point source approximation is likely not sufficient when linking observed seismic energy to subsurface physical processes.

The introduction of a time history to the spatially extended slip geometry adds to the complexity of observed wavefields. Time-staggered slip of segments at different source depths was modelled to simulate a migration of source locations with time. Observed P-waveforms of such helix-like model geometries were dependent on receiver azimuths, and displayed durations of 0.250 s longer, and more complex waveforms (Figs. 4.14 and 4.13) than those of single source-time functions.

Overall, the source geometry highly influences observed seismic waveforms and amplitudes, and cannot be neglected when investigating the source mechanisms of volcano seismic sources. Moment tensor inversions based on the point source assumption will be affected by the partial constructive and destructive interference of spatially extended source waveforms and their resulting changes in wave shape and size, and can therefore not be neglected. The consideration of spatially extended sources, as carried out in this study, will advance our understanding of the sub-surface processes leading to LF seismicity at volcanoes. As shown here, the effect of the spatially extended nature of the source is significant. A new link between observed seismic amplitudes and amount of slip at depth can be drawn, and once calibrated, magma ascent rate estimates can be improved on the basis of spatially extended source structures acting at depth.

Chapter 5

Classic moment tensor inversions of complex volcano seismic sources

While earthquake locations and waveform analyses only provide limited insight into the processes that drive seismogenic fracturing within the Earth, our understanding of the involved physical mechanisms can be enhanced by considering the seismic moment tensor representation of these events. This basic tool for quantifying earthquake sources provides a direct snapshot of the sub-surface processes occurring at depth. A detailed introduction of the moment tensor to describe volcanic earthquakes has been given in Chapter 1.6.1.

Moment tensor inversion (MTI) techniques are the most commonly used tool in obtaining information on the mechanisms at the source of LF seismicity generated at volcanoes (Chouet and Matoza, 2011). This technique enables the retrieval of the moment tensor of an earthquake from its seismic amplitudes (e.g. Godano et al., 2011), amplitude ratios (e.g. Miller et al., 1998a), or full waveforms (e.g. Bean et al., 2008). Full waveform inversions in particular have found increased application in volcanology, particularly when investigating the source mechanisms of low frequency volcanic events (Bean et al., 2008; Kriger, 2011; Nakano et al., 2007; Ohminato et al., 1998).

All MTI techniques share a point source approximation of the source. This will likely cause complications in settings such as volcanoes, and especially when investigating the trigger processes of LF seismic events which are thought to be more complex than a

single point source. This chapter aims to investigate the degree of error that is introduced into the retrieval of the source processes of LF volcanic seismicity by carrying out common moment tensor inversions (assuming a point source) of, in reality, spatially extended sources such as the ring fault structure. Analysis of the retrieved moment tensor decompositions and comparison with interpretations of moment tensor inversion results from the literature yield a quantitative assessment as to whether classical moment tensor inversion techniques are sufficient to resolve the source mechanisms underlying LF volcanic events.

5.1 Methodology

A recorded seismogram $d(t)$ is the result of three main contributing factors: the source (S), the path effects (Green's functions G), and a transfer function of the recording instrumentation (R) (Chung and Kanamori, 1980) (Fig. 5.1). It can be viewed as a

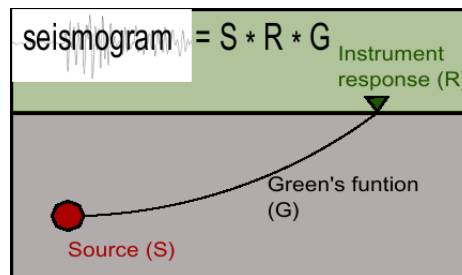


Figure 5.1: Schematic summarising the dependencies of a seismogram: every observed waveform is a convolution of the source time function, path effects, and the recording instrument. The recorded ground motion at a given station does not represent the true ground motion caused by the source. Filter effects of the Earth, as well as seismometer response, alter the original signal.

convolution ($*$) of these aforementioned three factors (see also Chapter 2.5):

$$d(t) = S * G * R \quad (5.1)$$

If instrument response and propagation effects on the wavefield are available, one can obtain the moment tensor (M) of the source S by solving the inverse problem of Equation 5.1. In the frequency domain, where temporal convolution is represented by multiplication of the respective Fourier transforms, this gives:

$$\mathbf{d} = \mathbf{G}\mathbf{M} \quad (5.2)$$

where \mathbf{d} are the displacements recorded at n stations, \mathbf{G} is a $6 \times n$ matrix containing the spatial derivatives of a set of Green's functions, and \mathbf{M} contains the sought moment tensor components of the source \mathcal{S} (Aki and Richards, 1980; Ohminato et al., 1998).

To simplify the inversion procedure, limitations are often accepted to decrease the number of unknowns. That is, for instance, a homogeneous time history of the source (Dahm and Krüger, 2014). Each inversion begins with a pre-defined starting model of synthetic seismograms that is compared to the observed data and the misfit between the two is determined using:

$$R = \sum_{\omega} \frac{(\mathbf{d} - \mathbf{G}\mathbf{m})^T (\mathbf{d} - \mathbf{G}\mathbf{m})}{\mathbf{d}^T \mathbf{d}}. \quad (5.3)$$

After each inversion run the starting model is altered to ultimately reach a minimal misfit between data and synthetics, which yields the moment tensor for the best fit solution of the source process.

All moment tensor inversion routines in seismology hence require access to Green's functions, seismological data, and an inversion framework to retrieve the moment tensor components. This study makes use of the 'Kiwi (Kinematic Waveform Inversion) tools' open source full waveform moment tensor inversion software that can be downloaded at: 10.5880/GFZ.2.1.2013.001 (Heimann, 2011; Cesca et al., 2010). The algorithm has the ability to retrieve point source parameters as well as parametrised kinematic rupture models (Cesca et al., 2010; Cesca and Heimann, 2013). This study aims to investigate the ability of resolving spatially extended sources with established and in volcano observatories implemented inversion techniques and will therefore only make use of the inversion steps to resolve point sources.

In the following sections the inversion algorithm is explained in more detail, the requirements for moment tensor inversions are defined and specified for the scope of this study, before classical moment tensor inversions are carried out for a catalogue of sources.

5.1.1 Application to volcanoes

Moment tensor inversions were first developed for the study of teleseismic events (Dziewonski and Woodhouse, 1981; Sipkin, 1982) where large distances allow the assumption of a point source acting at depth to generate the seismic energy recorded. Soon after, however, the technique was adapted and modified for regional settings which has enabled the study of smaller amplitude earthquakes at regional distances (Nakanishi et al., 1992). These new, regional inversion techniques opened the path to an application at volcanoes, with the aim of gaining insight into the sub-surface processes at the source of volcanic earthquakes, and ultimately volcanic eruptions.

Unlike in tectonic settings, MTI at volcanoes are complicated through several factors: (1) Volcanic edifices are extremely heterogeneous, containing fissures, solidified and fresh magma, pyroclastic flow materials etc. Due to unfavourable earthquake-station distribution seismic tomography is usually not able to resolve the shallow sub-surface, and as a result the velocity models of these shallow regions of interest are poorly resolved. This affects Green's functions calculations and adds to the overall misfit between data and synthetics. (2) Second, the effects that topographic changes have on the waveforms can be significant (Neuberg and Pointer, 2000; Cesca et al., 2008; O'Brien and Bean, 2009), with altitude changes of a few kilometres not unusual in volcanic regions. (3) The last, and possibly the most crucial, complication is the point source approximation at the base of all moment tensor inversion techniques. A source can be considered a point source when the wavelengths of observed seismicity are much longer than the spatial extent of the underlying source (Chouet and Matoza, 2011). While this assumption generally holds true for earthquakes recorded in global settings, it is questionable if this is also the case at volcanoes. Shallow source depths (up to 2 km), receivers in close proximity (see also Chap. 6), and conceptual models for the trigger mechanisms of LP events (see Chapter 2.2) suggesting a spatially extended source structure (e.g. the conduit), are arguments against a point source approximation.

Classical moment tensor inversion techniques *map* spatially extended sources into point source solutions, likely yielding erroneous inversion results. To ensure reliable forecasting it is therefore crucial to investigate the degree of error that is introduced into interpretations of the trigger mechanism of LF seismicity at volcanoes through these

inversion limitations. If classical MTI techniques prove to be insufficient, considerations of higher order moment tensor inversion techniques may be required to resolve spatially extended sources.

In the following, MTI are applied to a set of synthetic sources where the source geometry is known. MTI results and possible interpretations are compared to the initial input to investigate the deviations of the proposed point source solutions from the real sources.

5.1.2 Green's functions

Green's functions (GFs) describe the expected wave propagation from source to receiver, given a specific source process as well as the velocity structure of the medium the seismic energy has to travel through (Cesca and Heimann, 2013). They are used to obtain synthetic seismograms that can then be compared to real data as part of the moment tensor inversion procedure. For this study, velocity changes are only considered in 1D. All relevant properties, such as body wave velocities, density, and attenuation factors, solely change with depth. The symmetry of the hereby introduced model reduces the computation of the number of required Green's functions to cover all azimuths for a given pair of source depth and source-receiver distance (Cesca et al., 2010). Once computed, the Green's functions are stored in a Green's functions database.

There are a number of parameters that have to be chosen when attempting to compute a Green's functions database. Dependent on the area under investigation, a suitable velocity model, a range of epicentral distances and source depths, as well as GF grid density must be carefully selected. Green's functions can then only be calculated within an area limited by the maximum distance and depth ranges. The sampling interval limits the range of maximum reproducible frequencies, and since data and Green's functions need to be sampled with a common sampling frequency, the choice of GF sampling restricts the resolution potential further (Cesca and Heimann, 2013).

The choice of input parameters to compute the Green's functions for the scope of this study was straightforward because the data under investigation were synthetically computed. 1D velocity structure, source depth, epicentral distances, and sampling frequency are therefore well known, and the Green's functions database was computed

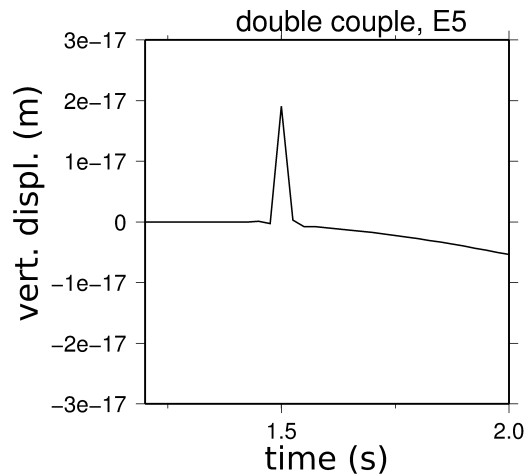


Figure 5.2: Displacement seismogram for a northwards striking DC source. Here, only the vertical component is shown for station E5 which is located 5km east of the earthquake epicentre, while all three components, north, east, and vertical, are used during the moment tensor inversion procedure.

for the following range of parameters: $v_p = 3.5$ km/s, $v_s = 2.0$ km/s, $\rho = 2200$ kg/m³, $q_p = 1378$, $q_s = 600$, sampling rate (initial): 1000 Hz, sampling rate (inversion): 40 Hz, receiver depth: 0 m, source depths: 1 – 2 km, and epicentral distances: 1 – 10 km.

5.1.3 Data

For the inversions carried out in this chapter three-component synthetically computed displacement seismograms were used as data source. Data calculations were performed using the same input parameters as for the Green's functions computation, data calculations were performed using the following input parameters (see Chapter 5.1.2) and an epicentral distance of 1km.

Data input is required as displacement seismograms, and an example can be seen in Fig. 5.2. The vertical component seismogram shown was computed for a northwards striking single double couple source at 1.5 km depth and recorded at station E5, 5 km to the east of the earthquake epicentre. The input moment was 8 Nm, and the source time function was a delta impulse.

Additionally to the displacement seismograms, the receiver network has to be defined. Because this is purely a synthetic study, receiver number and locations could be chosen freely. For realistic estimates of the source mechanism at least 7 stations are required

in close proximity of the source (Kumagai et al., 2002; Waite et al., 2008). To ensure both, good azimuthal and distance coverage, 12 stations were distributed around the source: 4 stations each at 1 km, 3 km, and 5 km epicentral distances and the four cardinal directions (see Fig. 2.5).

5.1.4 Moment tensor inversion tool

Given the Green's functions and data files as described above, moment tensor inversions were carried out using the open source python code 'rapidinv' (Cesca et al., 2010; Cesca and Heimann, 2013). The code is integrated into KIWI tools (Heimann, 2011), and obtains DC and full MT inversion results by performing 2 separate steps. Although 'rapidinv' also features an option to invert for kinematic parameters of spatially extended sources in a 3^{rd} inversion step, inversions within this study were carried out exclusively under the point source assumption (steps 1 and 2). The full point source moment tensor is retrieved by a two step approach (Fig. 5.3) (Cesca et al., 2010; Cesca and Heimann, 2013). Firstly, an amplitude spectra inversion is carried out to obtain the full moment tensor and moment tensor decomposition. Due to the execution of this inversion step in the frequency domain, dilatational and compressional first motions can not be distinguished, yielding two suggested solution configurations. This polarity ambiguity is resolved in the second step, which is carried out in the time domain and considers phase polarity information, to result in the best fit full point source moment tensor solution and decomposition.

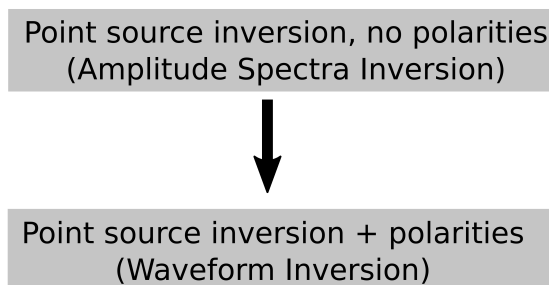


Figure 5.3: Schematic of the two step moment tensor inversion strategy. Step one is carried out in the frequency domain and retrieves a best fit full moment tensor solution and decomposition, but cannot resolve the polarity ambiguity, which is achieved during the second inversion step.

5.2 Results

The ring fault structure was introduced as a possible physical trigger of LF volcanic seismicity earlier in this study. In this chapter, moment tensor inversions of the ring fault and other spatially extended sources are performed. The inversions are carried out under the (wrong) assumption of an underlying point source rather than an extended source as the trigger, introducing an error of so far unknown scale. Here, the inversion results will be discussed, and how to interpret the moment tensor components (double couple, isotropic, or CLVD), which are based on a point source, in terms of an extended source.

5.2.1 Single double couple

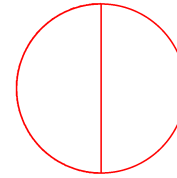
First, MTI was carried out for a point source to test the ‘rapidinv’ software and to ensure a smooth and accurate work flow. Therefore, synthetic seismograms were generated for a northwards striking, vertically dipping normal fault with an input moment of 8 Nm. The resulting displacement seismograms were then used as data input for the inversion. Green’s functions were generated as described in Chapter 5.1.2, and the usual station distribution as introduced earlier (see Fig. 2.5) was used. Being a synthetic study, where all input parameters are known, the moment tensor inversion results can be directly compared with the initial input to probe the performance of the inversion.

The first step in the inversion routine is undertaken in the frequency domain, and is subdivided into two sub-steps: step 1a accounts for double couple sources only, while step 1b considers all moment tensor elements. Only if a considerable improvement is gained by advancing from a DC solution to a full moment tensor description does step 1b become meaningful. Here, the source characteristics are sufficiently resolved by step 1a, whose output can be seen in Fig. 5.4. The top half of the output shows the suggested source parameters and misfit between data and synthetics after this inversion step, while the lower half displays the actual fits for the amplitude spectra of data and model for all stations and components.

Relative misfits at a fixed source depth of 1.5 km reach a minimum for a fault geometry with strike= 0°, dip= 90°, and rake= 90°. The source geometry is thus perfectly regained from the inversion. Furthermore, an estimated seismic moment of $M_0 = 8.33$

DC - point source solution (step 1a)

Lat Lon	16.71 N -62.17 E			
Strike	0.0	0.0	228.0	228.0
Dip	90.0	90.0	0.0	0.0
Rake	90.0	-90.0	138.0	-42.0
M_0	8.3265667Nm			
M_w	-5.4			
Depth	1.5km			
Duration	0.02s			
Misfit	0.075			
Method	Amplitude spectra			
Components	une			
Phases	P			
Bandpass	1 - 10 Hz			
Traces	36 (12 stations)			



Fit of Amplitude Spectra

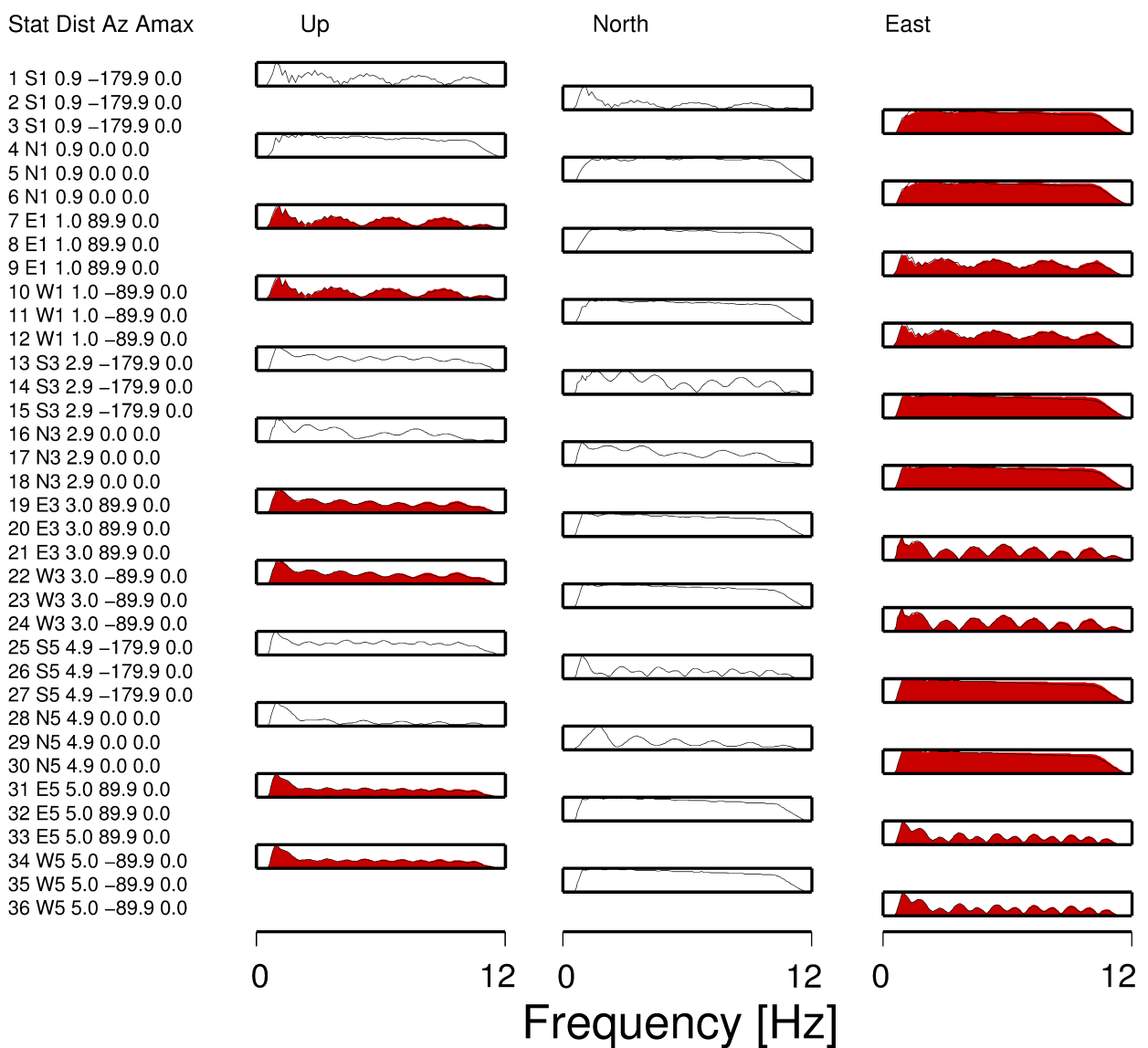
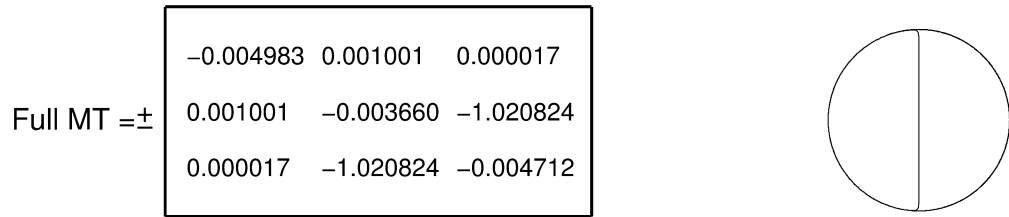


Figure 5.4: Double couple - Inversion solution after step 1a. The top panel shows the best fit (misfit= 7.5%) source geometry. The best solution resolves point source parameters as well as input moment and depth of the original source. Polarities cannot be resolved since this inversion step is carried out in the frequency domain. At the bottom of the output the fit of data and model amplitude spectra can be seen: black lines represent data and red shaded spectra represent synthetics.

DC - moment tensor solution (step 1b)



Misfit MT 0.072
 Method Amplitude spectra
 Components une
 Phases P
 Bandpass 1 – 10 Hz
 Traces 36 (12 stations)

Decomposition:

Deviatoric part:		Deviatoric part:	
DC = 99.0	%	ISO = 0.0	%
CLVD = 1.0	%		

Fit of Amplitude Spectra

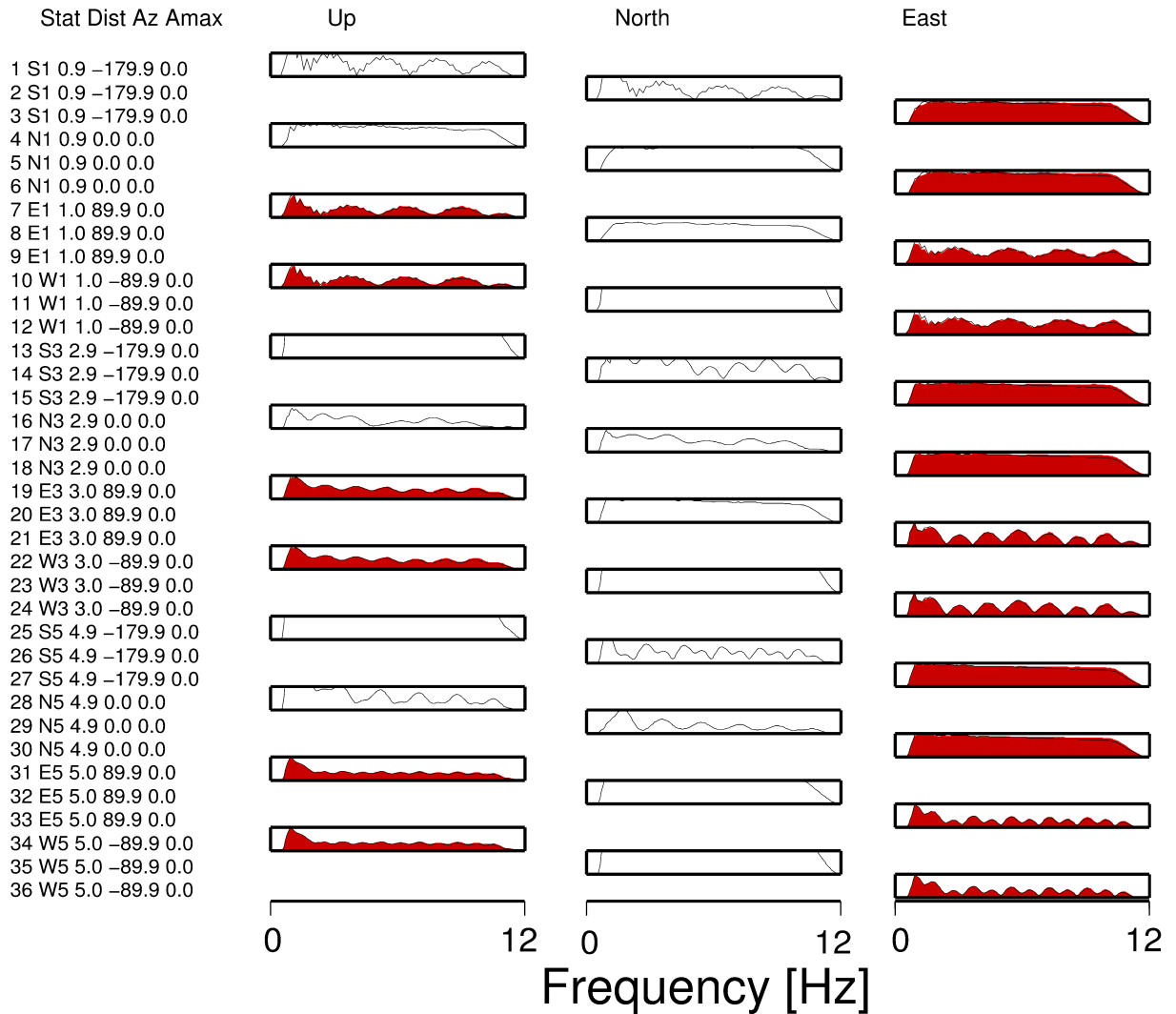


Figure 5.5: Double couple - Inversion solution after step 1b. The ability to identify non-DC components in the data does not improve the inversion, and the result stays with 99% DC component the same. The full moment tensor of the best fit solution is shown here.

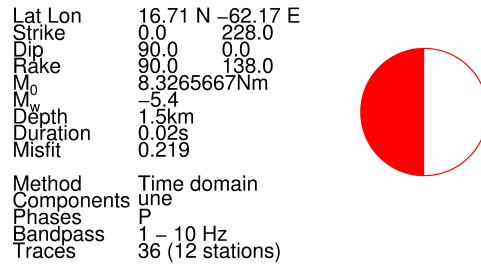


Figure 5.6: Double couple - Inversion solution after step 2. Step 2 is performed in the time domain. The ‘beach ball’ for the best solution is displayed, and clearly shows a vertical dipping normal fault as source mechanisms. The suggested seismic moment of $M_0 = 8.33$ Nm exceeds the original input of $M_0 = 8$ Nm only slightly.

Nm approaches the actual $M_0 = 8$ Nm, where the deviation from a perfect recovery of the seismic moment may be due to trace misalignments and poor distance coverage of the data.

The consideration of volumetric sources in step 1b does not improve the inversion result, with the DC component occupying 99% of the solution (Fig. 5.5). An overall misfit of 7.5% for step 1 provides information on the very good quality of the inversion result.

Step 2 is carried out in the time domain, to resolve the polarity of the motion (Chapter 5.1.4). The inversion output in Figs. 5.6 and 5.7 shows the waveform fit between data and synthetics (bottom), as well as the final ‘beach ball’ solution for the perfectly recovered double couple source mechanism.

The quality of inversion results for this test case proves the validity of code and method, hence in the following ‘rapidinv’ will be used to undertake moment tensor inversions (under the point source assumption) for CLVD and spatially extended sources, following the same inversion routine as outlined in the test case.

5.2.2 CLVD

Since CLVD sources are often discussed as potential explanations for low frequency seismicity on volcanoes (Chouet, 1996b; Waite et al., 2008), moment tensor inversion was carried out for a CLVD source, for comparison to the results obtained for spatially extended sources. Being expressed by moment tensors (Chapter 1.6.5), CLVDs can be fully recovered by inversion techniques. It is therefore no surprise that MTI of

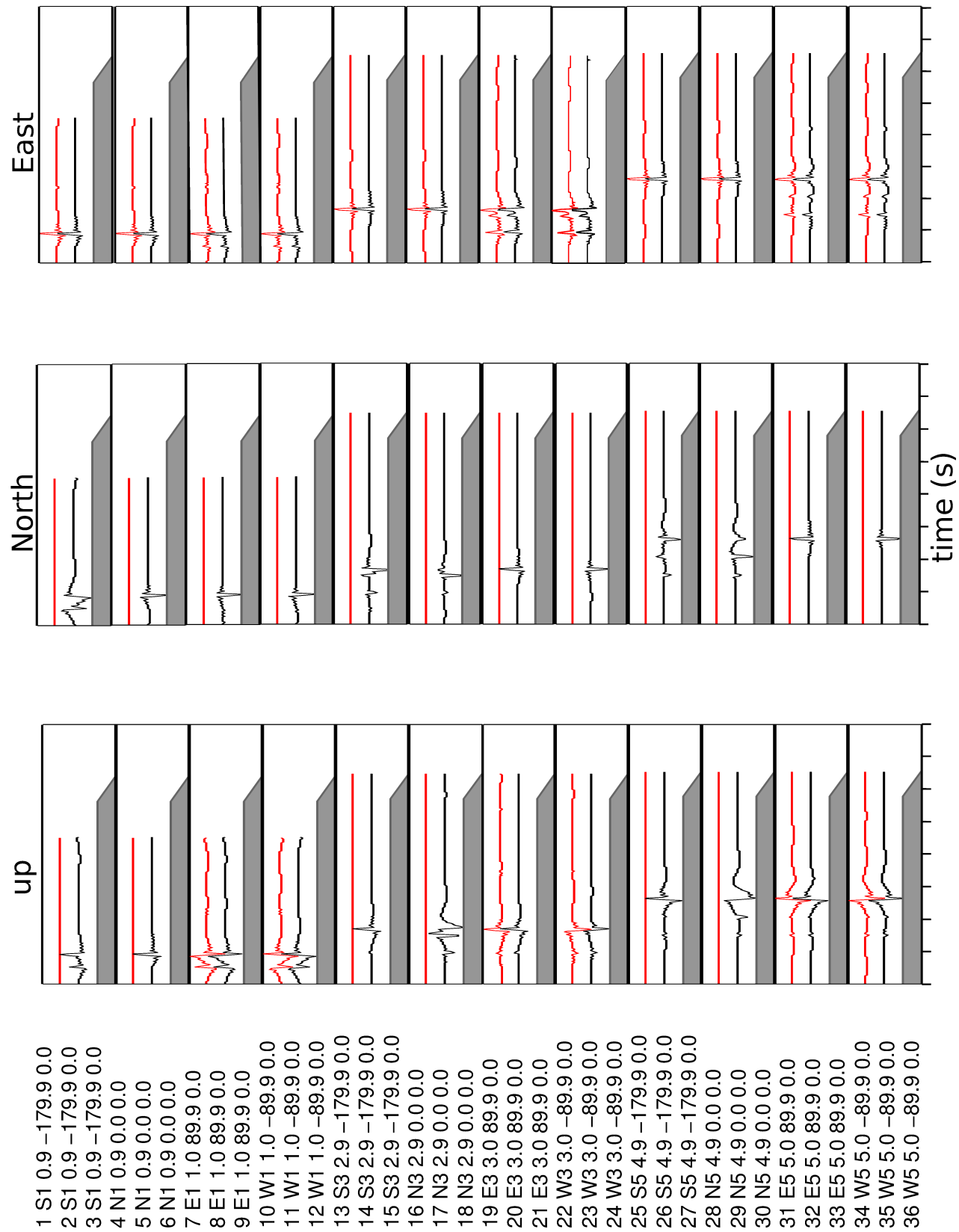


Figure 5.7: Double couple - Inversion solution after step 2. Step 2 is performed in the time domain and the fit of P-wave windowed displacements for the used traces is plotted: red traces represent real displacements, black traces represent synthetics, and the gray shaded are represents the applied taper.

the synthetic CLVD case as discussed in Chapter 2.3.1 yields a perfect recovery of 100% CLVD source mechanism and therefore displays the characteristic *eyeball/fried egg* appearance of CLVDs (Fig. 5.8).

An inversion misfit of 8.3% (in the same order as the misfit in the DC case) in the frequency domain indicates a high quality inversion result and an accurate recovery of the original source mechanism.

5.2.3 Ring fault

Moment tensor inversions are performed under the assumption of an underlying point source. This needs to be taken into account when inverting spatially extended sources, such as the ring fault structure. MTI cannot resolve the actual source parameters for such sources, as the inversion tool *maps* the actual scenario into a moment tensor source. However, since moment tensor inversions are a common technique applied to gain information on the source mechanisms of LF volcanic seismicity, it is important to investigate the consequences of a (wrongly) assumed point source. The inversion results of a ring fault are therefore discussed regarding possible misinterpretations that may arise from MTI.

Displacement seismograms for a 50 m wide , 1.5 km deep ring fault were calculated for the entire receiver network (Fig. 2.5), and used as data for the inversion. MTI results can be seen in Fig. 5.9, Fig. 5.10, and Fig. 5.11. The advancement from pure double couple to moment tensor source (5.9 and Fig. 5.10) yields a slightly better fit (63.5% compared to 64.1%), and suggests a complete non-DC source mechanism.

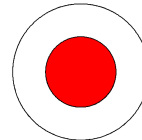
Step 2, performed in the time domain, where misalignments of waveforms cause an increase in misfit values, serves to resolve the motion polarity. The full moment tensor description as well as the corresponding ‘beach ball’ and decomposition can be seen in Fig. 5.11. The displayed full moment tensor ‘beach ball’ resembles an eye ball, and is the typical picture for a CLVD source mechanism (see also Chapter 1.6.5). The deviatoric moment tensor - generally composed of DC and CLVD components - in this case solely consists of CLVD. With a strong isotropic component of 63%, the deviatoric moment tensor only represents 37% of the full moment tensor. The overall poor fit of amplitude spectra (63.5%) is not surprising as the extended source nature cannot be

CLVD - moment tensor solution (step 2b)

Lat Lon 16.71 N -62.17 E

Full MT =

-0.349658	0.000001	0.000599
0.000001	-0.349638	-0.000082
0.000599	-0.000082	0.689947

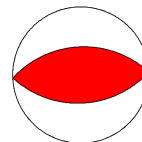


Misfit MT(2b) 0.218
 Method Time domain
 Components 3
 Phases P
 Bandpass 1 - 10 Hz
 Traces 36 (12 stations)

Decomposition:

DC =

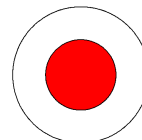
-0.000020	0.000001	0.000000
0.000001	-0.000000	-0.000000
0.000000	-0.000000	0.000020



0.0 %

CLVD =

-0.346521	-0.000000	0.000599
-0.000000	-0.346522	-0.000082
0.000599	-0.000082	0.693043



100.0 %

ISO =

-0.003116	0.000000	0.000000
0.000000	-0.003116	0.000000
0.000000	0.000000	-0.003116

0.0 %

Figure 5.8: CLVD - Inversion solution after step 2. Step 2 is performed in the time domain. The ‘beach ball’ for the best solution is displayed, and represents the familiar *fried egg* characteristic for CLVD sources. Full moment tensor and moment tensor decomposition are displayed. With 100% CLVD source mechanism, the original excitation mechanism can be fully recovered using MTI.

resolved by a common moment tensor description. The apparent seismic moment is with $M_0 = 1.10$ Nm highly underestimating the real input moment of $M_0 = 8$ Nm.

5.2.4 Dike

Moment tensor inversion of spatially extended sources is not restricted to the ring fault structure, but is also undertaken for seismogenic slip within a dike-like structure as source scenario. The forward problem and resulting waveforms are discussed in Chapter 2.3.1, while the point source inversion of this spatially extended source is presented here (Fig. 5.12).

With a fixed source depth of 1.5 km, the point source MTI solution of two oppositely directed, simultaneously acting double couple sources describing an EW striking vertical dike comprises a full MT ‘beach ball’ which suggests a CLVD motion at the source of the observed seismicity. MTI decomposition yields a mix of isotropic (32%) and deviatoric (68%) components, whereas the CLVD (60%) is the dominating deviatoric component of the overall solution.

With a suggested scalar moment of 0.5 Nm for a point source, the actual scalar input moment ($M_0 = 8$ Nm) of the dike structure is highly underestimated by the inversion. An inversion misfit of 58% of the best fit model suggests that, similar to the inversion result of the ring fault in Chapter 5.2.3, the MTI technique is not able to gain a good quality solution of this spatially extended source mechanism.

5.2.5 Ring fault segments

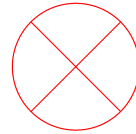
For cases where slip occurs on only parts of the ring shaped fault surface, moment tensor inversions were carried out to obtain solutions for two orientations of half conduits, as well as two further scenarios where only quarter of the conduit slips. The waveforms and amplitudes for slip along segments of the ring fault were discussed in Chap. 4, and here the inverse approach is used to constrain errors introduced when inverting such sources under the point source assumption.

Half conduit (1)

Half ring configuration (1) involves slip along a bent surface spanning over azimuths $\alpha = 0^\circ - 180^\circ$ (Fig. 4.2). Common MTI will not resolve the spatial extent of this source,

RF - point source solution (step 1a)

Lat Lon	16.71 N -62.17 E
Strike	135.0 135.0 225.0 225.0
Dip	90.0 90.0 90.0 90.0
Rake	180.0 -0.0 0.0 -180.0
M_0	1.1042597Nm
M_w	-6.0
Depth	1.5km
Duration	0.02s
Misfit	0.641
Method	Amplitude spectra
Components	une
Phases	P
Bandpass	1 - 10 Hz
Traces	36 (12 stations)



Fit of Amplitude Spectra

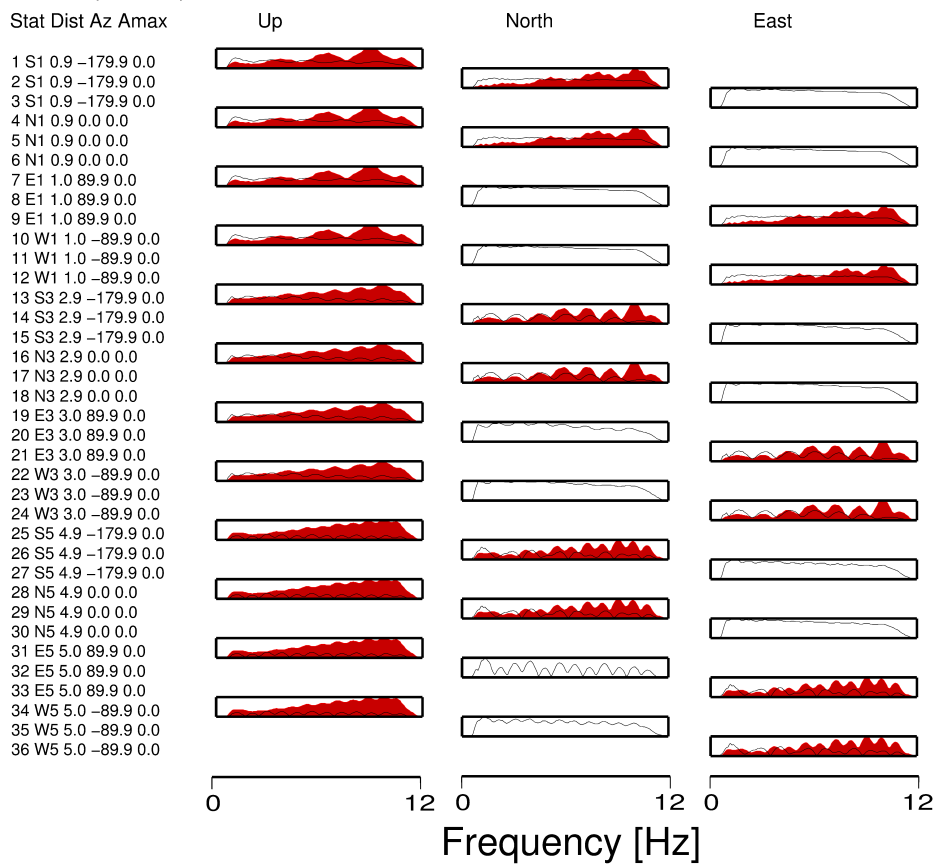
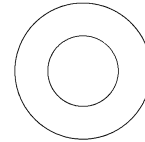


Figure 5.9: Ring fault - Inversion solution after step 1a. At the bottom of the output the fit of data and model amplitude spectra can be seen: black lines represent data and red shaded spectra represent synthetics. The top panel shows the best fit apparent source geometry without polarity. The best solution cannot resolve the extended source and highly underestimates its real input moment.

RF - moment tensor solution (step 1b)

Lat Lon 16.71 N -62.17 E

Full MT = ±	1.401610	-0.000011	-0.000796
	-0.000011	1.401572	-0.000556
	-0.000796	-0.000556	0.469292



Misfit MT 0.635
 Method Amplitude spectra
 Components P
 Phases 1
 Bandpass 1 - 10 Hz
 Traces 36 (12 stations)

Decomposition:

Deviatoric part:	Deviatoric part:
DC = 0.0 %	ISO = 63.0 %
CLVD = 100.0 %	

Fit of Amplitude Spectra

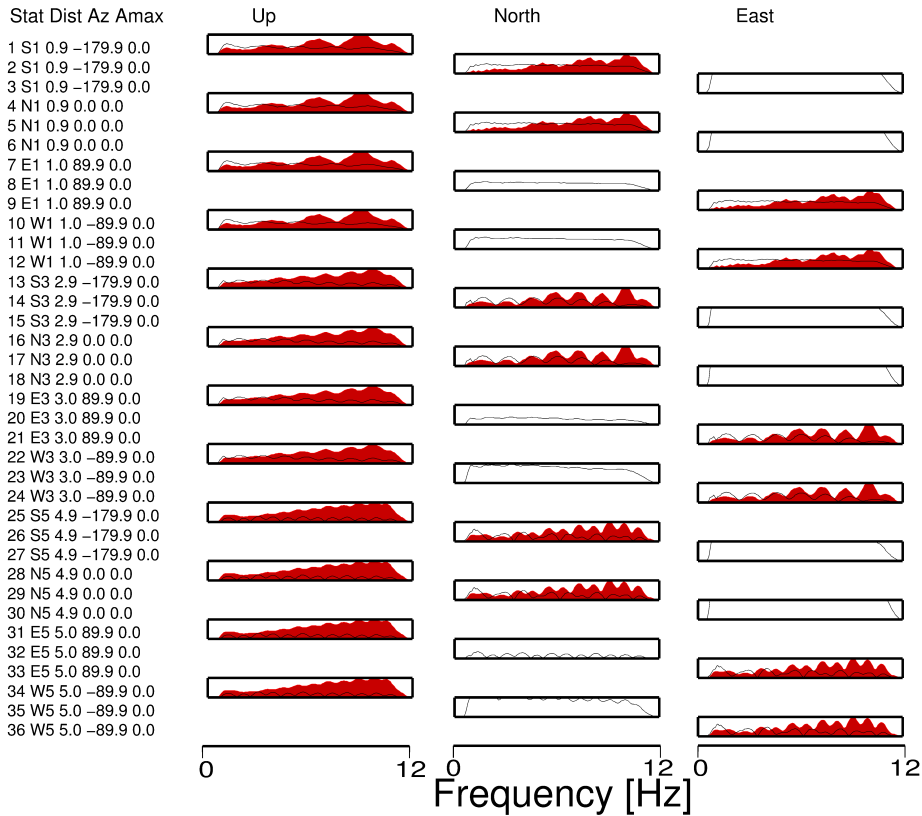


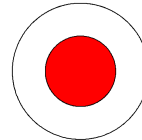
Figure 5.10: Ring fault - Inversion solution after step 1b. The ability to identify non-DC components in the data changes the inversion solution and suggest an apparent moment tensor decomposition as follows: 37% CLVD and 63% isotropic components. The full moment tensor of the best fit solution is shown here, while a misfit function of 63.5% is not surprising as the inversion procedure cannot resolve spatially extended sources.

RF - moment tensor solution (step 2b)

Lat Lon 16.71 N -62.17 E

Full MT =

-1.401610	0.000011	0.000796
0.000011	-1.401572	0.000556
0.000796	0.000556	-0.469292

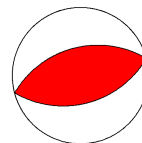


Misfit MT(2b) 1.009
 Method Time domain
 Components 1
 Phases P
 Bandpass 1 - 10 Hz
 Traces 36 (12 stations)

Decomposition:

DC =

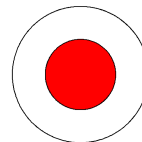
-0.000042	0.000011	0.000000
0.000011	-0.000003	0.000000
0.000000	0.000000	0.000044



0.0 %

CLVD =

-0.310744	0.000000	0.000796
0.000000	-0.310744	0.000556
0.000796	0.000556	0.621488



100.0 %

ISO =

-1.090825	0.000000	0.000000
0.000000	-1.090825	0.000000
0.000000	0.000000	-1.090825

63.0 %

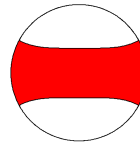
Figure 5.11: Ring fault - Inversion solution after step 2. Step 2 is performed in the time domain to obtain the polarities of the best fit model. The ‘beach balls’ for the best solution and decomposition are displayed. Moment tensor decomposition suggests 100% CLVD component of the deviatoric moment tensor as the excitation process.

Dike - Moment tensor solution (step 2b)

Lat Lon 16.71 N -62.17 E

Full MT =

-1.957734	0.000044	-0.006296
0.000044	-0.255460	-0.000967
-0.006296	-0.000967	0.278565

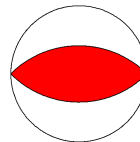


Misfit MT(2b) 1.157
 Method Time domain
 Components 3
 Phases P
 Bandpass 1 - 10 Hz
 Traces 36 (12 stations)

Decomposition:

DC =

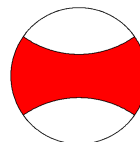
-0.534038	0.000016	-0.003007
0.000016	0.000002	-0.000967
-0.003007	-0.000967	0.534036



40.0 %

CLVD =

-0.778820	0.000028	-0.003289
0.000028	0.389414	0.000000
-0.003289	0.000000	0.389405



60.0 %

ISO =

-0.644877	0.000000	0.000000
0.000000	-0.644877	0.000000
0.000000	0.000000	-0.644877

32.0 %

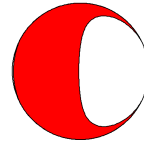
Figure 5.12: Dike - Inversion result with full moment tensor. The moment tensor decomposition of the apparent source comprises 40% DC and 60% CLVD of the deviatoric moment tensor, and 32% isotropic components.

HC - moment tensor solution (step 2b)

Lat Lon 16.71 N -62.17 E

Full MT =

0.203544	0.000711	0.000430
0.000711	0.036800	-1.064897
0.000430	-1.064897	-0.024244

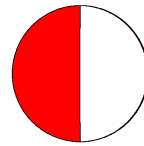


Misfit MT(2b) 0.518
 Method Time domain
 Components 1
 Phases P
 Bandpass 1 - 10 Hz
 Traces 36 (12 stations)

Decomposition:

DC =

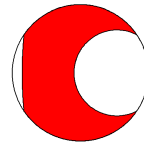
-0.000000	0.000536	0.000250
0.000536	0.024870	-0.867712
0.000250	-0.867712	-0.024870



76.0 %

CLVD =

0.131511	0.000175	0.000180
0.000175	-0.060104	-0.197185
0.000180	-0.197185	-0.071407



24.0 %

ISO =

0.072033	0.000000	0.000000
0.000000	0.072033	0.000000
0.000000	0.000000	0.072033

5.0 %

Figure 5.13: Half conduit (1) - Inversion result with full moment tensor. The moment tensor decomposition of the apparent source comprises a deviatoric moment tensor of 76% DC and 24% CLVD, plus 5% isotropic components.

and MTI results are analysed with the real source nature in mind, and in respect to possible misinterpretations.

The full moment tensor solution including ‘beach ball’ for the half ring scenario (1) can be seen in Fig. 5.13. The inversion misfit after the frequency spectrum inversion lies at 10.6%, which (misleadingly) suggests a good quality resolution of the underlying source mechanism. Moment tensor decomposition assigns a negligible 5% of the full MT an isotropic component, while the remaining 95% is represented by the deviatoric part, which is in turn split into 76% DC, and 24% CLVD. The suggested seismic moment,

by assuming a point source is, with 4.87 Nm, underestimating the real input moment of 8 Nm. Because the inversion technique is not able to resolve spatially extended sources, the source geometry of the input source is not resolved, and a wrong point source orientation (best fitting the data) is suggested instead.

Half conduit (2)

Inversions were also carried out for a second half conduit configuration, where the half ring shaped slip surface is rotated in comparison to half conduit (1), and spans over the azimuth range $\alpha = 90^\circ - 270^\circ$ (Fig. 4.2). Due to common symmetry characteristics of the two half conduit configurations, the radiated seismic energy recorded at the station is identical in both cases, only 90° rotated. This similarity is also reflected in the moment tensor inversion results (Fig. 5.14). Moment tensor decomposition therefore yields similar results, with 76% DC and 24% CLVD components forming the deviatoric MT, and 12% of the full MT allocated to the isotropic component. The quality of inversion, with a misfit of 10.6%, is equal to the previous case. The input moment of the model that best fits the data lies at 5.55 Nm. This is clearly below that of the actual seismic moment of $M_0 = 8$ Nm, and in the same manner as for half conduit (1), the suggested source geometry cannot match the real source, as its spatial extent cannot be captured.

Quarter Conduit (1)

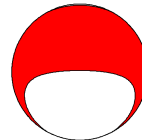
Moment tensor inversion results obtained when inverting the waveforms from slip along a quarter conduit are presented in Fig. 5.15. In this case, slip occurred along a bent slip surface spanning over a quarter ring with azimuths $\alpha = 0^\circ - 90^\circ$ (Fig. 4.5).

Full moment tensor decomposition indicates an excitation process that consists of a pure (99%) DC motion, while both, isotropic (2%) and CLVD (1% of the deviatoric MT) component, are negligible. A misfit of 7.5% from the frequency domain inversion indicates a good quality inversion result, although using the incorrect assumption of an underlying point source. However, best fit (point source) model geometry and actual slip surface (quarter ring) are not in agreement with each other, and with 7.17 Nm the seismic moment of the earthquake is slightly underestimated by 0.83 Nm.

HC - moment tensor solution (step 2b)

Lat Lon 16.71 N -62.17 E

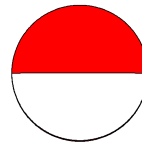
Full MT =	0.102956	0.000594	0.936955
	0.000594	0.251657	0.000178
	0.936955	0.000178	0.054038



Misfit MT(2b) 0.521
 Method Time domain
 Components 1
 Phases P
 Bandpass 1 - 10 Hz
 Traces 36 (12 stations)

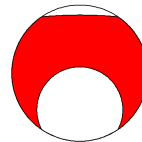
Decomposition:

DC =	0.019940	0.000532	0.763854
	0.000532	0.000000	0.000242
	0.763854	0.000242	-0.019940



76.0 %

CLVD =	-0.053201	0.000062	0.173101
	0.000062	0.115440	-0.000064
	0.173101	-0.000064	-0.062239



24.0 %

ISO =	0.136217	0.000000	0.000000
	0.000000	0.136217	0.000000
	0.000000	0.000000	0.136217

12.0 %

Figure 5.14: Half conduit (2) - Inversion result with full moment tensor. The moment tensor decomposition of the apparent source comprises a deviatoric moment tensor with 76% DC and 24% CLVD contributions, and 12% isotropic components. Due to the symmetry characteristics of the two half conduit orientations their solutions are very similar, but 90° rotated.

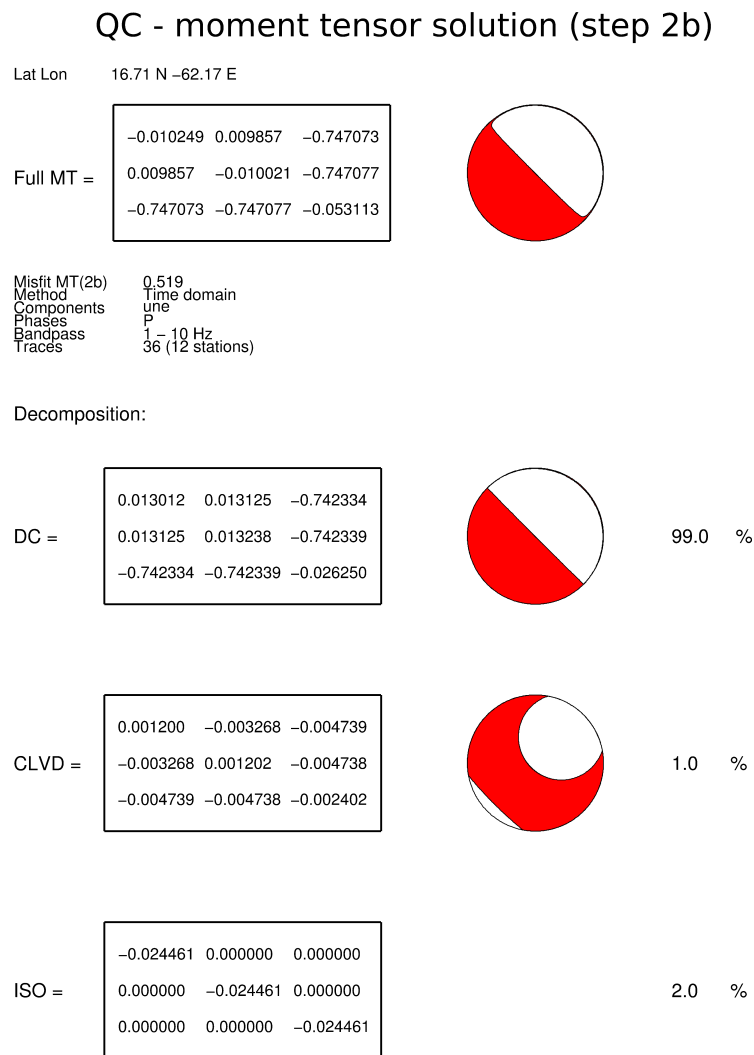


Figure 5.15: Quarter conduit (1) - Inversion result with full moment tensor. The moment tensor decomposition suggest insignificant CLVD and ISO contributions, with a dominant 99% DC component.

Quarter Conduit (2)

Similarly, MTI were performed for a different orientation of slip along a quarter conduit: azimuths of this bent slip surface range from $\alpha = 45^\circ - 135^\circ$ (Fig. 4.6). The inversion result, which can be seen in Fig. 5.16, resembles that of quarter conduit orientation (1): the source mechanism seems to consist of a pure (95%) double couple motion, while the isotropic component with 3% can be neglected in the interpretation.

Different to quarter conduit (1), the best fit slip surface in this case strikes NS. An inversion misfit of 7.6% (frequency domain) yields the misleading assumption of a good quality result, and without the knowledge of the actual fault geometry this inversion would lead to a misinterpretation of slip along a quarter conduit as slip along a northwards striking fault.

5.2.6 Two simultaneous ring faults

Additionally to slip along segments of a single ringfault structure, the possibility of two simultaneously acting ring faults has been investigated. The forward problem of two superimposed ring faults, one at 1400 m and one at 1500 m source depth, was discussed in Chapter 4.2. The resulting waveforms were used as data in an attempt to undertake moment tensor inversion to resolve the supposed point source mechanism triggering the observed events. For MTI, the source depth was fixed to 1450 m, which is the centroid of the two ring fault sources at 1.4 km and 1.5 km depth.

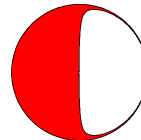
MTI results of the best fit point source solution are shown in Fig. 5.17, where the top panel displays the full moment tensor and its corresponding ‘beach ball’, while the lower part of the plot demonstrates a possible moment tensor decomposition. The isotropic component takes, with 63%, the major share of the full moment tensor, while the CLVD component dominates the remaining 37% of the deviatoric moment tensor part. As a result, the full moment tensor ‘beach ball’ strongly resembles an eye ball, a pattern characteristic for CLVD sources. When interpreted without knowing the initial source mechanism, two simultaneously acting ring faults would therefore be explained as a subhorizontal tensile crack, one of the most common interpretations of CLVD mechanisms in volcanoes (see also Chapter 1.6.5). Additionally, the suggested source’s

QC - moment tensor solution (step 2b)

Lat Lon 16.71 N -62.17 E

Full MT =

0.051616	-0.000209	-0.000025
-0.000209	0.041711	-0.931808
-0.000025	-0.931808	-0.005454

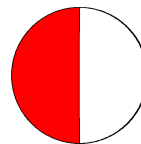


Misfit MT(2b) 0.537
 Method Time domain
 Components one
 Phases P
 Bandpass 1 - 10 Hz
 Traces 36 (12 stations)

Decomposition:

DC =

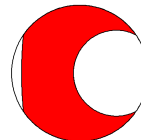
-0.000000	-0.000201	-0.000017
-0.000201	0.022735	-0.898331
-0.000017	-0.898331	-0.022735



95.0 %

CLVD =

0.022325	-0.000008	-0.000008
-0.000008	-0.010315	-0.033477
-0.000008	-0.033477	-0.012010



5.0 %

ISO =

0.029291	0.000000	0.000000
0.000000	0.029291	0.000000
0.000000	0.000000	0.029291

3.0 %

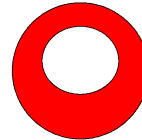
Figure 5.16: Quarter conduit (2) - Inversion result with full moment tensor. The moment tensor decomposition suggest insignificant CLVD and ISO contributions, with a dominant 99% DC component. The inversion results gained from this configuration are comparable to those gained from quarter conduit configuration (2).

2 rfs - Moment tensor solution (step 2b)

Lat Lon 16.71 N -62.17 E

Full MT =

1.515289	0.000378	-0.255510
0.000378	1.440858	0.001597
-0.255510	0.001597	0.573687

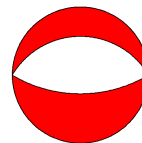


Misfit MT(2b) 1.126
 Method Time domain
 Components 1
 Phases P
 Bandpass 1 - 10 Hz
 Traces 36 (12 stations)

Decomposition:

DC =

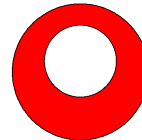
0.122427	0.000035	-0.066443
0.000035	-0.000000	0.000244
-0.066443	0.000244	-0.122427



20.0 %

CLVD =

0.216251	0.000343	-0.189068
0.000343	0.264247	0.001353
-0.189068	0.001353	-0.480498



80.0 %

ISO =

1.176611	0.000000	0.000000
0.000000	1.176611	0.000000
0.000000	0.000000	1.176611

63.0 %

Figure 5.17: MTI solution: Step 2, moment tensor solution for 2 simultaneously acting ring faults. Full moment tensor with corresponding ‘beach ball’, as well as a possible moment tensor decomposition suggesting 63% isotropic components, with the remaining 37% of the full moment tensor assigned to 20% DC and 80% CLVD deviatoric components.

scalar moment would, with $M_0 = 2.02 \text{ Nm}$, lie clearly under the actual 8 Nm of the ring faults.

With a misfit value of 63%, the quality of the best fit model has to be assessed with care, and may be indicative of the problems arising from trying to map spatially extended sources into point source mechanisms.

5.2.7 Staggered sources

This section discusses the moment tensor inversion results of 4 consecutively triggered ring fault structures, whose forward problem was considered in Chapter 4.2.2. Despite being a source with both spatial extent and time history, moment tensor inversion was again carried out under the point source assumption to explore possible misinterpretations of such complex volcanic source mechanisms.

The full moment tensor and suggested moment tensor decomposition of this inversion can be seen in Fig. 5.18. The source depth was fixed to the centroid of the spatially extended source, at 1425 m, and the best fit point source model represents a DC mechanism (97%) as trigger mechanism for the input data. An interpretation of this inversion result would therefore involve a misleading double couple source mechanisms, which fundamentally differs from the true scenario. Nonetheless, this solution shows a high misfit value of 83.5%, indicating a non-reliable inversion result for this source, and is perhaps indicative of the attempt to map a complex source scenario into a point source mechanism.

5.2.8 Helix

Similar to the staggered sources examined in the previous section, slip along a helix-like trajectory involves both time history and spatial extent of the source under investigation: different segments of the conduit in different depths slip at different times, describing a helix shaped slip surface. The resulting slip trajectory for two scenarios can be seen in Figs. 4.12, where the two cases describe scenarios of earthquake hypocentres migrating towards deeper or shallower depths with time.

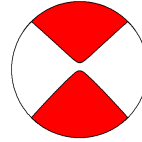
Common moment tensor inversion techniques cannot resolve the true source mechanism in this case. In real case scenarios, where the true nature of the source is unknown,

Staggered RFs - moment tensor solution

Lat Lon 16.71 N -62.17 E

Full MT =

1.131036	0.000456	-0.097873
0.000456	-1.127955	0.002133
-0.097873	0.002133	-0.009900

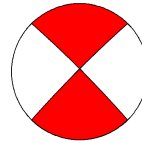


Misfit MT(2b) 1.176
 Method Time domain
 Components one
 Phases P
 Bandpass 1 - 10 Hz
 Traces 36 (12 stations)

Decomposition:

DC =

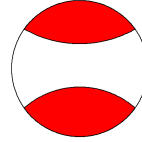
1.101738	0.000451	-0.093825
0.000451	-1.109724	0.002133
-0.093825	0.002133	0.007986



97.0 %

CLVD =

0.031571	0.000006	-0.004048
0.000006	-0.015958	-0.000000
-0.004048	-0.000000	-0.015613



3.0 %

ISO =

-0.002273	0.000000	0.000000
0.000000	-0.002273	0.000000
0.000000	0.000000	-0.002273

0.0 %

Figure 5.18: MTI solution: Step 2, moment tensor solution for the superposition of 4 staggered ring fault sources. Slip along the circumference of the cylindrical conduit initially ($t = 0$ s) occurred at 1500 m depth, and then migrated in 50 m increments and time delays of $\Delta t = 0.001$ s to shallower depths of 1450 m, 1400 m, and 1350 m. The source depths were fixed to the centroid of the spatially extended source at 1425 m.

moment tensor inversions under the point source assumption are, however, a commonly used tool in the investigation of rupture processes. Here, MTI is carried out on traces stemming from known helix-like sources, to examine the potential risks of source misinterpretations.

Helix with increasing source depths with time

The first helix-shaped configuration involves a migration of hypocentres towards greater depths with time, and the forward problem was discussed in Chapter 4.2.3. The best fit full moment tensor including ‘beach ball’ and suggested moment tensor decomposition are presented in Fig. 5.19.

The observed seismicity is suggested to originate from a pure (99%), NW-SE striking, vertically dipping DC source, whose ‘beach ball’ presents the typical DC pattern that can be seen here. While the solution misfit in the time domain is high, an improvement is obtained for the best fit model in the frequency domain inversion, with 58.38%. Additionally to the misleading point source interpretation, an estimated scalar moment of $M_0 = 4 \text{ Nm}$ is half that of the true scalar moment M_0 , which would lead to a drastic underestimation of magma ascent rate, purely due to the disregarding of the source nature of the real source.

Helix with decreasing source depths with time

Different to the previous case, the earthquake epicentres of helix configuration (2) migrate towards shallower depths with time. The moment tensor inversion result for this scenario can be seen in Fig. 5.20.

Similar to the results obtained from helix configuration (1) the moment tensor solution consists of negligible CLVD and isotropic components, and suggests with 99% a pure DC rupture motion. Interestingly, the strike direction of the best fit solution is rotated by 90° compared to the case where slip along the helix migrates to greater depths. With a misfit of 45.3% the quality of the inversion is similar to the other helix inversion, and also in this case an estimated scalar moment of $M_0 = 5 \text{ Nm}$ lies clearly under the true input moment of the source.

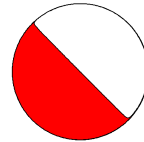
It is clear that the attempt to map these two helix configurations into a point source

Helix (1) - Moment tensor solution (step 2b)

Lat Lon 16.71 N -62.17 E

Full MT =

-0.003614	0.001084	-0.551167
0.001084	0.003957	-0.555851
-0.551167	-0.555851	-0.005188

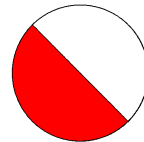


Misfit MT(2b) 1.160
 Method Time domain
 Components 3
 Phases P
 Bandpass 1 - 10 Hz
 Traces 36 (12 stations)

Decomposition:

DC =

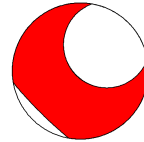
-0.002168	0.001585	-0.550455
0.001585	0.005402	-0.555140
-0.550455	-0.555140	-0.003233



99.0 %

CLVD =

0.000169	-0.000501	-0.000712
-0.000501	0.000170	-0.000711
-0.000712	-0.000711	-0.000339



1.0 %

ISO =

-0.001615	0.000000	0.000000
0.000000	-0.001615	0.000000
0.000000	0.000000	-0.001615

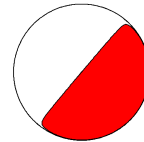
0.0 %

Figure 5.19: MTI solution: Step 2, moment tensor solution for slip along a helix-shaped trajectory whose source hypocentres migrate to greater depths with time. The full moment tensor represents a pure (99%) DC nature of the rupture process when wrongly mapping slip along a spatially extended helix into a point source.

Helix (2) - Moment tensor solution (step 2b)

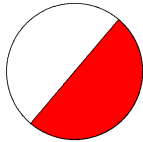
Lat Lon 16.71 N -62.17 E

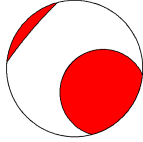
Full MT =
$$\begin{bmatrix} 0.006068 & -0.000222 & -0.524593 \\ -0.000222 & 0.007724 & 0.618975 \\ -0.524593 & 0.618975 & 0.015454 \end{bmatrix}$$



Misfit MT(2b) 1.174
 Method Time domain
 Components 3
 Phases P
 Bandpass 1 - 10 Hz
 Traces 36 (12 stations)

Decomposition:

DC =
$$\begin{bmatrix} -0.002469 & 0.002138 & -0.521486 \\ 0.002138 & -0.001608 & 0.615302 \\ -0.521486 & 0.615302 & 0.004077 \end{bmatrix}$$
  99.0 %

CLVD =
$$\begin{bmatrix} -0.001211 & -0.002360 & -0.003107 \\ -0.002360 & -0.000417 & 0.003673 \\ -0.003107 & 0.003673 & 0.001628 \end{bmatrix}$$
  1.0 %

ISO =
$$\begin{bmatrix} 0.009749 & 0.000000 & 0.000000 \\ 0.000000 & 0.009749 & 0.000000 \\ 0.000000 & 0.000000 & 0.009749 \end{bmatrix}$$
 1.0 %

Figure 5.20: MTI solution: Step 2, moment tensor solution for slip along a helix-shaped trajectory whose source hypocentres migrate to shallower depths with time. Similar to the results obtained for helix configuration (1), the full moment tensor for this case represents a pure DC nature of the rupture process.

Input source	Misfit	DC	CLVD	ISO
DC	7.2%	99%	0%	1%
CLVD	8.3%	0%	100%	0%
RF	63.5%	0%	37%	63%
Dike	58%	27%	41%	32%
HC 1	10.6%	72%	23%	5%
HC 2	10.6%	67%	21%	12%
QC 1	7.5%	97%	1%	2%
QC 2	7.6%	92%	5%	3%
2 RFs	63%	7%	30%	63%
Stag RFs	83.5%	97%	3%	0%
HELIX 1	58.4%	99%	1%	0%
HELIX 2	45.3%	99%	1%	1%

Table 5.1: Summary of MTI results. The frequency inversion step misfit value is shown together with the suggested moment tensor decompositions for all synthetic sources under investigation.

mechanism does not yield meaningful results. This means that the true motion at depth may remain unrecognised if a point source nature of the source is automatically assumed. Additionally to the wrong physical source process, the estimated scalar moment is also highly underestimated in both cases, yielding an underestimation of magma ascent rate when interpreted in volcanological context.

5.3 Discussion and Summary

Moment tensor inversions were carried out for a point source test case and a catalogue of spatially extended sources whose synthetic seismograms were calculated and analysed in Chapters 2 and 4. Classic moment tensor inversions assume point sources as source processes, and can therefore not resolve the source geometry of the here proposed spatially extended sources. Inversions can, however, determine the amount of error that is introduced into the solution, as well as what consequences this may have in regards of interpretations of inversion results, if the original underlying source process was unknown.

The source mechanism of the test case in Chapter 5.2.1, representing a single double couple, outlines the flawless work flow of the code: source mechanism, source depth, seismic moment M_0 , as well as source orientation of the fault are resolved well, with a

best solution misfit of only 7.2%. It is important that the inversion code can accurately resolve the source characteristics of point sources, as this reinforces that deviations of the proposed solutions from the actual source mechanisms in the following cases are purely due to the inability of the code to resolve the spatial extent of the proposed sources. While the inversion result of this test case resolves the original source geometry and mechanism well, this will not be the case when carrying out moment tensor inversions of spatially extended sources. Instead, an apparent best fit point source solution for the original data will be found.

The moment tensor solution for a 50 m wide ring fault structure can be found in Chapter 5.2.3. If original input parameters were unknown, the results gained from MTI would indicate a solution comprising 63% isotropic and 37% CLVD components. The proposed full moment tensor illustration shows a ring of dilatational first motion around a ring of compressional first motion, which strongly resembles the moment tensor solution of the CLVD case (Figs. 5.11 and 5.2.2). In a real case scenario, where the original input characteristics are unknown, the physical process at depth that was responsible for causing the observed seismic signal would be interpreted assuming a point source excitation process, based on the MTI result gained. Here, the suggested ‘beach ball’ and moment tensor solution leads to the misleading conclusion of a subhorizontal tensile crack acting at depth (see Chapter 1.6.5). There are, indeed, a number of examples in the literature where moment tensor inversion solutions of LF seismicity have been construed as such a tensile crack (Chouet, 1996b; Waite et al., 2008). While they examine their MTI results as point sources only, the findings of this study give evidence that slip along the conduit walls yields the same MTI result and should be considered as possible source mechanism in these cases. The importance of knowledge about the source nature - point or spatially extended - becomes eminently significant. The MTI results for another spatially extended source, a dike, whose full moment tensor description and ‘beach ball’ suggest a dominant CLVD source, only stress the findings from the ring fault case (Chapter 5.2.4).

By advancing from the idea of point sources as underlying physical source mechanisms of LF seismic signals, to spatially extended sources, slip along the conduit walls proposed here, represented by the ring fault structure, states an alternative excitation process for LF seismicity at volcanoes. To avoid possible misinterpretations of MTI

results it is therefore crucial to take spatially extended sources such as the ring fault structure into account.

While MTI results of the ring fault yield a combination of CLVD and isotropic sources with no DC contribution, inversion results for half conduits and quarter conduits reveal different moment tensors (Figs. 5.10, 5.14, 5.15, and 5.16). An apparent main contributor in all cases is the DC component, forming 76% and more than 90% of the moment tensor decomposition for half and quarter conduits, respectively. The ‘beach balls’ therefore closely resemble those of double couple sources. Low misfits of less than 15% indicate good quality inversion results which may lead to the wrong conclusion when interpreting the studied processes in terms of point sources.

All moment tensor inversions of spatially extended sources lead to an underestimation of the original seismic moment M_0 . The apparent seismic moment estimated for the ring fault case is with $M_0 = 1.10$ Nm about 8 times smaller than the original input seismic moment of 8.0 Nm. Similarly, apparent M_0 lies with 4.87 – 5.55 Nm consistently below the original 8.0 Nm for both half conduit cases. Only in the case of slip occurring along a quarter of the conduit walls the moment tensor inversion procedure succeeds to approach the real seismic moment with its estimates of 7.17 Nm and 8.12 Nm. As outlined in Chapter 2.5 the seismic moment can be linked to magma ascent rates. An underestimation of M_0 consequently leads to an underestimation of magma flow rate in depth, which can have severe implications for eruption prediction. That is, the time it takes for magma to reach the surface, as well as the energy stored in the system. By advancing towards an inversion technique for spatially extended sources the amount of seismic slip occurring in the conduit could be calibrated, which would ultimately contribute towards a critical value of magma ascent rate that may lead to a dome collapse (Hammer and Neuberg, 2009). A calibration of slip rates may also enable a better quantitative explanation for the link between low frequency swarms and deformation signals (Green, 2005).

The inversion results obtained for spatially extended sources in this chapter clearly stress that it is not sufficient to assume a point source nature in the processes involved in generating the observed seismicity. If the true trigger mechanism was unknown, moment tensor inversions would have lead to wrong source geometries and input mo-

ments in all discussed cases. Adapting spatially extended sources as possible trigger mechanisms for seismicity states that there is thus a need for a change of moment tensor inversion techniques towards the resolution of spatially extended sources with and without time history.

Chapter 6

A Case Study: Analysis of low frequency events at Soufrière Hills Volcano, Montserrat

One of the major advantages of monitoring volcano seismicity is that it allows us to link physical processes acting at depth with measurable geophysical variables at the surface. The detection of low frequency signals at active volcanoes is particularly interesting as this specific type of volcanic earthquake is thought to be the key to forecasting future behaviour of volcanic systems. The origin of LF seismic energy is believed to stem from excitation and resonance of fluid-filled bodies in the volcanic edifice, and therefore provides a unique opportunity to better understand the dynamics of the shallow volcanic plumbing system.

As mentioned in Chapter 1.4, LF seismic signals have been observed at many volcanoes worldwide, and an incomplete list includes Soufrière Hills Volcano (SHV), Montserrat (Miller et al., 1998a; Neuberg et al., 1998); Redoubt volcano, Alaska (Chouet et al., 1994; Stephens et al., 1994) and Asama volcano, Japan (Sawada, 1994). For the last 15 years, SHV has been the focus of various scientific endeavours which has resulted in an extensive collection of geological and geophysical data gathered during numerous cycles of dome growths and collapses. SHV therefore represents a prime location for a case study to investigate the unresolved challenges concerning the source mechanisms of low frequency events.

This chapter presents an in-depth analysis of a chosen set of low frequency events

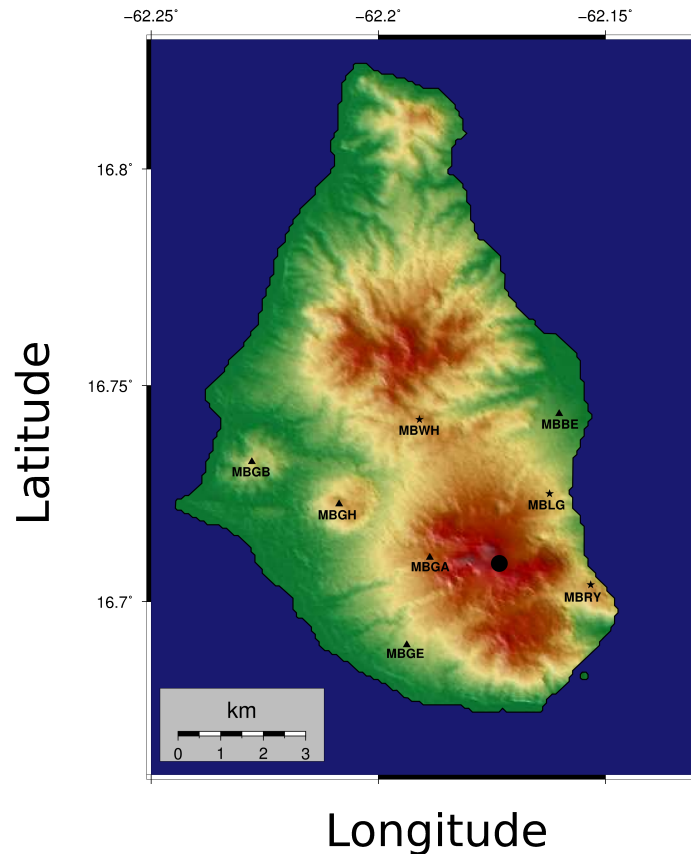


Figure 6.1: The Montserrat seismic network configuration in 1997. Triangles represent 3-component broadband seismometers, and stars represent vertical-component 1 Hz seismometers. The black dot indicates the position of the active lava dome. A gap in azimuthal coverage can be identified to the SEE of the active crater area.

at SHV, Montserrat. First, the Montserrat seismic network is introduced in Chapter 6.1, before the chosen seismic events are presented, and the motives for selecting this particular set of data are discussed in Chapter 6.2. A representative P-wave first motion examination is presented in Chapter 6.3, and moment tensor inversions are carried out in Chapter 6.4. Finally, the findings are compared to the synthetic inversion results from Chapter 5, regarding the nature of the physical mechanisms underlying LF seismicity at Montserrat in Chapter 6.6.

6.1 The Montserrat Seismic Network

Immediately after the re-awakening of the Soufrière Hills Volcano in 1995, a seismic network was deployed on the island by the U.S. Geological Survey (USGS) Volcano Disaster Assistance Program (Aspinall et al., 1998), to monitor the volcanic activity

Table 6.1: The 1D velocity model for Soufrière Hills Volcano, generated by the Montserrat Volcano Observatory and used for the scope of this study. Depths increase downwards from sea-level, with negative depths indicating elevations above sea level.

Top of layer (depth, km)	v_p (kms ⁻¹)
-1.0	2.5
2.0	3.5
3.0	6.0
15.0	7.0
30.0	8.0

(Figure 6.1). In 1996, an array of broadband seismometers was installed by the British Geological Survey (BGS) (Neuberg et al., 1998), and by 1997 five 3-component broadband instruments (Guralp CMG-40T) and three vertical component Integra LA100/F 1 Hz seismometers were operational (Luckett, 2009). With a circular arrangement around the active vent a good azimuthal coverage was reached, despite a small gap at about 110° to the SSE (Fig. 6.1).

For this case study, all stations that recorded the events under investigation were used to reach the best possible signal to noise ratios and allow good quality phase picks. The 1D MVO velocity model used in this study (Table 6.1) has resulted from a modified local velocity model, and minimises overall average rms errors for volcano-tectonic events occurring between 1995 and 1997 (Aspinall et al., 1998).

6.2 Dataset

After a long period of quiescence, the volcano re-activated in November 1995 with extrusion of a new lava dome. Initially slow extrusion rates of 0.1 – 0.5 m³s⁻¹ led into a phase of rapid dome growth with high extrusion rates of more than 5 m³s⁻¹ in May 1997 (Watts et al., 2002). During this period an acceleration of seismic activity as well as cyclic deformation of the edifice were observed to accompany high extrusion rates. Both signals died off in mid May (Young et al., 1998). On 22nd June, seismicity picked up again, causing hundreds of long period earthquakes to occur within the following three days, directly preceding a significant dome collapse event at approximately 12:45pm on 25nd June (Young et al., 1998; Robertson et al., 2000). Despite this major dome collapse event, during which about 5×10^6 m³ of material was removed from the edifice, cyclic activity continued after 25nd June and throughout July.

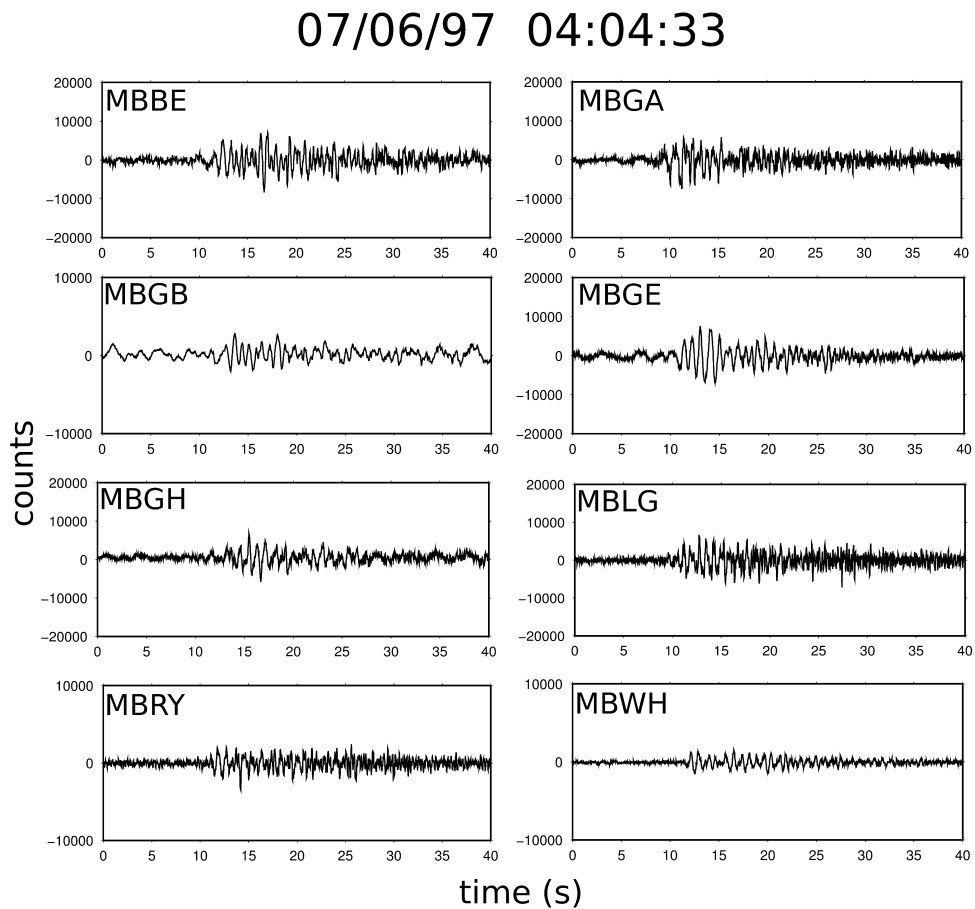


Figure 6.2: Vertical component seismograms of example event 07/06/97 04:04:33

The seismic activity of the volcano prior to this particular dome collapse event has been the focus of numerous studies. This study was carried out on selected events from June 1997, the period preceding the major dome collapse of SHV on 25nd June. 10 selected events were chosen because several studies (e.g. Green, 2005; Doyle, 2003) provided evidence that LF seismic signals were generated by ascending magma in this eruptive period. The dataset, including events that were classified as low frequency events by the Montserrat Volcano Observatory, was chosen based on the maximum number of stations that recorded individual events, signal to noise ratios, and first motion polarities. Vertical traces for two events are shown in Figs. 6.2 and 6.3 while traces of the remaining 8 events of this study can be found in Appendix C.

Calibrated velocity seismograms were obtained by the removal of the instrument response and digitiser gain (see Appendix A), and an integration to displacement seis-

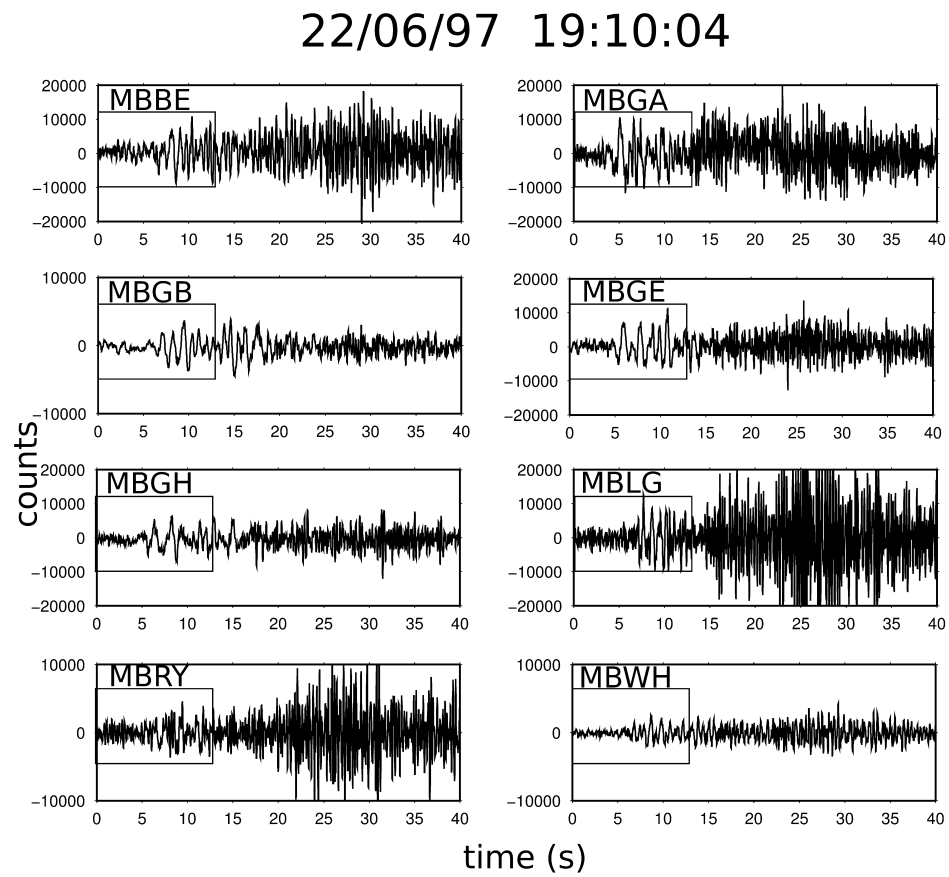


Figure 6.3: Vertical component seismograms of example event 22/06/97 19:10:04. The box indicates the chosen event.

mograms was carried. Data analysis within this work includes first motion polarities as well as moment tensor inversions, and will be presented in the following sections.

6.3 First motions

First motion polarity analysis of the direct P-wave can be used to make first insights into the physical processes that trigger the observed seismicity. First polarity analysis was carried out for the ten selected events that occurred at Montserrat in June 1997, and first motion polarities are summarised in the rose diagrams in Figures 6.4 and 6.5. At approximately 1 km from the active dome, station MBGA shows compressional (red) first motion for all cases. For seven out of the ten events, first motions of stations MBLG (approx. 2.2 km from the active vent) and MBRY (approx. 2.5 km from the active vent) also hold compressional P-wave polarities, while stations situated further from the active vent exhibit dilatational (blue) first motions. The rose diagrams of first motion polarities illustrate this nicely, but also outline an area of insufficient data coverage at epicentral distances greater than 2.5 km to the SE of the dome area. The sparse station distribution complicates accurate conclusions regarding radiation patterns, and will contribute to ambiguities and non-unique moment tensor inversion results. Station MBGB, at about 6 km from the vent, exhibits a high ratio of noise. This might be due to its proximity to the sea shore. The noise complicated first arrival picking, and is responsible for why six out of ten events appear to have emergent (grey) first motions there.

While all of the ten selected LF events exhibit similar first motion polarity patterns, these are only representative for a subset of events. Other LF seismic signals that occurred in the weeks before the June 1997 dome collapse show deviating P-wave first motions, and more extensive analyses of first motions for this time period can be found in the literature (Green, 2005; Johnson, 2007).

Fig. 6.6 shows an example of vertical component velocity seismograms of a LF event which occurred on 10th June 1997. The identified first motions define a region of compressional arrivals in the centre of the focal sphere surrounded by a ring of dilatational first motions at stations situated at greater distances. The observed radiation pattern is indicative of a CLVD mechanism when assuming a point source, with a qualitative

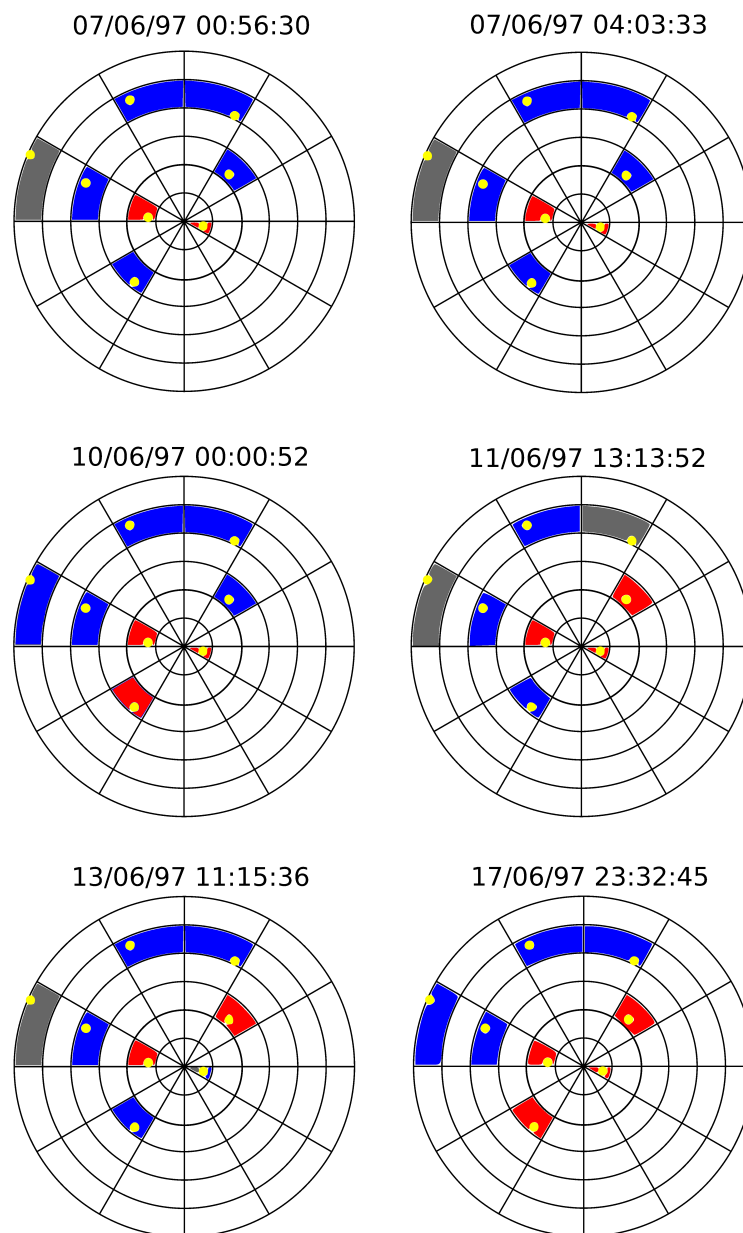


Figure 6.4: First motion polarity rose diagrams for six out of the chosen ten low frequency events that occurred in June 1997 at SHV, Montserrat. The black dot at the centre represents the event hypocentre, and rose segments are 1km by 30°. Yellow dots indicate stations, blue indicates dilatational and red indicates compressional first motion. All cases resemble each other, with a trend towards compressional first motions near to the source epicentre, and dilatational first motions at greater distances.

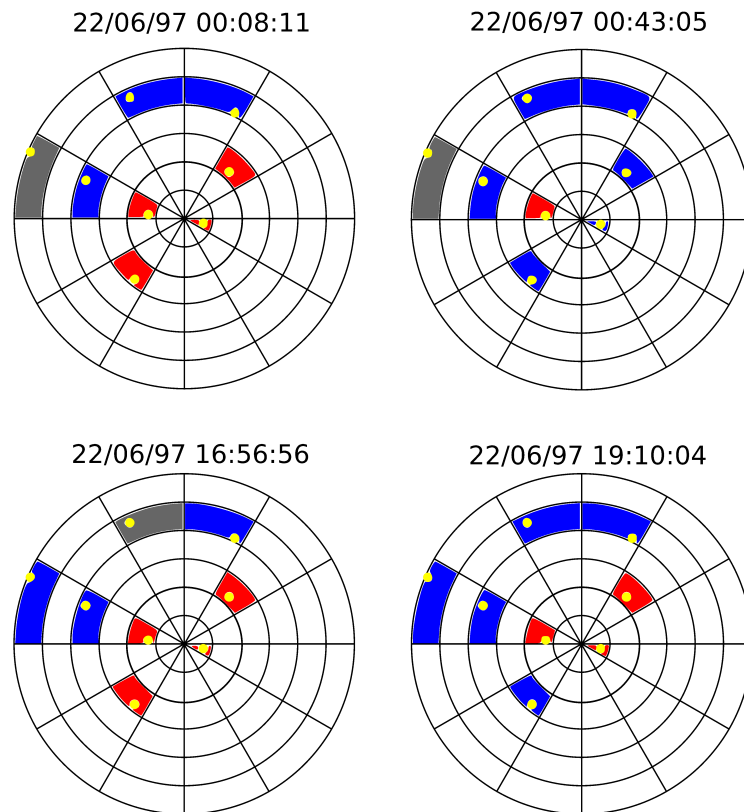


Figure 6.5: First motion polarity rose diagrams for the remaining 4 of the chosen ten low frequency events that occurred in June 1997 at SHV, Montserrat. The black dot at the centre represents the event hypocentre, and rose segments are 1km by 30°. Yellow dots indicate stations, blue indicates dilatational and red indicates compressional first motion. All cases resemble each other, with a trend towards compressional first motions near to the source epicentre, and dilatational first motions at greater distances.

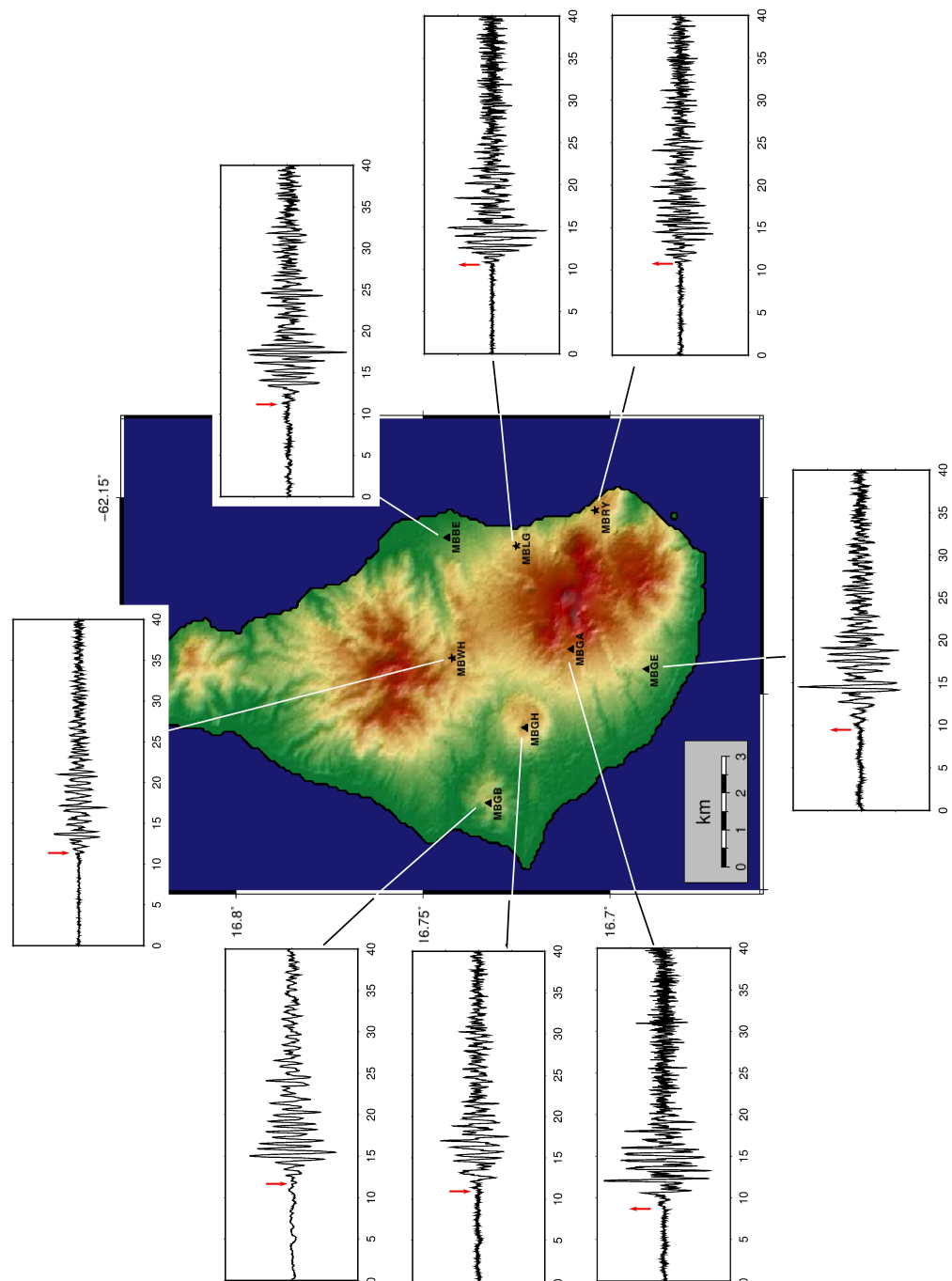


Figure 6.6: First motion polarity for an example LF event which was recorded on Montserrat on 10th June 1997. A central region including stations closest to the active dome (MBGA, MBLG, MBRY, MBGE) exhibits compressional first motions, and is surrounded by a ring of dilatational first motions (at stations MBGH, MBWH, MBBE, and MBGB).

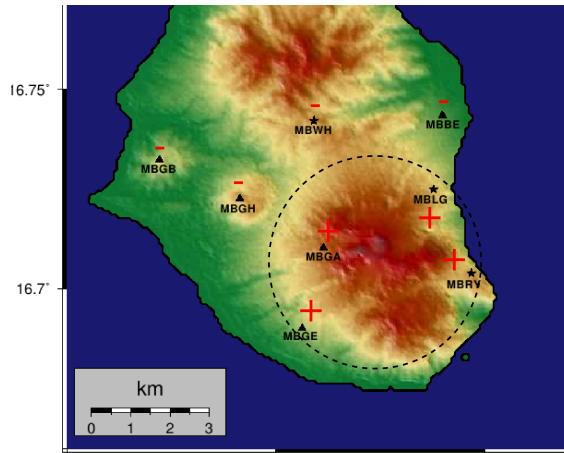


Figure 6.7: Qualitative radiation pattern interpretation of the example event that occurred on Montserrat on 10th June 1997. A ring of compressional first motion can be identified in the area around the active dome area. First motion polarity changes sign with greater distances from the source epicentre.

interpretation of the same event displayed in Figure 6.7.

As Aki (1984) first pointed out, first motions are not sufficient to constrain focal mechanisms in general and here we show that this is particularly the case for magma intrusion related CLVD mechanisms. In an attempt to identify the physical process triggering the observed seismic patterns, moment tensor inversions of the events under investigation are carried out in the next section. Under the point source assumption, MTI solutions cannot indicate potential spatially extended sources. To assess the possibility of a spatially extended source as the underlying trigger, the MTI results will therefore be compared to the results gained in Chapter 5, where synthetic seismograms of spatially extended sources were inverted under the point source assumption.

6.4 Moment tensor inversion results

Moment tensor inversion was carried out for the chosen set of ten LF events. 18 channels (3 per broadband, and 1 per single component station) were modelled and analysed using the velocity model listed in Table 6.1, and in the frequency bands 0.5-4 Hz and 0.5-2 Hz. Topography was neglected in all cases. Because LF seismicity on Montserrat almost exclusively occurs beneath the active dome and at source depths between 1 km and 2 km (see Appendix B and Green (2005)), and due to absolute location errors, inversions were run for events located below the summit area, and repeated for 1 km,

1.5 km, and 2 km source depth.

6.4.1 Inversion bandwidth 0.5-4 Hz

The best fit solution, based on residual errors R , for the event recorded at 04:03:33 on 7th June 1997 can be seen in Fig. 6.8, Fig. 6.9 and Fig. 6.10 for the inversions with fixed depths at 1 km, 1.5 km, and 2 km, respectively. Best solution moment tensors and ‘beach balls’ change with changing source depth. Frequency domain misfits are, with 83.9%, 88.3%, and 88.7%, high for all three cases. Note that indicated misfits in the figures are based on inversion step 2, which is carried out in the time domain, resulting in higher misfit values due to e.g. trace misalignments (Cesca et al., 2010). In the 2 km case (Fig. 6.10) the isotropic component is, at 1%, negligible. The deviatoric moment tensor, broken down into 41.0% DC and 59.0% CLVD components, dominates the 2 km moment tensor solution. In contrast, moment tensor decomposition suggests a significant contribution of 60% isotropic component to the source mechanism for source depths of 1 km (Fig. 6.8) and 1.5 km (Fig. 6.9). In these cases, the remaining 40% deviatoric moment tensors are in turn broken down very differently: 52.0% DC and 48.0% CLVD for 1 km, and a dominant 93% CLVD accompanied by a low 7.0% DC contribution for 1.5 km.

Figures 6.11, 6.12, and 6.13 show the frequency distributions of best fit model (black line) and data (red) corresponding to the three considered fixed depth inversions. Note that the data share similar frequency contents with main contributions of low frequencies (below 2 Hz) to the signal. As high misfit values indicate, general fit of amplitude spectra between data and best fit model for the inversion could not be reached. This is, the best fit model spectra exhibit even distributions across amplitudes while data frequency contributions are concentrated towards the lower frequencies.

Best fit solutions do not only change with source depth, but also across events. Full moment tensors after MTI of the event recorded at 00:00:52 on 22nd June 1997 are illustrated in Fig. 6.14, Fig. 6.15 and Fig. 6.16. Misfit values for this example are with 80.7% (1 km case), 82.6% (1.5 km case), and 82.1% (2 km case) comparably high to the previous case. Furthermore, the contribution to the solutions of the isotropic component only varies by 2% across all three source depths, with absolute values of 14.0%, 13.0%, and 15.0% for 1 km, 1.5 km, and 2 km, respectively. Hence, the devia-

MT solution - 07/06/1997 04:03:33

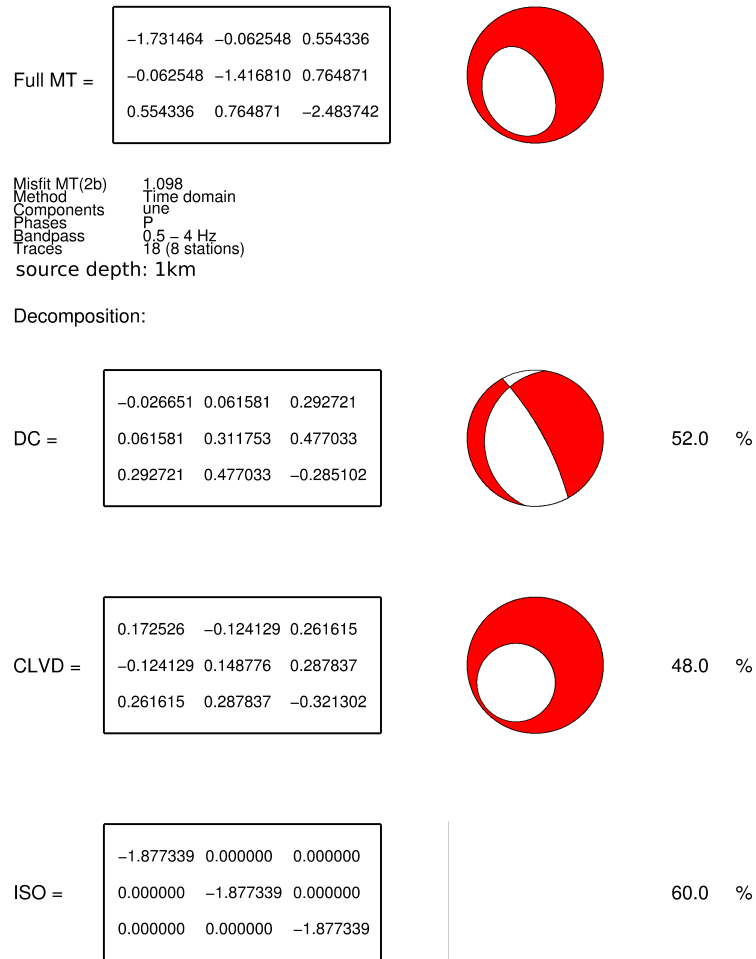


Figure 6.8: MTI solution for the event recorded at 04:03:33 on 7th June 1997. The event epicentre was fixed to the active dome region, while the source depth was fixed to 1 km. The full moment tensor and its ‘beach ball’ representation for an inversion in the frequency range 0.5-4 Hz are displayed in the top section, while the suggested decomposition is shown in the bottom section of the figure. The misfit value corresponds to the time domain inversion step (step 2), and, therefore, is higher than the overall inversion misfit.

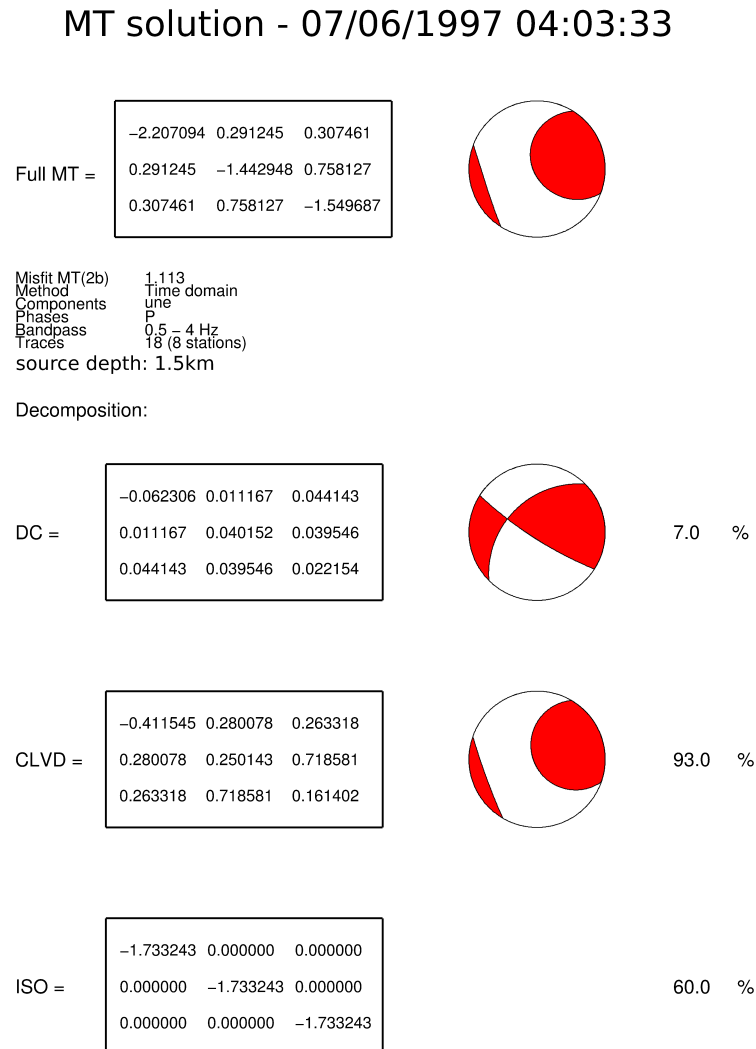


Figure 6.9: MTI solution for the event recorded at 04:03:33 on 7th June 1997. The event epicentre was fixed to the active dome region, while the source depth was fixed to 1.5 km. The full moment tensor and its ‘beach ball’ representation for an inversion in the frequency range 0.5-4 Hz are displayed in the top section of the figure, while the suggested decomposition is shown in the bottom section of the figure. The misfit value corresponds to the time domain inversion step (step 2), and therefore lies higher than the overall inversion misfit.

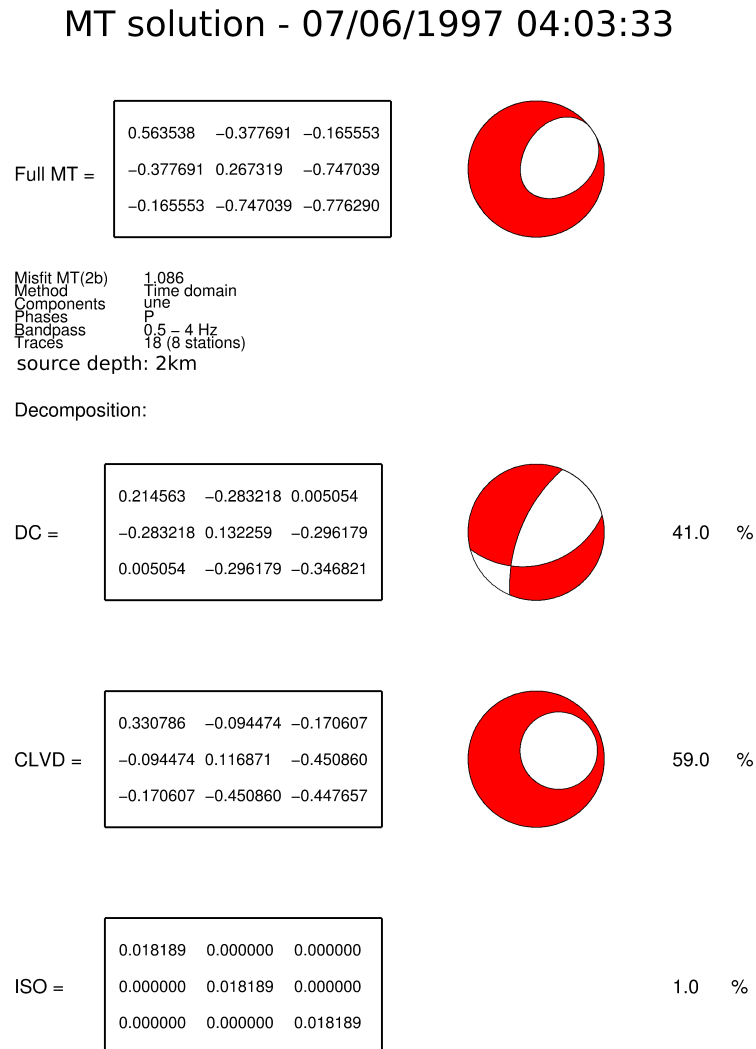


Figure 6.10: MTI solution for the event recorded at 04:03:33 on 7th June 1997. The event epicentre was fixed to the active dome region, while the source depth was fixed to 2 km. The full moment tensor and its ‘beach ball’ representation for an inversion in the frequency range 0.5-4 Hz are displayed in the top section, while the suggested decomposition is shown in the bottom section of the figure. The misfit value corresponds to the time domain inversion step (step 2), and, therefore, is higher than the overall inversion misfit.

07/06/97 - 04:03:33 - 1km

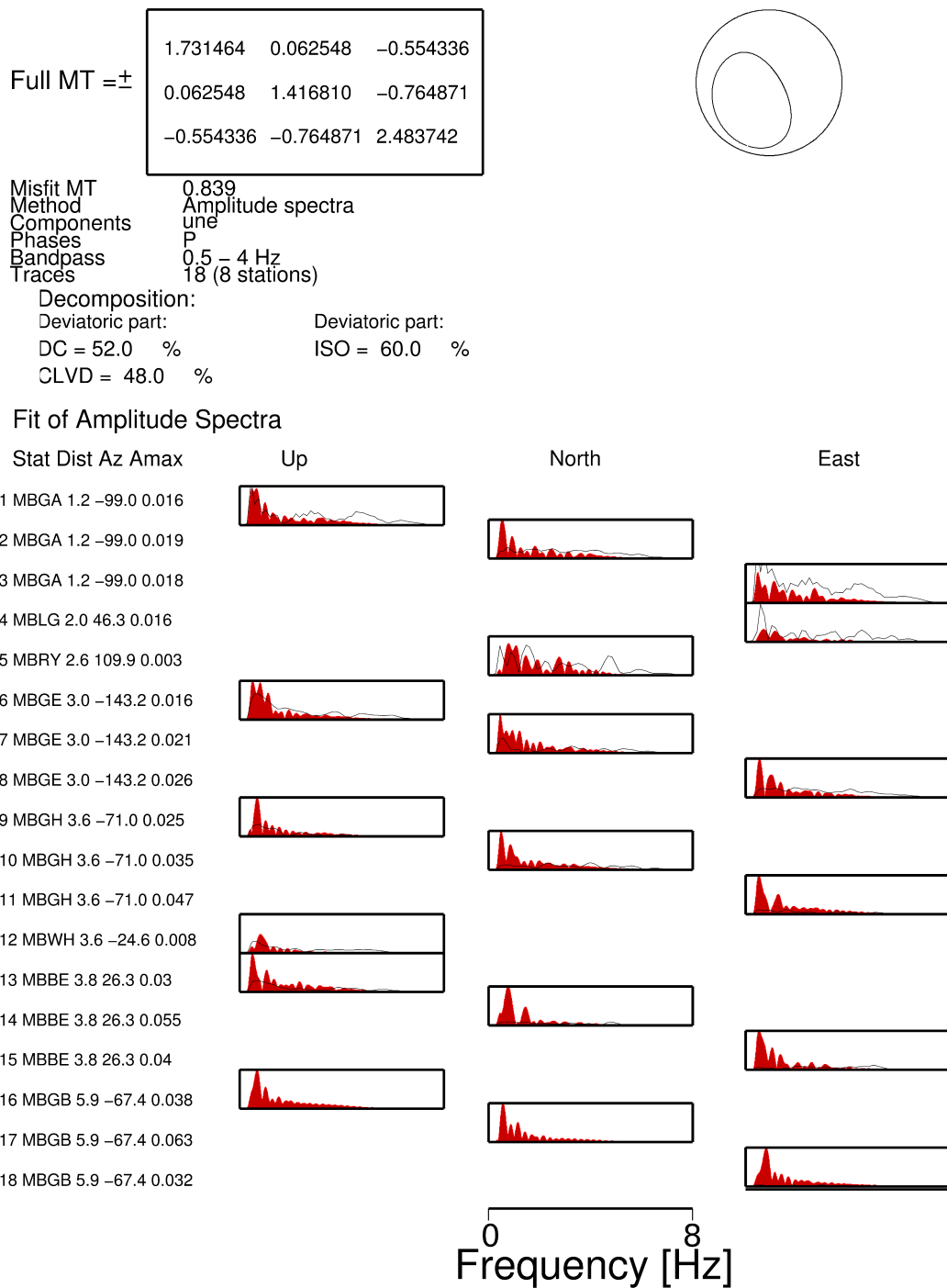


Figure 6.11: MTI solution for the event recorded at 04:03:33 on 7th June 1997. The event epicentre was fixed to the active dome region, while the source depth was fixed to 1 km. The full moment tensor and its ‘beach ball’ representation for an inversion in the frequency range 0.5-4 Hz are displayed in the top section, while the frequency fit between model and data is plotted below.

07/06/97 - 04:03:33 - 1.5km

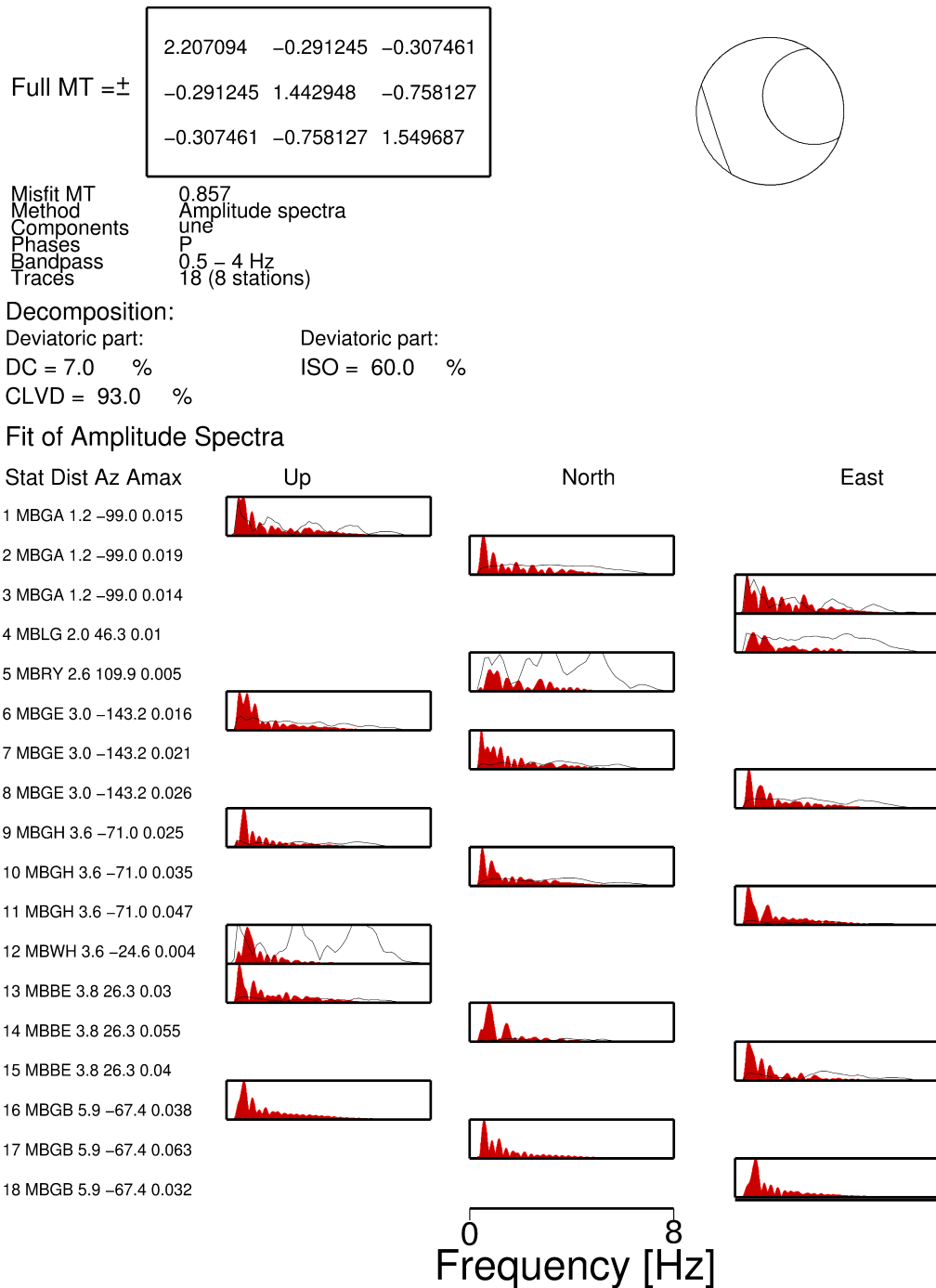
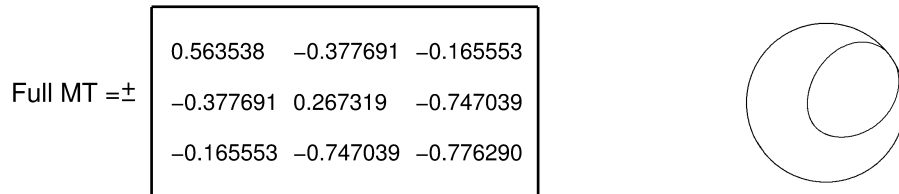


Figure 6.12: MTI solution for the event recorded at 04:03:33 on 7th June 1997. The event epicentre was fixed to the active dome region, while the source depth was fixed to 1.5 km. The full moment tensor and its ‘beach ball’ representation for an inversion in the frequency range 0.5-4 Hz are displayed in the top section, while the frequency fit between model and data is plotted below.

07/06/97 - 04:03:33 - 2km



Misfit MT 0.880
 Method Amplitude spectra
 Components one
 Phases P
 Bandpass 0.5 - 4 Hz
 Traces 18 (8 stations)

Decomposition:
 Deviatoric part: DC = 41.0 % Deviatoric part: ISO = 1.0 %
 CLVD = 59.0 %

Fit of Amplitude Spectra

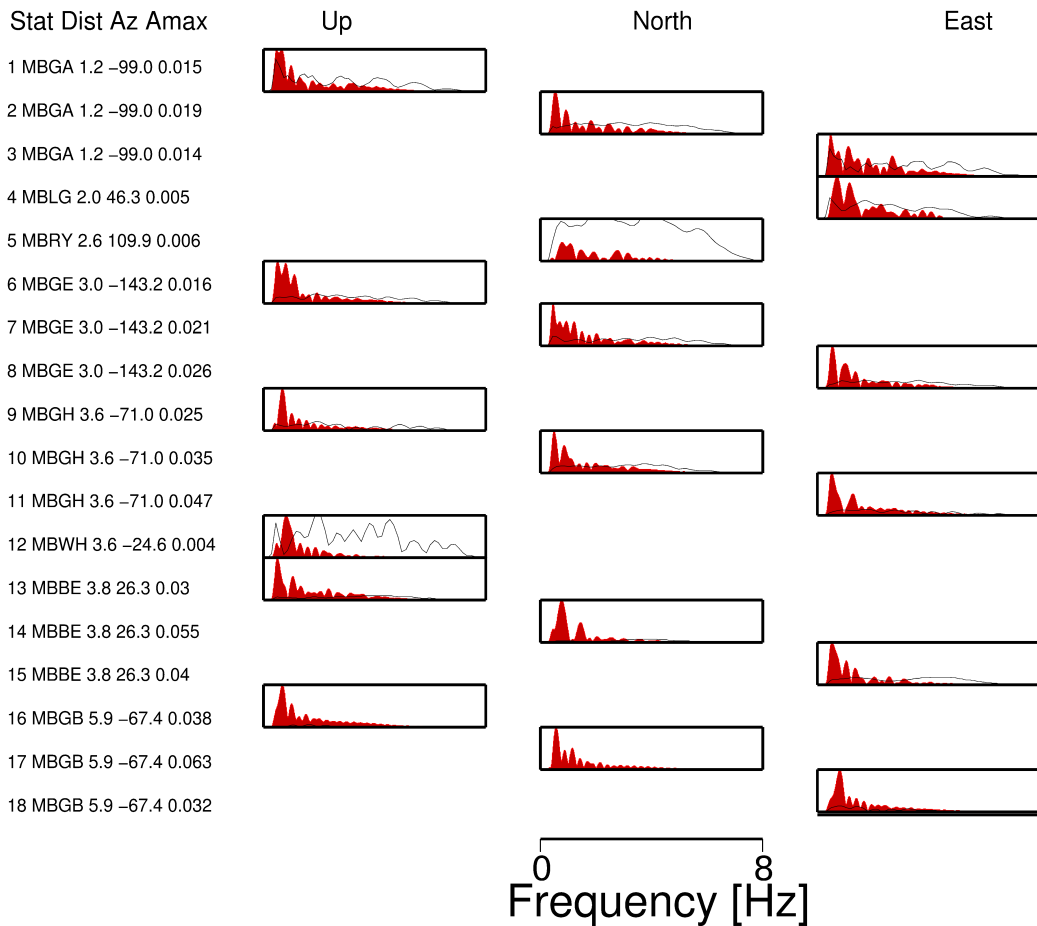


Figure 6.13: MTI solution for the event recorded at 04:03:33 on 7th June 1997. The event epicentre was fixed to the active dome region, while the source depth was fixed to 2 km. The full moment tensor and its ‘beach ball’ representation for an inversion in the frequency range 0.5-4 Hz are displayed in the top section, while the frequency fit between model and data is plotted below.

toric moment tensor dominates the solution in all three cases. At a fixed source depth of 1 km, decomposition of the best fit moment tensor consists of 95.0% CLVD and only 5.0% DC components. Differently, the deviatoric moment tensor in the 1.5 km case is broken down into 42.0% DC and 58.0% CLVD components, and resembles the best fit decomposition of the 2 km case (41.0% DC and 59.0% CLVD). Similar to the first LF event, amplitude spectra comparisons between data and best fit models outline poor inversion qualities of MTI carried out for the event that occurred on 22nd June 1997 (Figs. 6.17., 6.18 and 6.19). As in the previous case, frequency contents for all three source depths are concentrated towards low frequencies (0.5-2 Hz) for the event, while best fit model amplitude spectra show contributions of the whole range of frequencies.

6.4.2 Inversion bandwidth 0.5-2 Hz

Moment tensor inversions of the 10 events were also carried out for a frequency bandwidth of 0.5-2 Hz. MTI results for the same two LF events are presented and discussed here while best fit solutions for all other events can be found in Appendix C.

The best fit solution for the event recorded at 04:03:33 on 7th June 1997 is shown in Fig. 6.20, Fig. 6.21 and Fig. 6.22 for the inversions with fixed depths at 1 km, 1.5 km, and 2 km, respectively.

Again, best solution moment tensors and ‘beach balls’ change with changing source depth. Frequency domain misfits are, with 76%, 76.3%, and 81.8%, still high for all three cases, a slight improvement of inversion quality compared to MTI in the frequency range 0.5-4 Hz can, however, be noticed. In the 1 km case (Fig. 6.20) the isotropic component is, at 42%, slightly reduced compared to the 60% resolved for MTI at 0.5-4 Hz (Fig. 6.8). The relative breakdown of the deviatoric moment tensor, however, is with 55.0% DC and 45.0% CLVD components comparable to the first inversion case for 1 km fixed depth. The overall similar MTI results for both frequency bandwidths is represented in similar beach balls for both cases. While the absolute values of DC, CLVD, and isotropic component contributions change when changing the inversion frequency cut-off frequency from 4 Hz to 2 Hz, the relative distribution of component percentages is unchanged compared to the inversions carried out at 2 km source depth (Figs. 6.10 and 6.22). The main contributor to the overall MTI solution is, with 70%, the CLVD

MT solution - 22/06/1997 19:10:04

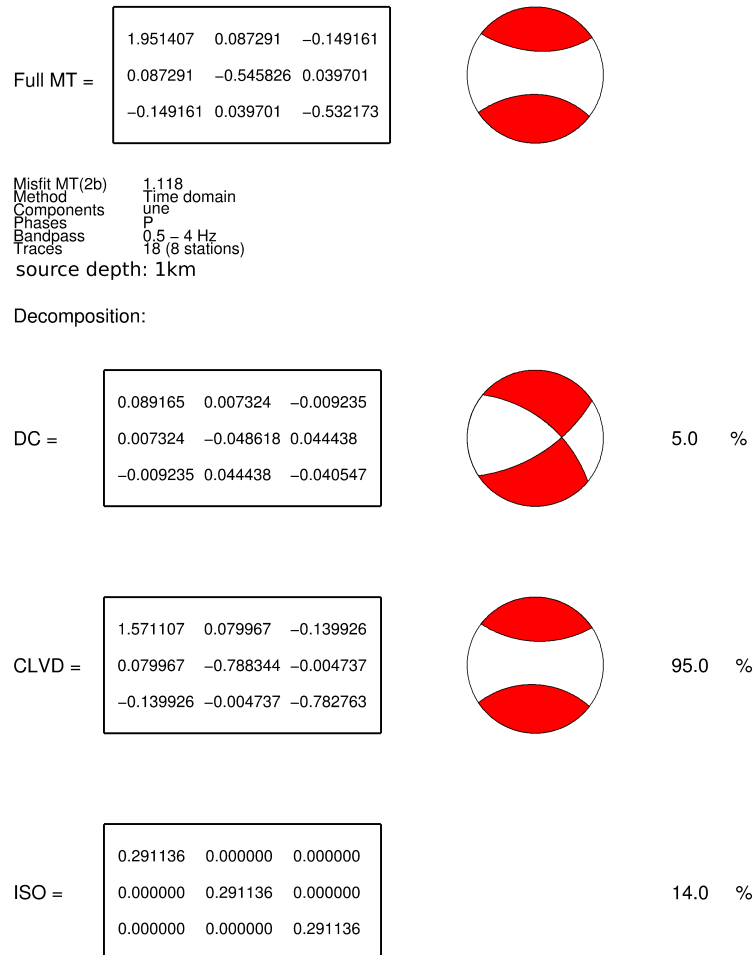


Figure 6.14: MTI solution for the event recorded at 19:10:04 on 22nd June 1997. The event epicentre was fixed to the active dome region, while the source depth was fixed to 1 km. The full moment tensor and its ‘beach ball’ representation for an inversion in the frequency range 0.5-4 Hz are displayed in the top section, while the suggested decomposition is shown in the bottom section of the figure. The misfit value corresponds to the time domain inversion step (step 2), and, therefore, is higher than the overall inversion misfit.

MT solution - 22/06/1997 19:10:04

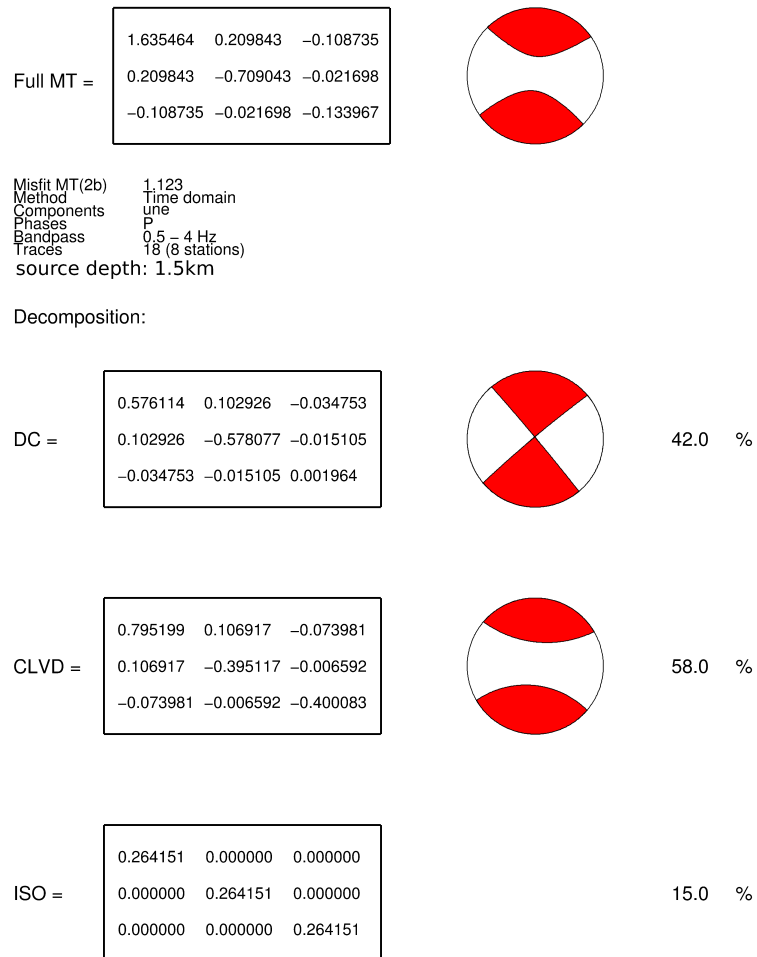


Figure 6.15: MTI solution for the event recorded at 19:10:04 on 22nd June 1997. The event epicentre was fixed to the active dome region, while the source depth was fixed to 1.5 km. The full moment tensor and its ‘beach ball’ representation for an inversion in the frequency range 0.5-4 Hz are displayed in the top section, while the suggested decomposition is shown in the bottom section of the figure. The misfit value corresponds to the time domain inversion step (step 2), and, therefore, is higher than the overall inversion misfit.

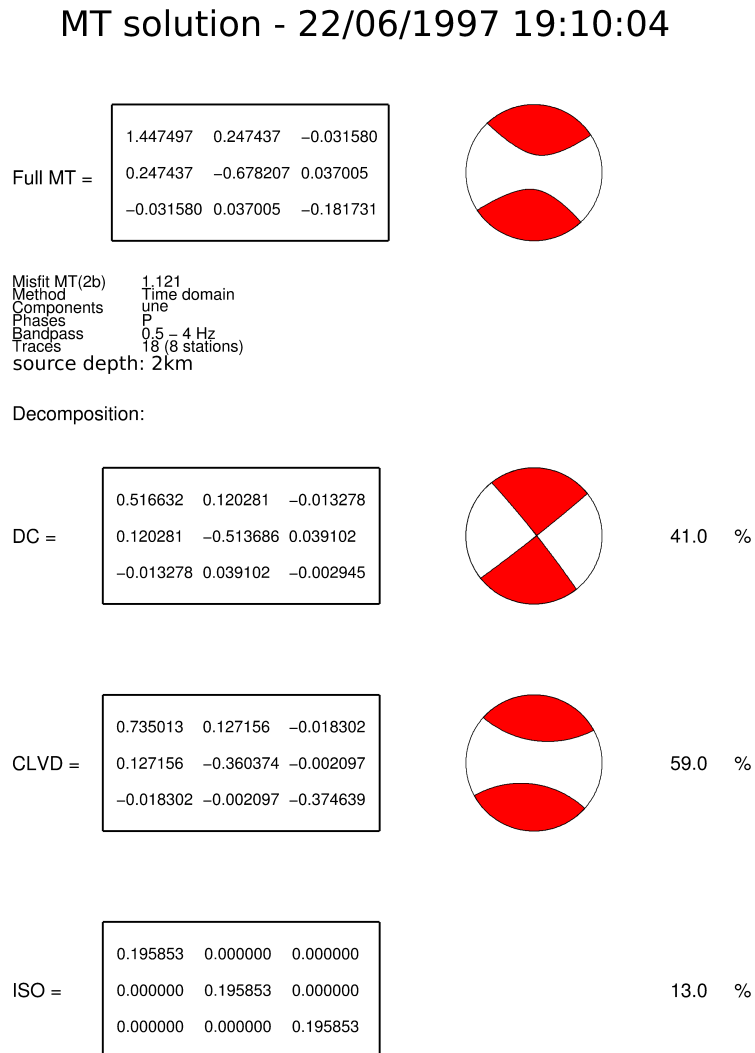


Figure 6.16: MTI solution for the event recorded at 19:10:04 on 22nd June 1997. The event epicentre was fixed to the active dome region, while the source depth was fixed to 2 km. The full moment tensor and its ‘beach ball’ representation for an inversion in the frequency range 0.5-4 Hz are displayed in the top section, while the suggested decomposition is shown in the bottom section of the figure. The misfit value corresponds to the time domain inversion step (step 2), and, therefore, is higher than the overall inversion misfit.

22/06/97 - 19:10:04 - 1km

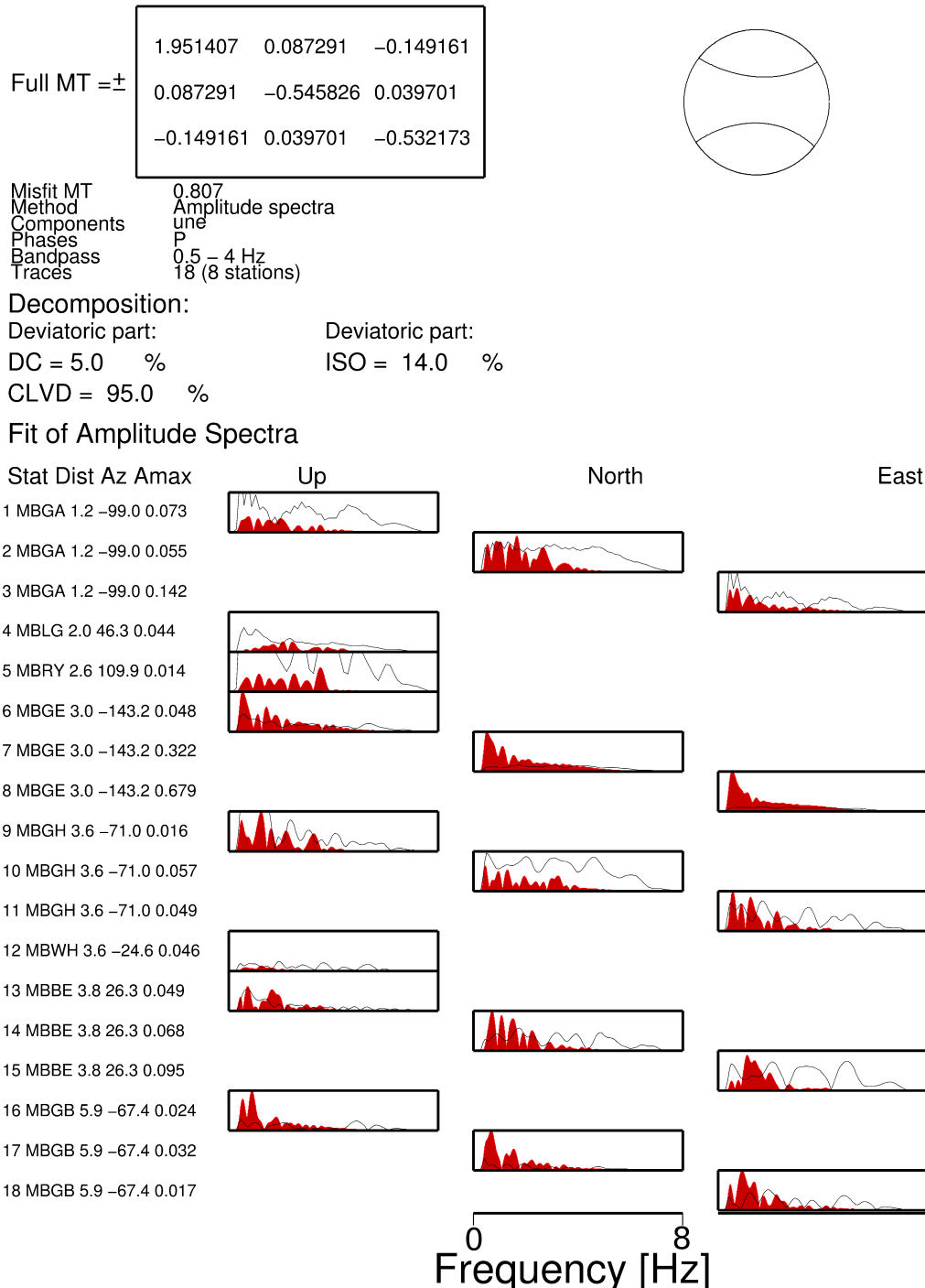
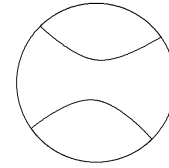


Figure 6.17: MTI solution for the event recorded at 19:10:04 on 22nd June 1997. The event epicentre was fixed to the active dome region, while the source depth was fixed to 1 km. The full moment tensor and its ‘beach ball’ representation for an inversion in the frequency range 0.5-4 Hz are displayed in the top section, while the frequency fit between model and data is plotted below.

22/06/97 - 19:10:04 - 1.5km

Full MT =±

-1.635464	-0.209843	0.108735
-0.209843	0.709043	0.021698
0.108735	0.021698	0.133967



Misfit MT 0.825
 Method Amplitude spectra
 Components one
 Phases P
 Bandpass 0.5 - 4 Hz
 Traces 18 (8 stations)

Decomposition:
 Deviatoric part: Deviatoric part:
 DC = 42.0 % ISO = 15.0 %
 CLVD = 58.0 %

Fit of Amplitude Spectra

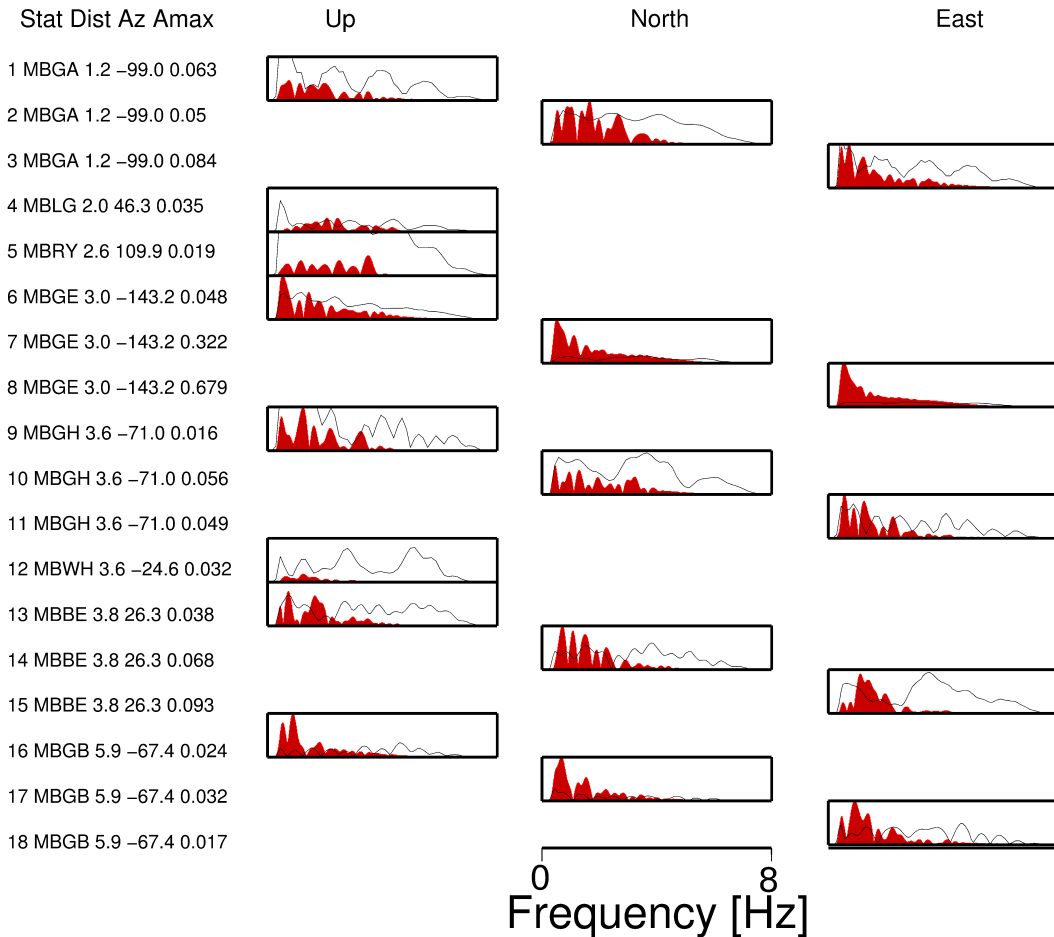


Figure 6.18: MTI solution for the event recorded at 19:10:04 on 22nd June 1997. The event epicentre was fixed to the active dome region, while the source depth was fixed to 1.5 km. The full moment tensor and its ‘beach ball’ representation for an inversion in the frequency range 0.5-4 Hz are displayed in the top section, while the frequency fit between model and data is plotted below.

22/06/97 - 19:10:04 - 2km

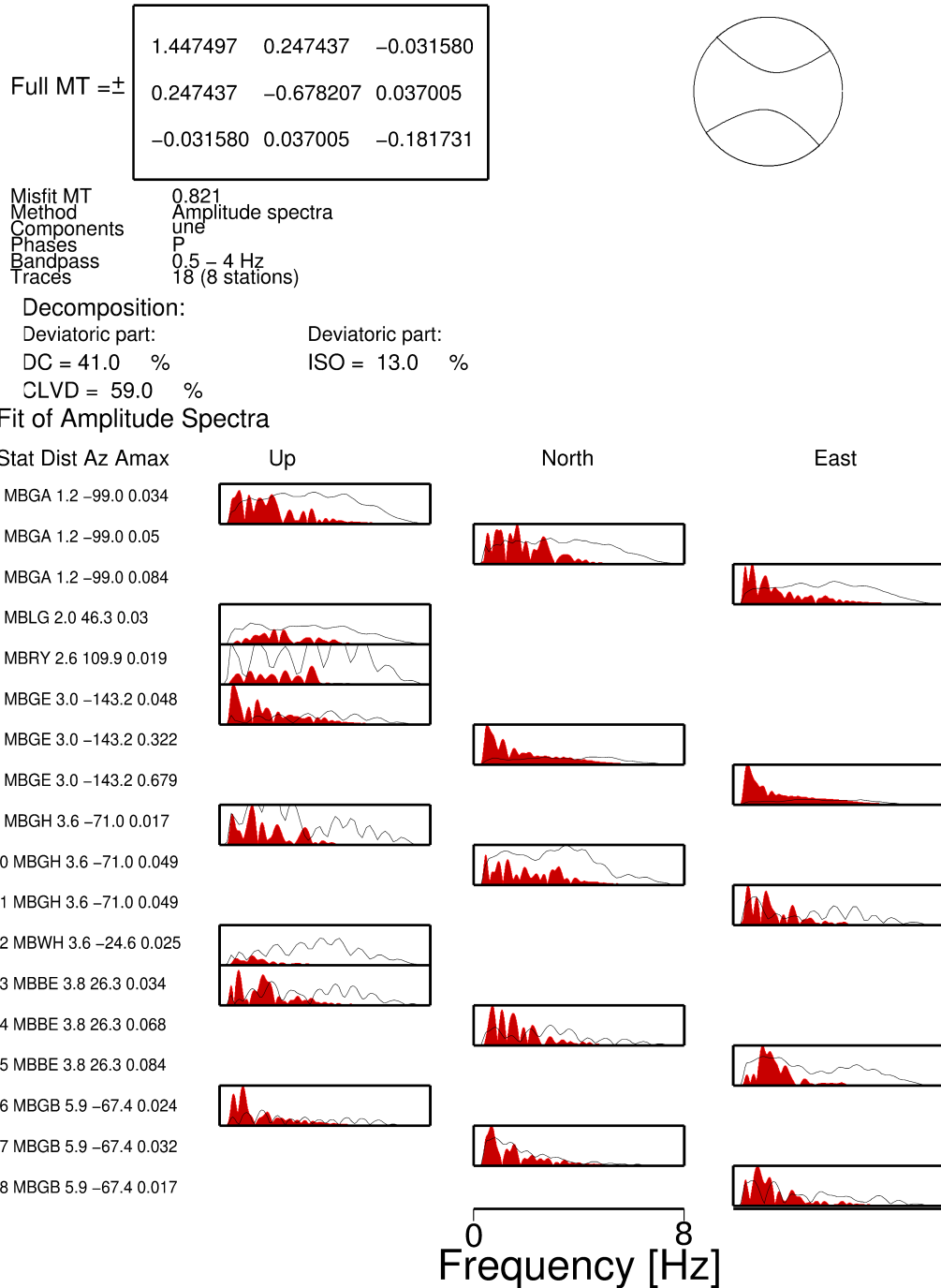


Figure 6.19: MTI solution for the event recorded at 19:10:04 on 22nd June 1997. The event epicentre was fixed to the active dome region, while the source depth was fixed to 2 km. The full moment tensor and its 'beach ball' representation for an inversion in the frequency range 0.5-4 Hz are displayed in the top section, while the frequency fit between model and data is plotted below.

MT solution - 07/06/1997 04:03:33

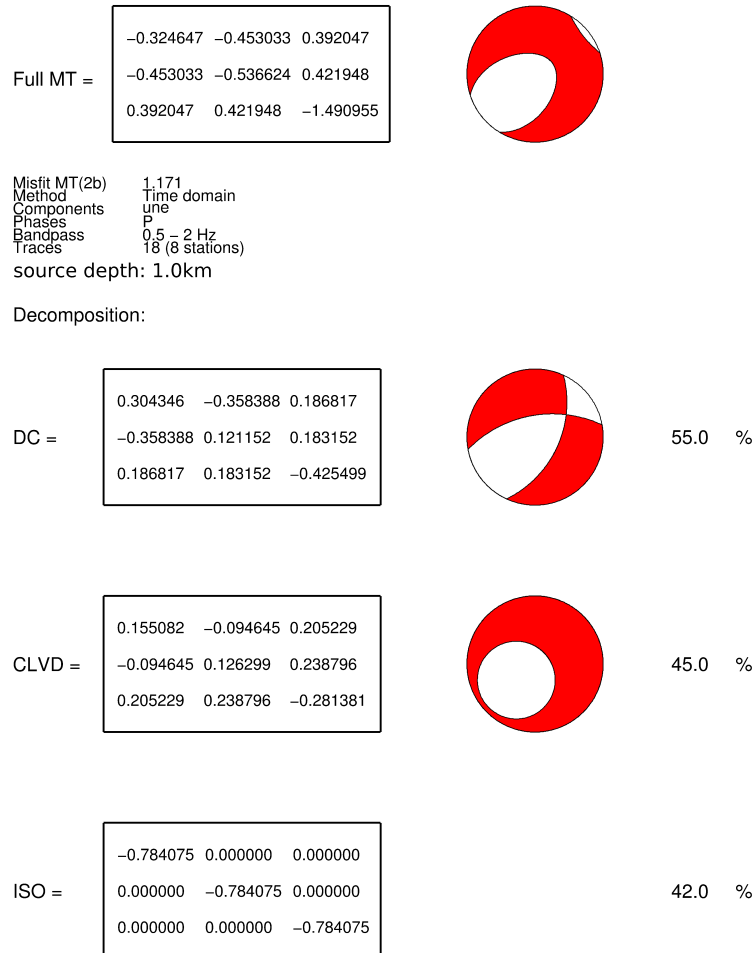


Figure 6.20: MTI solution for the event recorded at 04:03:33 on 7th June 1997. The event epicentre was fixed to the active dome region, while the source depth was fixed to 1 km. The full moment tensor and its ‘beach ball’ representation for an inversion in the frequency range 0.5-2 Hz are displayed in the top section, while the suggested decomposition is shown in the bottom section of the figure. The misfit value corresponds to the time domain inversion step (step 2), and, therefore, is higher than the overall inversion misfit.

MT solution - 07/06/1997 04:03:33

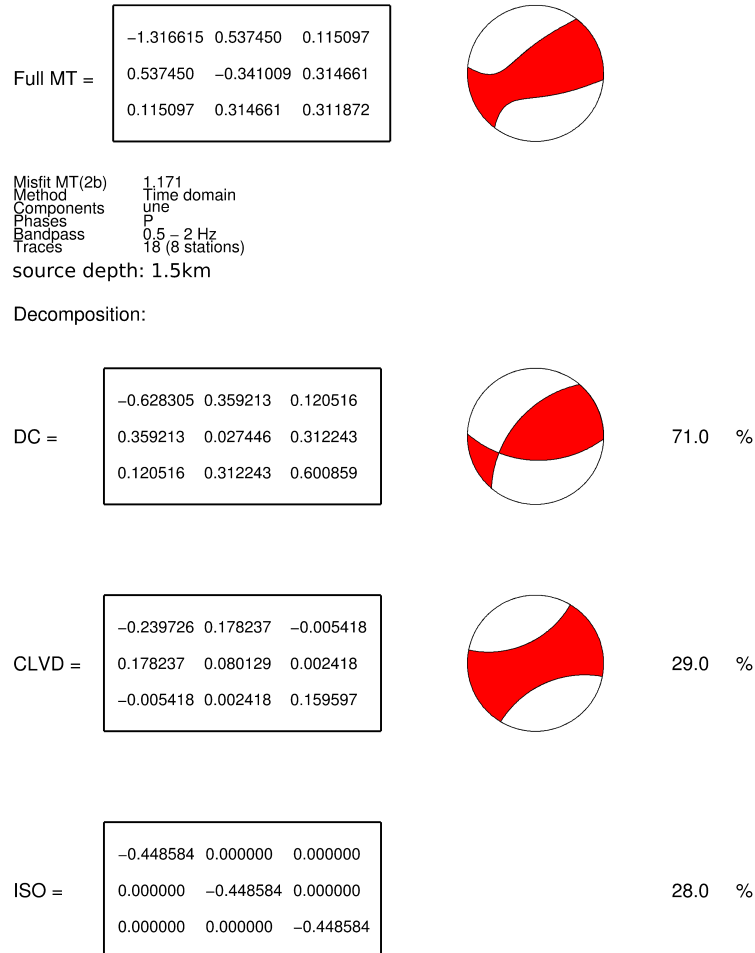


Figure 6.21: MTI solution for the event recorded at 04:03:33 on 7th June 1997. The event epicentre was fixed to the active dome region, while the source depth was fixed to 1.5 km. The full moment tensor and its ‘beach ball’ representation for an inversion in the frequency range 0.5-2 Hz are displayed in the top section of the figure, while the suggested decomposition is shown in the bottom section of the figure. The misfit value corresponds to the time domain inversion step (step 2), and therefore lies higher than the overall inversion misfit.

MT solution - 07/06/1997 04:03:33

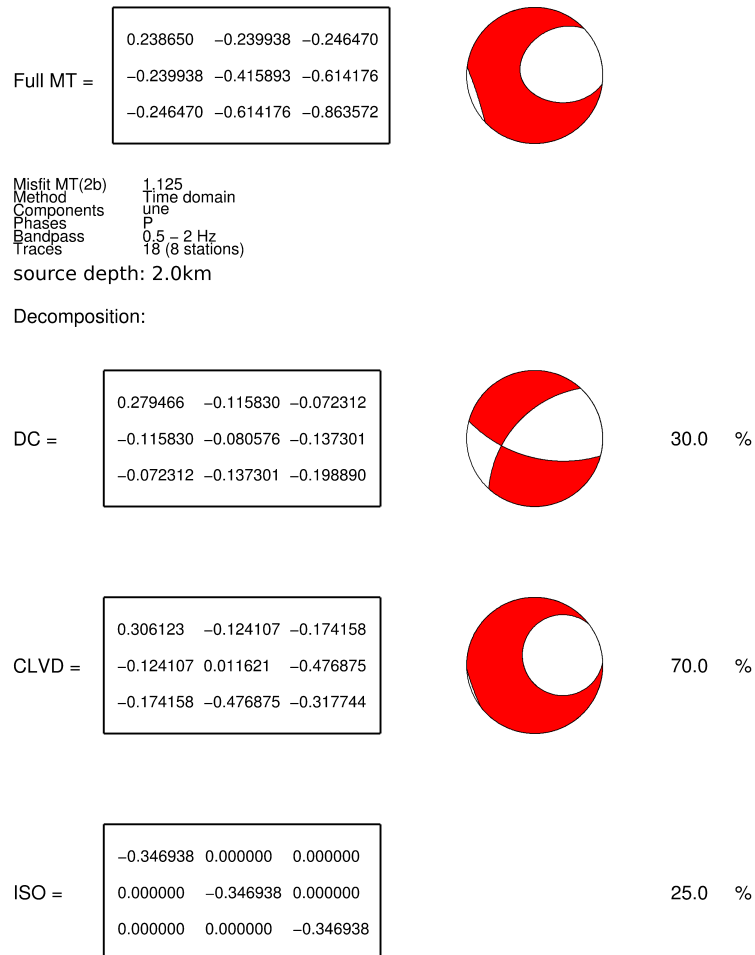


Figure 6.22: MTI solution for the event recorded at 04:03:33 on 7th June 1997. The event epicentre was fixed to the active dome region, while the source depth was fixed to 2 km. The full moment tensor and its ‘beach ball’ representation for an inversion in the frequency range 0.5-2 Hz are displayed in the top section, while the suggested decomposition is shown in the bottom section of the figure. The misfit value corresponds to the time domain inversion step (step 2), and, therefore, is higher than the overall inversion misfit.

component. As a result, best fit ‘beach balls’ hold fried egg characteristics for both frequency bands. The biggest change in MTI solutions and resulting moment tensor decompositions is obtained in the 1.5 km case, where MTI in the narrower frequency bandwidth results in a best fit solution comprised of 28% isotropic, and 29% CLVD and 71% DC deviatoric moment tensor components (Fig. 6.21).

Figures 6.23, 6.24, and 6.25 show the frequency distributions of best fit model (black line) and data (red) corresponding to the three considered fixed depth inversions. Again, no good fit between models and data are reached, similar to inversions carried out in the bandwidth 0.5-4 Hz, indicating poor inversion qualities in all three cases.

Full moment tensors of LF event 2 are illustrated in Fig. 6.26, Fig. 6.27 and Fig. 6.28. Misfit values for this example improve for the narrower frequency band of 0.5-2 Hz and lie at 77.5% (1 km case), 74.4% (1.5 km case), and 72.5% (2 km case). For all three source depths, the DC component dominates the moment tensor decomposition, contributing 96%, 94%, and 92% to the deviatoric moment tensor, respectively. In the 1.5 km and 2 km cases, isotropic and CLVD components lie below 10%, resulting in an overall moment tensor dominated by DC components. These similarities in MTI solutions result in very similar moment tensor descriptions and ‘beach balls’ for the 1.5 km and 2 km cases.

Additionally to the two examples analysed in this chapter, plots showing full moment tensors, moment tensor decompositions and ‘beach balls’ for the entire set of events can be found in Appendix C. It becomes clear that moment tensor inversion results strongly vary across source depths and events. Misfits consistently lie above 80% for inversions carried out in the frequency band 0.5-4 Hz and above 70% for inversions in the frequency band 0.5-2 Hz, which represents a slight improvement of inversion results for the narrower frequency band. Due to poor azimuthal coverage of the area, the inversion fails to define exact nodal planes, and can therefore be made partially responsible for increased misfit values and non-uniqueness of the solutions. This is common in volcanic settings (e.g. Cesca et al., 2013), and the non-uniqueness must be kept in mind when interpreting MTI results. Normally, conclusions concerning the physical trigger mechanism responsible for the observed seismicity would be drawn from the inversion results assuming a point source acting at depth. As it is one of the main objectives of

07/06/97 - 04:03:33 - 1km

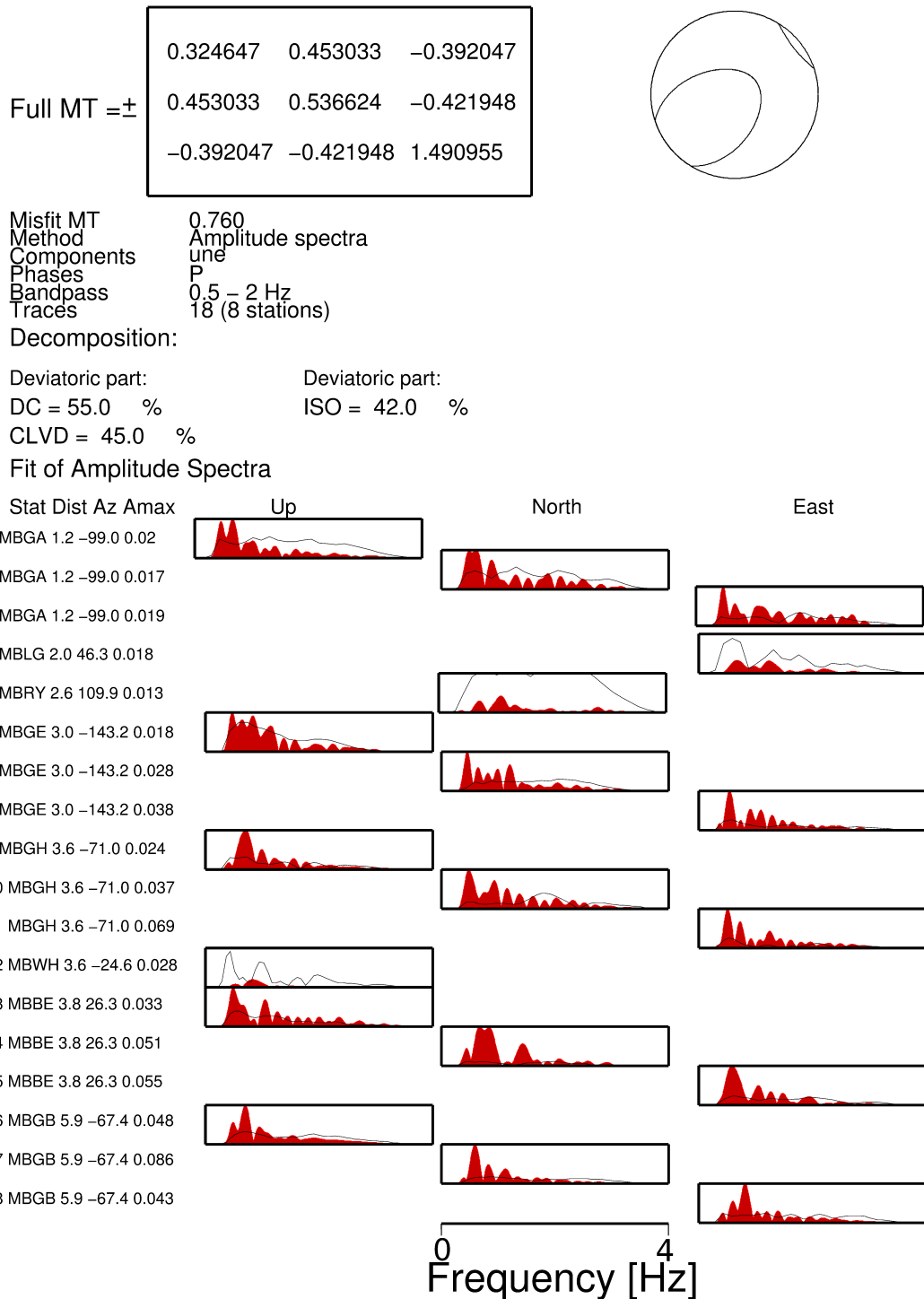


Figure 6.23: MTI solution for the event recorded at 04:03:33 on 7th June 1997. The event epicentre was fixed to the active dome region, while the source depth was fixed to 1 km. The full moment tensor and its ‘beach ball’ representation for an inversion in the frequency range 0.5-2 Hz are displayed in the top section, while the frequency fit between model and data is plotted below.

07/06/97 - 04:03:33 - 1.5km

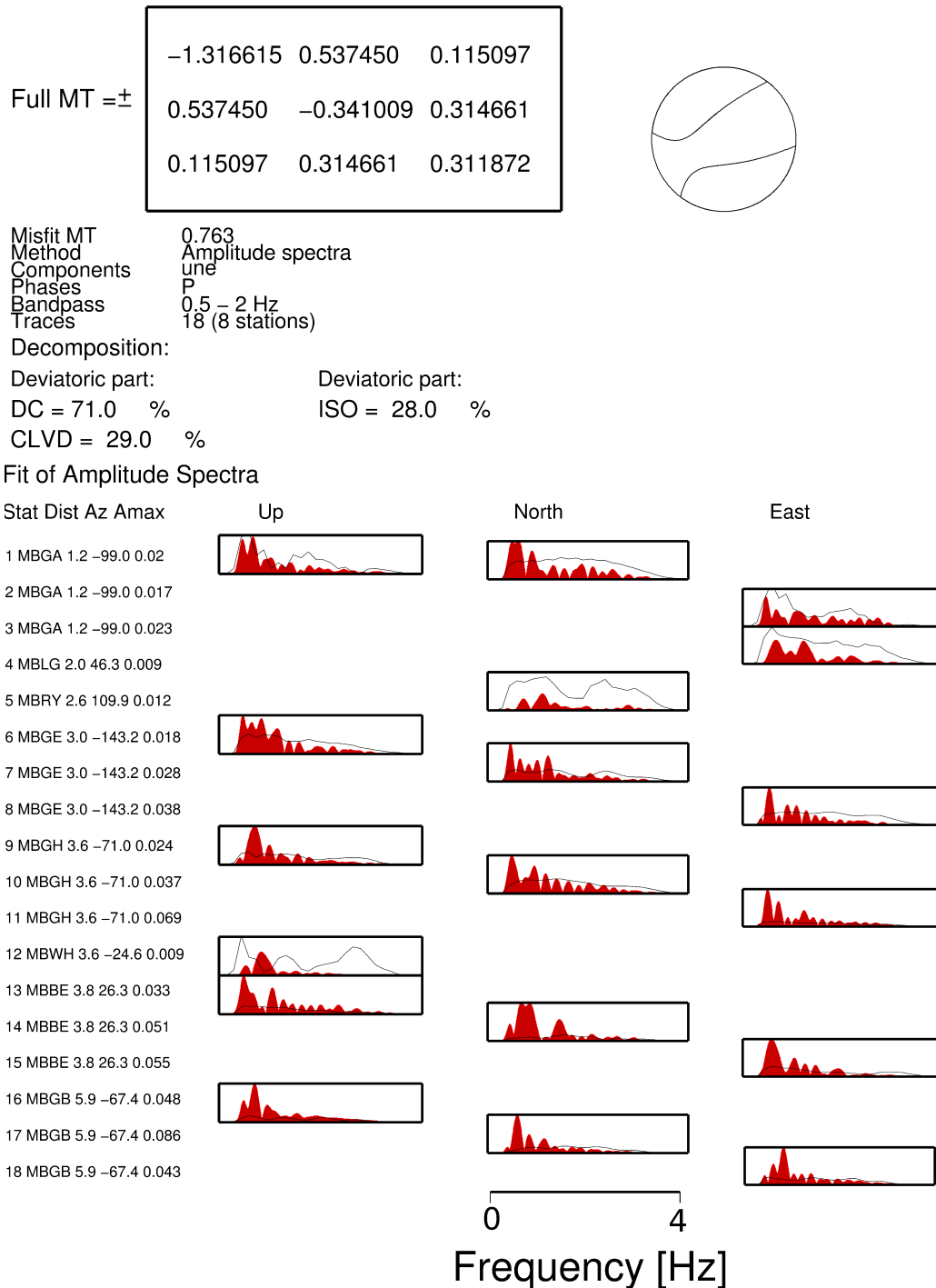
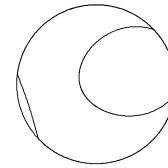


Figure 6.24: MTI solution for the event recorded at 04:03:33 on 7th June 1997. The event epicentre was fixed to the active dome region, while the source depth was fixed to 1.5 km. The full moment tensor and its ‘beach ball’ representation for an inversion in the frequency range 0.5-2 Hz are displayed in the top section, while the frequency fit between model and data is plotted below.

07/06/97 - 04:03:33 - 2km

Full MT = \pm

-0.238650	0.239938	0.246470
0.239938	0.415893	0.614176
0.246470	0.614176	0.863572



Misfit MT 0.818
 Method Amplitude spectra
 Components une
 Phases P
 Bandpass 0.5 - 2 Hz
 Traces 18 (8 stations)

Decomposition:

Deviatoric part: Deviatoric part:
 DC = 30.0 % ISO = 25.0 %
 CLVD = 70.0 %

Fit of Amplitude Spectra

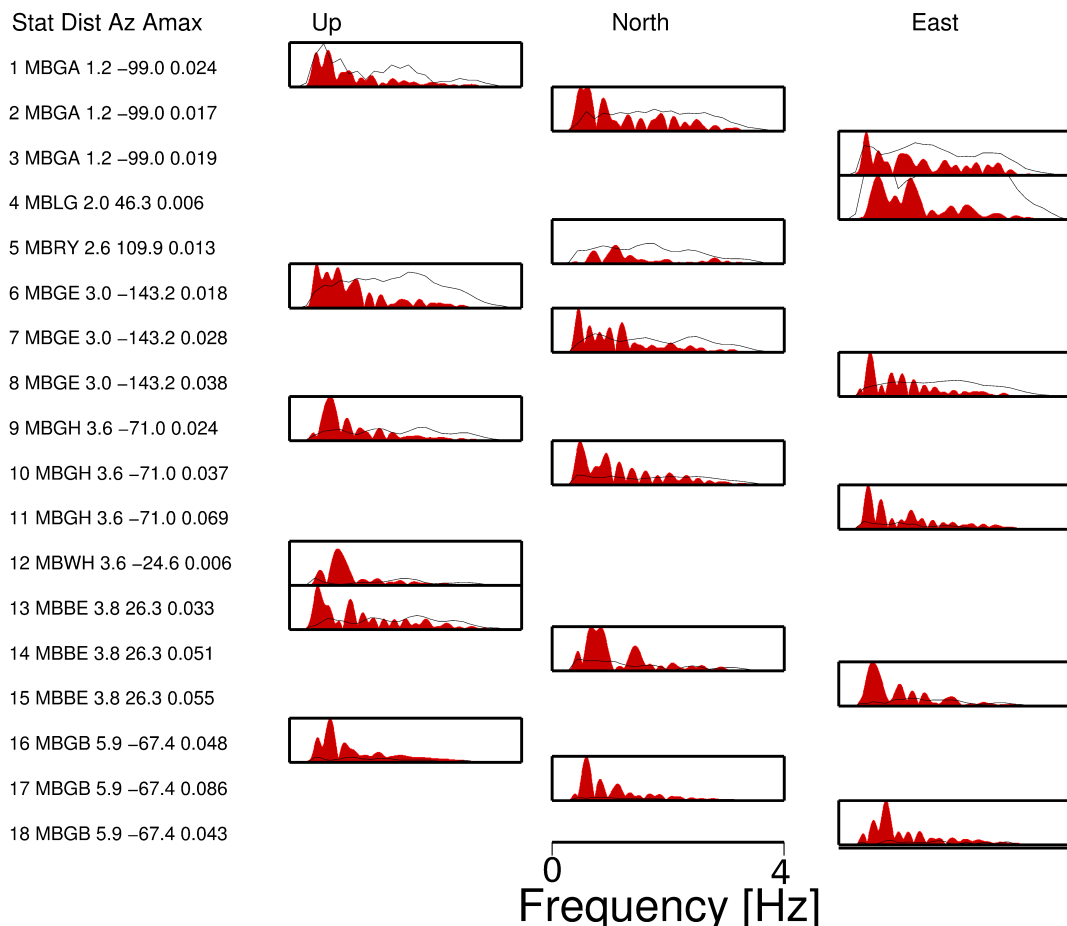


Figure 6.25: MTI solution for the event recorded at 04:03:33 on 7th June 1997. The event epicentre was fixed to the active dome region, while the source depth was fixed to 2 km. The full moment tensor and its ‘beach ball’ representation for an inversion in the frequency range 0.5-2 Hz are displayed in the top section, while the frequency fit between model and data is plotted below.

MT solution - 22/06/1997 19:10:04

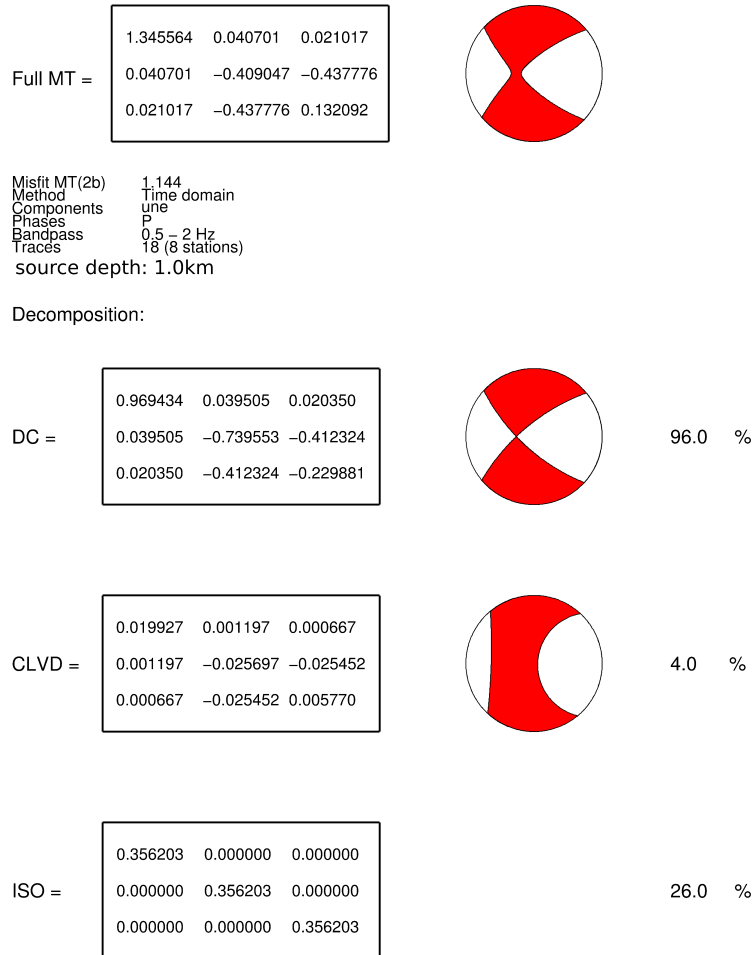


Figure 6.26: MTI solution for the event recorded at 19:10:04 on 22nd June 1997. The event epicentre was fixed to the active dome region, while the source depth was fixed to 1 km. The full moment tensor and its ‘beach ball’ representation for an inversion in the frequency range 0.5-2 Hz are displayed in the top section of the figure, while the suggested decomposition is shown in the bottom section of the figure. The misfit value corresponds to the time domain inversion step (step 2), and, therefore, is higher than the overall inversion misfit.

MT solution - 22/06/1997 19:10:04

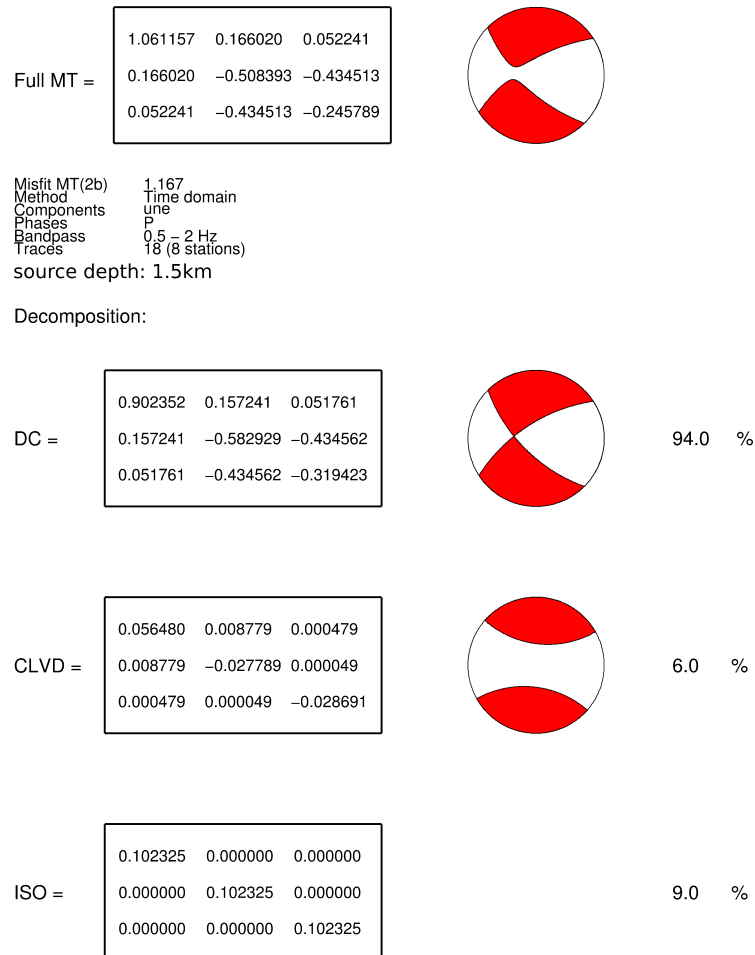


Figure 6.27: MTI solution for the event recorded at 19:10:04 on 22nd June 1997. The event epicentre was fixed to the active dome region, while the source depth was fixed to 1.5 km. The full moment tensor and its ‘beach ball’ representation for an inversion in the frequency range 0.5-2 Hz are displayed in the top section of the figure, while the suggested decomposition is shown in the bottom section of the figure. The misfit value corresponds to the time domain inversion step (step 2), and, therefore, is higher than the overall inversion misfit.

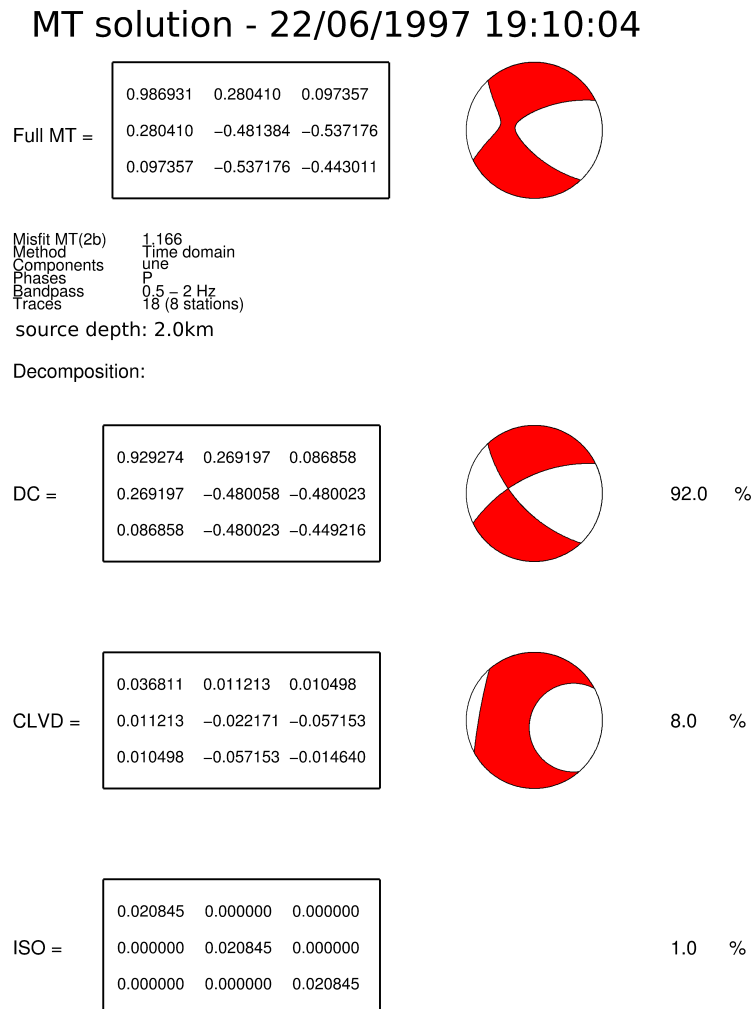


Figure 6.28: MTI solution for the event recorded at 19:10:04 on 22nd June 1997. The event epicentre was fixed to the active dome region, while the source depth was fixed to 2 km. The full moment tensor and its ‘beach ball’ representation for an inversion in the frequency range 0.5-2 Hz are displayed in the top section, while the suggested decomposition is shown in the bottom section of the figure. The misfit value corresponds to the time domain inversion step (step 2), and, therefore, is higher than the overall inversion misfit.

this study to provide alternatives to the point source assumption in MTIs, the findings reported in Chapters 2, 4 and 5 will be used to interpret the MTI inversion results in the context of spatially extended source mechanisms. To do this, the MTI results from the example events of this chapter will be compared to the results obtained from inversions of the synthetic spatially extended source data in Chapter 5.

6.5 Comparison with inversions of synthetic data

Due to different station distributions, a direct comparison of synthetic and real data inversion results is not possible. However, the radiation patterns of ring fault and dike derived in Chapter 3, the consideration of changes in P-waveforms and amplitudes with receiver azimuth and distance (Chapter 4), and the moment tensor inversions using an ideal station distribution still provide an understanding of the moment tensor solution under non-ideal conditions. While much less constrained, the overall pattern of MTI results will not differ crucially with changing, non-ideal station distributions as found on Montserrat. Additionally, the inversion procedure carried out in the frequency bandwidth 0.5-2 Hz appears to produce lower MTI misfit values; this is, however, mostly due to the loss of signal during filtering in this narrower frequency band compared to 0.5-4 Hz. To fully investigate the ideal filter for MTI a detailed study of the frequency content of the events under investigation would be necessary but was not included in this study. For that reason, only MTI results gained from inversions in the bandwidth 0.5-4 Hz will be considered in this section.

As discussed in Chapter 6.4, moment tensor inversion results of the LF event that was recorded on Montserrat on June 7th, 1997, strongly depend on the source depth defined for the inversion run and inversion bandwidth. A preferred MTI solution could only be identified following a thorough depth localisation study. However, given that inversions were carried out for a depth range at which most LF seismicity on Montserrat occurs (e.g. Rowe et al., 2004; Green, 2005), their interpretation will offer insights into the source mechanism. The suggested moment tensor for the 1.5 km fixed depth case resembles the solution obtained from the inversion of a single ring fault structure (Fig. 5.11). The three diagonal moment tensor components are negative for both cases, and hold opposite signs in the six remaining components. The decomposition of both solutions consists of a considerable isotropic component - 60% for the ring fault com-

pared to 63% for the real event - while the remaining deviatoric part is dominated by a CLVD mechanism (100% compared to 93%). The outlined similarities lead to the conclusion that a spatially extended physical mechanism, and in particular seismogenic magma ascent in the conduit, could well be responsible for the observed seismicity of this event. However, the MTI solutions from the runs with 1 km and 2 km fixed depth do not reflect the same result.

The inversion results of the event that occurred at 19:10:04 on 22nd June 1997 indicate, with 13% to 15%, a lower isotropic contribution than in the previous case (Figs. 6.14, 6.15 and 6.16). The moment tensor component M_{xx} is positive in all three cases, while a sign change takes place for M_{yy} and M_{zz} . The moment tensor decomposition outlines that there is little energy on the shear components, and the CLVD component dominates the solution. This becomes particularly clear in case 1 (1 km fixed source depth). The CLVD component represents 95% of the deviatoric moment tensor. When compared to the MTI results of synthetic sources in Chapter 5, a clear link to one of the treated spatially extended sources is not obvious. Parallels between the full MT and that of the staggered RFs (Fig. 5.18) can be drawn. However, the suggested decompositions differ from each other. With moment tensor decompositions being non-unique, the staggered RF case still represents a contender as trigger of the observed LF seismicity. The possibility of a completely different MT solution should not be ruled out. Due to the poor azimuthal station distribution different interpretations cannot be ruled out. Taking first motion polarities of the event into account, a ring of compressional first motions surrounded by a ring of dilatational first motions further away from the source is conceivable, even though this is not represented in the current best model moment tensor solution.

Deviations in solutions can be due to various reasons such as the already mentioned station distribution. The first motion polarities discussed in Chapter 6.3 clearly outline the difficulty in defining clear nodal planes with the available station distribution. The gap in data to the SE of the active dome area allows numerous interpretations, with an ‘eye ball’ radiation pattern being entirely within the range of possibilities. Another major challenge to reaching accurate interpretations are inaccuracies of the velocity structure in the volcanic edifice. Seismic velocities in volcanic regions are great oversimplifications of the highly heterogeneous structure of the subsurface. The 1D velocity

model used in this study is no exception, and this needs to be kept in mind during interpretation of the results. Endeavours to improve the velocity model of Montserrat are under way, the SEA-CALIPSO experiment (Kenedi et al., 2010) being the most recent development.

When the MTI results are taken together with the limitations discussed in the previous paragraph, the difficulty of finding the trigger mechanism of LF volcanic seismicity becomes clear. The results analysed here have been interpreted in terms of a spatially extended source acting in depth, and the comparison with the forward modelled examples for extended sources demonstrates that these types of sources are valid alternatives for the interpretation of MTIs. However, only a better data coverage to the SE of the dome will provide a definite answer.

6.6 Summary

The possibility of a spatially extended source mechanism for LF seismicity has been investigated in a case study of 10 chosen low frequency events that were recorded in the weeks prior to the June 1997 dome collapse event on Soufrière Hills Volcano, Montserrat. The events were analysed in respect to first motion polarities of the P-wave, before moment tensor inversion results were interpreted assuming a spatially extended source mechanism.

The rose diagrams in Figs. 6.4 and 6.5 show a clear trend towards compressional first motions close to the source region and dilatational first motions at stations at greater distances from the dome area. In all but two cases a typical eye ball radiation pattern is possible, indicating a CLVD if linked to a point source mechanism. As proven in previous chapters this pattern can also represent a ring fault structure as source scenario. Based on the findings of this work and additional, supporting arguments regarding their geological feasibility (Thomas and Neuberg, 2012; Hautmann et al., 2009) provide perfect alternatives to the usually quoted point sources to explain the generation of LFs in the wider volcanological context.

Moment tensor inversion results of the chosen set of events yield high misfit values and show a range of full moment tensor solutions and decompositions across fixed source

depths and events (Chapter 6.4 and Appendix C). The gap in the receiver network to the SE of the active crater area of SHV complicates the identification of a distinct solution for a single event. Similarities between real events and synthetically computed, spatially extended sources could nevertheless be established. MTI results would improve with an improved station distribution, and would ultimately contribute towards narrowing down the possible source scenarios.

Chapter 7

Discussion and Conclusions

This study presents a quantitative investigation into the source mechanisms of low frequency volcano-seismic events. In particular, the analyses are concentrated on spatially extended sources as the possible origin of this type of seismicity, and to test if the point source assumption is sufficient for moment tensor inversions of LF volcanic seismic signals. A catalogue of spatially extended sources, such as ring fault structure and dike, have been derived. The findings of this thesis outline that advancing from point sources towards spatially extended sources has pivotal consequences on the properties of observed seismic events. Combining these novel observations shows that interpretations under the point source assumption are inadequate, and spatially extended sources must be taken into account in future. Therefore, this work introduces a number of possible source mechanisms to act as foundation for future interpretations of LF seismicity. In this chapter the main results and contributions of the project are summarised and their implications discussed, along with ideas for future work to extend and complement this study.

7.1 Implications of spatially extended sources for waveforms and amplitudes

Low frequency events are one type of seismic signal often observed in volcanic settings, and in many cases occur during a phase of accelerating seismic activity of a volcanic complex prior to major eruptions. Low frequency events have been recognised as valuable precursors of eruptions. Various endeavours to explain the dominant low frequency nature of LF signals have been made, their true excitation process, however, is still controversial. Generally, resonance in fluid-filled bodies and/or fluid movements

are deemed responsible for the occurrence of LFs (see Chapter 1.4). While a number of models contend to explain the generation of this particular type of seismicity, most of them fail to account for the longevity and tight clustering in swarms during, and beyond single eruption events. As Thomas and Neuberg (2012) point out, only a conceptual model based on seismogenic rupture of magma and associated resonance in conjunction with conduit geometry changes succeeds in explaining all the observed characteristics.

Therefore, this study has focused on the trigger mechanism of low frequency earthquakes on volcanoes grounded upon the conceptual model proposed by Neuberg et al. (2006). In their conduit model, LF seismicity is generated by the fracture of magma at depths where viscosity and strain rates along the conduit walls are high enough to result in brittle behaviour of the magma. In a quantitative numerical approach the wavefield generated by seismogenic fracturing of magma along the volcanic conduit walls has been modelled. Shallow source depths (1 km to 2 km below the surface), and short epicentral distances to seismic receivers (in the order of a few kilometres), gave reason to realise the source as spatially extended rather than as a point source approximation. The spatial extent of seismic sources in a volcanic setting is something which has not been considered before by authors investigating the source mechanisms of LFs on volcanoes.

In Chapter 2 of this study the ring fault, a modelling approach to seismogenic slip along the conduit walls, by combining and integrating over several point sources. It was shown that the advancement from point to spatially extended sources greatly influences the radiated P-wave amplitudes and waveforms, alongside the P-wave radiation pattern, as examined in Chapter 3. The spatially extended nature of the source, as assumed throughout this study, shows a P-wave radiation pattern that is independent of receiver azimuth (Chapter 3), and exhibits rotational symmetry along the depth axis. The resultant radiation pattern shows remarkable similarity to the CLVD P-wave radiation pattern, especially for first motions radiated above the source. CLVDs are the most common equivalent force system observed in the context of LF volcanic seismicity, and are often interpreted as a subhorizontal tensile crack (e.g. Aki and Richards, 1980; Chouet, 1996b; Iguchi, 1994). However, with shallow source depths and small source receiver distances, only the upper part of the radiated seismicity will be recorded in

volcanic settings, hindering a differentiation between ring fault and CLVD mechanisms. Consequently, first motion polarity investigations of LF seismicity should not be carried out assuming point source mechanisms only, as can be found in the literature (e.g. Iguchi, 1994). Instead, analysis should involve spatially extended sources such as the ones considered in this study. By doing so, first motion pattern interpretations of LF events as undertaken at many volcanoes, e.g. Montserrat (see Chapter 6) and Mount St. Helens (Waite et al., 2008), would lead to seismogenic magma ascent in the conduit as explanation for the observed radiation patterns.

Green and Neuberg (2006) showed that accelerated magma movement can be linked to observed deformation cycles through LF swarms, and that seismicity is only generated if significant magma movement takes place. By calibrating the link between observed waveform amplitudes and the amount of seismogenic slip occurring during an LF swarm, low frequency seismicity can be used to estimate magma ascent rates. This will enable a crucial step towards eruption forecasting. The differences in observed P-wave amplitudes, as outlined in this study, clearly show that the correlation between observed waveform amplitudes and slip rates is different for point and spatially extended sources. This underlines the importance of identifying the type of system under investigation. Ring fault P-wave amplitudes are greatly reduced in comparison to double couples or compensated linear vector dipoles (see Chapters 2 and 4). By incorrectly assuming a point source, these reduced amplitudes may lead to misinterpretations, and in particular underestimations of the amount of slip at depth, and therefore an underestimation of magma ascent rates. As shown in Chapter 2, the amount of slip along a cylindrical fault structure must be up to a factor of three times the slip required of a point source to result in the same maximum P-wave amplitude, assuming the same rigidity and area on which slip occurs. If disregarded, the differences in estimated slip will bring about pivotal consequences for eruption forecasting because they lead to significant underpredictions of magma flow rates in the volcanic edifice.

Additionally, the spatial extent of the sources examined in Chapter 2 introduces a time derivative to the observed P-waveforms. If disregarded, this would lead to further misinterpretations concerning the physical motion responsible for causing the observed seismicity in a way that e.g. seismogenic magma ascent would be misinterpreted as a first ascending, but then slumping magma column (see Fig. 7.1). To avoid an under-



Figure 7.1: Time derivative relationship btw. DC and RF. By advancing to spatially extended sources an extra time derivative is introduced in the displacement. This may lead to misinterpretation of magma ascent (step function) as initially ascending, but then stagnating (pulse) magma.

estimation of magma volume reaching the surface it is therefore crucial to identify the source nature, and take this possible effect into account when interpreting LF seismic data in future.

It should be mentioned here that these findings are based on a homogeneous modelling space, with the properties of the conduit material being the same as the properties of the host rock. This is obviously an unrealistic simplification of the system under investigation, and e.g. attenuation of two rock types (here: hot magma in the conduit, and a mix of solidified eruption products forming the volcanic flanks) will alter the observed P-wave amplitudes and shapes.

7.2 Source depth and implications on first motions

The P-wave radiation pattern for the spatially extended ring fault structure was derived in Chapter 3. It shows a rotational symmetry about the depth axis, and consists of a large compressional lobe directly above the source and an inversely polarised, dilatational lobe with the same amplitude below it. Due to shallow source depths of 1 km to 2 km typical at volcanoes, close proximity of the seismic network, as well as small (< 3) event magnitudes, only seismicity radiated at limited take-off angles will likely be detected, and recorded above the source only. In these areas, the observed radiation patterns of ring fault and CLVD source are remarkably similar, and their distinction is difficult under these conditions. Nonetheless, magma flow modelling (Neuberg et al., 2006; Thomas and Neuberg, 2012), field evidence (Tuffen et al., 2003, 2008) and experimental studies (Alidibirov and Dingwell, 1996; Dingwell, 1996; Kendrick et al., 2014) conclude that seismogenic slip along the conduit walls is the geologically more relevant

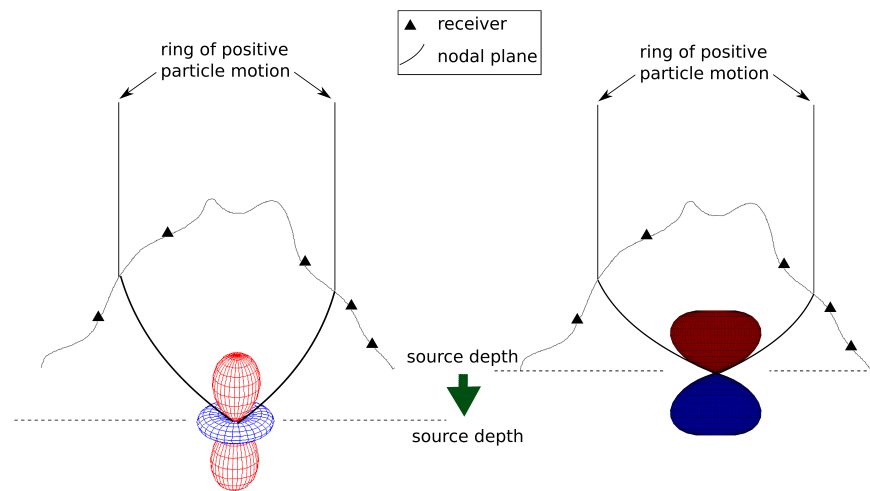


Figure 7.2: Schematic showing the dependence of the source depth on the areas with the same first motion polarities of RF and CLVD sources. Red indicates compressional, while blue indicates dilatational first motion. To yield the same radiation pattern the two sources must be located at different source depths.

and realistic model, and the ring fault approach should therefore be favoured over the CLVD.

For both CLVD and RF the nodal planes lie off the fault axes, and the transition from compressional to dilatational first motion is therefore dependent on the source depth of the event. This is demonstrated in Fig. 7.2, which schematically shows the change of compressional/dilatational first motions with source depth. From the nodal plane projection onto the volcanic edifice it becomes clear that first motions may be compressional at all seismic receivers, or a transition from compressional first motion in the centre to a ring of dilatational first motion at stations further from the top of the volcano may take place. It can also clearly be seen that an interpretation of radiation patterns resulting from both source scenarios may not succeed in distinguishing between the two. This is the case if the CLVD source is located deeper than the RF, to give the same nodal planes and first motions at all stations of the network (Fig. 7.2).

7.3 Subhorizontal tensile crack vs. conduit model

LF seismicity has been identified as key to understanding the physical processes that may lead to eruptions. Resonance of a fluid-filled conduit (Neuberg et al., 2006), crack (Chouet, 1996a), as well as magma wagging (Jellinek and Bercovici, 2011) explain the

low frequency coda of the observed events well. The study of this particular type of volcanic seismic signal has resulted in a number of observations whose interpretations allow further constraints on the actual trigger mechanism that starts the resonance itself. Neuberg (2000) investigated the clues for the source mechanism in a study based on Montserrat, and summarised the characteristics of a source mechanism for LF events as follows:

- The regularity of highly similar LF earthquakes during a swarm of activity hints at a common source mechanism within a source location not bigger than a few hundred metres.
- The re-occurrence of the same event families prior to several dome collapse events requires a non-destructive and repeatable source mechanism.
- The correlation between tilt measurements and LF seismic activity (inflation takes place during, and deflation takes place after LF swarms) evokes a link to the pressurisation of the volcanic system.

The physical mechanism to explain these observables is still highly disputed. Partial collapse of a steam-filled, subhorizontal crack (Waite et al., 2008) and seismogenic brittle failure of magma along the conduit walls (Neuberg et al., 2006) have been proposed for the generation of LF seismicity. The waveform characteristics of these two competing source models have, for the first time, been quantitatively compared in this work. In the following, I will discuss my findings in respect to depicting the actual trigger of LF seismicity at volcanoes, and their limitations will lead to suggestions for future endeavours in this area.

Both mechanisms, the subhorizontal tensile crack and seismogenic slip along the conduit walls, exhibit remarkably similar P-wave radiation patterns (Chapter 3). In both cases, the nodal planes lie off the fault axes, and the transition from compressional to dilatational first motion is therefore dependent on the source depth of the event. This is demonstrated in Fig. 7.2, which schematically shows the change in areas of compressional/dilatational first motions with source depth. From the nodal plane projection onto the volcanic edifice it becomes clear that first motions may be compressional at all seismic receivers, or a transition from compressional first motion in the centre to a ring of dilatational first motion at stations further from the top of the volcano may

take place, dependent on the depth at which the earthquake occurs. Difficulties in distinguishing between the two are further increased by small aperture seismic networks in volcanic settings, as well as uncertainties in absolute source depth estimates. Two examples of observed first motions of LF events are presented in Waite et al. (2008) and in Fig. 6.6 of this study. Due to their highly similar P-wave radiation patterns, both models can explain the observed constant first motion polarity across all stations. Waite et al. (2008) interpret the observed radiation pattern under the point source assumption only and conclude that a subhorizontal tensile crack is generating the LF events under investigation. Based on the findings of this study, I argue for revisiting these findings and to take the possibility of a spatially extended source as trigger mechanism into account. I demonstrate this in Chapter 6 where I interpret a very similar radiation pattern from an event recorded on Montserrat in terms of a spatially extended source as a generating mechanism. I show that the ring fault structure can explain the radiation pattern as well, and should therefore be considered in first motion polarity studies.

As shown in Chapter 2.3, ring fault and CLVD waveforms do not resemble each other. That is, while the spatially extended source generates Ricker (Ricker, 1953) shaped P-wavelets, a CLVD source produces 2-lobed Küpper (Küpper, 1985) P-waves. If the direct P-phase can be identified, the fundamental waveform differences of these two models could be used to separate these two source mechanisms. However, the discussed synthetic waveforms are a product of a chosen velocity structure. Volcanic complexes are highly heterogeneous, and the velocity model utilised in this study is a great simplification of the true host rock structure in volcanic settings. Deviations from the chosen velocity model will alter the waveforms, and unless our knowledge of the properties of the areas under investigation are improved, a direct comparison of the synthetic models in this study and real data examples is not feasible.

In addition to the waveforms themselves, maximum observed P-wave amplitudes for ring fault and CLVD sources differ greatly. At 5 km epicentral distance from the source, the amplitude differences feature an amplitude ratio of RF:CLVD=1:4.77 (Chapter. 2.3). If the nature of the source is known, magma ascent rates can be referred from measured amplitudes, and thus hold the key to successful eruption forecasting. If a spatially extended source is, however, mistaken as a point source, the discrepancies in

P-wave amplitudes will lead to an underestimation of the speed at which magma rises in the volcanic conduit, as discussed earlier in Chapter 2.5. Based on the amplitude ratios outlined in this study, individual volcanic systems can be calibrated by comparison to magma extrusion rates, and thus accurate estimates of magma flow rates can be obtained from interpreting LF seismicity. This will ultimately contribute towards identifying a critical magma ascent rate causing dome collapses (Hammer and Neuberg, 2009).

Moment tensor inversions have become a popular tool in resolving the apparent source mechanisms of LF seismicity on volcanoes. Most techniques work under the assumption of a point source in depth, and it was a key aim of this work to investigate whether this is a valid assumption in volcanic settings. Moment tensor inversions have therefore been carried out for synthetic waveforms representing both competing source scenarios (Chapter 5). MTIs of ring fault waveforms result in apparent CLVD source mechanisms, as well as wrong input moments. In a real case scenario, with unknown original input characteristics, the suggested ‘beach ball’ and moment tensor solution lead to the misleading conclusion of a subhorizontal tensile crack acting at depth. The failure of current MTI techniques to resolve spatially extended sources may be the reason why, in the literature (e.g. Chouet, 1996b; Waite et al., 2008), the trigger mechanism of LF seismicity is often found to be a subhorizontal crack. I thus strongly argue that it is inevitable that we advance towards moment tensor inversion techniques that can resolve spatially extended sources, to achieve a better understanding of the physical processes driving LF seismic activity on volcanoes, and ultimately resolve this source nature ambiguity.

This work has given evidence that seismogenic slip along the conduit walls can explain the observed P-wave characteristics and moment tensor inversion results for LF volcanic seismicity as well as a subhorizontal tensile crack. In fact, brittle failure of magma at multiple locations in the magma column is the only source mechanism that fulfils all requirements for the trigger mechanism of low frequency events, and should therefore be considered as alternative source model in the future.

7.4 Overview of conclusions

An entire set of spatially extended sources has been derived, to explain LF seismicity on volcanoes. These include: ring fault, dike, ring fault segments, two simultaneously acting ring faults, staggered sources, and a helix-like pattern. To provide a catalogue of potential source mechanisms for comparison with real data examples the P-wave radiation patterns as well as P-waveshapes and -amplitudes were investigated. The major conclusions are as follows:

- Extended sources have fundamentally different P-wave radiation patterns. Although modelled as a combination of double couple sources, the overall radiation patterns for ring faults and dikes are fundamentally different to those of a single double couple. The 3D P-wave radiation pattern of the ring fault source consists of a big lobe of compressional first motion directly above the source, and a smaller amplitude ring of dilatational first motion to its side. It shows a symmetry about the depth axis. In volcanic settings, seismic energy radiated in the upper hemisphere only is likely to be recorded. In this region, ring fault and CLVD radiation patterns strongly resemble each other. This may be the reason why LF seismicity is often believed to generate from a subhorizontal tensile crack, one of the interpretations of a CLVD mechanism. A ring fault structure, and hence seismogenic upwards movement of magma in the volcanic conduit, explains the observed seismicity equally well, and its consideration as a possible trigger mechanism of LFs is indispensable in future.
- Misinterpretation of time history through different P-waveforms. As shown in Chapter 2 the advancement from point source to the spatially extended ring fault introduces an extra time derivative. Incorrectly assuming a double couple source instead of the ring fault would result in the wrong time history of slip, meaning that the upwards movement of a magma batch, for example, would be misinterpreted as an initial upwards followed by a downwards movement of the magma.
- The shape of recorded P-waves changes with source geometry as well as receiver azimuth. The P-waveforms for all except single and double ring faults, which do not show a dependence of P-waveforms with receiver location, show a strong

dependence of the waveshapes with receiver azimuths. The shape of the recorded waveform depends on whether individual waveforms arrive at a given seismic station in phase and at what time. Ultimately, this is solely affected by the source diameter. Since this can only be defined for spatially extended sources, the point source approximation is not sufficient when linking observed seismic energy to subsurface physical processes.

- Underestimation of magma movement due to lower P-wave amplitudes. Linking event amplitudes to magma ascent rates is crucial for successful eruption forecasting. Point and extended source models yield great differences in observed P-wave amplitudes, leading to remarkable differences when interpreted as amount of slip and slip rates. In particular, observed amplitudes yield an underestimation of actual slip by more than a factor of 3 if interpreted as point source when in reality a spatially extended source acts at depth. The calibration of observed event amplitudes and corresponding magma ascent rate thus depends on the source nature, and advancing from point to spatially extended sources will contribute to finding an ascent rate threshold beyond which a dome collapse event is likely.
- MTI of spatially extended sources under the point source assumption. Classic moment tensor inversions assume point sources as source processes, and can therefore not resolve the source geometry of the here proposed spatially extended sources. Inversions can, however, determine the amount of error that is introduced into the solution, as well as what consequences this may have with regards to interpretations of inversion results, if the original underlying source process was unknown. The inversion results obtained for spatially extended sources clearly stress that it is not sufficient to assume a point source nature of the processes involved to generate the observed seismicity. If the true trigger mechanism was unknown, moment tensor inversions would lead to incorrect source geometries and input moments. In all cases, an underestimation of the original seismic moment occurs. This underestimation consequently leads to an underestimation of magma flow rate at depth, which can have severe implications for eruption prediction.

7.5 Future Work

This work provides a quantitative approach to spatially extended source mechanisms generating volcanic LF seismicity. To improve existing eruption forecasting tools with the help of the advancements towards a magma flow meter in this thesis, future endeavours should include:

- Investigating the deformation signal of spatially extended sources. A detailed modelling approach of the deformation signal generated by spatially extended sources such as the ring fault structure and a comparison to the findings of this study may yield an explanation of the link between observed tilt/deformation signals and LF seismic activity as described in 1.4.2.
- Identification of an ideal station distribution to distinguish between different spatially extended sources. This study showed that waveforms and -shapes of the ring fault structure are independent of receiver azimuth, while other spatially extended sources such as ring fault segments or helix-like structures do exhibit azimuthal dependence on their P-wavefield. An in-depth investigation in the changes of waveforms and -shapes with azimuth of all sources considered in this thesis may lead to recommendations for volcano observatories on ideal station distributions to differentiate between different source mechanisms.
- The study of other wave phases. While this study has concentrated on the P-wave radiation patterns, waveforms and amplitudes of spatially extended sources, the consideration of the S-phase as well as surface waves may prove useful in future. Possible differences of other wave phases between competing source mechanisms may contribute to resolving the source mechanism ambiguity.
- The study of combined excitation and resonance processes. To solve the unknowns of LF seismic signals it is inevitable to study the excitation processes together with the subsequent resonance. Future endeavours of both, the excitation and resonance parts of the signals, will show if the two can be distinguished and therefore allow insights into different physical processes in depth. It should be mentioned that noise in the signal will likely complicate this as it may be of the same magnitude as the signal of interest itself. The ability of isolating the signal from noise is therefore crucial and should be a focus of future investigations.

- The effects of magma properties on seismic wave propagation in the conduit near field, as well as on attenuation and amplitude decay. This work has concentrated on seismic wave propagation in the far field only. Due to the trend towards installation of seismic receivers in very close proximity to the crater regions of volcanic edifices, the additional study of the near field effects will give insight into the expected wavefields. The combination of the findings of this study and the near field effects this would cover all areas at which seismic receivers commonly record LF seismicity.
- The replacement of MTI of simple fault geometries by numerical models of motion on irregular faults and kinematic sources. This has already been implemented in earthquake seismology, and first undertakings to adapt these techniques into volcano seismology have been taken recently (e.g. Cesca et al., 2010; Cesca and Heimann, 2013). Full 3D relative motions of single fault elements should consider shear as well as tensile opening, leading to an advancement towards moment tensor densities from the common moment tensor description.
- The calibration of magma ascent rates. It was shown here that the commonly used link between observed amplitudes and slip occurring in depth does not hold true for spatially extended sources. By taking estimations of extrusion rates, degassing, and deformation into account in addition to the information obtained from seismic observations, individual systems can be calibrated. That is, an accurate link between observed seismic amplitudes and amount of slip may be found to ultimately successfully estimate magma flow rates in depth from seismicity.

Appendix A

Seismometer locations and responses

A.1 Seismometer and digitiser specifications

In 1997, the seismic network on Montserrat consisted of 5 Güralp CMG-40T broadband, and 3 single component, Integra LA100 shortperiod seismometers. Table A.1 shows the station names, their LAT/LON coordinates, corresponding instrument type, as well as digitiser specifications.

A.2 Signal restitution

Any recorded seismic signal is an altered representation of the true motion of the ground. The recorded signal is a bandpass filtered, differentiated version of the true ground displacement, $u(t)$. Which bandpass is applied depends on the instrument, and is described by the instrument response, $i(t)$. The recorded signal is thus the differentiated convolution (*) of the original motion with the instrument response:

$$v_{\text{data}} = \frac{d}{dt}[u(t) * i(t)]. \quad (\text{A.1})$$

By digitising the signal, true velocities are further converted into counts. In a first step to retrieve true ground motions, a conversion from counts into velocities must be carried out, dependent on the digitiser rate (given in Table A.1). The instrument response can then be removed through deconvolving the recorded signal with the instrument response, to obtain a ‘corrected’ seismogram (e.g. Zhu, 2003). This operation is often ignored, or carried out erroneously, and in the following I would like to provide a ‘How-to’ manual to elucidate potential causes for confusion when trying to obtain true motion seismograms from recorded signals.

Station	Instrument	Lat. (°N)	Lon. (°W)	Gain (vm^{-1}s)	Digitiser Rate (ct μV^{-1})
MBBE	Güralp CMG-40T	16.7435	62.1602	800	1.00
MBGA	Güralp CMG-40T	16.7102	62.1885	800	1.00
MBGB	Güralp CMG-40T	16.7324	62.2278	800	1.00
MBGE	Güralp CMG-40T	16.6900	62.1937	800	1.00
MBGH	Güralp CMG-40T	16.7226	62.2086	800	1.00
MBLG	Integra LA100	16.7250	62.1623	462	1.00
MBRY	Integra LA100	16.7039	62.1532	462	1.00
MBWH	Integra LA100	16.7422	62.1909	462	1.00

Table A.1: The Montserrat seismic network as deployed in 1997. 5 broadband Güralp CMG-40T (30 s corner frequency) and 3 short-period Integra LA100 1Hz instruments were deployed. Stations are referred to by a code. The gain is the voltage of the seismometer for a 1ms^{-1} seismic velocity. The digitiser rate is the number of counts which represent a $1\mu\text{V}$ output.

Integra LA100		Güralp CMG-40T (30 s)	
Zeros	Poles	Zeros	Poles
0	-0.7+0.7i	0	-80
0	-0.7-0.7i	0	-160
	-26.19834+26.19834i		-180
	-26.19834-26.19834i		-0.02356+0.02356i
			-0.02356-0.02356i
Normalisation factor A_0 at 1Hz		Normalisation factor A_0 at 1 Hz	
8626.35707		2304000	

Table A.2: The instrument responses for the Güralp CMG-40T (30 s) and Integra L100 instruments expressed in poles and zeros as velocity in Hz.

Based on the convolution theorem, convolution in the time domain corresponds to multiplication in the frequency domain, and the desired deconvolution can hence be written as:

$$U(f) = \frac{V_{\text{data}}(f)}{I(f)}. \quad (\text{A.2})$$

The instrument response of a system is defined by the Fourier transform of the output divided by the Fourier Transform of the input:

$$T_{\text{vel}}(i\omega) = \frac{\text{Output}(i\omega)}{\text{Input}_{\text{vel}}(i\omega)}, \quad (\text{A.3})$$

where $\omega = 2\pi f$ is the angular frequency. Input and output of a system can be fully described by the poles and zeros of a given transfer function. The poles and zeros for both types of seismometers in use on Montserrat in 1997, as provided by the manufacturer, are summarised in Table A.2. Here, poles and zeros are given in the velocity domain and in units of Hz.

Instrument response conversion from Hz to Radian

Some operations may require poles and zeros input in radians per second (rad/s). The conversion from Hz to rad/s is carried out by a multiplication of 2π (Scherbaum, 2001):

$$\begin{aligned} \text{Pole}(\text{rad}) &= \text{Pole}(\text{Hz}) \times 2\pi \\ \text{Zero}(\text{rad}) &= \text{Zero}(\text{Hz}) \times 2\pi \end{aligned}$$

The difference in the number of poles and zeros, and therefore the difference between 2π conversion factors in the nominator and denominator, must be taken into account when converting the calibration factor A_0 to radian/s. The right conversion is therefore:

$$A_0(\text{rad}) = A_0\text{Hz} \times (2\pi)^{(\text{No.Poles}-\text{No.Zeros})}$$

For the two seismometers used within this study, a conversion from Hz to radian/s gives a new set of poles and zeros for each instrument, and the values can be found in Table A.3.

Integra LA100		Güralp CMG-40T (30s)	
Zeros	Poles	Zeros	Poles
0	-4.39823+4.39823i	0	-502.65482
0	-4.39823-4.39823i	0	-1005.30965
	-164.6090+164.6090i		-1130.97336
	-164.6090-164.6090i		-0.14803+0.14803i
			-0.14803-0.14803i
Normalisation factor A_0		Normalisation factor A_0	
54201		5.71507×10^8	

Table A.3: The instrument responses for the Güralp CMG-40T (30s) and Integra L100 instruments expressed in poles and zeros as velocity in radian/s.

Integra LA100		Güralp CMG-40T (30s)	
Zeros	Poles	Zeros	Poles
0	-4.39823+4.39823i	0	-502.65482
0	-4.39823-4.39823i	0	-1005.30965
0	-164.6090+164.6090i	0	-1130.97336
	-164.6090-164.6090i		-0.14803+0.14803i
			-0.14803-0.14803i
Normalisation factor A_0		Normalisation factor A_0	
54201		9.09583×10^7	

Table A.4: The instrument responses for the Güralp CMG-40T (30s) and Integra L100 instruments expressed in poles and zeros as displacement in radian.

Instrument response conversion from velocity to displacement

Equivalent to the expression in the velocity domain (Equation A.3), the frequency response of a system can be described in terms of displacement (Scherbaum, 2001):

$$T_{\text{disp}}(i\omega) = \frac{\text{Output}(i\omega)}{\text{Input}_{\text{disp}}(i\omega)}, \quad (\text{A.4})$$

Velocity and displacement inputs in the time domain are linked through differentiation of the latter, which is equivalent to multiplication of the displacement input spectrum with $i\omega$ in the frequency domain. Doing this gives the frequency response in terms of displacement, expressed by displacement input:

$$T_{\text{disp}}(i\omega) = T_{\text{vel}}(i\omega) \times i\omega \quad (\text{A.5})$$

This operation is equivalent to adding one more zero to the pole-zero representation (Scherbaum, 2001), and the resulting instrument specifications for the Montserrat instruments expressed in displacement and in radians are: Note that the normalisation factors A_0 has changed due to a change in the number of zeros from two to three zeros.

Comp	Seis Vel Output [V/m/s]	Dig cal- ibration [μ V/count]	dis \rightarrow seis [counts/nm]	vel \rightarrow seis [counts/nm/s]	seis \rightarrow dis [nm/counts]	seis \rightarrow vel [nm/s/counts]
E	2 \times 399.8	1	5.024	0.7996	0.1990	1.2506
N	2 \times 400.4	1	5.0316	0.8008	0.1987	1.2488
Z	2 \times 399.7	1	5.0228	0.7994	0.1991	1.2509
Z	2 \times 462	1	5.8057	0.9240	0.1722	1.0823

Table A.5: Step by step determination of the calibration factors to obtain true amplitude velocity and displacement seismograms from uncorrected traces. The values in the top three rows correspond to the Güralp CMG-40T (30 s) broadband instruments, while the bottom row represents the calibration factors for the single component Integra L100.

If the recorded signal frequencies of interest are entirely within the passband of the instrument, signal restitution is not required. Instead, a multiplication of the signal with a scaling factor is sufficient to obtain true amplitude seismograms. The calibration factor takes into account both, seismometer and digitiser, effects. The seismic velocity output for each component of a seismometer, as well as digitiser calibration factors are provided by the instrument manufacturer, and the values for the MVO 1997 seismometers can be found in Table A.5.

Within the passband, a recorded signal is converted from units of counts to Volts by multiplication with a, for each digitiser unique, conversion factor. Subsequent division by the seismometer velocity output gives the calibration factor. A recorded velocity signal can then be multiplied by this calibration factor to obtain a ‘corrected’, true amplitude velocity seismogram. If displacements are favoured over velocity seismograms, the initial, uncorrected velocity trace should be integrated and multiplied by a different calibration factor. Taking the integration into account, the calibration factor in this case can be determined by multiplying the previously calculated factor (for velocity true amplitudes) by 2π . The integrated seismometer output can then be multiplied by this calibration factor to gain a true amplitude displacement seismogram, respectively. A table of the forward problem and displacement and velocity calibration factors is provided here (Table A.5).

Appendix B

Earthquake location tables

B.1 Absolute locations of long period earthquakes

B.1.1 Methodology

The Fortran based software package Hypoinverse-2000 was used to provide estimates of earthquake hypocentres for a chosen set of seismic data from Montserrat. It is the latest of a series of similar single event location algorithms provided by the USGS (Klein, 2002). Hypo-2000 searches for hypocentres using Geiger's method, the linearisation of the travel time equation in a first order Taylor series, to minimise the rms residuals between observed and theoretical travel times.

The accuracy of this technique is controlled by many factors, such as azimuthal coverage of seismic station network, available phases, arrival time reading accuracy, and knowledge of the velocity profile in the area (Gomberg et al., 1990). Absolute location techniques are highly sensitive to velocity changes, and therefore location estimates strongly depend on the quality and choice of the velocity model. This study adapts the widely used MVO 5 layer velocity model as outlined in Table 6.1. For all earthquakes in the analysed set, P- and S-phase arrival times were manually picked and assigned a quality factor of 0-3 according to estimated measurement errors of 0.05, 0.1, 0.15, and 0.2 s for P phases, and 0.1, 0.175, 0.2, and 0.3 s for S phases, respectively. Furthermore, correlations between estimated solutions cause trade-offs between interlinked parameters, e.g. the trade-off between origin-time and depth (e.g. Shearer (1999, p.87)), which is strongly pronounced by the ring shaped station configuration of the Montserrat seismic network (Fig. 6.1).

B.1.2 Results

The optimised picks of P- and S-phases for all events and stations provided the input into Hypo-2000, together with the MVO velocity model. The resulting hypocentral locations can be seen in Figure B.1 and a detailed list of all results is shown in Table

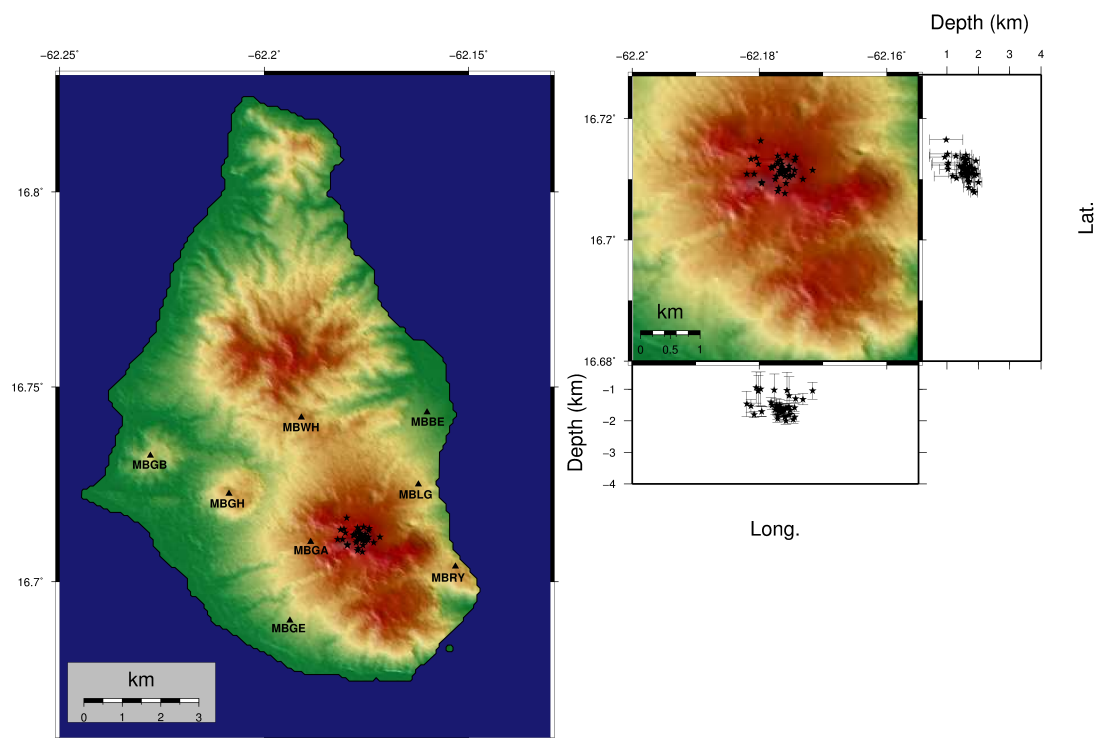


Figure B.1: Hypocentral location results for a set of 45 earthquakes using the MVO 1D velocity model (Table 6.1). All earthquakes occurred on the two days prior to a major dome collapse event of SHV on 25nd June, and belong to one event family (cross correlation coefficient > 0.7).

B.1. All 45 events plot within the summit area of Soufrière Hills Volcano, with a maximum horizontal spread of 1100 m. Source depths vary from 940 km to 2000 m, with a strong cluster at just below 1500 m. The mean rms travel-time residual is 0.09 s and yields maximum vertical errors of ± 590 m, with 36 events having a vertical error of or smaller than ± 200 m.

The earthquake cluster shows consistently smaller errors than the shallower events, indicating more precise location estimates for the events in that depth range.

Table B.1: Absolute location results for a set of 45 long period events that occurred at SHV on 24th and 25th June 1997, using the MVO 1D velocity model.

Date/Time	stations	Lat.	Long.	Depth (km)	ERZ (km)	RMS res. (s)
24/06/97 12:13	8	16.7163	-62.1798	0.98	0.53	0.08
24/06/97 12:14	8	16.7108	-62.1808	1.80	0.10	0.09
24/06/97 12:15	8	16.7115	-62.1763	1.68	0.14	0.07
24/06/97 12:16	8	16.7131	-62.1766	1.67	0.18	0.07
24/06/97 12:33	8	16.7140	-62.1756	1.03	0.57	0.10
24/06/97 12:34	8	16.7105	-62.1760	1.88	0.15	0.08
24/06/97 12:37	7	16.7135	-62.1805	0.94	0.50	0.13
24/06/97 12:42	8	16.7121	-62.1753	1.56	0.20	0.06
24/06/97 12:52	8	16.7116	-62.1755	1.59	0.14	0.06
24/06/97 13:09	8	16.7105	-62.1773	1.49	0.20	0.09
24/06/97 13:10	8	16.7108	-62.1766	1.64	0.15	0.07
24/06/97 13:30	8	16.7093	-62.1758	2.00	0.11	0.06
24/06/97 13:31	8	16.7100	-62.1731	1.31	0.18	0.09
24/06/97 13:32	8	16.7115	-62.1745	1.89	0.12	0.07
24/06/97 13:34	8	16.7116	-62.1753	1.81	0.15	0.08
24/06/97 13:34	8	16.7125	-62.1765	1.62	0.17	0.09
24/06/97 13:41	8	16.7131	-62.1745	1.58	0.13	0.09
24/06/97 13:46	8	16.7095	-62.1796	1.70	0.15	0.09
24/06/97 13:49	8	16.7111	-62.1761	1.62	0.16	0.07
24/06/97 13:49	8	16.7083	-62.1716	1.04	0.27	0.19

Continued on next page

Table B.1 – continued from previous page

Date/Time	stations	Lat.	Long.	Depth (km)	ERZ (km)	RMS res. (s)
24/06/97 13:50	8	16.7115	-62.1768	1.49	0.18	0.06
24/06/97 13:51	7	16.7105	-62.1773	1.60	0.13	0.10
24/06/97 13:53	8	16.7100	-62.1775	1.65	0.14	0.11
24/06/97 13:56	8	16.7093	-62.1796	1.70	0.17	0.11
24/06/97 13:57	8	16.7135	-62.1743	1.29	0.13	0.09
24/06/97 13:58	8	16.7138	-62.1771	1.61	0.19	0.08
24/06/97 14:01	8	16.7125	-62.1801	1.05	0.51	0.10
24/06/97 14:11	8	16.7076	-62.1760	1.87	0.11	0.10
24/06/97 14:13	8	16.7111	-62.1768	1.60	0.15	0.08
24/06/97 14:14	8	16.7133	-62.1813	1.52	0.20	0.11
24/06/97 14:19	8	16.7108	-62.1820	1.46	0.40	0.10
25/06/97 00:32	8	16.7105	-62.1771	1.31	1.08	0.40
25/06/97 00:32	8	16.7120	-62.1781	1.41	0.15	0.07
25/06/97 00:32	8	16.7128	-62.1771	1.93	0.11	0.06
25/06/97 00:42	8	16.7118	-62.1780	1.50	0.14	0.06
25/06/97 00:52	8	16.7085	-62.1770	1.70	0.17	0.10
25/06/97 00:52	8	16.7110	-62.1765	1.67	0.21	0.09
25/06/97 01:13	8	16.7120	-62.1765	1.73	0.13	0.07
25/06/97 01:14	8	16.7080	-62.1771	1.83	0.13	0.14
25/06/97 01:14	8	16.7121	-62.1776	1.02	0.51	0.08
25/06/97 01:16	8	16.7111	-62.1758	1.59	0.14	0.07
Continued on next page						

Table B.1 – continued from previous page

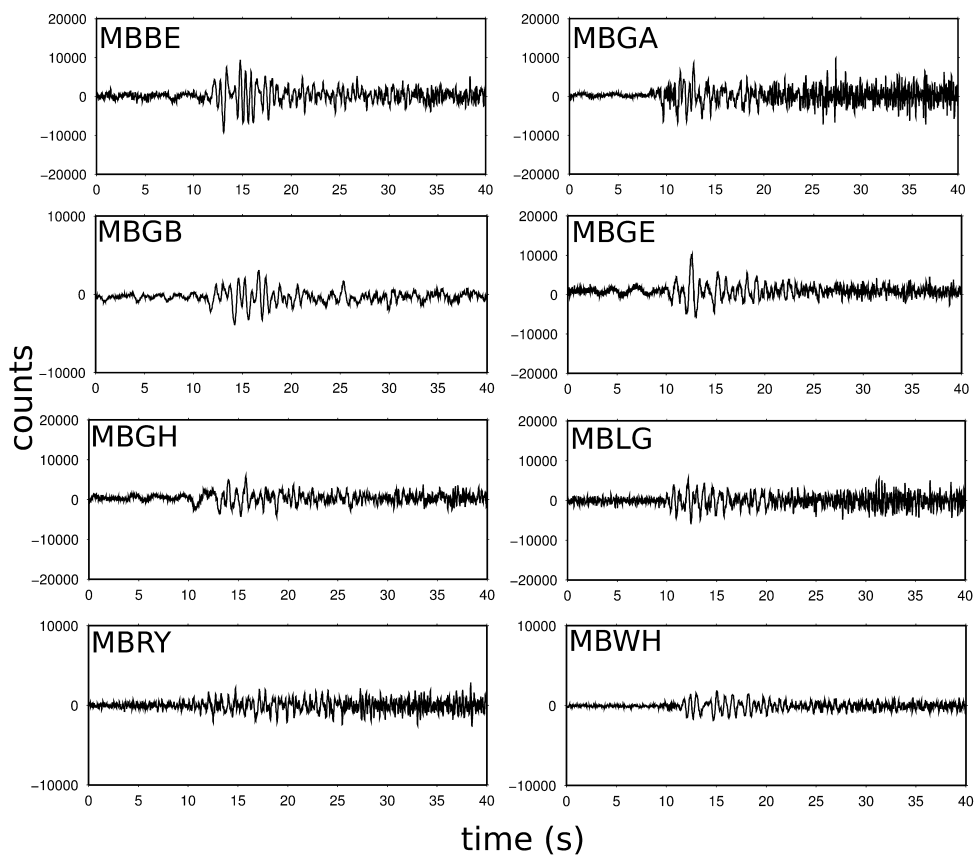
Date/Time	stations	Lat.	Long.	Depth (km)	ERZ (km)	RMS res. (s)
25/06/97 01:16	8	16.7106	-62.1751	1.66	0.15	0.07
25/06/97 01:18	8	16.7106	-62.1746	1.95	0.12	0.09
25/06/97 01:21	8	16.7116	-62.1761	1.65	0.13	0.10

Appendix C

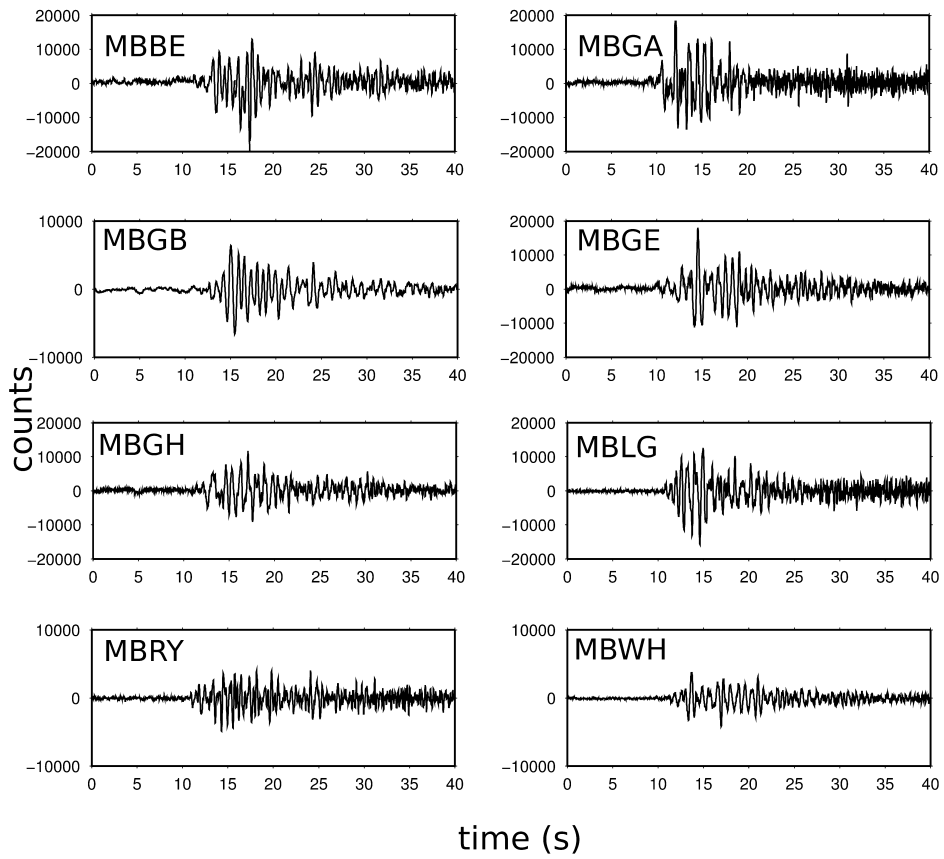
Supplementary seismograms and moment tensor inversion results

LF events for case study

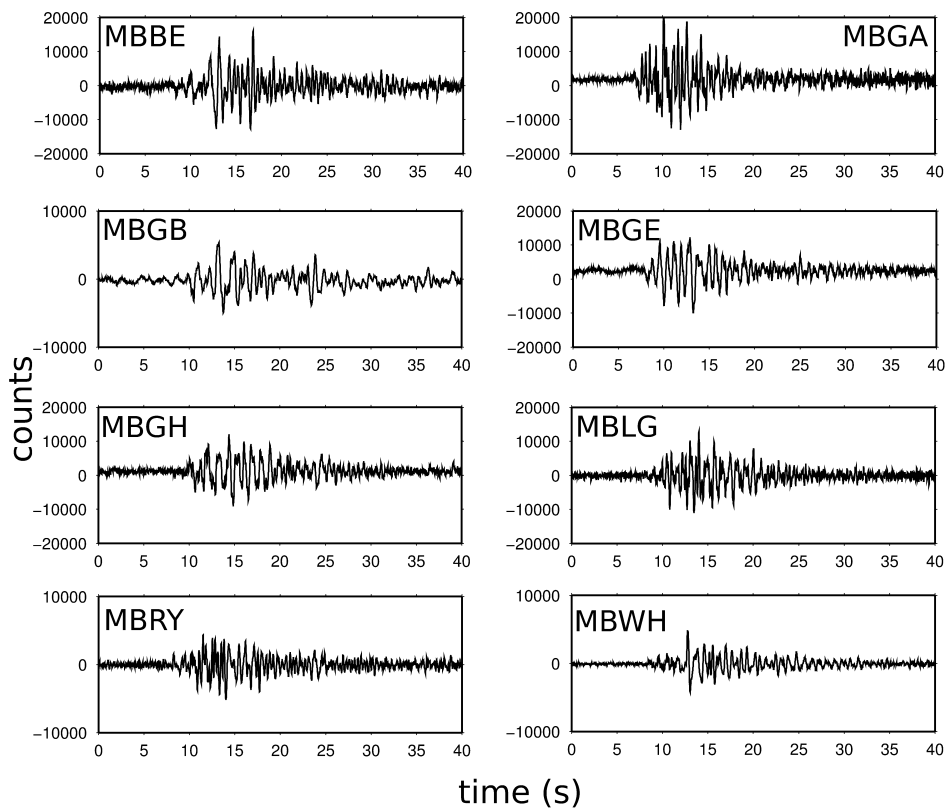
07/06/97 00:56:30



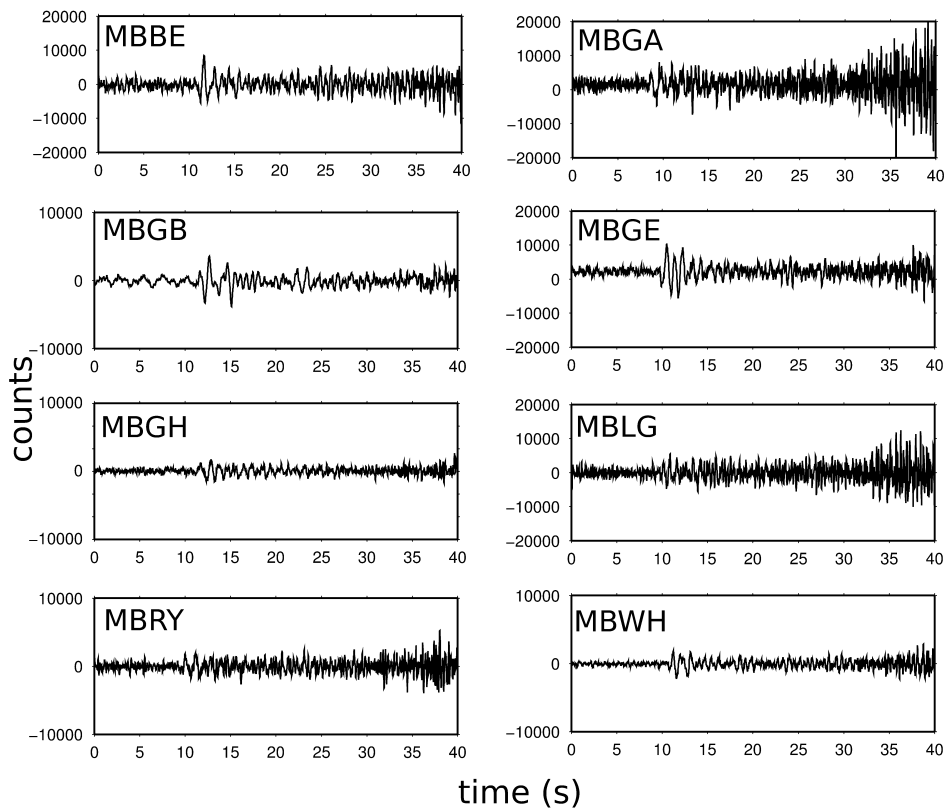
10/06/97 00:00:52



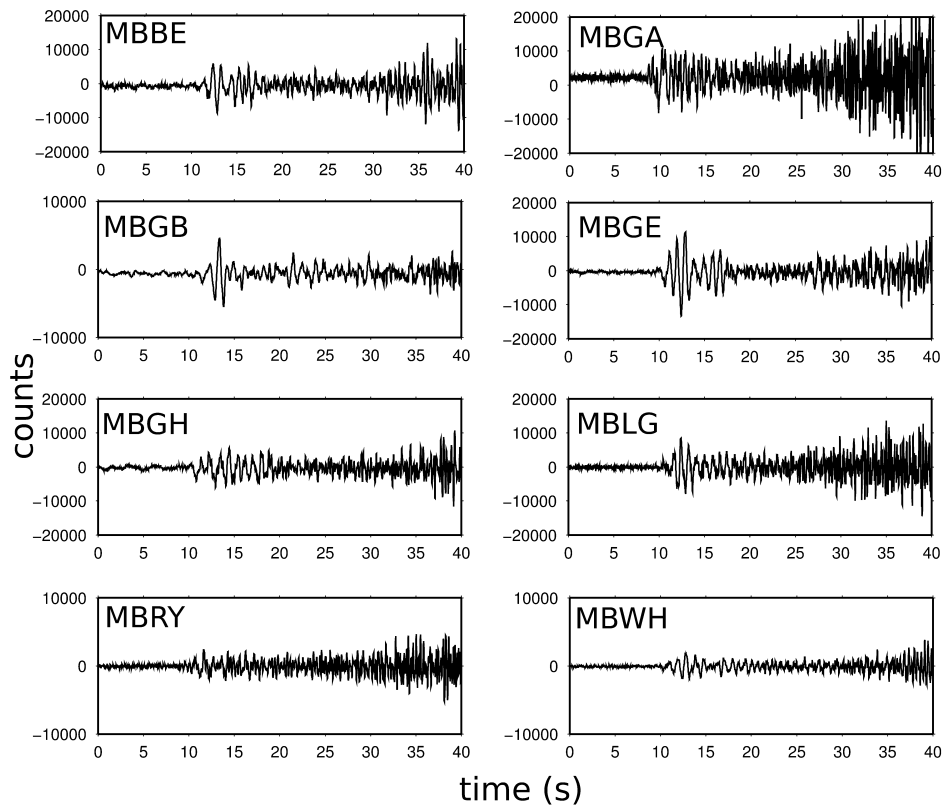
11/06/97 13:13:52



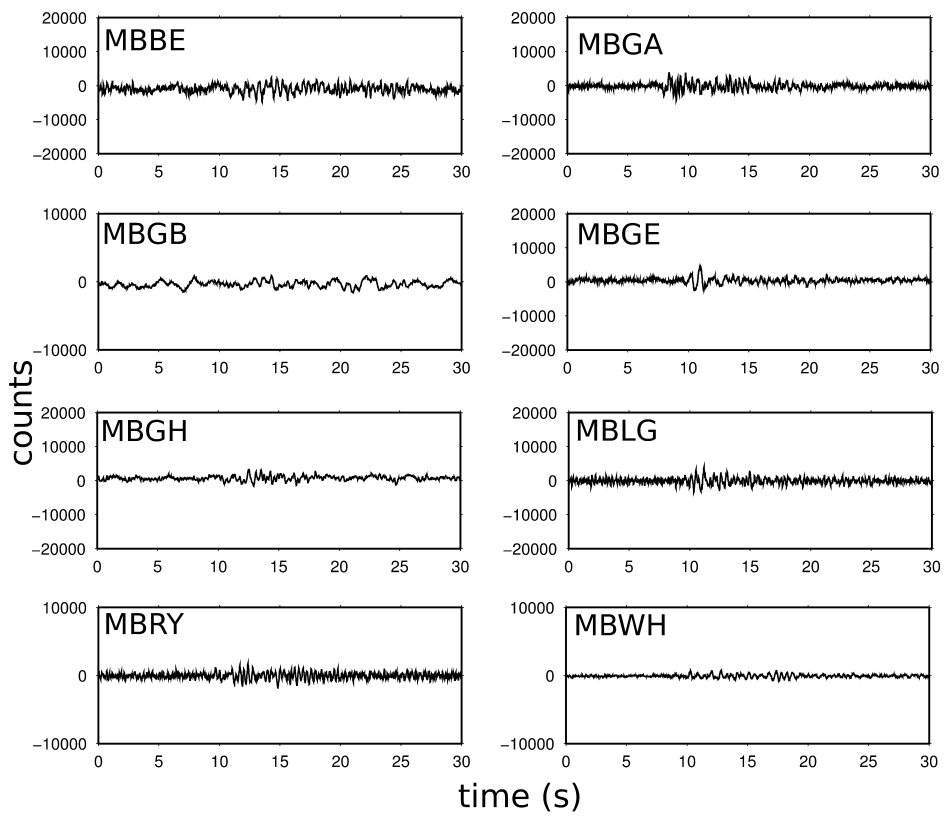
13/06/97 11:15:36



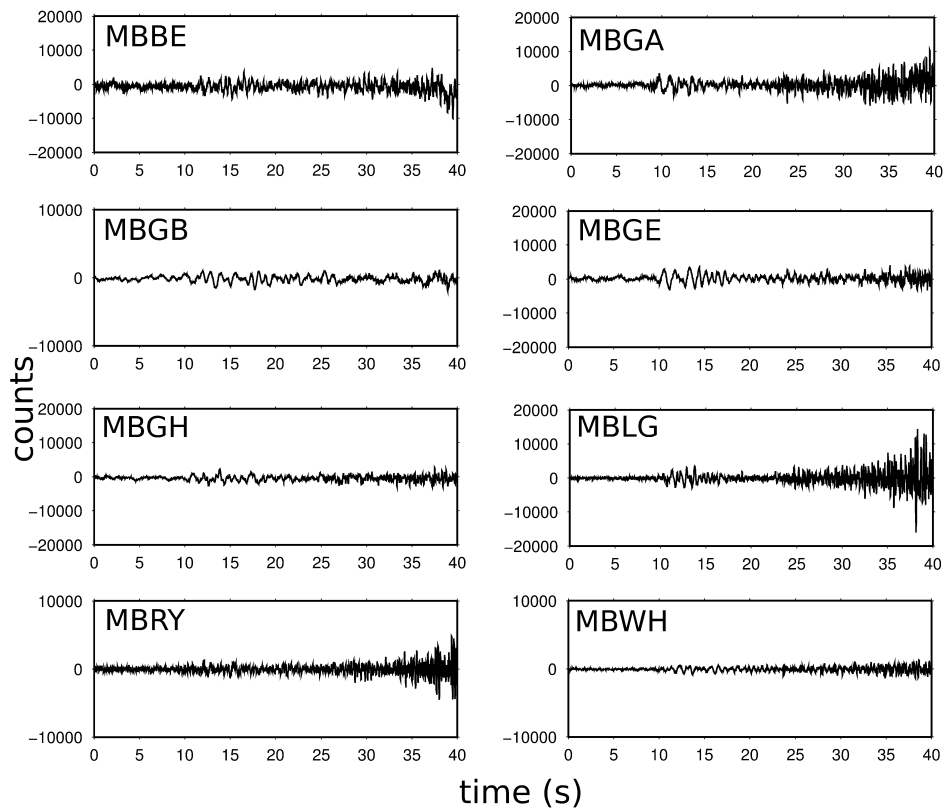
17/06/97 23:32:45



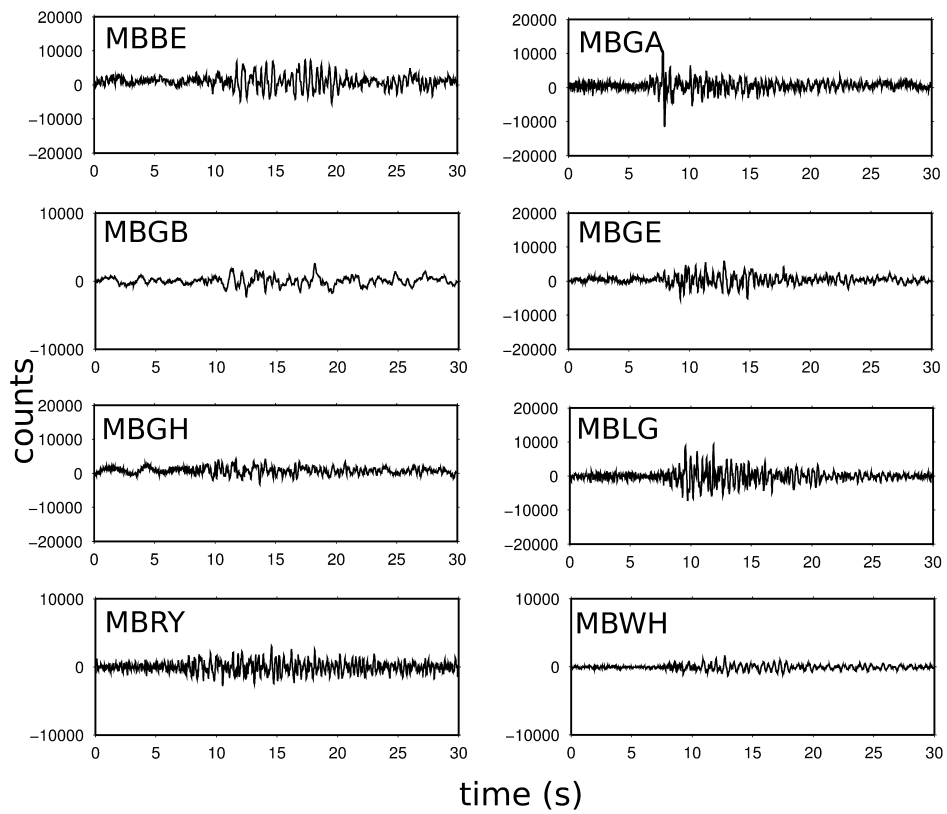
22/06/97 00:08:11



22/06/97 00:43:05



22/06/97 16:56:15

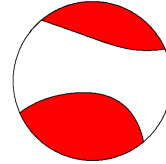


Inversion band width 0.5-4 Hz

MT solution - 07/06/1997 00:56:30

Full MT =

1.011153	0.560527	-0.901595
0.560527	-1.252928	0.036907
-0.901595	0.036907	-1.176211



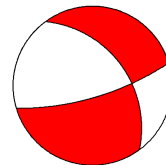
Misfit MT(2b) 1.172
 Method Time domain
 Components one
 Phases P
 Bandpass 0.5 - 4 Hz
 Traces 18 (8 stations)

source depth: 1km

Decomposition:

DC =

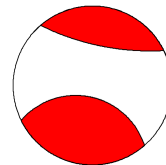
0.338213	0.179927	-0.262259
0.179927	-0.136780	0.167261
-0.262259	0.167261	-0.201433



24.0 %

CLVD =

1.145603	0.380600	-0.639337
0.380600	-0.643486	-0.130355
-0.639337	-0.130355	-0.502116



76.0 %

ISO =

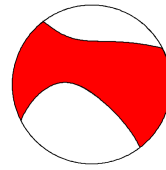
-0.472662	0.000000	0.000000
0.000000	-0.472662	0.000000
0.000000	0.000000	-0.472662

19.0 %

MT solution - 10/06/1997 00:00:52

Full MT =

-2.061850	-0.363737	0.615685
-0.363737	-0.533563	0.497253
0.615685	0.497253	-0.844232

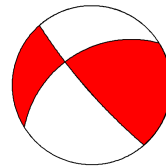


Misfit MT(2b) 1.113
 Method Time domain
 Components one
 Phases P
 Bandpass 0.5 - 4 Hz
 Traces 18 (8 stations)
 source depth: 1km

Decomposition:

DC =

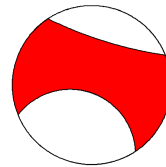
-0.485868	-0.125671	0.251513
-0.125671	0.348791	0.384289
0.251513	0.384289	0.137077



48.0 %

CLVD =

-0.429434	-0.238066	0.364171
-0.238066	0.264194	0.112964
0.364171	0.112964	0.165240



52.0 %

ISO =

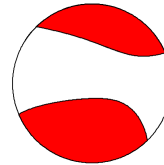
-1.146549	0.000000	0.000000
0.000000	-1.146549	0.000000
0.000000	0.000000	-1.146549

46.0 %

MT solution - 11/06/1997 13:13:52

Full MT =

0.523584	0.274117	-0.483644
0.274117	-0.768597	0.132269
-0.483644	0.132269	-0.896191



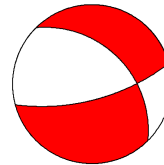
Misfit MT(2b) 1.142
 Method Time domain
 Components one
 Phases P
 Bandpass 0.5 - 4 Hz
 Traces 18 (8 stations)
 source depth: 1km

Decomposition:

DC =

0.383053	0.141973	-0.245248
0.141973	-0.103907	0.170391
-0.245248	0.170391	-0.279146

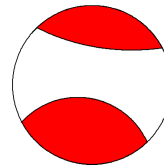
43.0 %



CLVD =

0.520932	0.132144	-0.238396
0.132144	-0.284288	-0.038123
-0.238396	-0.038123	-0.236644

57.0 %



ISO =

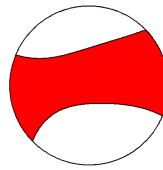
-0.380402	0.000000	0.000000
0.000000	-0.380402	0.000000
0.000000	0.000000	-0.380402

25.0 %

MT solution - 13/06/1997 11:15:36

Full MT =

-0.598877	0.325376	0.421857
0.325376	1.021329	0.080282
0.421857	0.080282	1.228049

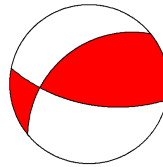


Misfit MT(2b) 1.158
 Method Time domain
 Components une
 Phases P
 Bandpass 0.5 - 4 Hz
 Traces 18 (8 stations)
 source depth: 1km

Decomposition:

DC =

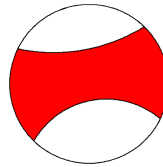
-0.332755	0.102939	0.158881
0.102939	0.055277	0.126302
0.158881	0.126302	0.277478



29.0 %

CLVD =

-0.816288	0.222437	0.262977
0.222437	0.415885	-0.046020
0.262977	-0.046020	0.400403



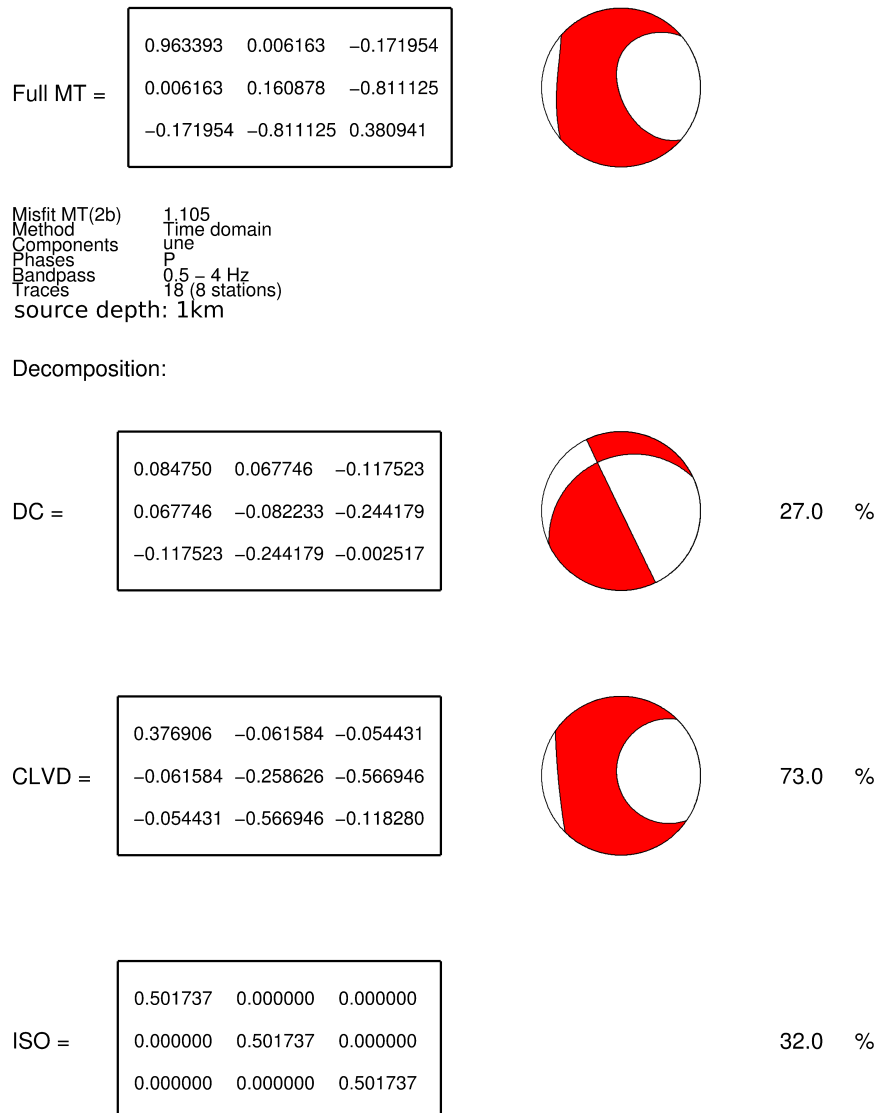
71.0 %

ISO =

0.550167	0.000000	0.000000
0.000000	0.550167	0.000000
0.000000	0.000000	0.550167

29.0 %

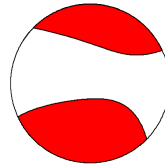
MT solution - 17/06/1997 23:32:45



MT solution - 22/06/1997 00:08:11

Full MT =

0.502676	0.405058	-0.740804
0.405058	-1.746683	0.232690
-0.740804	0.232690	-1.892027

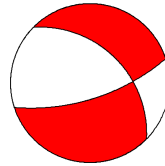


Misfit MT(2b) 1.144
 Method Time domain
 Components one
 Phases P
 Bandpass 0.5 - 4 Hz
 Traces 18 (8 stations)
 source depth: 1km

Decomposition:

DC =

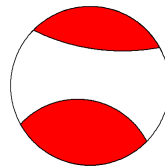
0.613148	0.203938	-0.347664
0.203938	-0.195055	0.286525
-0.347664	0.286525	-0.418093



40.0 %

CLVD =

0.934873	0.201120	-0.393140
0.201120	-0.506284	-0.053836
-0.393140	-0.053836	-0.428589



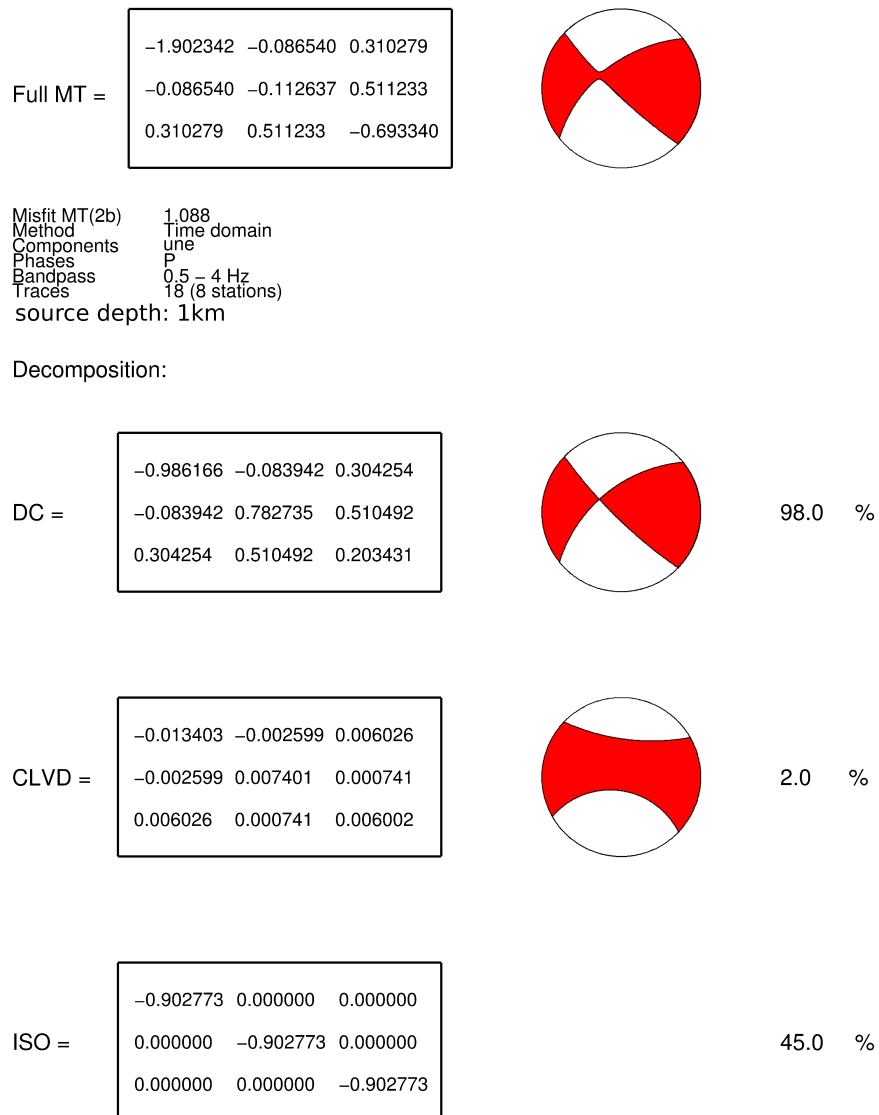
60.0 %

ISO =

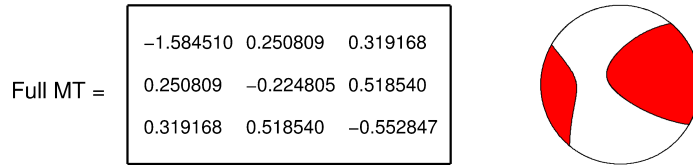
-1.045344	0.000000	0.000000
0.000000	-1.045344	0.000000
0.000000	0.000000	-1.045344

36.0 %

MT solution - 22/06/1997 00:43:05

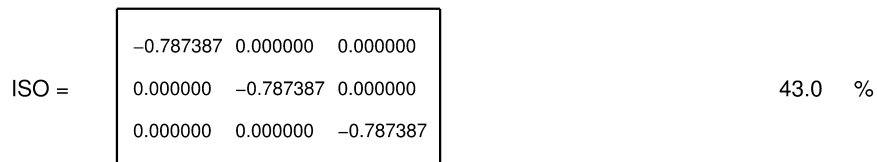
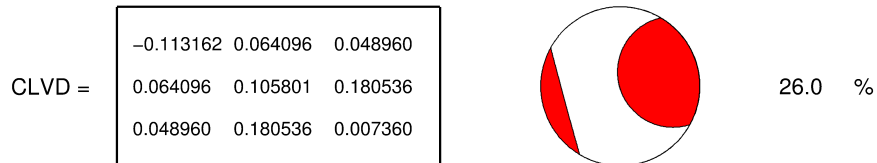
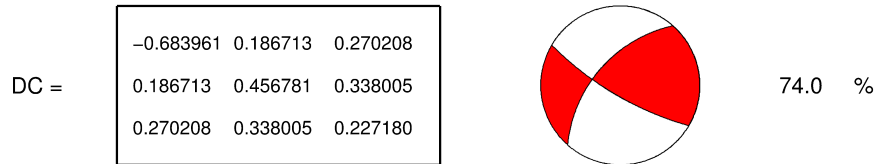


MT solution - 22/06/1997 16:56:15

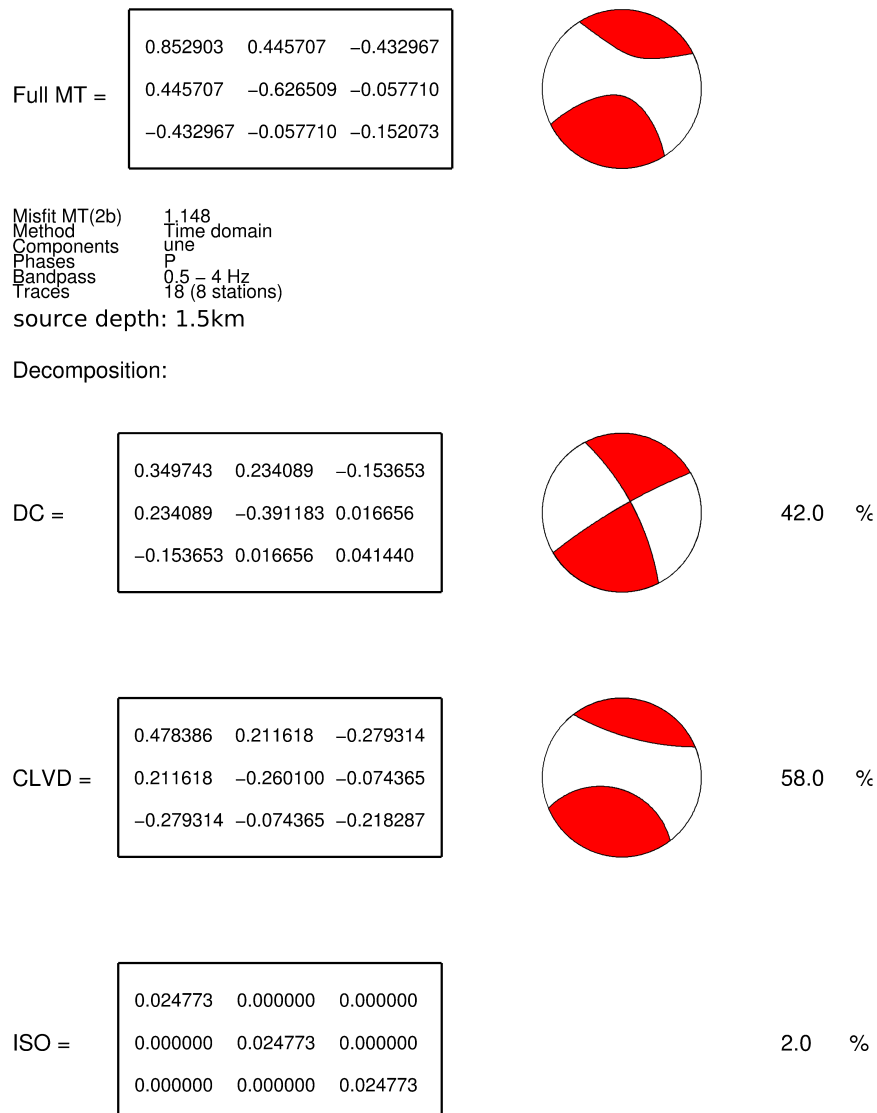


Misfit MT(2b) 1.100
 Method Time domain
 Components 1
 Phases P
 Bandpass 0.5 - 4 Hz
 Traces 18 (8 stations)
 source depth: 1km

Decomposition:



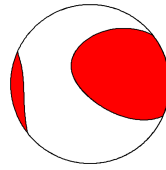
MT solution - 07/06/1997 00:56:30



MT solution - 10/06/1997 00:00:52

Full MT =

-1.379359	0.105782	0.431881
0.105782	-0.556502	0.635485
0.431881	0.635485	-0.375757

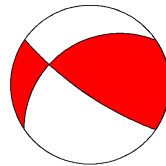


Misfit MT(2b) 1.120
 Method Time domain
 Components one
 Phases P
 Bandpass 0.5 - 4 Hz
 Traces 18 (8 stations)
 source depth: 1.5km

Decomposition:

DC =

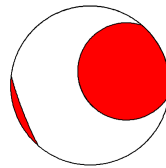
-0.398681	-0.003710	0.296171
-0.003710	0.184599	0.285863
0.296171	0.285863	0.214083



51.0 %

CLVD =

-0.210139	0.109492	0.135710
0.109492	0.029439	0.349622
0.135710	0.349622	0.180700



49.0 %

ISO =

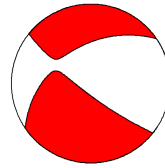
-0.770539	0.000000	0.000000
0.000000	-0.770539	0.000000
0.000000	0.000000	-0.770539

42.0 %

MT solution - 11/06/1997 13:13:52

Full MT =

1.109200	0.035679	-0.338650
0.035679	0.171710	-0.401488
-0.338650	-0.401488	0.222363

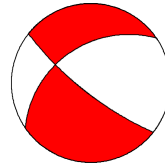


Misfit MT(2b) 1.116
 Method Time domain
 Components one
 Phases P
 Bandpass 0.5 - 4 Hz
 Traces 18 (8 stations)
 source depth: 1.5km

Decomposition:

DC =

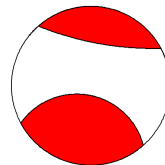
0.592727	0.031033	-0.328431
0.031033	-0.320068	-0.399629
-0.328431	-0.399629	-0.272659



97.0 %

CLVD =

0.015383	0.004645	-0.010220
0.004645	-0.009314	-0.001859
-0.010220	-0.001859	-0.006069



3.0 %

ISO =

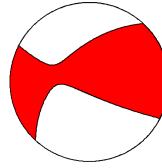
0.501091	0.000000	0.000000
0.000000	0.501091	0.000000
0.000000	0.000000	0.501091

40.0 %

MT solution - 13/06/1997 11:15:36

Full MT =

-0.319598	0.241072	0.443229
0.241072	1.000373	0.399128
0.443229	0.399128	0.894866



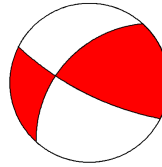
Misfit MT(2b) 1.149
 Method Time domain
 Components 2
 Phases P
 Bandpass 0.5 - 4 Hz
 Traces 18 (8 stations)
 source depth: 1.5km

Decomposition:

DC =

-0.765643	0.230795	0.405775
0.230795	0.430378	0.402212
0.405775	0.402212	0.335265

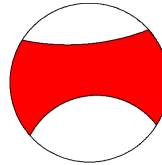
90.0 %



CLVD =

-0.079169	0.010277	0.037454
0.010277	0.044781	-0.003084
0.037454	-0.003084	0.034387

10.0 %

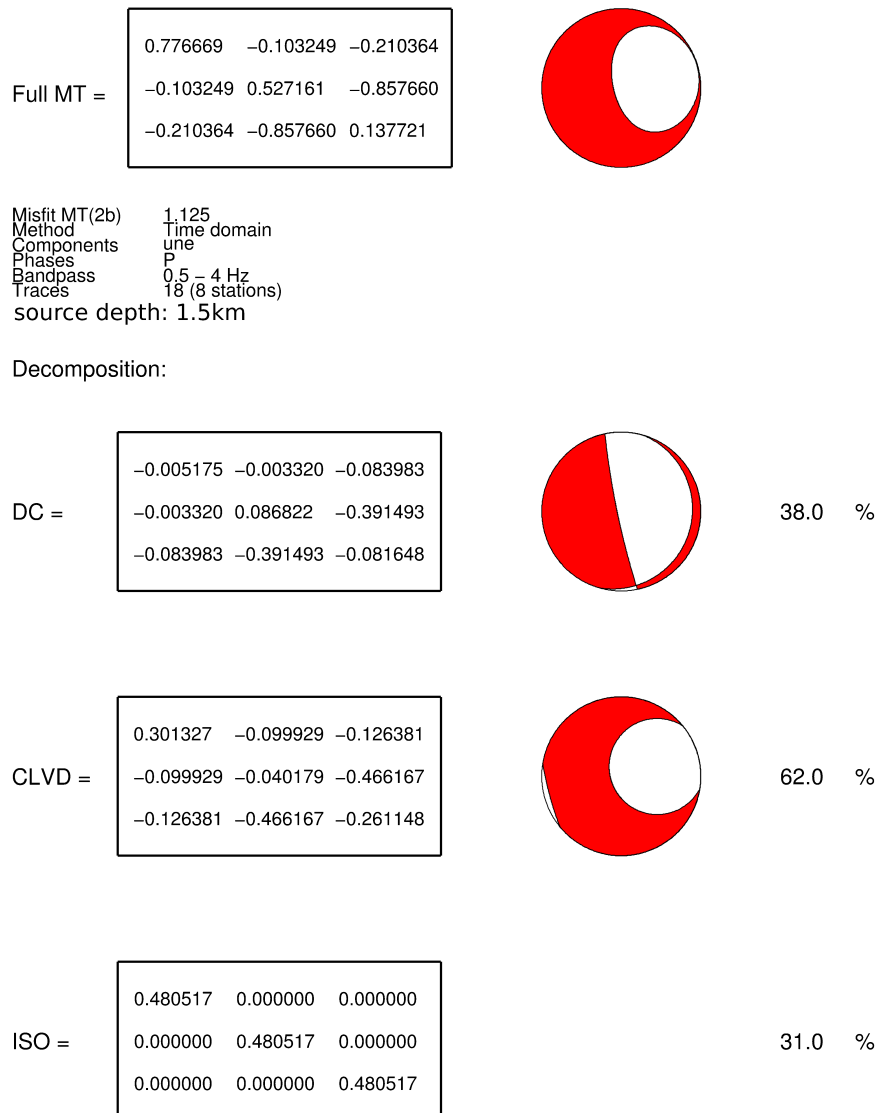


ISO =

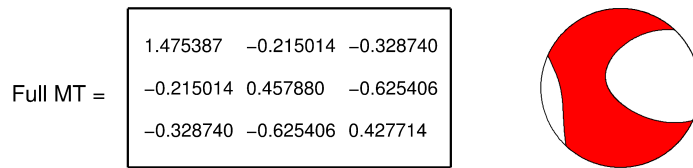
0.525214	0.000000	0.000000
0.000000	0.525214	0.000000
0.000000	0.000000	0.525214

34.0 %

MT solution - 17/06/1997 23:32:45

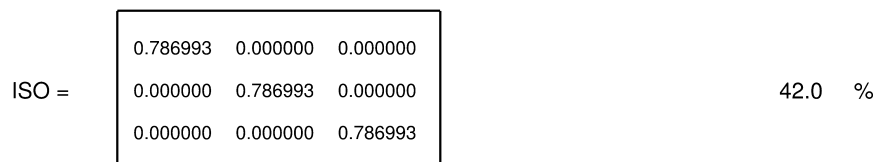
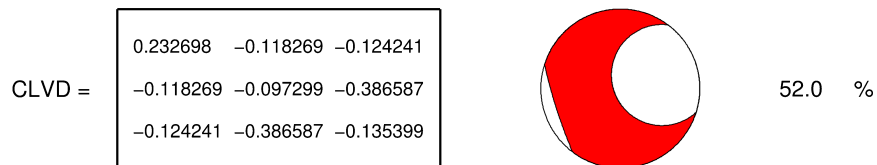
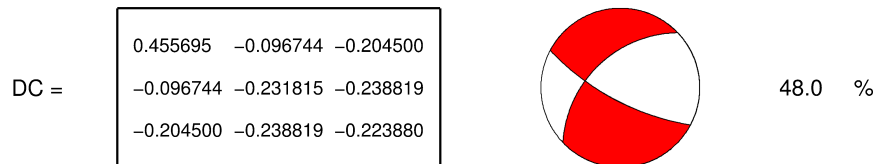


MT solution - 22/06/1997 00:08:11

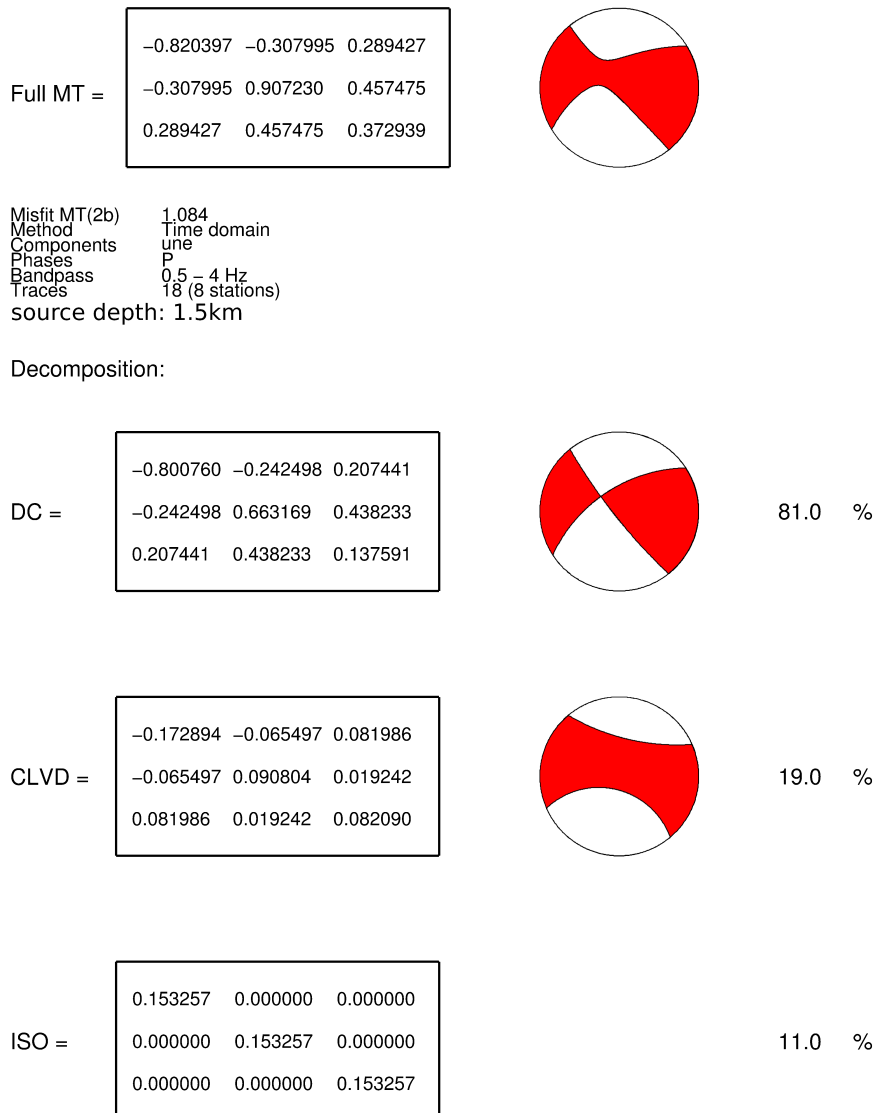


Misfit MT(2b) 1.110
 Method Time domain
 Components une
 Phases P
 Bandpass 0.5 - 4 Hz
 Traces 18 (8 stations)
 source depth: 1.5km

Decomposition:



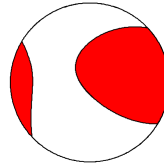
MT solution - 22/06/1997 00:43:05



MT solution - 22/06/1997 16:56:15

Full MT =

-1.436513	0.115283	0.361668
0.115283	-0.354177	0.637217
0.361668	0.637217	-0.456173

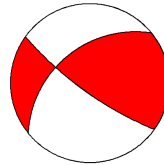


Misfit MT(2b) 1.132
 Method Time domain
 Components une
 Phases P
 Bandpass 0.5 - 4 Hz
 Tracés 18 (8 stations)
 source depth: 1.5km

Decomposition:

DC =

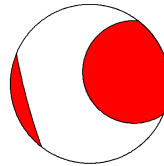
-0.481410	0.022839	0.271586
0.022839	0.283055	0.303176
0.271586	0.303176	0.198355



55.0 %

CLVD =

-0.206149	0.092444	0.090082
0.092444	0.111723	0.334041
0.090082	0.334041	0.094426



45.0 %

ISO =

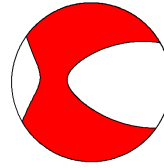
-0.748954	0.000000	0.000000
0.000000	-0.748954	0.000000
0.000000	0.000000	-0.748954

41.0 %

MT solution - 07/06/1997 00:56:30

Full MT =

0.991999	0.065310	-0.027298
0.065310	-0.390510	-0.576258
-0.027298	-0.576258	-0.577722



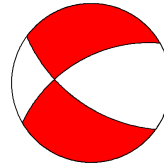
Misfit MT(2b) 1.128
 Method Time domain
 Components 1
 Phases P
 Bandpass 0.5 - 4 Hz
 Traces 18 (8 stations)

source depth: 2km

Decomposition:

DC =

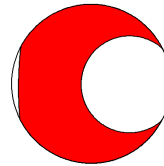
0.897399	0.063545	-0.029371
0.063545	-0.375789	-0.447869
-0.029371	-0.447869	-0.521609



83.0 %

CLVD =

0.086678	0.001765	0.002073
0.001765	-0.022643	-0.128389
0.002073	-0.128389	-0.064035



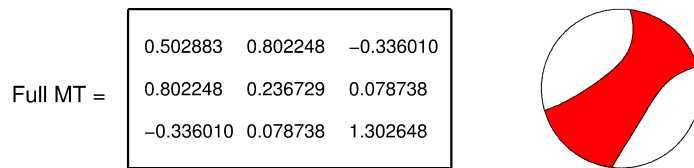
17.0 %

ISO =

0.007923	0.000000	0.000000
0.000000	0.007923	0.000000
0.000000	0.000000	0.007923

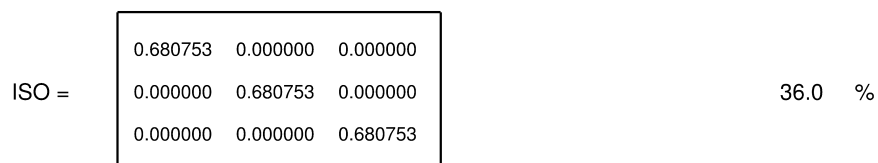
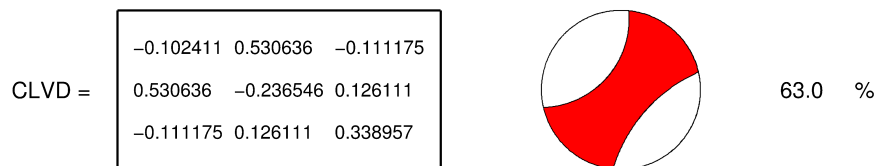
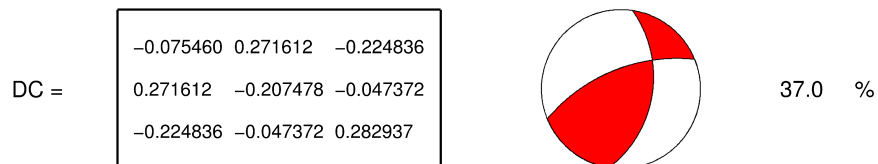
0.0 %

MT solution - 10/06/1997 00:00:52



Misfit MT(2b) 1.116
 Method Time domain
 Components one
 Phases P
 Bandpass 0.5 - 4 Hz
 Traces 18 (8 stations)
 source depth: 2km

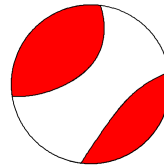
Decomposition:



MT solution - 11/06/1997 13:13:52

Full MT =

-0.436065	-0.853535	0.418296
-0.853535	-0.383474	-0.248343
0.418296	-0.248343	-1.107552

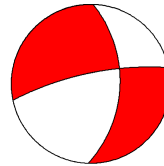


Misfit MT(2b) 1.129
 Method Time domain
 Components one
 Phases P
 Bandpass 0.5 - 4 Hz
 Traces 18 (8 stations)
 source depth: 2km

Decomposition:

DC =

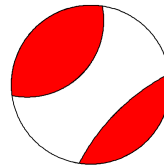
0.011098	-0.178093	0.149453
-0.178093	0.074547	0.018348
0.149453	0.018348	-0.085645



20.0 %

CLVD =

0.195201	-0.675443	0.268843
-0.675443	0.184342	-0.266691
0.268843	-0.266691	-0.379543



80.0 %

ISO =

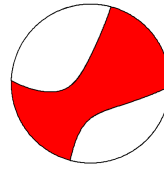
-0.642363	0.000000	0.000000
0.000000	-0.642363	0.000000
0.000000	0.000000	-0.642363

34.0 %

MT solution - 13/06/1997 11:15:36

Full MT =

0.147700	0.785967	-0.062777
0.785967	0.630241	0.398788
-0.062777	0.398788	0.927766

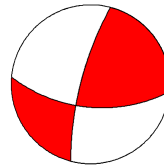


Misfit MT(2b) 1.130
 Method Time domain
 Components 1
 Phases P
 Bandpass 0.5 - 4 Hz
 Traces 18 (8 stations)
 source depth: 2km

Decomposition:

DC =

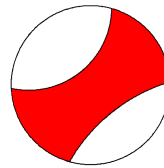
-0.244697	0.462490	0.045985
0.462490	0.087531	0.312398
0.045985	0.312398	0.157166



56.0 %

CLVD =

-0.176172	0.323477	-0.108762
0.323477	-0.025859	0.086390
-0.108762	0.086390	0.202031



44.0 %

ISO =

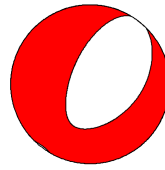
0.568569	0.000000	0.000000
0.000000	0.568569	0.000000
0.000000	0.000000	0.568569

34.0 %

MT solution - 17/06/1997 23:32:45

Full MT =

-0.027740	-0.428771	-0.006182
-0.428771	0.195202	-0.562367
-0.006182	-0.562367	-1.206726

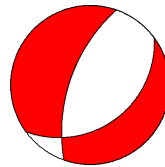


Misfit MT(2b) 1.128
 Method Time domain
 Components one
 Phases P
 Bandpass 0.5 - 4 Hz
 Traces 18 (8 stations)
 source depth: 2km

Decomposition:

DC =

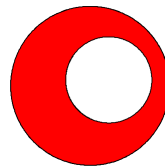
0.233258	-0.418166	0.021719
-0.418166	0.486020	-0.475005
0.021719	-0.475005	-0.719279



83.0 %

CLVD =

0.085423	-0.010605	-0.027900
-0.010605	0.055603	-0.087362
-0.027900	-0.087362	-0.141026



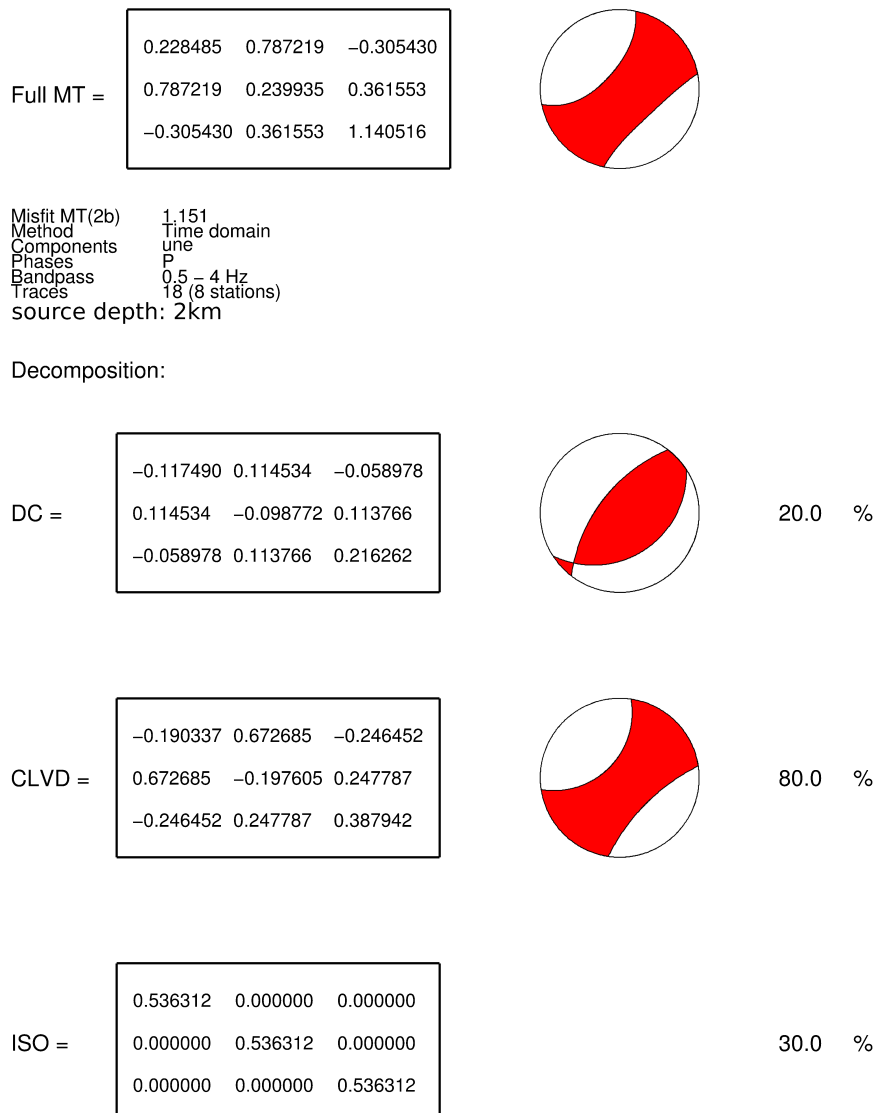
17.0 %

ISO =

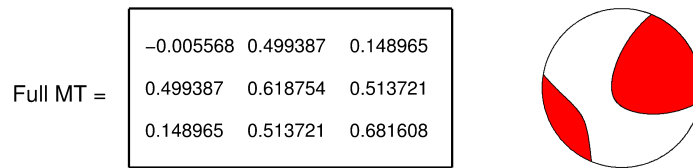
-0.346421	0.000000	0.000000
0.000000	-0.346421	0.000000
0.000000	0.000000	-0.346421

24.0 %

MT solution - 22/06/1997 00:08:11

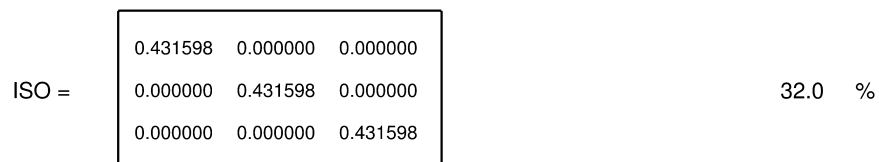
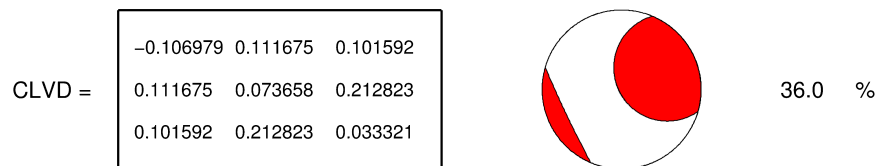
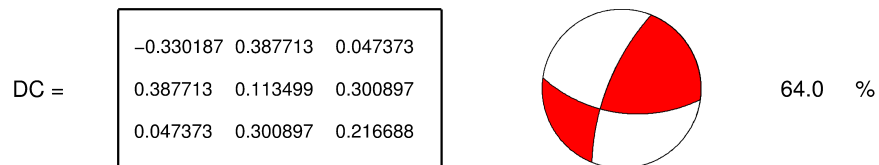


MT solution - 22/06/1997 00:43:05

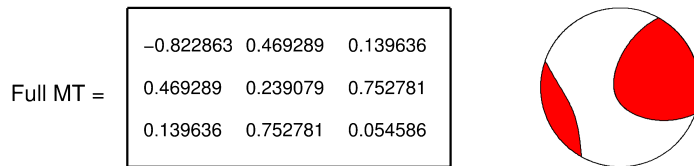


Misfit MT(2b) 1.095
 Method Time domain
 Components one
 Phases P
 Bandpass 0.5 - 4 Hz
 Traces 18 (8 stations)
 source depth: 2km

Decomposition:



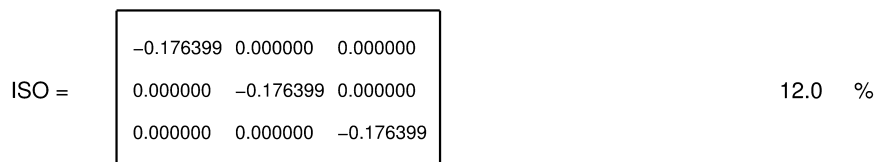
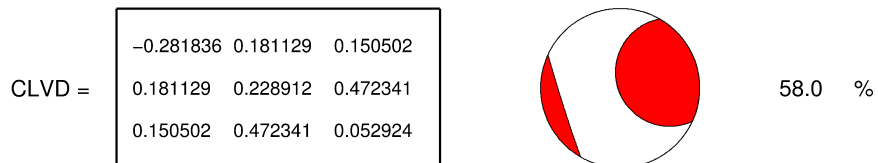
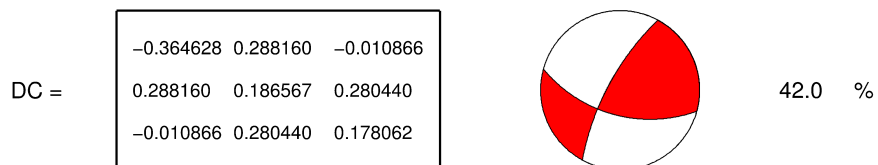
MT solution - 22/06/1997 16:56:15



Misfit MT(2b) 1.133
 Method Time domain
 Components 1
 Phases P
 Bandpass 0.5 - 4 Hz
 Traces 18 (8 stations)

source depth: 2km

Decomposition:

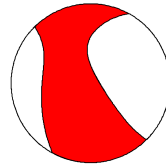


Inversion band width 0.5-2 Hz

MT solution - 07/06/1997 00:56:30

Full MT =

1.540437	-0.154987	-0.426089
-0.154987	0.457724	-0.600938
-0.426089	-0.600938	1.481419



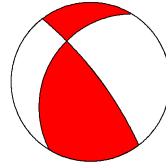
Misfit MT(2b) 1.149
 Method Time domain
 Components one
 Phases P
 Bandpass 0.5 - 2 Hz
 Traces 18 (8 stations)

source depth: 1.0km

Decomposition:

DC =

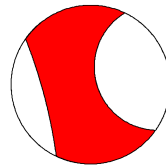
0.207703	-0.034914	-0.363893
-0.034914	-0.447962	-0.363444
-0.363893	-0.363444	0.240259



61.0 %

CLVD =

0.172874	-0.120073	-0.062196
-0.120073	-0.254174	-0.237494
-0.062196	-0.237494	0.081300



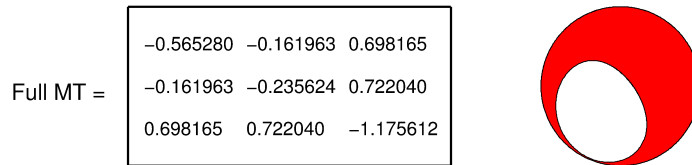
39.0 %

ISO =

1.159860	0.000000	0.000000
0.000000	1.159860	0.000000
0.000000	0.000000	1.159860

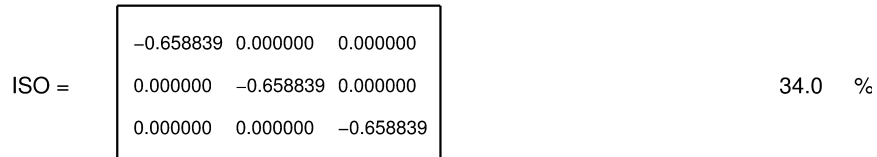
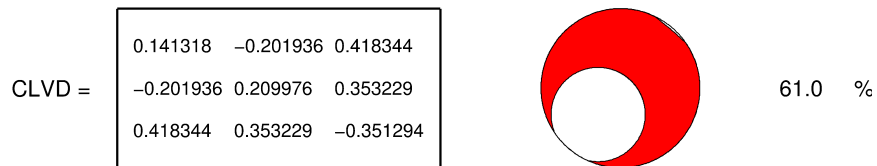
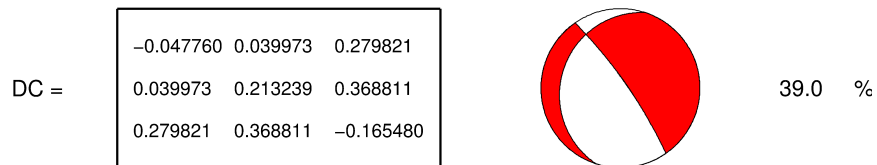
52.0 %

MT solution - 10/06/1997 00:00:52



Misfit MT(2b) 1.160
 Method Time domain
 Components one
 Phases P
 Bandpass 0.5 - 2 Hz
 Traces 18 (8 stations)
 source depth: 1.0km

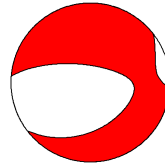
Decomposition:



MT solution - 11/06/1997 13:13:52

Full MT =

-1.461428	-0.257821	0.612248
-0.257821	-2.261171	0.274780
0.612248	0.274780	-2.924889

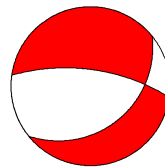


Misfit MT(2b) 1.190
 Method Time domain
 Components one
 Phases P
 Bandpass 0.5 - 2 Hz
 Traces 18 (8 stations)
 source depth: 1.0km

Decomposition:

DC =

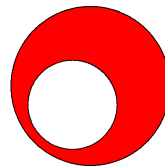
0.720550	-0.239932	0.564352
-0.239932	-0.080950	0.229178
0.564352	0.229178	-0.639600



89.0 %

CLVD =

0.033852	-0.017888	0.047896
-0.017888	0.035608	0.045602
0.047896	0.045602	-0.069460



11.0 %

ISO =

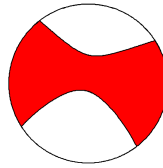
-2.215830	0.000000	0.000000
0.000000	-2.215830	0.000000
0.000000	0.000000	-2.215830

67.0 %

MT solution - 13/06/1997 11:15:36

Full MT =

-1.791319	-0.362180	0.347254
-0.362180	0.247481	0.114912
0.347254	0.114912	-0.499385

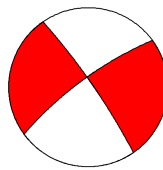


Misfit MT(2b) 1.195
 Method Time domain
 Components one
 Phases P
 Bandpass 0.5 - 2 Hz
 Traces 17 (7 stations)
 source depth: 1.0km

Decomposition:

DC =

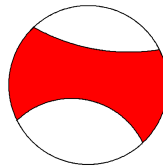
-0.644400	-0.231055	0.160374
-0.231055	0.683559	0.081538
0.160374	0.081538	-0.039159



57.0 %

CLVD =

-0.465844	-0.131125	0.186881
-0.131125	0.244996	0.033374
0.186881	0.033374	0.220848



43.0 %

ISO =

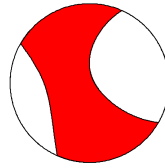
-0.681074	0.000000	0.000000
0.000000	-0.681074	0.000000
0.000000	0.000000	-0.681074

35.0 %

MT solution - 22/06/1997 00:08:11

Full MT =

1.412308	-0.441636	-0.288515
-0.441636	0.207118	-0.536874
-0.288515	-0.536874	1.034097

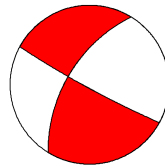


Misfit MT(2b) 1.124
 Method Time domain
 Components 2
 Phases P
 Bandpass 0.5 - 2 Hz
 Traces 18 (8 stations)
 source depth: 1.0km

Decomposition:

DC =

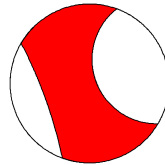
0.238482	-0.129822	-0.129852
-0.129822	-0.211285	-0.095456
-0.129852	-0.095456	-0.027197



27.0 %

CLVD =

0.289318	-0.311814	-0.158663
-0.311814	-0.466105	-0.441418
-0.158663	-0.441418	0.176786



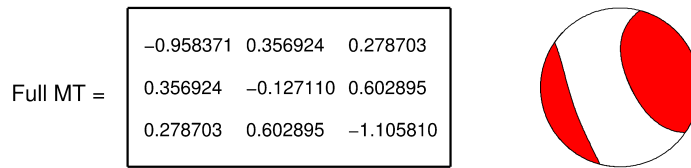
73.0 %

ISO =

0.884508	0.000000	0.000000
0.000000	0.884508	0.000000
0.000000	0.000000	0.884508

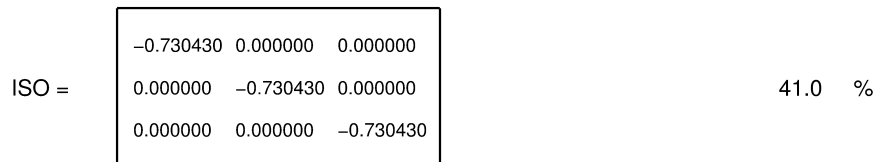
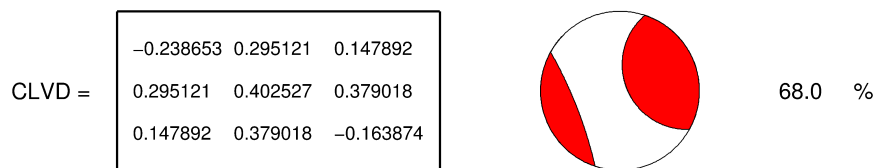
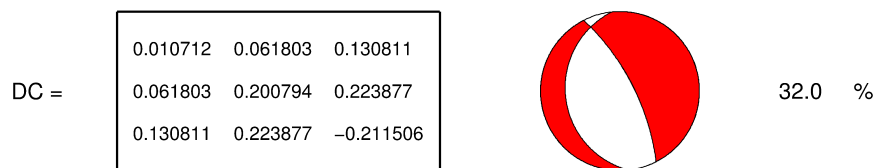
44.0 %

MT solution - 22/06/1997 00:43:05



Misfit MT(2b) 1.116
 Method Time domain
 Components une
 Phases P
 Bandpass 0.5 – 2 Hz
 Traces 18 (8 stations)
 source depth: 1.0km

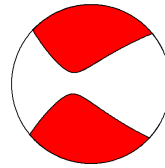
Decomposition:



MT solution - 22/06/1997 16:56:56

Full MT =

1.455563	0.054644	0.001443
0.054644	-0.478062	-0.376743
0.001443	-0.376743	0.098488

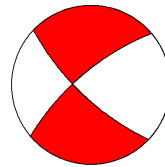


Misfit MT(2b) 1.141
 Method Time domain
 Components une
 Phases P
 Bandpass 0.5 - 2 Hz
 Traces 20 (8 stations)
 source depth: 1.0km

Decomposition:

DC =

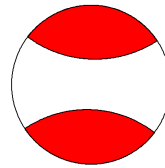
0.948076	0.048026	0.003041
0.048026	-0.762405	-0.376696
0.003041	-0.376696	-0.185671



86.0 %

CLVD =

0.148824	0.006617	-0.001598
0.006617	-0.074320	-0.000047
-0.001598	-0.000047	-0.074504



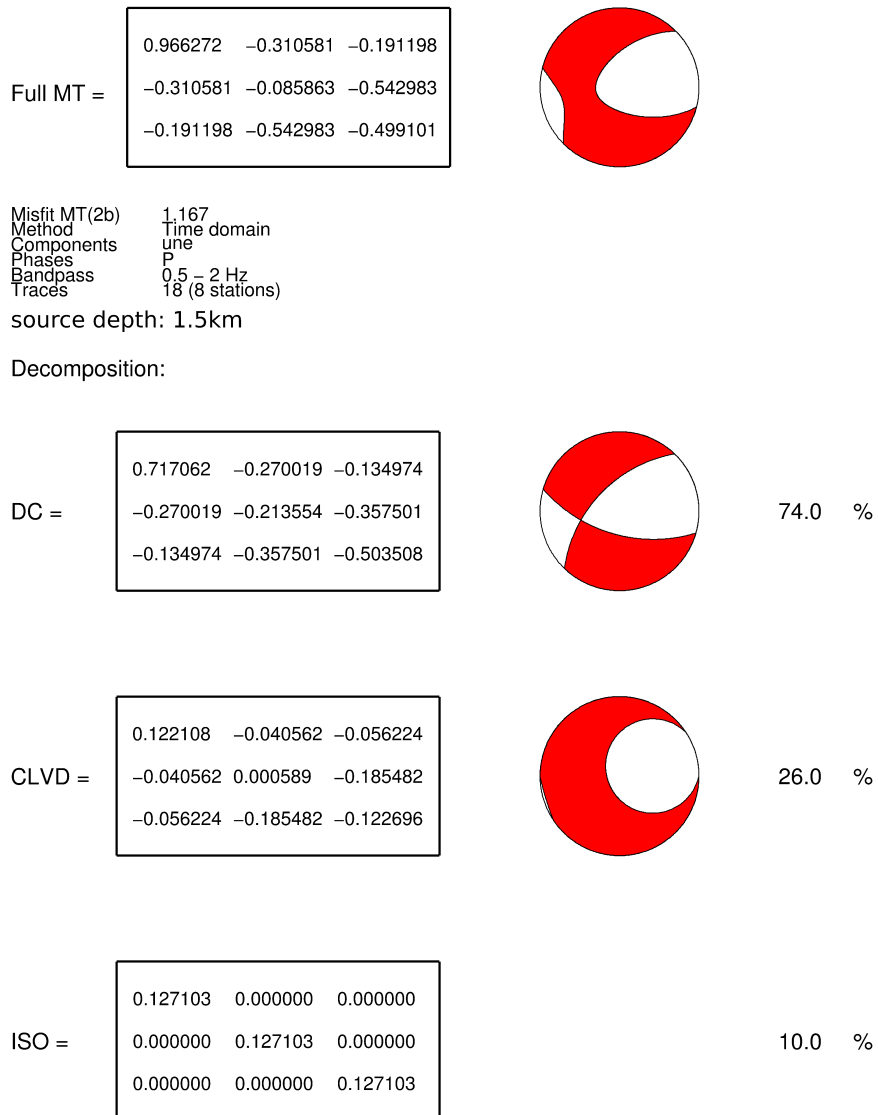
14.0 %

ISO =

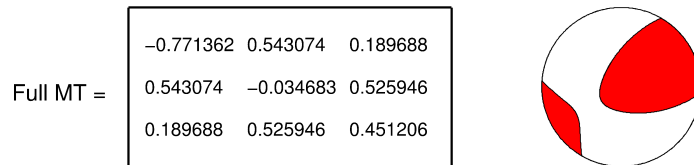
0.358663	0.000000	0.000000
0.000000	0.358663	0.000000
0.000000	0.000000	0.358663

24.0 %

MT solution - 07/06/1997 00:56:30

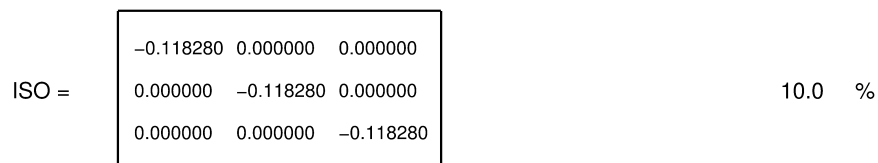
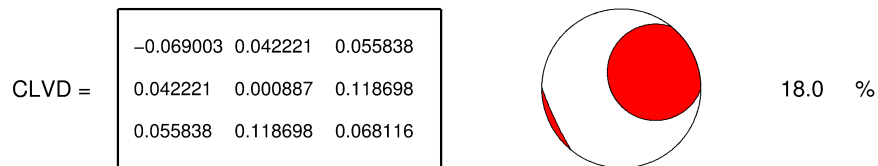
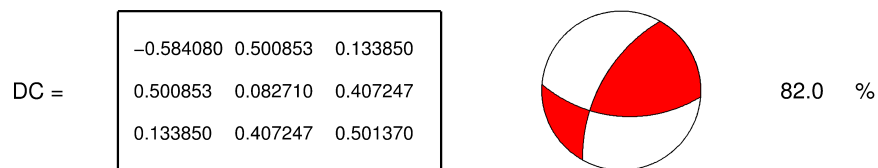


MT solution - 10/06/1997 00:00:52



Misfit MT(2b) 1.169
 Method Time domain
 Components one
 Phases P
 Bandpass 0.5 - 2 Hz
 Tracés 18 (8 stations)
 source depth: 1.5km

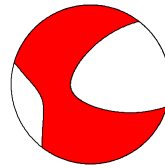
Decomposition:



MT solution - 11/06/1997 13:13:52

Full MT =

1.033130	-0.403063	-0.214478
-0.403063	-0.062793	-0.541582
-0.214478	-0.541582	-0.261769

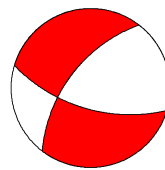


Misfit MT(2b) 1.150
 Method Time domain
 Components une
 Phases P
 Bandpass 0.5 - 2 Hz
 Traces 18 (8 stations)
 source depth: 1.5km

Decomposition:

DC =

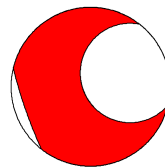
0.697817	-0.351562	-0.156692
-0.351562	-0.268528	-0.376021
-0.156692	-0.376021	-0.429289



77.0 %

CLVD =

0.099123	-0.051501	-0.057787
-0.051501	-0.030454	-0.165561
-0.057787	-0.165561	-0.068670



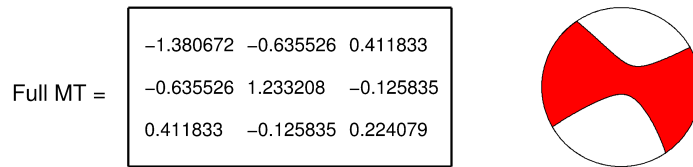
23.0 %

ISO =

0.236189	0.000000	0.000000
0.000000	0.236189	0.000000
0.000000	0.000000	0.236189

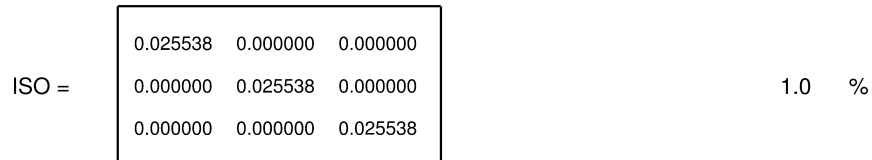
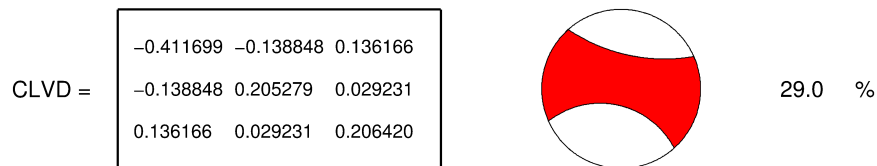
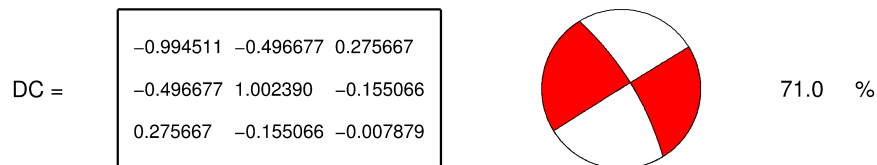
18.0 %

MT solution - 13/06/1997 11:15:36



Misfit MT(2b) 1.206
 Method Time domain
 Components one
 Phases P
 Bandpass 0.5 - 2 Hz
 Traces 17 (7 stations)
 source depth: 1.5km

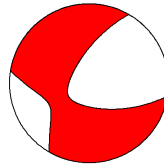
Decomposition:



MT solution - 22/06/1997 00:08:11

Full MT =

0.716622	-0.558084	-0.161379
-0.558084	-0.193106	-0.526177
-0.161379	-0.526177	-0.509984

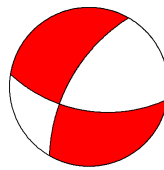


Misfit MT(2b) 1.168
 Method Time domain
 Components one
 Phases P
 Bandpass 0.5 - 2 Hz
 Traces 18 (8 stations)
 source depth: 1.5km

Decomposition:

DC =

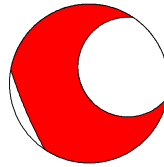
0.670475	-0.530770	-0.130194
-0.530770	-0.186555	-0.452764
-0.130194	-0.452764	-0.483920



89.0 %

CLVD =

0.041637	-0.027315	-0.031185
-0.027315	-0.011062	-0.073412
-0.031185	-0.073412	-0.030575



11.0 %

ISO =

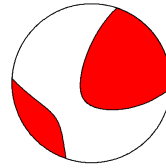
0.004511	0.000000	0.000000
0.000000	0.004511	0.000000
0.000000	0.000000	0.004511

0.0 %

MT solution - 22/06/1997 00:43:05

Full MT =

-0.279038	0.617949	0.151167
0.617949	0.222283	0.621287
0.151167	0.621287	0.494373



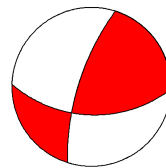
Misfit MT(2b) 1.119
 Method Time domain
 Components 3
 Phases P
 Bandpass 0.5 - 2 Hz
 Traces 18 (8 stations)

source depth: 1.5km

Decomposition:

DC =

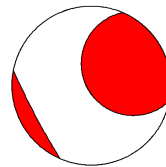
-0.332273	0.518793	0.050083
0.518793	0.033776	0.429975
0.050083	0.429975	0.298497



72.0 %

CLVD =

-0.092638	0.099156	0.101084
0.099156	0.042634	0.191312
0.101084	0.191312	0.050003



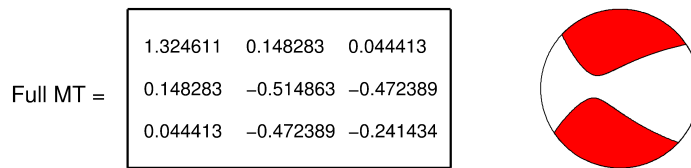
28.0 %

ISO =

0.145873	0.000000	0.000000
0.000000	0.145873	0.000000
0.000000	0.000000	0.145873

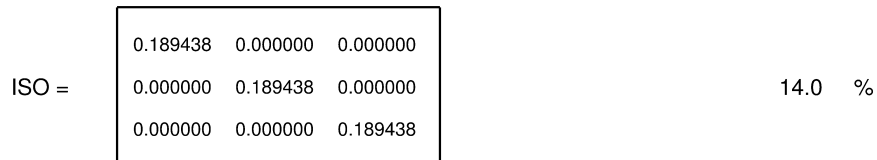
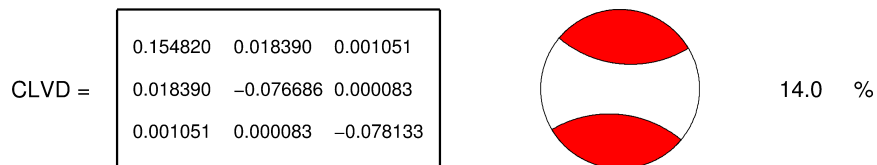
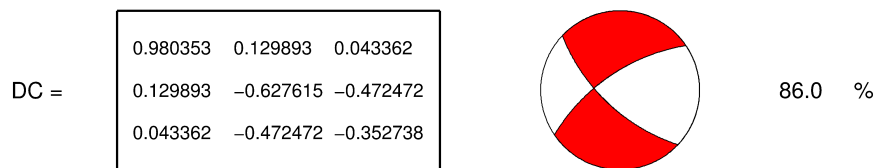
12.0 %

MT solution - 22/06/1997 16:56:56

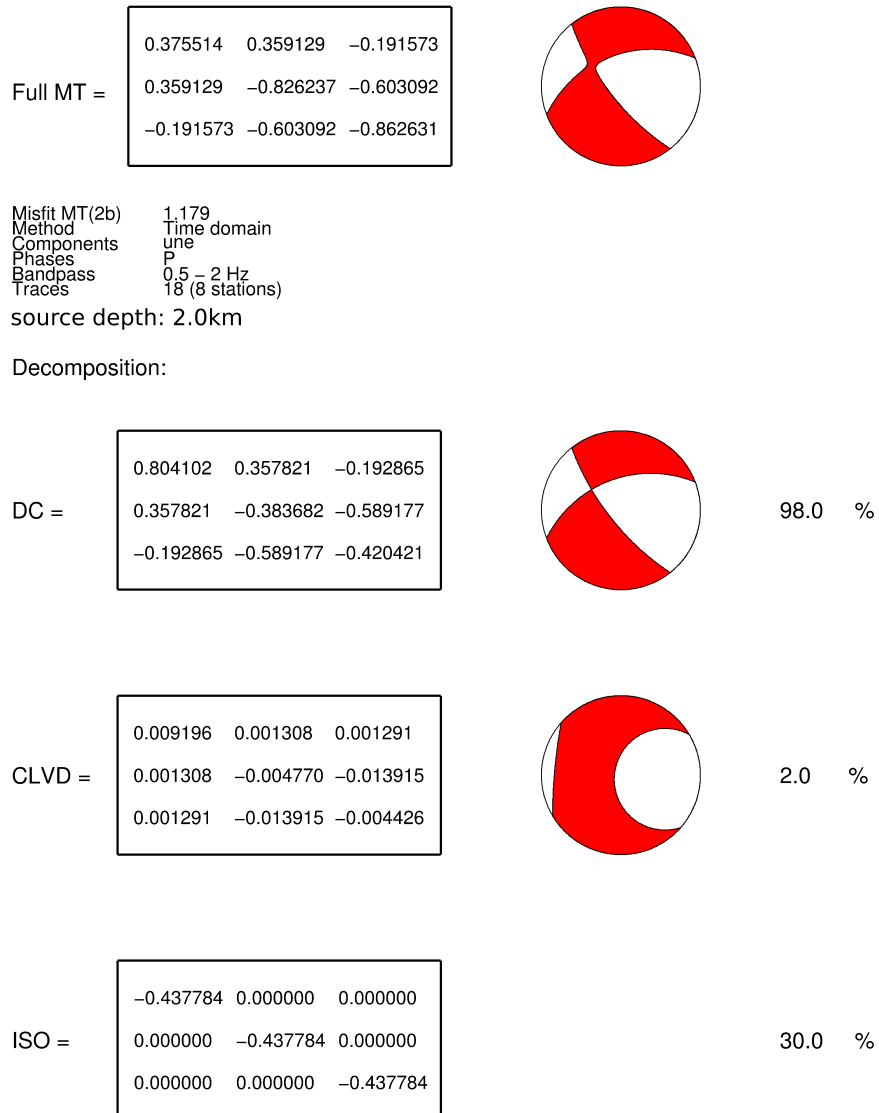


Misfit MT(2b) 1.164
 Method Time domain
 Components one
 Phases P
 Bandpass 0.5 - 2 Hz
 Traces 20 (8 stations)
 source depth: 1.5km

Decomposition:

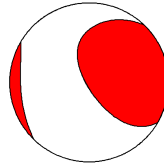


MT solution - 07/06/1997 00:56:30



MT solution - 10/06/1997 00:00:52

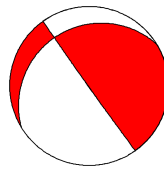
Full MT =	0.193185	0.086371	0.425070
	0.086371	0.811360	0.809455
	0.425070	0.809455	0.722350



Misfit MT(2b) 1.142
 Method Time domain
 Components one
 Phases P
 Bandpass 0.5 - 2 Hz
 Traces 18 (8 stations)
 source depth: 2.0km

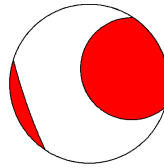
Decomposition:

DC =	-0.141863	-0.056008	0.280225
	-0.056008	0.122495	0.398462
	0.280225	0.398462	0.019368



46.0 %

CLVD =	-0.240584	0.142378	0.144845
	0.142378	0.113233	0.410993
	0.144845	0.410993	0.127351



54.0 %

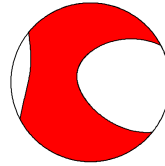
ISO =	0.575632	0.000000	0.000000
	0.000000	0.575632	0.000000
	0.000000	0.000000	0.575632

34.0 %

MT solution - 11/06/1997 13:13:52

Full MT =

0.806037	0.112579	-0.098754
0.112579	-0.329678	-0.741925
-0.098754	-0.741925	-0.450505



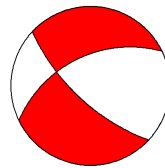
Misfit MT(2b) 1.120
 Method Time domain
 Components one
 Phases P
 Bandpass 0.5 - 2 Hz
 Traces 18 (8 stations)

source depth: 2.0km

Decomposition:

DC =

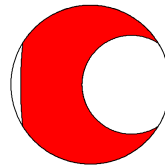
0.496860	0.111405	-0.100028
0.111405	-0.224433	-0.292556
-0.100028	-0.292556	-0.272427



47.0 %

CLVD =

0.300559	0.001174	0.001273
0.001174	-0.113863	-0.449369
0.001273	-0.449369	-0.186696



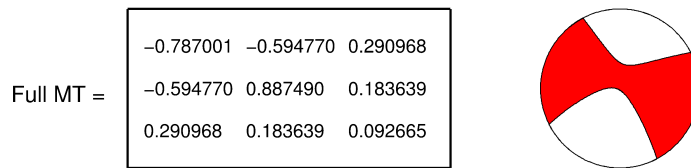
53.0 %

ISO =

0.008618	0.000000	0.000000
0.000000	0.008618	0.000000
0.000000	0.000000	0.008618

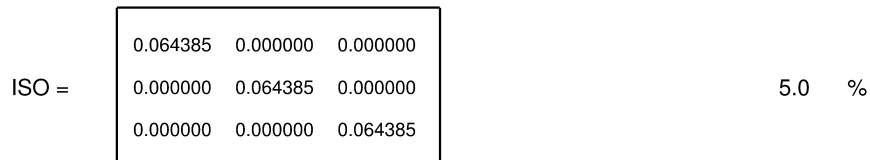
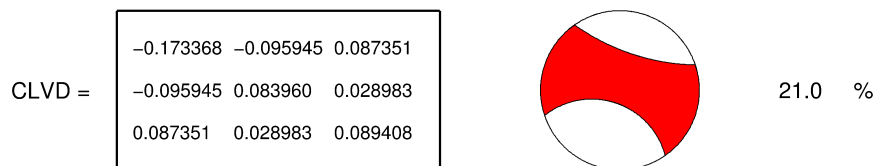
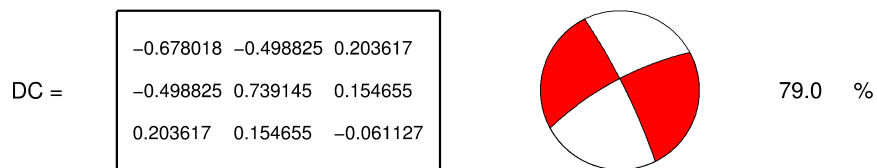
0.0 %

MT solution - 13/06/1997 11:15:36



Misfit MT(2b) 1.216
 Method Time domain
 Components une
 Phases P
 Bandpass 0.5 - 2 Hz
 Traces 17 (7 stations)
 source depth: 2.0km

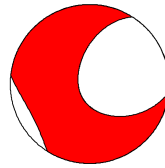
Decomposition:



MT solution - 22/06/1997 00:08:11

Full MT =

0.053670	-0.370743	-0.185550
-0.370743	-0.533681	-0.721751
-0.185550	-0.721751	-0.869595

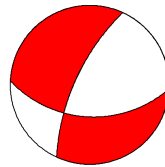


Misfit MT(2b) 1.166
 Method Time domain
 Components une
 Phases P
 Bandpass 0.5 - 2 Hz
 Traces 18 (8 stations)
 source depth: 2.0km

Decomposition:

DC =

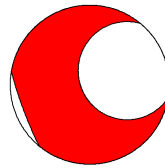
0.199106	-0.211770	0.004049
-0.211770	-0.021567	-0.213682
0.004049	-0.213682	-0.177539



32.0 %

CLVD =

0.304433	-0.158973	-0.189598
-0.158973	-0.062246	-0.508069
-0.189598	-0.508069	-0.242187



68.0 %

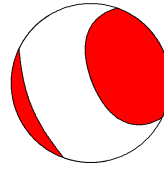
ISO =

-0.449869	0.000000	0.000000
0.000000	-0.449869	0.000000
0.000000	0.000000	-0.449869

29.0 %

MT solution - 22/06/1997 00:43:05

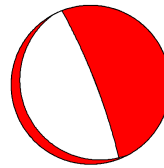
Full MT =	0.360000	0.253160	0.319172
	0.253160	0.872983	0.811168
	0.319172	0.811168	0.503891



Misfit MT(2b) 1.141
 Method Time domain
 Components one
 Phases P
 Bandpass 0.5 - 2 Hz
 Traces 18 (8 stations)
 source depth: 2.0km

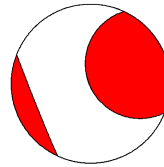
Decomposition:

DC =	0.018648	0.041725	0.144862
	0.041725	0.091028	0.377815
	0.144862	0.377815	-0.109676



39.0 %

CLVD =	-0.237606	0.211435	0.174310
	0.211435	0.202997	0.433353
	0.174310	0.433353	0.034609



61.0 %

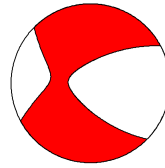
ISO =	0.578958	0.000000	0.000000
	0.000000	0.578958	0.000000
	0.000000	0.000000	0.578958

35.0 %

MT solution - 22/06/1997 16:56:56

Full MT =

1.107164	0.229393	0.108177
0.229393	-0.444217	-0.553193
0.108177	-0.553193	-0.379753

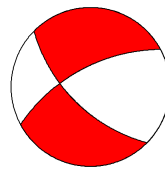


Misfit MT(2b) 1.159
 Method Time domain
 Components one
 Phases P
 Bandpass 0.5 - 2 Hz
 Traces 20 (8 stations)
 source depth: 2.0km

Decomposition:

DC =

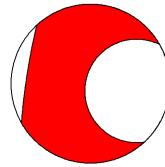
0.972706	0.218986	0.098514
0.218986	-0.514013	-0.491639
0.098514	-0.491639	-0.458694



92.0 %

CLVD =

0.040060	0.010408	0.009663
0.010408	-0.024602	-0.061554
0.009663	-0.061554	-0.015458



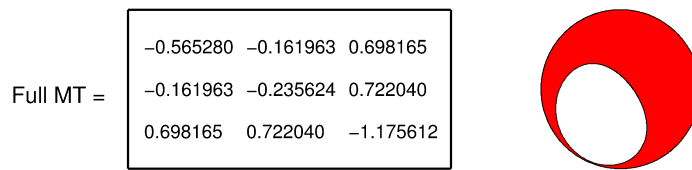
8.0 %

ISO =

0.094398	0.000000	0.000000
0.000000	0.094398	0.000000
0.000000	0.000000	0.094398

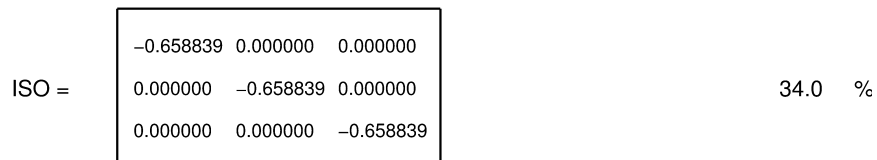
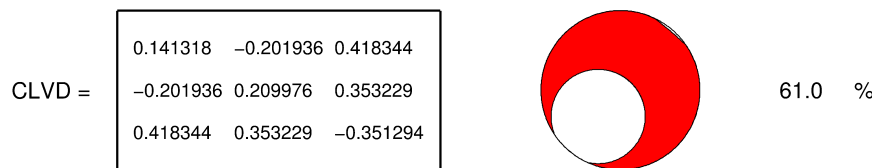
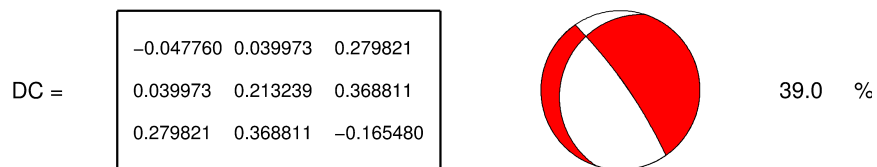
7.0 %

MT solution - 10/06/1997 00:00:52

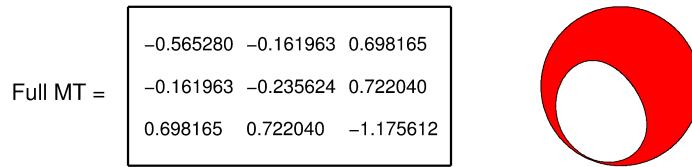


Misfit MT(2b) 1.160
 Method Time domain
 Components one
 Phases P
 Bandpass 0.5 - 2 Hz
 Traces 18 (8 stations)
 source depth: 1.0km

Decomposition:

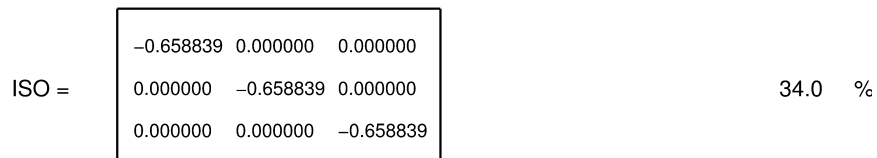
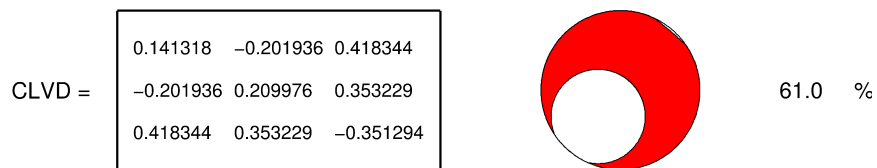
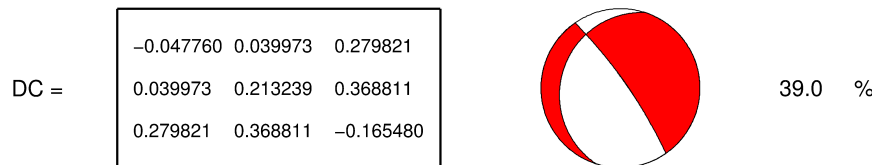


MT solution - 10/06/1997 00:00:52



Misfit MT(2b) 1.160
 Method Time domain
 Components one
 Phases P
 Bandpass 0.5 - 2 Hz
 Traces 18 (8 stations)
 source depth: 1.0km

Decomposition:



References

- Aki, K. (1984), Evidence for magma intrusion during the Mammoth Lakes earthquakes of May 1980 and implications of the absence of volcanic (harmonic) tremor, *J. Volcanol. Geophys. Res.*, *89*(B9), 7689–7696. 6.3
- Aki, K., and P. Richards (1980), *Quantitative Seismology*, First Edition ed., University Science Books, Sausalito, California. 1.6.5, 2.2.3, 3, 5.1, 7.1
- Aki, K., and P. Richards (2002), *Quantitative Seismology*, Second Edition ed., University Science Books, Sausalito, California. 3, 3.2.1, 3.2.1
- Aki, K., M. Fehler, and S. Das (1977), Source mechanism of volcanic tremor: fluid-driven crack models and their application to the 1963 Kilauea eruption, *J. Volcanol. Geotherm. Res.*, *2*, 259–287. 1.5.2, 1.5.2
- Alidibirov, M., and D. Dingwell (1996), Magma fragmentation by rapid decompression, *Nature*, *380*, 146–148. 2.2, 7.2
- Aspinall, W., A. Miller, L. Lynch, J. Latchman, R. Stewart, R. White, and J. Power (1998), Soufrière Hills eruption, Montserrat, 1995-1997: Volcanic earthquake locations and fault plane solutions, *Geophysical Research Letters*, *25*, 3397–3400. 1.4.1, 6.1, 6.1
- Barclay, J., M. Rutherford, M. Carroll, M. Murphy, J. Devine, J. Gardner, and S. R.S.J. (1998), Experimental phase equilibria constraints on pre-eruptive storage conditions of the Soufrière Hills magma, *Geophys. Res. Lett.*, *25*(18), 3437–3440, doi:10.1029/98GL00856. 1.7.1
- Baxter, P., and A. Gresham (1997), Deaths and injuries in the eruption of Galeras Volcano, Columbia, 14 January 1993, *J. Volcanol. Geotherm. Res.*, *77*, 325–338. 1.4
- Bean, C., I. Lokmer, and G. O’Brien (2008), Influence of near-surface volcanic structure on long-period seismic signals and on moment tensor inversion: Simulated examples from Mount Etna, *Journal of Geophysical Research*, *113*, doi:10.1029/2007JB005468. 1.6.3, 5
- Benoit, J., and S. McNutt (1997), New constraints on source processes of volcanic tremor at Arenal Volcano, Costa Rica, using broadband seismic data, *Geophys. Res. Lett.*, *24*, 449–452. 1.4.1
- Biot, M. (1952), Propagation of elastic waves in a cylindrical bore containing a fluid, *J. Appl. Phys.*, *42*, 82–92. 1.5.2
- Blong, R. (1982), *The time of darkness: Local legends and Volcanic Reality in Papua New Guinea*, Australian National University Press. 1.1
- Burlini, L., S. Vinciguerra, G. Di Torro, G. De Natale, P. Meredith, and J. Burgh (2007), Seismicity preceding volcanic eruptions: New experimental insights, *Geology*, *35*, 183–186. 1.3

- Burridge, R., and L. Knopoff (1964), Body force equivalents for seismic dislocation, *Bull. Seismol. Soc. Am.*, *54*, 1875–1888. 1.6.3
- Calder, E., R. Lockett, R. Sparks, and B. Voight (2002), *The Eruption of Soufrière Hills Volcano, Montserrat, from 1995 to 1999*, vol. 21, chap. Mechanisms of lava dome instability and generation of rockfalls and pyroclastic flows at Soufrière Hills Volcano, Montserrat, pp. 173–190, Geological Society Memoirs, London. 1.7.2
- Calder, E., J. Cortés, J. Palma, and R. Lockett (2005), Probabilistic analysis of rockfall frequencies during an andesite lava dome eruption: The Soufrière Hills Volcano, Montserrat, *Geophys. Res. Lett.*, *32*(16), L16,309. 1.7.2
- Carn, S., R. Watts, G. Thompson, and G. Norton (2004), Anatomy of a lava dome collapse: the 20 March 2000 event at Soufrière Hills Volcano, Montserrat, *J. Volcanol. Geotherm. Res.*, *131*(3-4), 241–264. 1.7.1
- Cesca, S., and S. Heimann (2013), A practical on moment tensor inversion using the Kiwi tools, *Tech. rep.*, Helmholtz Centre Potsdam, GFZ German Research Centre for Geosciences. 5.1, 5.1.2, 5.1.4, 7.5
- Cesca, S., J. Battaglia, T. Dahm, E. Tessmer, S. Heimann, and P. Okubo (2008), Effects of topography and crustal heterogeneities on the source estimation of LP events at Kilauea volcano, *Geophys. J. Int.*, *172*, 1219–1236, doi:10.1111/j.1365-246X.2007.03695.x. 5.1.1
- Cesca, S., S. Heimann, L. Stammler, and T. Dahm (2010), Automated procedure for point and kinematic source inversion at regional distances, *J. Geophys. Res.*, *115*, B6304, doi:10.1029/2009JB006450. 5.1, 5.1.2, 5.1.4, 6.4.1, 7.5
- Cesca, S., A. Rohr, and T. Dahm (2013), Discrimination of induced seismicity by full moment tensor inversion and decomposition, *J. Seismol.*, *17*(1), 147–163, doi:10.1007/s10950-012-9305-8. 6.4.2
- Chouet, B. (1986), Dynamics of a fluid-driven crack in three dimensions by the finite difference method, *J. Geophys. Res.*, *91*, 13,967–13,992. 1.5.2, 1.5.2, 1.5.2
- Chouet, B. (1988), Resonance of a fluid-driven crack: Radiation properties and implications for the source of long-period events and harmonic tremor, *J. Geophys. Res.*, *93*(B5), 4375–4400. 1.5.2, 1.5.2, 1.5.2
- Chouet, B. (1996a), Long-period volcano seismicity, its source and use in eruption forecasting, *Nature*, *380*, 309–316, doi:10.1038/380309a0. 1.4, 1.4.1, 1.5, 7.3
- Chouet, B. (1996b), New methods and future trends in seismological volcano monitoring, *Monitoring and Mitigation of Volcano Hazards*, pp. 23–97. 1.4.1, 1.5, 1.5.2, 1.5.2, 1.6.5, 2.3.1, 3.2.2, 5.2.2, 5.3, 7.1, 7.3
- Chouet, B., and B. Julian (1985), Dynamics of an expanding fluid-filled crack, *J. Geophys. Res.*, *90*(B13), 11,187–11,198. 1.5.2
- Chouet, B., and R. Matoza (2011), A multi-decadal view of seismic methods for detecting precursors of magma movement and eruption, *J. Volc. Geoth. Res.*, *252*, 108–175. 5, 5.1.1
- Chouet, B., R. Page, C. Stephens, J. Lahr, and J. Power (1994), Precursory swarms of long-period events at Redoubt volcano (1989–1990), Alaska: Their origin and use as a forecasting tool, *J. Volcanol. Geotherm. Res.*, *62*, 95–135. 1.4, 1.5.2, 6
- Chouet, B., P. Dawson, T. Ohminato, M. Martini, G. Saccorotti, F. Giudicepietro, G. De Luca, G. Milana, and R. Scarpa (2003), Source mechanisms of explosions at Stromboli Volcano, Italy, determined from moment-tensor inversions of very-long-period data, *Journal of Geophysical Research*, *108*, 2019–2042, doi:10.1029/2002JB001919. 1.3.1, 1.6.3

- Chung, W., and H. Kanamori (1980), Variation of seismic source parameters and stress drops within a descending slab and its implications in plate mechanics, *Phys. Earth Planet. Interiors*, *23*, 134–159. 5.1
- Cole, P., V. Bass, T. Christopher, C. Eligon, M. Fergus, L. Gunn, H. Odbert, R. Robertson, R. Simpson, R. Stewart, A. Stinton, J. Stone, R. Syer, R. Watts, and P. Williams (2010), Report to the Scientific Advisory Committee on Montserrat Volcanic Activity, Open-file Report 10/01, *Tech. rep.*, Montserrat Volcano Observatory. 1.7.1
- Collier, L. (2005), The interaction of gas-charged magma and seismic waves, Ph.D. thesis, The University of Leeds. 1.4, 1.5.2
- Collier, L., and J. Neuberg (2006), Incorporating seismic observations into 2D conduit flow modelling, *J. Volcanol. Geotherm. Res.*, *152*, 331–346. 1.5.1, 2.2, 4.2.2
- Dahm, T., and F. Krüger (2014), Moment tensor inversion and moment tensor interpretation, *New Manual of Seismological Observatory Practice 2*, pp. 1–38. 5.1
- De Barros, L., I. Lokmer, and C. Bean (2013), Origin of spurious single forces in the source mechanism of volcanic seismicity, *Journal of Volcanology and Geothermal Research*. 1.6.3
- Dingwell, D. (1996), Volcanic dilemma: Flow or blow?, *Science*, *273*(5278), 1054–1055, doi:10.1126/science.273.5278.1054. 1.5.1, 2.2, 7.2
- Doyle, E. (2003), Characteristics of low frequency events at Montserrat, Master’s thesis, School of Earth Sciences & School of the Environment. 6.2
- Druitt, T., S. Young, B. Baptie, C. Bonadonna, E. Calder, A. Clarke, P. Cole, C. Harford, R. Herd, R. Luckett, G. Ryan, and B. Voight (2002), *The Eruption of Soufrière Hills Volcano, Montserrat, from 1995 to 1999*, vol. 21, chap. Episodes of cyclic Vulcanian explosive activity with fountain collapse at Soufrière Hills Volcano, Montserrat, pp. 281–306, Geological Society Memoirs, London. 1.7.1
- Dziewonski, A., and D. Anderson (1981), Preliminary reference Earth model, *Phys. Earth Planet. Inter.*, *25*, 297–356. 2.1.2
- Dziewonski, A., and H. Woodhouse (1981), An experiment in systematic study of global seismicity: Centroid-moment tensor solutions for 201 moderate and large earthquakes of 1981, *J. Geophys. Res.*, *88*, 3247–3271, doi:10.1029/JB088iB04p03247. 5.1.1
- Eichelberger, J. (1995), Silicic volcanism: Ascent of viscous magmas from crustal reservoirs, *Ann. Rev. Earth Planet. Sci.*, *23*(1), 41–63. 1.5.2
- Elgasri, S., A. Ayadi, and F. Elhalouani (2011), Effect of die geometry on helical defect during extrusion of PDMS across a radial flow upstream the contraction, *Journal of Non-Newtonian Fluid Mechanics*, *166*(23-24), 1415–1420. 4
- Fehler, M., and B. Chouet (1982), Operation of a digital seismic network on Mount St. Helens Volcano and observations of long-period seismic events that originate under the volcano, *Geophys. Res. Lett.*, *9*, 1017–1020. 1.5
- Ferrazzini, V., and K. Aki (1987), Slow waves trapped in a fluid-filled crack: implications for volcanic tremor, *J. Geophys. Res.*, *92*, 9215–9223. 1.5.2, 1.5.2, 1.5.2
- Fischer, T., M. Morrissey, M. Calvache, D. G’omez, R. Torres, J. Stix, and S. Williams (1994), Correlations between SO₂ flux and long-period seismicity at Galeras volcano, *Nature*, *368*, 135–137. 1.4, 1.5.2
- Gilbert, F. (1970), Excitation of the normal modes of the Earth by earthquake sources, *The Geophysical Journal of the Royal Astronomical Society*, *22*, 223–226. 1.6.1
- Gilbert, G. (1984), A theory of the earthquakes of the Great Basin, with a practical application, *American Journal of Science*, *27*, 49–53. 1.6.4

- Godano, M., T. Bardainne, M. Regnier, and A. Deschamps (2011), Moment-tensor determination by nonlinear inversion of amplitudes, *Bull. Seism. Soc. Am.*, *93*, 2432–2444. 5
- Gomberg, J., K. Shedlock, and S. Roecker (1990), The effect of S-wave arrival times on the accuracy of hypocenter estimation, *Bull. Seism. Soc. Am.*, *80*, 1605–1628. B.1.1
- Gómez, M., and C. Torres (1997), Unusual low-frequency volcanic seismic events with slowly decaying coda waves observed at Galeras and other volcanoes, *J. Volcanol. Geotherm. Res.*, *77*, 173–193. 1.5
- Gonnermann, H., and M. Manga (2003), Explosive volcanism may not be an inevitable consequence of magma fragmentation, *Nature*, *39*, 321–356. 2.2
- Gonnermann, H., and M. Manga (2007), The fluid mechanics inside a volcano, *Annual Review of Fluid Mechanics*, *39*, 321–356. 2.2
- Goto, A. (1999), A new model of volcanic earthquakes at Unzen Volcano: melt rupture model, *Geophys. Res. Lett.*, *26*, 2541–2544. 1.4
- Green, D. (2005), Multi-parameter monitoring and modelling of cyclic volcanic activity, Ph.D. thesis, The University of Leeds. 1.3, 1.4.2, 1.7.2, 2.1.2, 5.3, 6.2, 6.3, 6.4, 6.5
- Green, D., and J. Neuberg (2006), Waveform classification of volcanic low-frequency earthquake swarms and its implication at Soufrière Hills Volcano, Montserrat, *J. Volcanol. Geotherm. Res.*, *153*, 51–63. 1.4.1, 1.5.1, 2.2, 4, 4.2, 7.1
- Green, D., J. Neuberg, and V. Cayol (2006), Shear stress along the conduit wall as a plausible source of tilt at Soufrière Hills Volcano Montserrat, *Geophys. Res. Lett.*, *33*(L10306). 1.4.2, 1.7.2
- Hale, A., E. Calder, S. Loughlin, G. Wadge, and G. Ryan (2009), Modelling the lava dome extruded at Soufrière Hills Volcano, Montserrat, August 2005–May 2006: Part II: Rockfall activity and talus deformation, *J. Volcanol. Geotherm. Res.*, *187*(1–2), 69–84. 1.7.2
- Hammer, C. (2007), Wellenformigenschaften seismischer Signale vulkanischen Ursprungs im Nah- und Fernfeld, Master’s thesis, Universität Potsdam. 3.3.1
- Hammer, C., and J. Neuberg (2009), On the dynamical behaviour of low-frequency earthquake swarms prior to a dome collapse of Soufrière Hills Volcano, Montserrat, *Geophys. Res. Lett.*, *36*, doi:10.1029/2008GL036837. 1.4.1, 1.7.2, 5.3, 7.3
- Hanks, T., and H. Kanamori (1979), A moment magnitude scale, *J. Geophys. Res.*, *84*(B5), 2348–2350, doi:10.1029/2FJB084iB05p02348. 2.3.1
- Harford, C., M. Pringle, R. Sparks, and S. Young (2002), *The eruption of Soufrière Hills Volcano, Montserrat, from 1995 to 1999*, vol. 21, chap. The volcanic evolution of Montserrat using $^{40}\text{Ar}/^{39}\text{Ar}$ geochronology, pp. 93–113, Geological Society of London Memoir. 1.7.1
- Harrington, R., and E. Brodsky (2007), Volcanic hybrid earthquakes that are brittle-failure events, *Geophys. Res. Lett.*, *34*(6), doi:10.1029/2006GL028714. 1.5
- Hautmann, S., J. Gottsmann, R. Sparks, A. Costa, O. Melnik, and B. Voight (2009), Modelling ground deformation caused by oscillating overpressure in a dyke conduit at Soufrière Hills Volcano, Montserrat, *Tectonophysics*, *471*, 87–95. 2.4.2, 6.6
- Heimann, S. (2011), A robust Method to estimate kinematic earthquake source parameters., Ph.D. thesis, University of Hamburg, Hamburg, Germany. 2.1, 5.1, 5.1.4
- Hellweg, M. (2003), The polarization of volcanic seismic signals: medium or source?, *J. Volcanol. Geotherm. Res.*, *128*, 159–176. 1.4.1

- Herd, R., E. M., and V. Bass (2003), Catastrophic lava dome failure at Soufrière Hills Volcano, Montserrat, 12-13 July 2003, *J. Volcanol. Geotherm. Res.*, *148*(3-4), 234–252. 1.7.1
- Holland, A., I. Watson, J. Phillips, L. Caricchi, and M. Dalton (2011), Degassing processes during lava dome growth: Insights from Santiaguito lava dome, Guatemala, *J. Volcanol. Geotherm. Res.*, *202*(1-2), 153–166. 2.4.2
- Hutton, J. (1795), *Theory of the Earth with proofs and illustrations*, WM Creech, Edinburgh. 1.1
- Iguchi, M. (1994), A vertical expansion source model for mechanisms of earthquakes originating in the magma conduit of an andesitic volcano, Japan, *Bull. Volcanol. Soc. Jpn.*, *39*, 49–67. 3.6, 7.1
- Iverson, R., D. Dzurisin, C. Gardner, T. Gerlach, R. LaHusen, M. Lisowski, J. Major, S. Malone, J. Messerich, S. Moran, J. Pallister, A. Qamar, S. Schilling, and J. Vallance (2006), Dynamics of seismogenic volcanic extrusion at Mount St. Helens in 2004-05, *Nature*, *444*, 439–443. 1.4, 1.5.1
- Jellinek, M., and D. Bercovici (2011), Seismic tremors and magma wagging during explosive volcanism, *Nature*, *470*, 522–525, doi:10.1038/nature09828. 1.4, 7.3
- Johnson, J. (2007), Investigations into the trigger mechanism of long-period events at Soufrière Hills Volcano, Montserrat, Master's thesis, School of Earth and Environment. 6.3
- Jolly, A., G. Thompson, and G. Norton (2002), Locating pyroclastic flows on Soufrière Hills Volcano, Montserrat, West Indies, using amplitude signals from high dynamic range instruments, *J. Volcanol. Geotherm. Res.*, *118*(3-4), 299–317. 1.7.2
- Jousset, P., J. Neuberg, and S. Sturton (2003), Modelling the time-dependent frequency content of low-frequency volcanic earthquakes, *J. Volcanol. Geophys. Res.*, *128*, 201–223. 1.4, 1.5.2
- Jousset, P., A. Jolly, and J. Neuberg (2004), Modelling low-frequency earthquakes in a viscoelastic medium with topography, *Geophys. J. Int.*, *159*, 776–802. 1.5.2
- Julian, B. (1994), Volcanic tremor: Nonlinear excitations by fluid flow, *J. Geophys. Res.*, *99*(B6), 11,859–11,877. 1.4, 1.5.1
- Julian, B., A. Miller, and G. Foulger (1998), Non-double-couple earthquakes: 1. Theory, *Rev. Geophys.*, *36*(4), 525–549. 3
- Kay, D., P. Carreau, P. Lafleur, L. Robert, and B. Vergnes (2003), A study of stick-slip phenomenon in single-screw extrusion of linear polyethylene, *Polimer Engineering and Science*, *43*(1), 78–90. 4
- Kendrick, J., Y. Lavallée, K.-U. Hess, S. De Angelis, A. Ferk, H. Gaunt, D. Meredith, B. Dingwell, and R. Leonhardt (2014), Seismogenic frictional melting in the magmatic column, *Solid Earth*, *5*, 199–208, doi:10.5194/se-5-199-2014. 2.2, 3.6, 7.2
- Kenedi, C., R. Sparks, P. Malin, P. Voight, S. Dean, T. Minshull, M. Paulatto, C. Perice, and E. Shalev (2010), Contrasts in morphology and deformation offshore Montserrat: new insights from the SEA-CALIPSO marine cruise data, *Geophys. Res. Lett.*, *37*, doi:10.1029/2010GL043925. 6.5
- Klein, F. (2002), User's Guide to HYPOINVERSE-2000, a Fortran Program to solve for earthquake locations and magnitudes, *USGS Numbered Series*. B.1.1
- Kruger, L. (2011), Automated inversion of long period signals from shallow volcanic and induced seismic events, Ph.D. thesis, University of Hamburg, Hamburg, Germany. 5

- Kumagai, H., B. Chouet, and M. Nakano (2002), Waveform inversion of oscillatory signatures in long-period events beneath volcanoes, *J. Geophys. Res.*, *107*(B11), 2156–2202, doi:10.1029/2001JB001704. 1.5.2, 5.1.3
- Kumagai, H., B. Chouet, and P. Dawson (2005), Source process of a long-period event at Kilauea volcano, Hawaii, *Geophys. J. Int.*, *161*(1), 243–254. 1.5.2
- Küpper, F. (1985), Theoretische Untersuchungen bei der Mehrfachaufstellung von Geophonen, *Geophys. Prospect*, *6*, 194–256. 2.6, 7.3
- Lawson, A. (1908), *The California Earthquake of April 18, 1906: Report of the State Earthquake Investigation Commission*, vol. 1, Carnegie Inst. of Washington, Washington, D. C. 1.6.4
- LeFriant, A., C. Harford, C. Deplus, G. Boudon, R. Sparks, R. Herd, and J.-C. Komorowski (2004), Geomorphological evolution of Montserrat (West Indies): importance of flank collapse and erosional processes, *J. Geol. Soc. London*, *161*(1), 147–160. 1.7.1
- Loughlin, S., T. Christopher, R. Luckett, L. Jones, and B. Baptie (2007), Large volume dome collapse at the Soufrière Hills Volcano, Montserrat, 20 May 2006, in *Geophysical Research Abstracts*, vol. 9, p. 11090, European Geosciences Union, General Assembly 2007. 1.7.1
- Luckett, R. (2009), Seismic data from the Montserrat eruption at BGS, *Tech. rep.*, British Geological Survey Open Report. 6.1
- Maruyama, T. (1963), On the force equivalents of dynamic elastic dislocations with reference to the earthquake mechanism, *Bull. Earthquake Res. Inst. Univ. Tokyo*, *41*, 467–486. 1.6.3
- McNutt, S. (2002), Volcanic Seismology, *Ann. Rev. Earth Planet. Sci.*, *33*(1), 461–491. 1.3
- Miller, A., R. Stewart, R. White, R. Luckett, B. Baptie, W. Aspinall, J. Latchman, L. Lynch, and B. Voigth (1998a), Seismicity associated with dome growth and collapse at the Soufrière Hills Volcano, Montserrat, *Geophys. Res. Lett.*, *25*, 3401–3404. 1.3.1, 1.4, 1.4.1, 1.7.2, 5, 6
- Miller, A., G. Foulger, and B. Julian (1998b), Non-double-couple earthquakes: 2. Observations, *Rev. Geophys.*, *36*(4), 551–568. 3.6
- Molina, I., H. Kumagai, and H. Yepes (2004), Resonances of a volcanic conduit triggered by repetitive injections of ash-laden gas, *Geophys. Res. Lett.*, *31*(L03603). 1.4
- Molina, I., H. Kumagai, A. Garea-Aristizbal, M. Nakano, and P. Mohtes (2008), Source process of very-long-period events accompanying long-period signals at Cotopaxi Volcano, Ecuador, *J. Volcanol. Geotherm. Res.*, *176*(1), 119–133. 1.5.2
- Morrissey, M., and B. Chouet (2001), Trends in long-period seismicity related to magmatic fluid compositions, *J. Volcanol. Geotherm. Res.*, *108*, 265–281. 1.5.2
- Nakanishi, I., Y. Hanakago, and T. Moriya (1992), Performance test on long-period moment tensor determination for near earthquakes by a sparse local network, *Geophys. Res. Lett.*, *18*(2), 223–226. 5.1.1
- Nakano, M., and H. Kumagai (2005), Waveform inversion of volcano-seismic signals assuming possible source geometries, *Geophys. Res. Lett.*, *32*(12), L12,302. 1.5.2
- Nakano, M., H. Kumagai, and B. Chouet (2003), Source mechanism of long-period events at Kusatsu-Shirane Volcano, Japan, inferred from waveform inversion of the effective excitation functions, *J. Volcanol. Geophys. Res.*, *122*(3-4), 149–164. 1.5.2

- Nakano, M., H. Kumagai, B. Chouet, and P. Dawson (2007), Waveform inversion of volcano-seismic signals for an extended source, *J. Geophys. Res.*, *112*(B2), B02,306. 5
- Nettles, M., and Ekström (1998), Faulting mechanism of anomalous earthquakes near Bardarbunga Volcano, Iceland, *J. Geophys. Res.*, *103*, 17,973–17,983. 1.6.5
- Neuberg, J. (2000), Characteristics and causes of shallow seismicity in andesite volcanoes, *Phil. Trans. R. Soc. Lond.*, *358*, 1533–1546. 1.11, 1.7.2, 7.3
- Neuberg, J. (2011), *Encyclopedia of Solid Earth Geophysics*, chap. Earthquakes, Volcanogenic, pp. 261–269, Encyclopedia of Earth Sciences Series, Springer. 1.3
- Neuberg, J., and C. O’Gorman (2002), *The eruption of Soufrière Hills Volcano, Montserrat, from 1995 to 1999*, vol. 21, chap. A model of the seismic wavefield in gas-charged magma: application to Soufrière Hills volcano, Montserrat, pp. 603–609, Geological Society of London Memoir. 1.5.2
- Neuberg, J., and T. Pointer (2000), Effects of volcano topography on seismic broadband waveforms, *Geophys. J. Int.*, *143*, 239–248. 5.1.1
- Neuberg, J., R. Luckett, M. Ripepe, and T. Braun (1994), Highlights from a seismic broadband array on Stromboli Volcano, *Geophysical Research Letters*, *21*(9), 749–752. 1.3
- Neuberg, J., B. Baptie, R. Luckett, and R. Stewart (1998), Results from the broadband seismic network on Montserrat, *Geophysical Research Letters*, *25*, 3661–3664. 1.4, 1.4.1, 1.5.2, 1.7.2, 6, 6.1
- Neuberg, J., R. Luckett, B. Baptie, and K. Olsen (2000), Models of tremor and low-frequency earthquake swarms on Montserrat, *J. Volcanol. Geotherm. Res.*, *101*, 83–104. 1.4.1, 1.4.1, 1.4.2, 1.5, 1.5.2, 1.5.2, 1.7, 1.7.2
- Neuberg, J., H. Tuffen, D. Collier, T. Powell, and D. Dingwell (2006), The trigger mechanism of low-frequency earthquakes on Montserrat, *J. Volcanol. Geotherm. Res.*, *153*, 37–50. 1.4, 1.4.1, 1.4.2, 1.5.1, 1.10, 1.7.2, 2.2, 2.2, 2.4.1, 2.6, 2.6, 3.6, 4.2.2, 7.1, 7.2, 7.3
- O’Brien, G., and C. Bean (2009), Volcano topography, structure and intrinsic attenuation: their relative influences on a simulated 3D visco-elastic wavefield, *Journal of Volcanology and Geothermal Research*, *183*, 123–137. 5.1.1
- Ohminato, T., B. Chouet, P. Dawson, and S. Kedar (1998), Waveform inversion of very long period impulsive signals associated with magmatic injection beneath Kilauea Volcano, Hawaii, *Journal of Geophysical Research*, *103*, doi:10.1029/98JB01122. 1.6.3, 5, 5.1
- Ohminato, T., M. Takeo, H. Kumagai, T. Yamashina, J. Oikawa, E. Koyama, H. Tsuji, and T. Urabe (2006), Vulcanian eruptions with dominant single force components observed during the Asama 2004 volcanic activity in Japan, *Earth, Planets, and Space*, *58*, 583–593. 1.6.3
- Ottenmöller, L. (2008), Seismic hybrid swarm precursory to a major lava dome collapse: 9–12 July 2003, Soufrière Hills volcano, Montserrat, *J. Volcanol. Geotherm. Res.*, *177*, 903–910. 1.5.1, 4.2
- Piau, J.-M., S. Nigen, and N. El Kissi (2000), Effect of die entrance filtering on mitigation of upstream instability during extrusion of polymer melts, *Journal of Non-Newtonian Fluid Mechanics*, *91*(1), 37–57. 4
- Powell, T., and J. Neuberg (2003), Time dependent features in tremor spectra, *J. Volcanol. Geotherm. Res.*, *128*, 177–185. 1.4.1

- Rea, W. (1974), The volcanic geology and petrology of Montserrat, West Indies, *J. Geol. Soc. London*, *130*, 341–366. 1.7.1
- Ricker, N. (1953), The form and laws of propagation of seismic wavelets, *Geophysics*, *18*, 10–40. 2.6, 7.3
- Robertson, R., W. Aspinall, R. Herd, G. Norton, R. Sparks, and S. Young (2000), The 1995–1998 eruption of Soufrière Hills Volcano, Montserrat, WI, *Phil. Trans. R. Soc. Lond. A*, *358*, 1619–1637. 6.2
- Roman, D., and K. Cashman (2006), The origin of volcano-tectonic earthquake swarms, *Geology*, *34*(6), 457–460. 1.3.1, 1.7.2
- Roman, D., S. De Angelis, J. Latchman, and R. White (2008), Patterns of volcanotectonic seismicity and stress during the ongoing eruption of the Soufrière Hills Volcano Montserrat (1995–2007), *J. Volcanol. Geotherm. Res.*, *173*, 230–244. 1.7.2
- Rowe, C., C. Thurber, and R. White (2004), Dome growth behavior at Soufrière Hills Volcano, Montserrat, revealed by relocation of volcanic event swarms, 1995–1996, *J. Volcanol. Geotherm. Res.*, *134*(3), 199–221. 1.5.1, 4.2, 6.5
- Sakuma, S., T. Kajiwara, S. Nakada, K. Uto, and H. Shimizu (2008), Drilling and logging results of USDP-4: Penetration into the volcanic conduit of Unzen volcano, Japan, *J. Volcanol. Geotherm. Res.*, *175*(1-2), 1–12. 2.4.2
- Sawada, M. (1994), B-type and explosion earthquakes observed at Asama volcano, central Japan, *J. Volcanol. Geotherm. Res.*, *63*(3-4), 111–128. 1.4, 6
- Scherbaum, F. (2001), *Of Poles and Zeros*, Kluwer Academic Publishers. A.2, A.2, A.2
- Schmincke, H.-U. (1982), *Rheinisch-Westfälische Akademie der Wissenschaft*, vol. Vorträge N315, chap. Vulkane und ihre Wurzeln, pp. 35–78, Westdeutscher Verlag. 1.1, 1.1
- Scrope, G. (1825), *Considerations on volcanoes. The probable cause of their phenomena, the laws which determine their march, the disposition of their products, and their connexion with the present state and past history of the globe; leading to the establishment of a new theory of the Earth*, W. Philipps, London. 1.1
- Shearer, P. (1999), *Introduction to Seismology*, Cambridge University Press. B.1.1
- Sipkin, S. (1982), Estimation of earthquake source parameters by the inversion of waveform data: synthetic waveforms, *Phys. Earth. planet. Inter.*, *30*, 242–259. 5.1.1
- Smith, P. (2010), Attenuation of volcanic seismic signals, Ph.D. thesis, The University of Leeds, UK. 1.5.2, 2.1.2
- Sparks, R. (2003), Forecasting volcanic eruptions, *Earth and Planetary Science Letters*, *210*. 1.3
- Stein, S., and M. Wysession (2003), *An Introduction to Seismology, Earthquakes and Earth Structure*, Blackwell Publishing Ltd. Oxford, U.K. 2.1.1, 3.1, 3.1, 3.1, 3.2
- Stephens, C., B. Chouet, R. Page, J. Lahr, and J. Power (1994), Seismological aspects of the 1989–1990 eruptions at Redoubt Volcano, Alaska: the SSAM perspective, *J. Volcanol. Geotherm. Res.*, *62*, 153–182. 1.4, 6
- Stewart, R., T. Christopher, V. Clouard, S. De Angelis, F. Dondin, N. Fournier, E. Joseph, J.-C. Komorowski, R. Robertson, and R. Syers (2008), Report to the Scientific Advisory Committee on Montserrat Volcanic Activity, Open-file Report 08/02, *Tech. rep.*, Montserrat Volcano Observatory. 1.7.2

- Takei, Y., and M. Kumazawa (1994), Why have the single force and torque been excluded from seismic source models?, *Geophysical Journal International*, *118*, 20–30. 1.6.3
- Thomas, M., and J. Neuberg (2012), What makes a volcano tick - A first explanation of deep multiple seismic sources in ascending magma, *Geology*, *40*, 351–354, doi:10.1130/G32868.1. 2.2, 4, 4.2.2, 4.2.3, 6.6, 7.1, 7.2
- Tuffen, H., D. Dingwell, and H. Pinkerton (2003), Repeated fracture and healing of silicic magma generate flow banding and earthquakes, *Geology*, *31*, 1089–1092. 2.2, 7.2
- Tuffen, H., R. Smith, and P. Sammonds (2008), Evidence for seismogenic fracture of silicic magma, *Nature*, *453*, 511–514. 1.5.1, 7.2
- Umakoshi, K., N. Takamura, N. Shinzato, K. Uchida, N. Matsuwo, and H. Shimizu (2008), Seismicity associated with the 1991-1995 dome growth at Unzen Volcano, Japan, *J. Volcanol. Geotherm. Res.*, *175*(1-2), 91–99. 1.5.1
- Varley, N., R. Aràmbula-Mendoza, G. Reyes Dávila, J. Stevenson, and R. Harwood (2010), Long-period seismicity during magma movement at Volcàn de Colima, *Bull. Volcanol.*, pp. 1–15. 1.5.1
- Vitaliano, D. (1973), *Legends of the earth: their geologic origins*, Bloomington, London: Indiana university Press. 1.1
- Voight, B., R. Hoblitt, A. Clarke, A. Lockhart, A. Miller, L. Lynch, and J. McMahon (1998), Remarkable cyclic ground deformation monitored in real-time on Montserrat, and its use in eruption forecasting, *Geophys. Res. Lett.*, *25*(18), 3405–3408. 1.4.2, 1.7.1
- Wadge, G., R. Herd, G. Ryan, E. Calder, and J.-C. Komorowski (2010), Lava production at Soufrière Hills Volcano, Montserrat: 1995-2009, *Geophys. Res. Lett.*, *37*, doi:10.1029/2009GL041466. 1.7.1
- Waite, G., B. Chouet, and P. Dawson (2008), Eruption dynamics at Mount St. Helens imaged from broadband seismic waveforms: Interaction of the shallow magmatic and hydrothermal systems, *Journal of Geophysical Research*, *113*, doi:10.1029/2007JB005259. 1.5.2, 1.6.5, 2.3.1, 3.2.2, 3.6, 5.1.3, 5.2.2, 5.3, 7.1, 7.3
- Wang, R. J. (1999), A simple orthonormalization method for stable and efficient computation of Green's functions, *Bulletin of the Seismological Society of America*, *89*, 733–741. 2.1
- Watts, R., R. Herd, R. Sparks, and S. Young (2002), Growth patterns and emplacement of the andesitic lava dome at Soufrière Hills Volcano, Montserrat, *The Eruption of Soufrière Hills Volcano, Montserrat from 1995 to 1999*, *21*, 115–152. 1.7.1, 1.7.2, 6.2
- Webb, S., and D. Dingwell (1990), Non-Newtonian rheology of igneous melts at high stresses and strain rates: Experimental results for rhyolite, andesite, basalt, and nephelinite, *J. Geophys. Res.: Solid Earth*, *95*(B10), 15,695–15,701. 2.2
- White, R., A. Miller, L. Lynch, and J. Power (1998), Observations of hybrid seismic events at Soufrière Hills Volcano, Montserrat: July 1995 to September 1996, *Geophys. Res. Lett.*, *25*(19), 3657–3660. 1.7.2
- Yamamoto, M., H. Kawakatsu, S. Kaneshima, T. Mori, T. Tsutsui, Y. Sudo, and Y. Morita (1999), Detection of a crack-like conduit beneath the active crater at Aso Volcano Japan, *Geophys. Res. Lett.*, *26*(24), 3677–3680. 1.3
- Young, S., R. Sparks, W. Aspinall, L. Lynch, A. Miller, T. Robertson, and J. Shepherd (1998), Overview of the eruption of Soufrière Hills Volcano, Montserrat, 18 July 1995 to December 1997, *Geophys. Res. Lett.*, *25*, 3677–3680. 1.7.1, 6.2

-
- Zhu, L. (2003), Recovering permanent displacements from seismic records of the June 9, 1994 Bolivia deep earthquake, *Geophys. Res. Lett.*, *30*(14). A.2
- Zimanowski, B. (1998), *From Magma to Tephra*, chap. Phreatomagmatic explosions, pp. 25–53, Elsevier. 1.4, 1.5.1